Development of X-nuclei Hyperpolarised Contrast Agents for Magnetic Resonance Imaging using Dynamic Nuclear Polarisation

Catriona H. E. Rooney

Wadham College
University of Oxford

A thesis submitted in partial fulfilment of the requirements for the degree of
Doctor of Philosophy

Trinity 2024

Abstract

Magnetic Resonance Imaging (MRI) is a non-invasive clinical imaging modality that suffers from inherently low sensitivity due to low spin population differences. Dynamic Nuclear Polarisation is a technique that "hyperpolarises" or redistributes spins to achieve population differences greater than that obtained at thermal equilibrium to achieve enhancements in MR signal. Dissolution Dynamic Nuclear Polarisation (d-DNP) facilitates this through the use of low temperature, high magnetic field strength, microwave irradiation, and culminates in the rapid dissolving of hyperpolarised samples with a hot pressurised solvent to generate injectable hyperpolarised contrast agents (HCAs). Current limitations in the preclinical development of HCAs, however, include: low throughput, low levels of signal enhancement, and rapid signal decay rates. Thus, for d-DNP to be more widely adopted these limitations need to be addressed and the versatility of the technique broadened.

Herein, three different HCAs were developed each with a different nucleus of interest and a different potential clinical application: ^{29}Si in the form of silicon nanoparticles (SiNPs), ^{13}C-alanine, and ^{15}N-urea. The SiNP HCA was developed for use as a theragnostic agent and aspects across the full d-DNP workflow were targeted for optimisation. The strategies which appeared to have greatest impact on addressing current limitations were the consideration of the microwave power used and the addition of 30 mM TEMPO during sample preparation. Putting all the optimisations into practice, a liquid state nuclear T_1 relaxation time of >30 minutes was measured *in vitro* at room temperature. The second HCA, ^{13}C-alanine, was developed as an alternative metabolic probe using a novel method for the generation of endogenous radicals. *In vitro*, polarisation levels of 17.7% and 12.4% were recorded with corresponding liquid state nuclear T_1 relaxation times of 77.3 s and 63.5 s. *In vivo*, the signal was comparable to that recorded from samples containing an exogenous chemical radical species. Lastly, the optimised ^{15}N-urea HCA resulted in polarisation levels of 3.2 ± 1.1 % and a nuclear T_1 relaxation time of 78 ± 13 s *in vitro* at room temperature. The preparation was subsequently tested as a perfusion agent using an *in vivo* stroke model.

It is hoped that the work set out in this thesis could be applied to other compounds for their development as X-nuclei HCAs and provide a framework to acquire new, clinically relevant information and widen the applications of hyperpolarised MRI.

Development of X-nuclei Hyperpolarised Contrast Agents for Magnetic Resonance Imaging using Dynamic Nuclear Polarisation

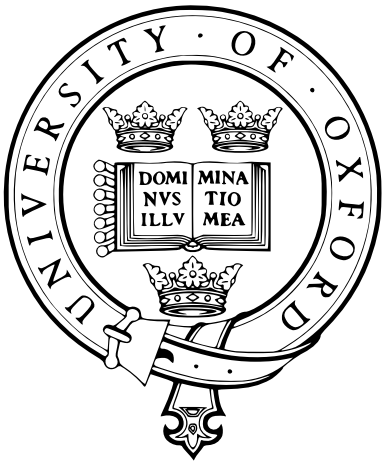

Catriona H. E. Rooney

Wadham College

University of Oxford

A thesis submitted in partial fulfilment of the requirements for the degree of

Doctor of Philosophy

Trinity 2024

To my family.

Acknowledgements

Institutional

The research presented in this thesis was made possible through the funding of the Medical Research Council and Engineering and Physical Sciences Research Council as part of the Oxford Nottingham Biomedical Imaging Doctoral Training Centre.

Personal

First and foremost, my thanks must go to my supervisors **Professor Damian Tyler** and **Associate Professor Jack Miller**. Thank you for the guidance and endless encouragement you provided throughout my DPhil which continued even throughout the closure of the University during the course of the COVID-19 pandemic. One of your indirect teachings that I will take with me is that, when it comes to science, there is always room for humour.

I was fortunate to meet and work alongside many other wonderful people as part of the **Cardiac Metabolism Research Group** and the **Oxford Centre for Clinical Magnetic Resonance Research**. **Vicky Ball**, my desk neighbour, thank you for fueling me with "gf" goodies and positivity. **Nneoma Akaniro-Ejim**, thank you for all of the laughter, calmness, and for sharing your wisdom. **James Grist**, there are many things I could thank you for; for brevity I mention the wholesome Milo content. Thanks also go to **Claudia Montes Aparicio**, **Marcos Castro Guarda**, and **Ayaka Shinozaki** (to name a few!) for enriching my time at the University of Oxford in innumerable ways.

Some of the experiments presented here would not have been possible without the scientific discussions with and expertise of **Dr Justin Lau**, **Professor Kristoffer Petersson** and **Dr Iain Tullis**. Not to mention the support of **Jonathan Denton**, **Lee Boreham**, and others at the **Department of Physics workshop** to make my CAD dreams a reality in all spatial dimensions.

I am also thankful for the opportunity of international collaborations with **Professor Rachel Katz-Brull** and **Professor Christoffer Laustsen**. In particular, I wish to thank **Duy Anh Dang**, **Nichlas Vous Christensen**, **Esben Søvsø Szocska Hansen**, and the rest of the team at Aarhus University for hosting me and for their depth of knowledge and enthusiasm.

Outwith the lab, I extend my deepest gratitude to **Dr Shona Matthew** who took me on as a summer research student at Ninewells Hospital, Dundee whilst I was an undergraduate student at the University of St Andrews. Had it not been for that opportunity I would not have had this one.

I am, and will forever be, grateful to the friends who became extended family and to the family members whom I consider to be amongst the greatest of friends: **Indra Rudiansyah**, **Ujang Purnama**, **Maria Kreger Karabova**, **Philippa Sinclair**, **Sophie Berdugo**, **Joseph Agnew**, and **Claire Doyle**. A special mention goes to **Alyssa Shepherd**, not only for your endless wit, but also for your generosity of spirit. At the risk of sounding cliché I truly cannot put into words how much I value your friendship.

Javier Gilbert Jaramillo, la palabra "gracias" simplemente no es suficiente. Estaré siempre en deuda contigo por tu inquebrantable paciencia y confianza en mí.

Finally, I consider the unconditional love and support from my family whilst I navigated this doctorate (and all the years preceding it!) to be of the utmost importance. This research is dedicated to my parents, **Catherine** and **Edmund**, my brothers, **Aidan** and **Colin**, and beloved cat **Isabella Scoosh**.

Abstract

Magnetic Resonance Imaging (MRI) is a non-invasive clinical imaging modality that suffers from inherently low sensitivity due to low spin population differences. Dynamic Nuclear Polarisation is a technique that "hyperpolarises" or redistributes spins to achieve population differences greater than that obtained at thermal equilibrium to achieve enhancements in MR signal. Dissolution Dynamic Nuclear Polarisation (d-DNP) facilitates this through the use of low temperature, high magnetic field strength, microwave irradiation, and culminates in the rapid dissolving of hyperpolarised samples with a hot pressurised solvent to generate injectable hyperpolarised contrast agents (HCAs). Current limitations in the preclinical development of HCAs, however, include: low throughput, low levels of signal enhancement, and rapid signal decay rates. Thus, for d-DNP to be more widely adopted these limitations need to be addressed and the versatility of the technique broadened.

Herein, three different HCAs were developed each with a different nucleus of interest and a different potential clinical application: ^{29}Si in the form of silicon nanoparticles (SiNPs), ^{13}C-alanine, and ^{15}N-urea. The SiNP HCA was developed for use as a theragnostic agent and aspects across the full d-DNP workflow were targeted for optimisation. The strategies which appeared to have greatest impact on addressing current limitations were the consideration of the microwave power used and the addition of 30 mM TEMPO during sample preparation. Putting all the optimisations into practice, a liquid state nuclear T_1 relaxation time of >30 minutes was measured *in vitro* at room temperature. The second HCA, ^{13}C-alanine, was developed as an alternative metabolic probe using a novel method for the generation of endogenous radicals. *In vitro*, polarisation levels of 17.7% and 12.4% were recorded with corresponding liquid state nuclear T_1 relaxation times of 77.3 s and 63.5 s. *In vivo*, the signal was comparable to that recorded from samples containing an exogenous chemical radical species. Lastly, the optimised ^{15}N-urea HCA resulted in polarisation levels of 3.2 ± 1.1 % and a nuclear T_1 relaxation time of 78 ± 13 s *in vitro* at room temperature. The preparation was subsequently tested as a perfusion agent using an *in vivo* stroke model.

It is hoped that the work set out in this thesis could be applied to other compounds for their development as X-nuclei HCAs and provide a framework to acquire new, clinically relevant information and widen the applications of hyperpolarised MRI.

Research Outcomes

Patent

- J. Y. C. Lau, C. Laustsen, J. J. Miller, **C. H. E. Rooney**, D. J. Tyler. (2024) "A method of preparing a Magnetic Resonance Imaging (MRI) contrast agent for Dynamic Nuclear Polarization (DNP) being stable for weeks". European Patent Application No. 24168322.6

Peer-Reviewed Journal Articles

- "Ultra-high dose rate 6 MeV electron irradiation generates stable [1-13C]-alanine radicals suitable for medical imaging with dissolution Dynamic Nuclear Polarisation", **C. H. E. Rooney***, J. Y. C. Lau*, E. S. S. Hansen, N. V. Christensen, D. A. Dang, K. Petersson, I. Tullis, B. Vojnovic, S. Smart, J. Lewis, W. Myers, Z. Richardson, B. W. C. Kennedy, A. M. Bowen, L. B. Bertelsen, C. Laustsen, D. J. Tyler, J. J. Miller. arXiv:2504.16621 [physics.med-ph] (2025) Preprint; submitted to *Nature Communications*

- "Hyperpolarized Carbon 13 MRI: Clinical Applications and Future Directions in Oncology. Radiology: Imaging Cancer", S. S. Deen, **C. H. E. Rooney**, A. Shinozaki, J. McGing, J. T. Grist, D. J. Tyler, E. Serrão, & F. A. Gallagher. Radiology: Imaging Cancer (2023)

- "Directly Bound Deuterons Increase X-Nuclei Hyperpolarization using Dynamic Nuclear Polarization", **C. H. E. Rooney**, A. Gamliel, D. Shaul, D. J. Tyler, J. T. Grist, & R. Katz-Brull. ChemPhysChem (2023)

- "Assessing the effect of anesthetic gas mixtures on hyperpolarized ^{13}C pyruvate metabolism in the rat brain", R. Healicon*, **C. H. E. Rooney***, V. Ball, A. Shinozaki, J. J. Miller, S. Smart, D. Radford-Smith, D. Anthony, D. J. Tyler, & J. T. Grist. Magnetic Resonance in Medicine (2022)

* *Equal contribution*

Peer-Reviewed Conference Abstracts

- "6 MeV electron irradiated ^{13}C-alanine as a sterile, transportable probe with long-lived radicals for dissolution Dynamic Nuclear Polarization", **C. H. E. Rooney**, J. Y. C. Lau, B. W. C. Kennedy, A. M. Bowen, W. K. Myers, I. D. C. Tullis, K. Petersson, J. Lewis, D. A. Dang, N. V. Christensen, E. S. S. Hansen, C. Laustsen, D. J. Tyler & J. J. Miller. International Society of Magnetic Resonance in Medicine Annual Meeting (Singapore 2024)

- "Effect of Radical Structure and Concentration on the Hyperpolarization of Silicon Nanoparticles using Dynamic Nuclear Polarization", **C. H. E. Rooney**, J. J. Miller, & D. J. Tyler. British and Irish Chapter International Society of Magnetic Resonance in Medicine (Cardiff 2022)

- "Effect of Radical Concentration on the Hyperpolarization of Silicon Nanoparticles using Dynamic Nuclear Polarization", **C. H. E. Rooney**, J. J. Miller, & D. J. Tyler. International Society of Magnetic Resonance in Medicine Annual Meeting (Online 2021)

- "Optimisation of Silicon Nanoparticles as Hyperpolarized Contrast Agents for Magnetic Resonance Imaging", **C. H. E. Rooney**, D. J. Tyler, & J. J. Miller. Magnetic Resonance and Magnetic Phenomena in Chemical and Biological Physics. VI International School for Young Scientists (Online 2020)

Awards

- Medical Physics Group PhD Prize, Institute of Physics (2024)
  Annual prize awarded for an outstanding PhD thesis in medical physics. Judged by an expert panel on scientific excellence, originality, presentation quality, and research rigour.

Contents

List of Figures **xv**

List of Tables **xviii**

Glossary **xix**

1 Introduction **1**

1.1 Background 2
1.2 Fundamental properties of particles 3
1.2.1 Spin 3
1.2.2 Magnetic moment 6
1.3 The Zeeman effect 9
1.4 The Boltzmann distribution 10
1.5 Thermal polarisation 13
1.6 Hyperpolarisation 14
1.7 Monitoring hyperpolarisation via spectroscopy 14
1.7.1 NMR 14
1.7.2 EPR 20
1.8 Hyperpolarisation techniques 21
1.9 Dissolution Dynamic Nuclear Polarisation 21
1.9.1 Polarisation transfer mechanisms 22
1.9.1.1 The Solid Effect 24
1.9.1.2 The Cross Effect and Thermal Mixing 25
1.9.1.3 "Multi-spin" mechanisms 31
1.9.2 Measures of polarisation transfer efficiency 33
1.9.3 The translation from polariser to MR scanner 34
1.9.4 Current limitations and optimisation methods 34
1.10 Motivation and overview 35

2 Methods **37**
2.1 Chapter overview . . . 38
2.2 Dynamic Nuclear Polarisation . . . 38
2.2.1 Apparatus . . . 38
2.2.2 Sample preparation . . . 40
2.2.2.1 ^{29}Si samples . . . 40
2.2.2.2 ^{13}C samples . . . 41
2.2.2.3 ^{15}N samples . . . 42
2.2.2.4 Samples containing gadolinium . . . 43
2.2.3 Signal generation and readout . . . 43
2.2.4 Microwave frequency sweep profiles . . . 45
2.2.5 Build-up profiles . . . 47
2.2.6 Decay profiles . . . 48
2.2.7 Determining polarisation levels . . . 50
2.3 Magnetic Resonance Spectroscopy/Imaging . . . 51
2.3.1 Apparatus . . . 51
2.3.2 Sample preparation . . . 52
2.3.3 Set-up and monitoring signal . . . 52
2.4 Electron Paramagnetic Resonance . . . 54
2.4.1 Apparatus . . . 54
2.4.2 Sample preparation . . . 56
2.4.3 Set-up and signal acquisition . . . 56
2.5 X-ray diffraction . . . 57
2.5.1 Apparatus . . . 58
2.5.2 Sample preparation . . . 58
2.6 Data processing and analysis . . . 58

3 ^{29}Si - Hyperpolarised Silicon Nanoparticles **61**
3.1 Background . . . 62
3.2 Chapter overview and aim . . . 63
3.2.0.1 Prior to DNP . . . 64
3.2.0.2 During DNP . . . 64
3.2.0.3 Post DNP . . . 64
3.3 ^{29}Si laboratory set-up . . . 65
3.3.0.1 Background . . . 65
3.3.1 Calibration of the ^{29}Si tuning-and-matching circuit . . . 66
3.3.1.1 Introduction . . . 66
3.3.1.2 Methods . . . 66
3.3.1.3 Results . . . 67

3.3.1.4 Discussion . . . 68
3.3.2 Microwave power optimisation . . . 69
3.3.2.1 Introduction . . . 69
3.3.2.2 Methods . . . 70
3.3.2.3 Results . . . 70
3.3.2.4 Discussion . . . 71
3.3.3 Signal readout optimisation . . . 72
3.3.3.1 Introduction . . . 72
3.3.3.2 Methods . . . 73
3.3.3.3 Results . . . 75
3.3.3.4 Discussion . . . 77
3.4 Silicon nanoparticle DNP . . . 79
3.4.0.1 Background . . . 79
3.4.1 Hyperpolarisation via intrinsic endogenous radicals . . . 79
3.4.1.1 Introduction . . . 79
3.4.1.2 Methods . . . 81
3.4.1.3 Results . . . 82
3.4.1.4 Discussion . . . 84
3.4.2 Hyperpolarisation via exogenous radicals . . . 85
3.4.2.1 Introduction . . . 85
3.4.2.2 Methods . . . 88
3.4.2.3 Results . . . 89
3.4.2.4 Discussion . . . 97
3.4.3 Hyperpolarisation via irradiation generated radicals . . . 100
3.4.3.1 Introduction . . . 100
3.4.3.2 Methods . . . 102
3.4.3.3 Results . . . 104
3.4.3.4 Discussion . . . 110
3.5 Beyond the polariser: using ^{29}Si polarisation . . . 113
3.5.0.1 Background . . . 113
3.5.0.2 Introduction . . . 113
3.5.0.3 Methods . . . 114
3.5.0.4 Results . . . 116
3.5.0.5 Discussion . . . 118
3.6 Conclusion . . . 120

4 ^{13}C - Hyperpolarised Alanine 121
4.1 Background . . . 122
4.2 Chapter overview . . . 124
4.3 Chapter aims . . . 124
4.4 Generation of nonpersistent radicals for DNP . . . 125
4.4.1 Irradiation-induced endogenous radicals . . . 125
4.4.1.1 Introduction . . . 125
4.4.1.2 Methods . . . 127
4.4.1.3 Results . . . 128
4.4.1.4 Discussion . . . 130
4.4.2 Hyperpolarisation via endogenous radicals . . . 132
4.4.2.1 Introduction . . . 132
4.4.2.2 Methods . . . 132
4.4.2.3 Results . . . 133
4.4.2.4 Discussion . . . 140
4.5 Microwave modulation during DNP . . . 142
4.5.0.1 Introduction . . . 142
4.5.0.2 Methods . . . 142
4.5.0.3 Results . . . 144
4.5.0.4 Discussion . . . 154
4.6 *In vivo* study of metabolism . . . 156
4.6.0.1 Introduction . . . 156
4.6.0.2 Methods . . . 156
4.6.0.3 Results . . . 158
4.6.0.4 Discussion . . . 165
4.7 Conclusion . . . 167

5 ^{15}N - Hyperpolarised Urea 168
5.1 Background . . . 169
5.2 Chapter overview . . . 171
5.3 Chapter aims . . . 172
5.4 Tuning and matching circuit . . . 172
5.4.0.1 Background . . . 172
5.4.0.2 Introduction . . . 172
5.4.0.3 Methods . . . 173
5.4.0.4 Results . . . 174
5.4.0.5 Discussion . . . 175
5.5 Sample optimisation . . . 177
5.5.0.1 Background . . . 177

5.5.1 Solvent . . . 177
5.5.1.1 Introduction . . . 177
5.5.1.2 Methods . . . 178
5.5.1.3 Results . . . 179
5.5.1.4 Discussion . . . 181
5.5.2 Radical . . . 182
5.5.2.1 Introduction . . . 182
5.5.2.2 Methods . . . 182
5.5.2.3 Results . . . 183
5.5.2.4 Discussion . . . 184
5.5.3 Concentration of gadolinium . . . 186
5.5.3.1 Introduction . . . 186
5.5.3.2 Methods . . . 186
5.5.3.3 Results . . . 187
5.5.3.4 Discussion . . . 188
5.5.4 Glassing matrix . . . 189
5.5.4.1 Introduction . . . 189
5.5.4.2 Methods . . . 189
5.5.4.3 Results . . . 190
5.5.4.4 Discussion . . . 192
5.5.5 Dual-labelling . . . 192
5.5.5.1 Introduction . . . 192
5.5.5.2 Methods . . . 193
5.5.5.3 Results . . . 193
5.5.5.4 Discussion . . . 195
5.6 Liquid-state polarisation . . . 196
5.6.0.1 Background . . . 196
5.6.0.2 Introduction . . . 196
5.6.0.3 Methods . . . 196
5.6.0.4 Results . . . 199
5.6.0.5 Discussion . . . 203
5.7 *In vivo* study of perfusion . . . 204
5.7.0.1 Background . . . 204
5.7.0.2 Introduction . . . 204
5.7.0.3 Methods . . . 205
5.7.0.4 Results . . . 207
5.7.0.5 Discussion . . . 214
5.8 Conclusion . . . 214

6 Discussion **215**
6.1 Overview 215
6.2 Hyperpolarised ^{29}Si-silicon nanoparticles 216
6.3 Hyperpolarised ^{13}C-alanine 217
6.4 Hyperpolarised ^{15}N-urea 218

7 Concluding Remarks **220**

References **221**

List of Figures

1.1 The classical representation of spin 4
1.2 Quantisation of spin 5
1.3 The Zeeman effect 9
1.4 Boltzmann distribution 12
1.5 Thermal spin reservoir polarisations 13
1.6 The evolution of the net magnetisation vector during NMR 17
1.7 The effect of T_1 and T_2 relaxation on the net magnetisation vector . 19
1.8 Energy splittings and resulting EPR spectra 21
1.9 Allowed transitions of a two spin system 23
1.10 The Solid Effect 25
1.11 Triple spin system at thermal equilibrium 26
1.12 Triple spin mechanism during DNP 27
1.13 Spin reservoir model: Thermal Mixing 28
1.14 Spin reservoir model: Thermal Mixing and the Cross Effect 30
1.15 Spin reservoir model for large spin systems 31
1.16 Spin diffusion barrier 32

2.1 The prototype polariser 38
2.2 The HyperSense 39
2.3 The SpinAligner 39
2.4 The benchtop NMR spectrometer 40
2.5 Example flip angle calibration data set 44
2.6 Pulse sequence diagram for hyperpolarised samples 45
2.7 Example microwave frequency sweep profile 46
2.8 Example build-up profile 47
2.9 Example decay profile before and after correction 48
2.10 Example liquid state decay profile 49
2.11 7 T preclinical scanner 51
2.12 3 T clinical scanner 52
2.13 Flip angle calibration on a non-hyperpolarised phantom 54
2.14 EMXmicro spectrometer 55
2.15 E680 spectrometer 55

2.16 Derivation of Bragg's Law . . . 57
2.17 X-ray diffraction spectrometer . . . 58
2.18 The process to obtain an EPR spin count . . . 59

3.1 Laboratory set-up . . . 65
3.2 ^{29}Si tuning and matching circuit . . . 68
3.3 Flip angle calibration . . . 68
3.4 Microwave power . . . 70
3.5 Example data from experiment and simulation . . . 75
3.6 Optimisation of signal readout for different PWs . . . 76
3.7 Typical structure of a silicon nanoparticle . . . 80
3.8 Samples polarised via naturally occurring endogenous radicals . . . 83
3.9 The selected radical species selected and their structures . . . 87
3.10 30 mM TEMPO enhanced silicon nanoparticle polarisation . . . 90
3.11 TEMPO concentration affected silicon nanoparticle polarisation . . . 91
3.12 AH111501 hindered silicon nanoparticle polarisation . . . 93
3.13 Radical-specific concentration-specific effects . . . 95
3.14 Structurally analogous radicals had similar effects on polarisation . . . 96
3.15 Gadolinium did not increase the efficiency of polarisation . . . 97
3.16 Vacancies and interstitials . . . 102
3.17 X-ray diffraction diffractometer . . . 103
3.18 Design of sample holder compatible with existing LinAc set-up . . . 105
3.19 LinAc sample holder . . . 105
3.20 Irradiation hindered silicon nanoparticle polarisation . . . 106
3.21 Irradiation had little-to-no effect on particle structure . . . 106
3.22 More particle interactions predicted with greater sample density . . . 107
3.23 Pellet maker . . . 108
3.24 Increased sample density lowered the spin count . . . 108
3.25 Pellet making increased the crystallinity of silicon nanoparticles . . . 109
3.26 "Dry" dissolution set up . . . 116
3.27 Calibration of the ^{29}Si/^{1}H volume coil . . . 117
3.28 B_1 map of the ^{29}Si volume coil . . . 117
3.29 Liquid state polarisation . . . 118

4.1 Alanine and pyruvate uptake . . . 123
4.2 L-alanine molecular structure . . . 123
4.3 L-alanine irradiation-induced radical species . . . 127
4.4 Confirmation of endogenous radical generation . . . 129
4.5 Simulations of EPR spectra . . . 130
4.6 ^{13}C-alanine DNP sample preparation optimisation at 3.35 T . . . 135

4.7 Comparison of exogenous and endogenous radical EPR spectra . . . 136
4.8 Stability of endogenous radicals . . . 137
4.9 Cryogenic EPR spectra . . . 138
4.10 X-ray diffraction spectra . . . 139
4.11 SpinAligner microwave settings . . . 143
4.12 Initial testing of the microwave settings . . . 144
4.13 Comparison of irradiation dose . . . 146
4.14 Optimisation of modulation . . . 148
4.15 The effect of AM and FM on the polarisation constants . . . 149
4.16 Comparison of frequency modulation settings at 25 MHz AM . . . 151
4.17 Repeats: solid state data . . . 152
4.18 Repeats: liquid state data . . . 153
4.19 Comparison of exogenous and endogenous radicals: solid state . . . 159
4.20 Comparison of exogenous and endogenous radicals: liquid state . . . 160
4.21 Comparison of exogenous and endogenous radicals: 2D spectra . . . 161
4.22 Comparison of exogenous and endogenous radicals: 3D spectra . . . 162
4.23 SPSP: Metabolite fittings . . . 163
4.24 Comparison of exogenous and endogenous radicals: MRSI . . . 164

5.1 Smith chart trace . . . 174
5.2 Flip angle calibration . . . 175
5.3 ^{15}N compounds and their structures . . . 178
5.4 Effect of deuteration . . . 180
5.5 Effect of radical choice . . . 184
5.6 Effect of gadolinium concentration . . . 188
5.7 Effect of glycerol deuteration . . . 191
5.8 Effect of dual-labelling . . . 194
5.9 Calibration of the ^{15}N/^{1}H coil set-up . . . 199
5.10 B_1 ratio map of the ^{15}N surface coil . . . 200
5.11 Surface coil power calibrations . . . 200
5.12 Liquid state ^{15}N polarisation . . . 202
5.13 Gamma-variate curve profile . . . 205
5.14 ^{15}N vascular traces: healthy models . . . 208
5.15 Vascular tracer parameters: healthy models . . . 209
5.16 ^{15}N vascular traces: stroke models . . . 210
5.17 Vascular tracer parameters: stroke models . . . 211
5.18 Ratios of the vascular tracer parameters . . . 212
5.19 Examples of a ^{1}H image and perfusion parameter map . . . 212
5.20 DSC: perfusion parameters . . . 213

List of Tables

1.1 Predictions for nuclear spin quantum numbers 5

3.1 Pulse widths and corresponding flip angles used in the Bloch simulation 74
3.2 Pulse widths and corresponding flip angles used in the experiments 74
3.3 Summary of each signal readout sequence 77
3.4 Bare SiNPs: Optimal microwave frequencies 82
3.5 Polarisation constants: effect of TEMPO concentration 92
3.6 Polarisation constants: effect of AH111501 concentration 94
3.7 Polarisation constants: structural analogues 96

4.1 Summary of different alanine samples 133
4.2 Polarisation constants: effect of modulation 147
4.3 Polarisation constants: further optimsiation of modulation 150
4.4 pH of samples injected *in vivo* 163

5.1 Polarisation constants: effect of solvent 181
5.2 Polarisation constants: effect of radical choice 183
5.3 Polarisation constants: effect of gadolinium concentration 187
5.4 Polarisation constants: effect of deuterated glycerol 190
5.5 Polarisation constants: effect of dual-labelling 195

Glossary

ALT . . . . . Alanine transaminase

ASL . . . . . Arterial Spin Labeling

APS . . . . . Average particle size

AUC . . . . . Area under the curve

BFI . . . . . Blood flow index

CBF . . . . . Cerebral blood flow

CE . . . . . Cross Effect

CW . . . . . Continous wave

DA . . . . . Double angle

dd-H_2O . . . . Double-distilled water

d-DNP . . . . Dissolution Dynamic Nuclear Polarisation

DCE . . . . . Dynamic Contrast Enhanced

DSC . . . . . Dynamic Susceptibility Contrast

E-beam . . . . Electron beam

EPA . . . . . Electron Polarising Agent

EPR . . . . . Electron Paramagnetic Resonance

GAMOS . . . Geant4-based Architecture for Medicine-Oriented Simulation

GBCAs . . . . Gadolinium-based contrast agents

Gd . . . . . Gadolinium

IAEA . . . . . International Atomic Energy Agency

LDH . . . . . Lactate dehydrogenase

LinAc . . . . . Linear Accelerator

MCTs . . . . . Monocarboxylate transporters

MR . . . . . Magnetic Resonance

MRI . . . . . Magnetic Resonance Imaging

MRS . . . . . Magnetic Resonance Spectroscopy

MTT . . . . . Mean transit time

MW . . . . . Molecular weight

NMR . . . . . Nuclear Magnetic Resonance

SAR . . . . . Stable alanine radical

SD . . . . . Standard deviation

SE . . . . . Solid Effect

SiMPs . . . . . Silicon microparticles

SiNPs . . . . . Silicon nanoparticles

SNR . . . . . Signal-to-noise ratio

TEM . . . . . Transmission Electron Microscopy

TM . . . . . Thermal Mixing

T&M . . . . . Tuning and matching

TMS . . . . . Tetramethylsilane

$\mathbf{T}_p$ . . . . . Time to peak

TR . . . . . Repetition time

VFA . . . . . Variable flip angle

VTI . . . . . Variable temperature insert

$\mathbf{Y}_p$ . . . . . Peak intensity

. . . you cannot appreciate the destination without knowing the starting point; you cannot revel in the simplicity unless you remember the alternatives.

— David Eagleman

1 Introduction

Contents

1.1 Background 2
1.2 Fundamental properties of particles 3
1.2.1 Spin 3
1.2.2 Magnetic moment 6
1.3 The Zeeman effect 9
1.4 The Boltzmann distribution 10
1.5 Thermal polarisation 13
1.6 Hyperpolarisation 14
1.7 Monitoring hyperpolarisation via spectroscopy 14
1.7.1 NMR 14
1.7.2 EPR 20
1.8 Hyperpolarisation techniques 21
1.9 Dissolution Dynamic Nuclear Polarisation 21
1.9.1 Polarisation transfer mechanisms 22
1.9.1.1 The Solid Effect 24
1.9.1.2 The Cross Effect and Thermal Mixing 25
1.9.1.3 "Multi-spin" mechanisms 31
1.9.2 Measures of polarisation transfer efficiency 33
1.9.3 The translation from polariser to MR scanner 34
1.9.4 Current limitations and optimisation methods 34
1.10 Motivation and overview 35

1.1 Background

Curiosity forms an integral part of the human condition and drives the continuous growth of our knowledge. One measure of the knowledge gained from this is the production of innovative technologies. Another measure, however, lies in the discovery of new applications for existing technologies and their ensuing development. In the field of biomedical imaging, many of the advancements made since the late nineteenth century have benefited from the process of repurposing.

One such example is Magnetic Resonance Spectroscopy (MRS) which is based on the principles of Nuclear Magnetic Resonance (NMR) by which chemical compounds are investigated non-invasively to generate spectra indicating the relative concentrations of the different compounds. The only difference between NMR and MRS is that the latter can be used in a clinical setting. By combining MRS with MRI, spectra from anatomical locations of interest can be recorded and used to aid diagnosis by uncovering hallmarks of various pathologies. As a clinical imaging technique, MRI offers soft tissue contrast without the use of ionising radiation and its flexibility as a diagnostic tool is reflected by its numerous applications which include: studying cardiac function, locating tumours, and assessing brain injuries. An inherent limitation of NMR and thus, by extension both MRS and MRI, however, is low sensitivity (i.e. low signal-to-noise ratio (SNR)) which can lead to poor spatial, temporal, and spectral resolutions, low contrast, and long scan times. To partially compensate for this, signal averaging and the use of exogenous contrast agents are typically employed.

In 2003, Ardenkjær-Larson *et al.* demonstrated the feasibility of "hyperpolarising" exogenous contrast agents by combining NMR with a technique known as Dynamic Nuclear Polarisation (DNP) to establish dissolution-DNP (d-DNP)[1]. Through repurposing DNP[1], not only did their work address the issue of sensitivity by achieving 10,000-fold gain in SNR, but it enabled the exploration of nuclei beyond protons and laid the foundations for the intravenous use of such compounds

[1]DNP was first used in the production of targets for high energy particle scattering experiments[2].

in vivo[3]. The ability to monitor relative concentrations of nuclei that hold physiological relevance and their locations led to the diversification of the types of information that could be gathered from an MR scan, such as the monitoring of intracellular pH[4]. Moreover, hyperpolarisation provided the ability to track X-nuclei that hold no physiological relevance — for drug delivery applications, for example — which, in addition to broadening the applications of MR, led to measurements with no, or at least undetectable, background signal[5].

The term "hyperpolarisation" refers to a temporary enhancement of NMR or MR signal beyond that expected at thermal equilibrium that has been achieved through exploiting the interactions of subatomic particles during physical processes, sometimes under extreme environmental conditions. Such conditions can include high magnetic field strengths and temperatures close to absolute zero. Here, the idea of hyperpolarisation is first explored with a generalised description of the effect of magnetic field and temperature on the particles comprising a hyperpolarised contrast agent (HCA). This is given through consideration of the fundamental properties of these particles, the Zeeman effect, and the Boltzmann distribution.

1.2 Fundamental properties of particles

1.2.1 Spin

Spin is a form of angular momentum and is an intrinsic property of the majority of elementary particles[2]. Specifically, any change to the total angular momentum of a system ($\vec{J}$) that does not originate from a change in motion (i.e. orbital angular momentum ($\vec{L}$)) can be attributed to a change in its spin angular momentum ($\vec{S}$):

$$\vec{S} = \vec{J} - \vec{L} \tag{1.1}$$

A common classical representation of spin is as a small bar magnet; whereby in the absence of a magnetic field it would be randomly orientated in space but,

[2]Currently, the Higgs Boson is the only elementary particle known to have zero spin.

in the presence of a magnetic field, it would tend to orientate itself parallel or antiparallel to the magnetic field vector (Figure 1.1).

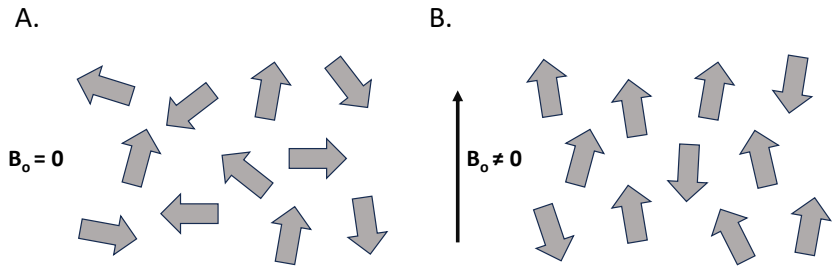

Figure 1.1: The classical representation of spin
A 2D schematic demonstrating the effect of a magnetic field on the behaviour of spins. A) In the absence of a magnetic field the spins have no preferred orientation. B) In the presence of a magnetic field the spins tend to favour orientations that are parallel or antiparallel to the direction of the magnetic field vector (represented by a black arrow).

Despite protons and neutrons being composites of elementary particles, they exhibit the same spin ($\vec{I}$) as that shown by electrons ($\vec{S}$)[3]. Essentially, they are all spin-$\frac{1}{2}$ particles (which themselves are often referred to as "spins") and, synonymous to the bar magnet, these spins will adopt one of two states within a magnetic field[4]. Commonly referred to as spin "up" and spin "down", these states refer to a parallel or antiparallel alignment to the magnetic field vector, respectively.

This behaviour upon exposure to a magnetic field arises as a result of spin being a quantised property in units of $\hbar$; where $\hbar$ is the reduced Planck's constant. For example, for nuclear spins:

$$\left|\vec{I}\right| = \sqrt{I(I+1)}\hbar \tag{1.2}$$

where $I = 0, \frac{1}{2}, 1, \frac{3}{2} \ldots$ and I is the nuclear spin quantum number. The quantisation of the direction of the spin angular momentum vector means there are only a set number of values the spin angular momentum can adopt when its vector

[3]The different labels for the spin angular momentum of these subatomic particles follows convention.

[4]To enable a classical description of these systems, the state that such a spin adopts is typically presented as a dichotomy. In quantum mechanics, however, the wave function ($\Psi = a|+\frac{1}{2}\rangle + b|-\frac{1}{2}\rangle$) describing the system also allows for a spin to exist as a linear combination of these states (known as eigenstates viz. $|+\frac{1}{2}\rangle$ and $|-\frac{1}{2}\rangle$).

is projected onto an arbitrarily chosen axis. For instance, the z-component of $\vec{I}$ (I_z) is described by:

$$I_z = m\hbar \tag{1.3}$$

where m is the magnetic quantum number and can take on a value between $\pm I$ in integer steps. Hence, the possible number of orientations or states available to a particle of spin I is $2I+1$. This concept is depicted pictorially in Figure 1.2 where a spin-$\frac{1}{2}$ particle has two possible orientations.

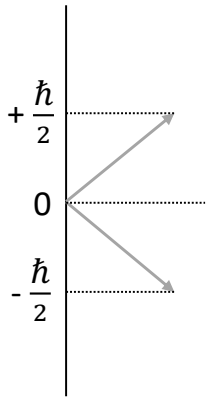

Figure 1.2: Quantisation of spin
A schematic demonstrating for a spin-$\frac{1}{2}$ particle the quantisation of its spin angular momentum both in terms of magnitude and direction on an arbitrary axis.

Notably, for nuclei comprising multiple protons and neutrons, the spin angular momentum is not simply the sum of the individual spins of its protons and neutrons owing to the complex rules for the addition of angular momentum in quantum systems. As a general guide, the nuclear spin quantum number can be predicted based on whether there are any unpaired protons or neutrons (Table 1.1).

Number of protons	Number of neutrons	Nuclear spin quantum number
Even	Even	0
Even	Odd	Half-integer
Odd	Even	Half-integer
Odd	Odd	Integer

Table 1.1: Predictions for nuclear spin quantum numbers

Nuclei that have overall non-zero spin are also known as "magnetic nuclei" due to their resulting magnetic moments.

1.2.2 Magnetic moment

Each spin has an associated magnetic moment vector ($\vec{\mu}$), the origins of which become intuitive and are most easily described by extending the classical representation of spin. A crude analogy of a spin could be an electrically charged particle that rotates on its own axis with some angular momentum. From Faraday's law, a magnetic field is induced when an electrical charge is in motion. In this scenario, the strength of the magnetic field is the magnetic moment and its direction is determined by the direction of the spin.

The magnitude of the magnetic moment vector gives a measure of the tendency of a spin to align with an external magnetic field as, in the presence of a magnetic field ($\vec{B_0}$), the magnetic moment will experience a torque ($\vec{\tau}$):

$$\vec{\tau} = \vec{\mu} \times \vec{B_0} \tag{1.4}$$

where $\vec{\mu}$ is directly proportional to the spin angular momentum and in the case of nuclear spins:

$$\vec{\mu} = \gamma \vec{I} = g\frac{q}{2m}\vec{I} \tag{1.5}$$

The constant of proportionality (γ) is the gyromagnetic ratio and is specific to each nucleus. The other variables, q and m, are the charge and mass of the nucleus and the addition of the dimensionless g-factor — the definition of which will be elaborated on in due course — follows historical measurements on the spin magnetic moment.

The relation described in Equation 1.5 arises as a result of the Wigner-Eckart Theorem where, due to symmetry, spin and magnetic moment are not only directly proportional but are also co-linear. Some nuclei have a negative gyromagnetic ratio meaning their magnetic moment points in an opposite direction to that of their spin - this also holds true for electrons. In fact, many parallels can be drawn between the

derivation of the magnetic moments of nuclear spins and their negatively charged counterparts. For instance, the gyromagnetic ratio of an electron is defined as:

$$\gamma_e = \frac{e}{2m_e}|g| \tag{1.6}$$

where e is the magnitude of electric charge carried by one electron and m_e is its mass.

The magnetic moment associated with an electron spin, however, comprises two different magnetic moments; in addition to the spin magnetic moment electrons also have an orbital magnetic moment. The origin of the orbital magnetic moment is most easily understood by returning to the classical analogy where an electron is likened to a moving electrical charge. Consider an electron following a circular orbit around a nucleus; this moving charge is synonymous to a current (I):

$$I = \frac{q}{T} = \frac{-e}{T} = -\frac{ev}{2\pi r} \tag{1.7}$$

where T is the orbital period, v is the speed at which the electron is orbiting, and r is the radius of its orbit. In this scenario, the direction of the magnetic field is determined by the direction of the spin and orbit of the charge (i.e. the electron). Using Equation 1.7, the orbital magnetic moment ($\vec{\mu_L}$) can be described by:

$$\vec{\mu_L} = IA = -\frac{ev}{2\pi r}\pi r^2 = -\frac{evr}{2} = -\frac{evrm}{2m} = -\frac{e}{2m}\vec{L} \tag{1.8}$$

Analogous to the spin magnetic moment of a nuclear spin, the spin magnetic moment of an electron is directly proportional to its spin angular momentum:

$$\vec{\mu_S} \propto \vec{S} \tag{1.9}$$

Based on $\vec{\mu_L}$, the expected value of $\vec{\mu_S}$ takes the form:

$$\vec{\mu_S} = -\frac{e}{2m}\vec{S} \tag{1.10}$$

Unlike $\vec{\mu_L}$, however, experimentally obtained values do not match that determined by Equation 1.10 and rather differ by approximately a factor of two. Hence, the spin magnetic moment of an electron is redefined as:

$$\vec{\mu_S} = -g\frac{e}{2m}\vec{S} \tag{1.11}$$

where g is the aforementioned g-factor and is dimensionless ($g \approx 2$). The importance of the g-factor lies in the fact that it provides information regarding the atomic and electron structure of a compound. The g-factor for a free electron (g_e) is 2.00232, known very accurately via quantum electrodynamics, and any deviation from this value indicates some interaction that an electron may be subject to in a molecular environment. For an electron:

$$g = -\frac{\gamma\hbar}{\mu_B} \tag{1.12}$$

Using Equation 1.6 the Bohr magneton (μ_B) can be defined:

$$\mu_B = \frac{e\hbar}{2m_e} \tag{1.13}$$

The two magnetic moments of an electron are typically expressed in terms of this constant and thus, the orbital and spin magnetic moments projected onto the z-axis can be rewritten:

$$\vec{\mu_L} = -\frac{e}{2m}\vec{L} = -\frac{e\hbar}{2m_e}m_l = -m_l\mu_B \tag{1.14}$$

$$\vec{\mu_S} = -g\frac{e}{2m_e}\vec{S} = -g\frac{e\hbar}{2m_e}m_s = -gm_s\mu_B \tag{1.15}$$

Returning to Equation 1.4, the torque exerted on the magnetic moment is perpendicular to the angular momentum and thus, leads to the precession of the magnetic moment around the magnetic field vector at a frequency known as the Larmor frequency (ω). The different orientations available to a magnetic moment (and thus, by extension, a spin) within an external magnetic field require different energies which is a consequence of a phenomenon known as the Zeeman effect.

1.3 The Zeeman effect

The Zeeman effect describes the splitting of atomic energy levels upon exposure to an external magnetic field. If a system composed of spin-$\frac{1}{2}$ particles were to be placed within a magnetic field, there would be an energy difference of ΔE between the particles whose magnetic moment vectors orientated parallel to the magnetic field vector and those that orientated antiparallel (Figure 1.3).

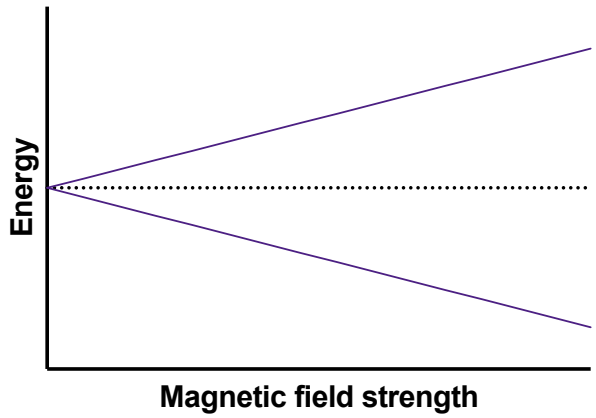

Figure 1.3: The Zeeman effect
A schematic showing the Zeeman effect on a system comprising a spin-$\frac{1}{2}$ particle. In the absence of a magnetic field the energy levels are degenerate. Upon application of a magnetic field the energy levels split and degeneracy is lost. As the magnetic field strength increases, the energy difference between the two energy levels also increases.

The difference in energy between these two states scales linearly with the external magnetic field strength (B_0) and is described by the Zeeman equation:

$$\Delta E = \gamma \hbar B_0 \tag{1.16}$$

Due to the gyromagnetic ratio being specific to each particle and nucleus, the differences in energy that arise between energy levels varies between different particles and sample types.

For any system, it is preferential to minimise its total energy. Hence, as it is more energetically favourable for a magnetic moment to be aligned parallel with the magnetic field vector, one would assume, spins would tend to populate lower energy level. Even at high magnetic field strengths, however, a low spin

population difference exists between the two energy levels which contributes to the low sensitivity of MRI[6].

For spin-$\frac{1}{2}$ systems the distribution of spin populations among energy levels split by the Zeeman effect can be derived from Boltzmann statistics as:

$$P = \frac{N_\uparrow - N_\downarrow}{N_\uparrow + N_\downarrow} = \tanh \frac{\Delta E}{2k_B T} \tag{1.17}$$

where $N_\uparrow$ and $N_\downarrow$ denote the spin-up and spin-down populations, respectively. Using Equation 1.16, this becomes:

$$P = \tanh \frac{\gamma \hbar B}{2k_B T} \tag{1.18}$$

Low differences in spin populations (i.e. low levels of polarisation) can be explained by considering the thermal energy of the spins which leads to the Boltzmann distribution.

1.4 The Boltzmann distribution

In the presence of a magnetic field, changes in temperature can be used to manipulate the distribution of spins among the $2I + 1$ energy levels. As most systems comprise a very large number of particles, it is therefore appropriate to rely upon thermal and statistical physics to describe the collective behaviour of these particles upon changes in temperature.

Suppose a system consists of N particles and the total energy of the system (U) is distributed among these particles. The total number of particles (N) can then be described by:

$$N = \sum_i n_i \tag{1.19}$$

where n_i represents the occupation number of the ith energy level. From this, the total energy of the system can be described by:

$$U = \sum_i \epsilon_i n_i \tag{1.20}$$

where a certain number of particles n_i have an energy ϵ_i (under the assumption that energy is quantised).

The most probable macrostate of the system can be determined by considering the distribution of microstates (n_i) which is described by:

$$n_i = Ae^{-\frac{\epsilon_i}{k_B T}} \tag{1.21}$$

where, A is a constant, k_B is the Boltzmann constant, and T is the temperature. This description can be extended to the total number of particles (N):

$$N = A\sum_i e^{-\frac{\epsilon_i}{k_B T}} \tag{1.22}$$

For these N particles to be allowed to be at thermal equilibrium, the interactions between them must be assumed to be small in comparison to the energies of the particles themselves. This is a reasonable assumption simply due to the majority of samples being paramagnetic (all the samples explored within this thesis fall under this category) and not ferri- or ferromagnetic. Based on this assumption, the partition function is defined as:

$$Z = \sum_i e^{-\frac{\epsilon_i}{k_B T}} \tag{1.23}$$

Substituting for A using Equations (1.22), and (1.23), Equation (1.21) becomes:

$$n_i = \frac{N}{Z} e^{-\frac{\epsilon_i}{k_B T}} \tag{1.24}$$

which is the Boltzmann distribution for distinguishable particles.

Bringing all the above together, the proportion of particles being in a state ϵ_i is:

$$\frac{n_i}{N} = \frac{e^{-\frac{\epsilon_i}{k_B T}}}{Z} \tag{1.25}$$

Thus, the probability of a particle being in a state ϵ_i is:

$$P(\epsilon_i) = \frac{e^{-\frac{\epsilon_i}{k_B T}}}{Z} \tag{1.26}$$

and hence,

$$P(\epsilon_i) \propto e^{-\frac{\epsilon_i}{k_B T}} \tag{1.27}$$

This probability distribution is shown in Figure 1.4 which illustrates the effect of temperature on a system; by lowering the temperature, the particles within the system are more likely to occupy a lower energy level. As a consequence, and in agreement with Equation 1.18, greater polarisation can be achieved.

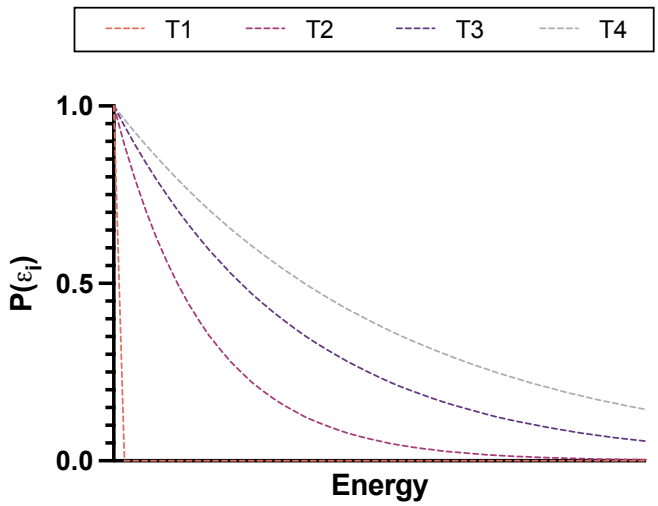

Figure 1.4: Boltzmann distribution
A schematic showing the Boltzmann distribution for a spin-$\frac{1}{2}$ particle over a range of different temperatures where $T1 < T2 < T3 < T4$.

Therefore, in addition to changes in the magnetic field strength (as described in Subsection 1.3), the difference in populations between high and low energy states within a system can be governed by temperature. Whilst greater levels of spin polarisation can be generated through increasing the magnetic field strength and lowering the temperature, the improvement is limited due to the thermal energy ($k_B T$) of the particles dominating the energy required to change the orientation of their spin (ΔE) even at temperatures close to absolute zero.

Following the effects of any external stimuli, the spin polarisation of a system will approach a new steady state called thermal polarisation.

1.5 Thermal polarisation

The thermal polarisation is the difference in spin populations among split energy levels at thermal equilibrium. From Equation 1.18, it follows that the extent of the population difference is proportional, not only to the magnetic field strength and temperature, but also to the gyromagnetic ratio of the species within the sample. An important result of this is the difference in electron and nuclear spin populations that can be achieved at a set magnetic field strength and temperature. The gyromagnetic ratio of an electron is approximately 600 times greater than that of a proton. Consequently, high levels of electron polarisation can be achieved using a superconducting magnet with a magnetic field strength of a few tesla and the use of cryogens, whereas generating equipollent levels of nuclear polarisation requires temperatures even closer to absolute zero (Figure 1.5).

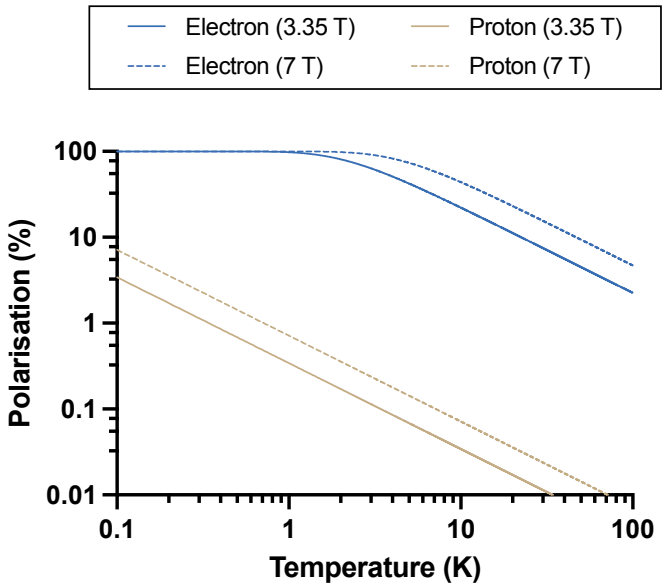

Figure 1.5: Thermal spin reservoir polarisations
Depiction of the thermal polarisation levels of nuclear and electron spins over a range of temperatures and at different magnetic field strengths. At 3.35 T, due to the larger gyromagnetic ratio exhibited by electrons, approximately 100% polarisation is achieved amongst an electron spin reservoir at temperatures close to 1 K. In contrast, the polarisation level of a nuclear spin reservoir struggles to approach 1% even when the magnetic field strength is doubled.

When the population difference between energy levels exceeds that achieved at thermal equilibrium the sample is said to be hyperpolarised.

1.6 Hyperpolarisation

The maximum possible enhancement in NMR signal (ϵ_{max}) at thermal equilibrium by the use of polarisation transfer schemes is limited by the ratio of the gyromagnetic ratios of the spins in question. As the gyromagnetic ratio of an electron is higher than that of nuclei, this is:

$$\epsilon_{max} = \frac{\gamma_S}{\gamma_I} \tag{1.28}$$

Maximum enhancement only occurs in the event where nuclear relaxation is negligible and in the presence of somewhat complex cross polarisation experiments designed explicitly to exploit this difference. There are, however, multiple ways in which the relaxation of spins can manifest which either limits the maximum possible nuclear polarisation level that can be built or reduces that which has been previously generated. The relaxation processes are attributed to the spin system exchanging energy with its surroundings (or "lattice") and to spin-spin interactions. The characteristic times during which these sources of relaxation occur are known as the spin-lattice relaxation time (T_1) and the spin-spin relaxation time (T_2), respectively. Further context on both of these processes follows in Section 1.7.

1.7 Monitoring hyperpolarisation via spectroscopy

The polarisation of nuclear and electron spins can be monitored through spectroscopic techniques known as NMR and Electron Paramagnetic Resonance (EPR).

1.7.1 NMR

NMR involves the induction of nuclear spin flips following the application of a pulse of energy which has a frequency that matches the resonance condition. In terms of the energy level diagram (Figure 1.3), pulses of energy excite nuclear spins to higher energy levels which, after some time, relax back to the lower energy levels restoring the system to equilibrium. Upon relaxation, the excess energy, which is proportional to the difference between the energy levels, is released and

detected. Due to the strength of the magnetic fields used for MRS/MRI and hyperpolarisation, the transition between energy levels typically requires energy at MHz frequency, which is why it is described as radio frequency (RF). Thus, RF coils are used to generate these pulses and either the same or another set of coils are used as the detectors for signal.

Hereafter, a classical description of the NMR process will be followed and is justified by the fact that, whilst monitoring nuclear polarisation, the recorded signal is in itself a combination of the signals generated from individual spins. If the magnetic moment from each spin were to be plotted on a set of axes, the transverse and longitudinal components of various different magnetic moments would cancel each other out. Meanwhile, the remaining components would constructively contribute to produce a net magnetisation:

$$M = \sum_i \mu_i \tag{1.29}$$

In the same manner that individual magnetic moments are subjected to a torque within a magnetic field, so too is the net magnetisation and accordingly, the net magnetisation vector ($\vec{M}$) will precess at the Larmor frequency around the magnetic field vector ($\vec{B}$):

$$\frac{d\vec{M}}{dt} = \gamma(\vec{M} \times \vec{B}) \tag{1.30}$$

The magnetisation vector can be resolved into three spatial components; the transverse components $\mathrm{M}_x(\mathrm{t})$, $\mathrm{M}_y(\mathrm{t})$, and the longitudinal component, $\mathrm{M}_z(\mathrm{t})$.

In 1946, Felix Bloch derived a set of coupled equations to describe the evolution of the net magnetisation vector during NMR[7]. The detection of NMR signal follows the perturbation of the magnetisation vector by the application of an RF pulse of energy matching the nuclear Larmor frequency, which generates an oscillating secondary magnetic field (B_1) perpendicular to the static main magnetic field (B_0). Bloch found empirically that, following perturbation, the net magnetisation vector would exponentially return to its initial value and used time constants, termed T_1 and T_2, to describe the changes in its longitudinal and transverse components,

respectively. Specifically, for a hyperpolarised sample, the value of T_1 represents the time it takes for the longitudinal component of the magnetisation vector to decay to approximately 37% of its initial value. When the sample is no longer hyperpolarised, the value of T_1 reflects the time for the magnetisation vector to recover approximately 63% of its initial value. Whereas, T_2 reflects the time it takes for the transverse component of the magnetisation vector to reduce to approximately 37% of its maximum.

Accordingly, these relaxation constants are included in the definition of the Bloch equations:

$$\frac{dM_x}{dt} = \gamma(\vec{M} \times \vec{B})_x - \frac{M_x}{T_2} \tag{1.31}$$

$$\frac{dM_y}{dt} = \gamma(\vec{M} \times \vec{B})_y - \frac{M_y}{T_2} \tag{1.32}$$

$$\frac{dM_z}{dt} = \gamma(\vec{M} \times \vec{B})_z + \frac{(M_0 - M_z)}{T_1} \tag{1.33}$$

By considering B_0 to be aligned to the z-axis[5], it follows that the Bloch equations can be rewritten as:

$$\begin{aligned} \frac{dM_x}{dt} &= \omega M_y - \frac{M_x}{T_2} \\ \frac{dM_y}{dt} &= -\omega M_x - \frac{M_y}{T_2} \\ \frac{dM_z}{dt} &= \frac{(M_0 - M_z)}{T_1} \end{aligned} \tag{1.34}$$

where the solutions take the form:

$$\begin{aligned} M_x(t) &= (M_x(0)\cos(\omega t) + M_y(0)\sin(\omega t))e^{\frac{-t}{T_2}} \\ M_y(t) &= (M_y(0)\cos(\omega t) - M_x(0)\sin(\omega t))e^{\frac{-t}{T_2}} \\ M_z(t) &= M_z(0)e^{\frac{-t}{T_1}} + M_0(1 - e^{\frac{-t}{T_1}}) \end{aligned} \tag{1.35}$$

[5]The choice of alignment with the z-axis here was for simplicity and follows convention, however, the main static magnetic field can be orientated in any direction.

A numerical solution can be found by considering the initial conditions of the magnetisation vector, say at time $t = 0$, that corresponds to the moment immediately following an RF pulse. The longitudinal and transverse components following an RF pulse that tilts $\vec{M}$ by an angle α with respect to the z-axis are: $M_x(0) = 0$, $M_y(0) = M_0 \sin(\alpha)$, and $M_z(0) = M_0 \cos(\alpha)$. Substituting:

$$\begin{aligned} M_x(t) &= (M_0 \sin(\alpha) \sin(\omega t)) e^{\frac{-t}{T_2}} \\ M_y(t) &= (M_0 \sin(\alpha) \cos(\omega t)) e^{\frac{-t}{T_2}} \\ M_z(t) &= M_0(1 - (1 - \cos(\alpha) e^{\frac{-t}{T_1}}) \end{aligned} \tag{1.36}$$

Due to the transience of B_1 and the participation of relaxation processes, there is a finite time during which signal can be detected. Classically, the detection of signal can be described as the magnetisation vector inducing a current within the RF coil positioned in the xy-plane as it precesses (Figure 1.6). The signal recorded during an NMR experiment is proportional to the magnitude of the magnetisation vector which in turn is a function of the nuclear spin population imbalance.

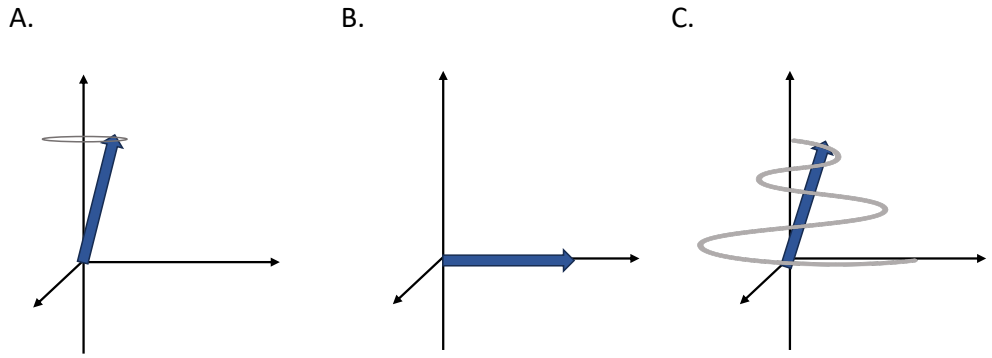

Figure 1.6: The evolution of the net magnetisation vector during NMR
A schematic showing the evolution of the net magnetisation vector during NMR. A) Prior to the application of pulses, the net magnetisation vector is precessing around the magnetic field vector at the Larmor frequency. B) Following a radio frequency pulse (to satisfy the resonance condition), the spins and thus, the net magnetisation vector, is flipped into the xy-plane by an angle proportional to the duration and power of the radio frequency pulse. Here, the net magnetisation vector is shown to be flipped fully into the xy-plane. C) Due to the finite time with which the radio frequency pulse is applied and the participation of relaxation processes, the net magnetisation vector will over time return to equilibrium.

Figure 1.7A and B depicts the effect of the T_1 and T_2 relaxation processes on the longitudinal and transverse components of a net magnetisation vector, respectively. The effect on the longitudinal component of the magnetisation vector (M_z) (i.e. spin-lattice relaxation) can occur in samples that are hyperpolarised, have not been hyperpolarised, or have since lost their hyperpolarisation. In these different situations, the value of T_1 either characterises the rate of signal decay or signal recovery processes. If a sample is hyperpolarised, the magnitude of the net magnetisation vector (M_{Hyp}) is greater than that recorded from a sample that has thermal polarisation (M_0). Following hyperpolarisation the spins will have little tendency to remain ordered and thus, the longitudinal component of the magnetisation vector decays over time (Figure 1.7A). Eventually, the polarisation levels achievable at thermal equilibrium are restored. If an RF pulse were to be applied, the magnitude of the longitudinal component of the net magnetisation vector would decrease whilst simultaneously the magnitude of the transverse component would increase. Following the RF pulse, the longitudinal component recovers back to its magnitude at thermal equilibrium. The transverse component, however, is subject to decay irrespective of whether the sample is hyperpolarised or not due to the dephasing of the individual spins in the xy-plane (Figure 1.7B). Spin-spin relaxation is characterised by the time constant T_2 and arises from the spins experiencing slightly different environments. Despite the name, spin-spin interactions are not solely responsible for this relaxation process. The observed T_2 (T_2^*) is sometimes shorter than the true T_2 value due to magnetic field inhomogeneities:

$$\frac{1}{T_2^*} = \frac{1}{T_2} + \frac{1}{T_2'} \tag{1.37}$$

where T_2' is proportional to the variation of B_0 within a voxel. Whilst T_2 and T_1 are distinctly defined, T_1 cannot occur without T_2 also taking place. Hence, $T_2 \leq T_1$.

The rate of T_1 relaxation is significantly faster for electron spins than that concerning nuclear spins. For hyperpolarised samples at low temperatures, $T_{1e} \approx 100\,\text{ms}$ whereas the relaxation of the nuclear spins – which partially depends on the nuclear species of the sample – is often on the order of hours[8].

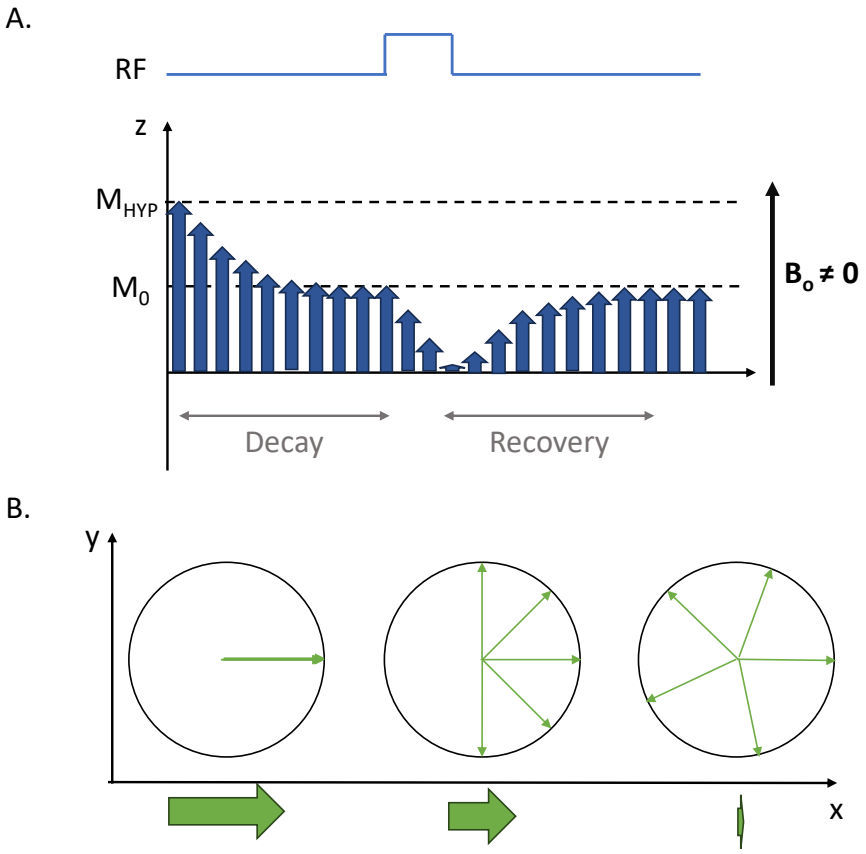

Figure 1.7: The effect of T_1 and T_2 relaxation on the net magnetisation vector Schematic of A) the different T_1 relaxation processes and their effect on the z-component of the magnetisation vector (M_z). In the presence of a non-zero magnetic field the magnetisation vector precesses around the z-axis (arbitrarily chosen). The magnitude of M_z from a hyperpolarised sample is greater than that recorded from a sample that has thermal polarisation. Following hyperpolarisation the longitudinal component of the magnetisation vector begins to decay. Eventually, the polarisation levels are restored to those achievable at thermal equilibrium. Following an RF pulse, the magnetisation vector would be flipped by an angle α into the xy-plane. Over time, the longitudinal component recovers back to its magnitude at thermal equilibrium. Whereas the transverse component — which has arbitrarily been chosen to be aligned with the x-axis (M_x) — decays due to the dephasing of the individual spins in the xy-plane. The transverse component (arbitrarily chosen to be aligned with the x-axis) is subject to decay irrespective of whether the sample is hyperpolarised or not.

At room temperature, the rate of nuclear spin relaxation within a hyperpolarised sample is typically on the order of tens of seconds. This has been shown to be slow enough to enable detection of nuclear polarisation during MR scans, however, the development of strategies to lengthen the nuclear T_1 relaxation time has become a research area of interest[9].

1.7.2 EPR

There are many parallels between the spectroscopic techniques of EPR and NMR; many of the same fundamental concepts apply. For instance, spin states are altered by the absorption and emission of electromagnetic radiation at the resonance condition whilst adhering to the same selection rules for the transition between different spin states. Additionally, just as the NMR signal is proportional to the concentration of nuclear spins, a measure of the concentration of unpaired electrons within a sample (i.e. spin count) can be found from the EPR spectra.

In contrast to NMR, due to the larger gyromagnetic ratio of an electron, the splittings of energy levels at the same magnetic field strength are larger. Consequently, the pulses of energy applied to the system during EPR are of microwave frequency. In terms of exploring resonances of different energies, EPR is typically conducted at a set microwave frequency whilst the spectrometer linearly sweeps the magnetic field. This is due to the use of an electromagnet which enables the magnetic field to be precisely varied with relative ease.

A further difference concerns the way in which the absorption spectra are reported. To improve SNR, microwave modulation is applied and as a consequence it is customary to report EPR spectra as the first derivative of the absorption spectrum. Examples of EPR spectra are illustrated in Figure 1.8 which also shows the effect of Zeeman energy splitting and hyperfine splittings arising from the nearby presence of a nucleus on the EPR line shape.

For hyperpolarised studies, the acquisition of EPR spectra goes beyond monitoring electron polarisation or recording the g-factor (Equation 1.12) to identify species. The line shape and line width features of EPR spectra and the spin count can be used to indicate the mechanism(s) by which hyperpolarisation occurs and provide direction for the optimisation of NMR signal enhancements.

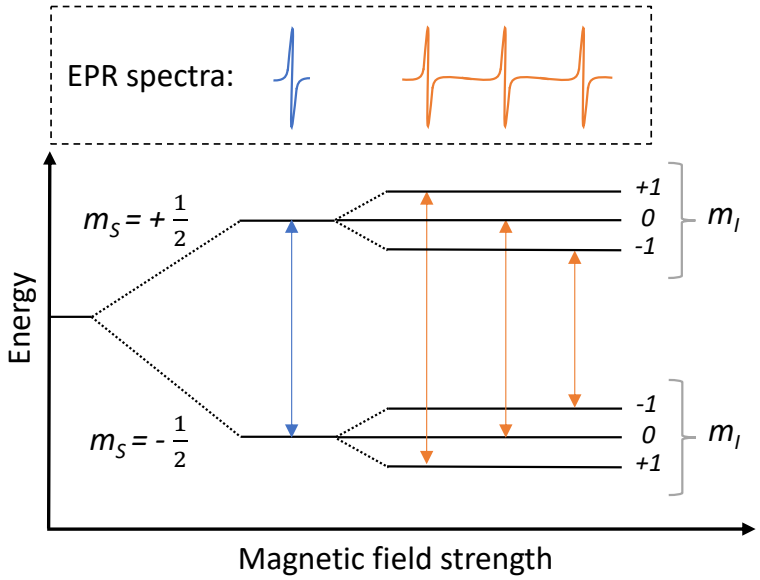

Figure 1.8: Energy splittings and resulting EPR spectra
A schematic showing the splitting of the energy levels for an electron spin ($S = \frac{1}{2}$) upon exposure to a magnetic field and the effect of a hyperfine interaction with a nuclear spin ($I = \frac{1}{2}$). The resulting electron paramagnetic resonance spectra are also shown.

1.8 Hyperpolarisation techniques

To achieve hyperpolarisation, various techniques have been developed, namely: Brute Force Polarisation (BFP), Spin Exchange Optical Pumping (SEOP), Signal Amplification By Reversible Exchange (SABRE), Chemically-Induced Dynamic Nuclear Polarisation (CIDNP), photo CIDNP, Parahydrogen Induced Polarisation (PHIP), and dissolution Dynamic Nuclear Polarisation (d-DNP). Out of these techniques, d-DNP is seen as the most versatile and consequently it has been used widely with samples comprising various nuclear species[10].

1.9 Dissolution Dynamic Nuclear Polarisation

Due to its versatility, d-DNP has evolved as a key tool in the production of HCAs. To conduct d-DNP, a sample comprising a concentrated form of the contrast agent is inserted into an apparatus known as a polariser. The bulk of the polariser comprises either a superconducting magnet housed in a shelled container filled with cryogens or a superconducting dry magnet cooled by a pulse tube cryocooler.

Through the centre of the polariser is a variable temperature insert (VTI) with which the sample space is accessed. Upon insertion into the polariser, a sample is exposed to a temperature close to absolute zero and a strong magnetic field strength (typically 3.35 – 11.8 T). As a result, and as described in Sections 1.3 and 1.4, the spins within the sample redistribute themselves among split energy levels but the population differences amongst the nuclear spins remain low.

d-DNP overcomes these low levels of nuclear polarisation by making use of the relative ease with which electron polarisation can be generated whereby the spin angular momentum of the electrons is transferred to nearby nuclei through the use of microwave irradiation. Whilst the feasibility of d-DNP was first demonstrated in the early 2000s, it was already in 1953 that Albert Overhauser proposed that NMR signals from samples containing free electrons could be enhanced through the use of microwave irradiation[11]. Following Overhauser's prediction, it transpired that there are multiple ways in which the polarisation transfer between electron and nuclear spins can occur.

1.9.1 Polarisation transfer mechanisms

The transfer of polarisation between electron and nuclear spins is made possible due to their coupling via the magnetic dipole-dipole interaction known as hyperfine coupling but the mechanism(s) by which the polarisation is transferred can vary. In the presence of a magnetic field, there are "forbidden" and "allowed" transitions between different spin states. The energy required for an allowed transition can be found by referring back to the Zeeman equation (Equation (1.16)).

$$\Delta E = \gamma \hbar B_0 = \hbar \omega \tag{1.38}$$

where ω is the Larmor frequency. Accordingly, the Larmor equation can be written as:

$$\omega = \gamma B_0 \tag{1.39}$$

From Equation 1.39, applying energy at the Larmor frequency of a nuclear spin (ω_I) would satisfy the resonance condition i.e. enable it to transition between neighbouring energy levels and, similarly, the same holds true for an electron at its Larmor frequency (ω_S). This initial case refers to the basis of NMR and the latter EPR. As an example, a schematic of the allowed transitions for a system composed of one nuclear spin and one electron spin is shown in Figure 1.9.

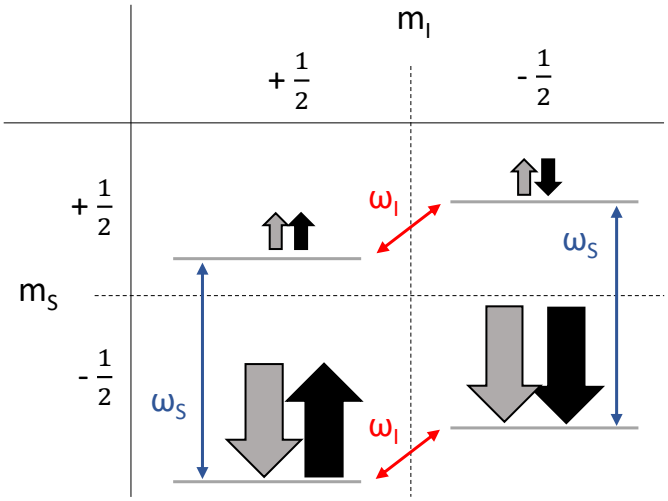

Figure 1.9: Allowed transitions of a two spin system
A schematic representing the splitting of energy levels upon exposing a nuclear spin ($I = \frac{1}{2}$) and an electron spin ($S = \frac{1}{2}$) to a magnetic field. The allowed transitions between the split energy levels are indicated by the double-headed coloured arrows where ω_I and ω_S refer to the frequencies of electromagnetic radiation applied during NMR and EPR, respectively. The size of the single-headed arrows represents the relative population of each energy level at thermal equilibrium. The electron and nuclear spins are represented by grey and black arrows, respectively. Here, $+\frac{1}{2}$ is the higher energy level for the electron and $-\frac{1}{2}$ is the lower due to the direction of its magnetic moment being opposite to that of its spin.

The forbidden transitions of a system can become partially allowed upon irradiation with electromagnetic radiation in the microwave regime that matches specific frequency criteria. Just as the activation of the allowed transitions causes the reorientation of spins, so does the activation of the forbidden transitions. The flipping of nuclear and electron spins, however, no longer occurs independently. Instead, nuclear spin flips are induced via the flipping of electron spins.

To date, three mechanisms underlying continuous wave (CW) d-DNP have been identified, namely the: Solid Effect, Cross Effect, and Thermal Mixing. Distin-

guishing between these mechanisms has been far from trivial, owing in part to the difficulty in investigating them experimentally (much of the hardware development lagged behind the theory by decades) and due to the mechanisms sometimes occurring simultaneously. Much remains unknown about these mechanisms, however, a brief description of each theory to date is outlined in the following subsections.

1.9.1.1 The Solid Effect

Of the three mechanisms, the Solid Effect (SE) is the simplest and most well understood. The SE can be thought of as occurring within a two-spin system comprising an electron ($S = \frac{1}{2}$) and a neighbouring nuclear spin ($I = \frac{1}{2}$) which undergo a flip-flop interaction (i.e. simultaneous transition between different energy levels). Within this two-spin system, there are four possible combinations of spin states: $S_{\uparrow}I_{\downarrow}$, $S_{\downarrow}I_{\uparrow}$, $S_{\uparrow}I_{\uparrow}$, and $S_{\downarrow}I_{\downarrow}$. Between these there are four possible transitions namely, the first-order optical ("allowed") transitions and the second-order ("forbidden") transitions. For the SE to occur, the nuclear Larmor frequency must be narrower than the EPR line width — regardless of whether it is homogenous (δ) or inhomogenous (Δ) — and the microwave frequency must fulfil the condition of being equal to the sum or difference of the electron and nuclear resonance frequencies i.e. $\omega_m = \omega_S \pm \omega_I$. Following irradiation at $\omega_s - \omega_I$ or $\omega_s + \omega_I$ the spin state represented in the lower right or left quadrant of Figure 1.10 will be excited to the spin state represented in the upper left/right quadrant. Thereupon relaxation of the electron spin, the nuclear spin remains flipped and the final state of the spin system is that represented in the lower left/right quadrant.

There are two varieties of this mechanism: the well-resolved SE and the differential SE. The former occurs with samples that exhibit a narrow line width EPR spectrum where only positive polarisation or negative polarisation can be transferred to the nuclei at any one time. The latter encompasses that which occurs with a broad line width EPR spectrum where its width has approximately the same magnitude as ω_I. In this situation, at some frequencies of microwave irradiation, there will be electrons that obey the matching condition for positive polarisation

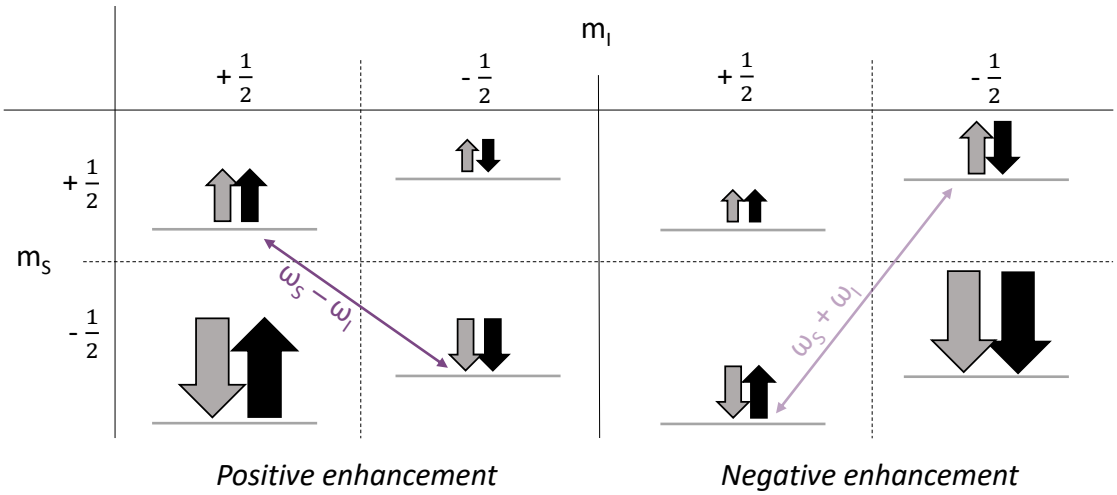

Figure 1.10: The Solid Effect
A schematic showing the split energy levels and their populations following DNP via the Solid Effect. The Solid Effect occurs between an electron ($S = \frac{1}{2}$) and a neighbouring nuclear spin ($I = \frac{1}{2}$) which undergo a flip-flop interaction. For the Solid Effect to take place, the frequency of the applied microwaves must be equal to the sum or difference of the electron and nuclear resonance frequencies i.e. $\omega_m = \omega_S \pm \omega_I$. The transitions that occur upon satisfying this condition are indicated by the double-headed coloured arrows. The size of the single-headed arrows represents the relative population of each energy level at thermal equilibrium as dictated by the Boltzmann distribution. The electron and nuclear spins are represented by grey and black arrows, respectively.

transfer and others for negative polarisation transfer resulting in positive and negative polarisation being simultaneously transferred with the net polarisation being the difference between the two.

1.9.1.2 The Cross Effect and Thermal Mixing

The Cross Effect (CE) and Thermal Mixing (TM) both occur via a three-spin system comprising two electron spins and a nearby nuclear spin. To become the dominant polarisation transfer mechanisms, the EPR line width must be wider than the nuclear Larmor frequency. Historically, the CE and TM have been treated as two standalone polarisation transfer mechanisms. For example, the CE is typically explained using a treatment analogous to that of the SE in the previous subsection, whereas a spin temperature model is used for describing TM.[6] In 2019, however,

[6]Due to the complexity of DNP a composite quantum-classical approach in the description of its underlying principles is customary.

a generalised framework labelled "the triple spin flip" – which describes three spin systems during DNP – unified the previous descriptions of these mechanisms and found that they can occur simultaneously as part of a single process[12, 13]. Here, the traditional descriptions of these mechanisms will be explored to then be considered in light of the new framework.

In line with the quantum mechanical approach, the possible combinations of spin states for a triple spin system at thermal equilibrium is shown in Figure 1.11.

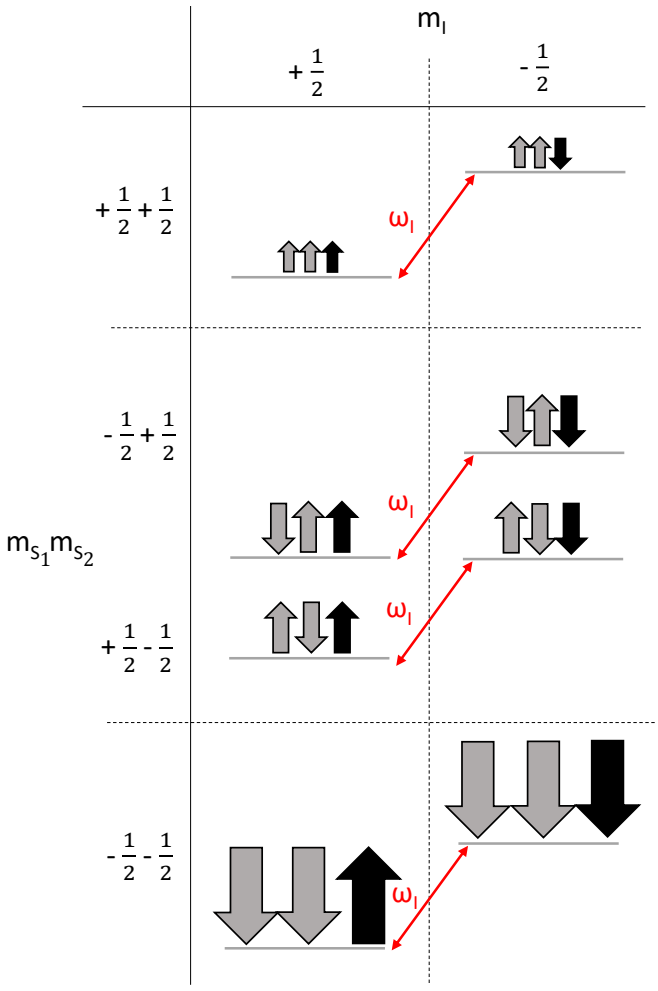

Figure 1.11: Triple spin system at thermal equilibrium
A schematic showing the split energy levels and their populations at thermal equilibrium as governed by the Boltzmann distribution. The transitions that have a non-zero probability of occurring upon irradiation at the nuclear Larmor frequency (ω_I, i.e. the frequency required to induce nuclear spin flips) are indicated by the double-headed coloured arrows. The size of the single-headed arrows represents the relative population of each energy level at thermal equilibrium as dictated by the Boltzmann distribution. The electron and nuclear spins are represented by grey and black arrows, respectively.

The allowed transitions are indicated by the double-headed coloured arrows where ω_I is the frequency required to induce nuclear spin flips. The forbidden transitions between energy levels that become activated during the CE are shown in Figure 1.12.

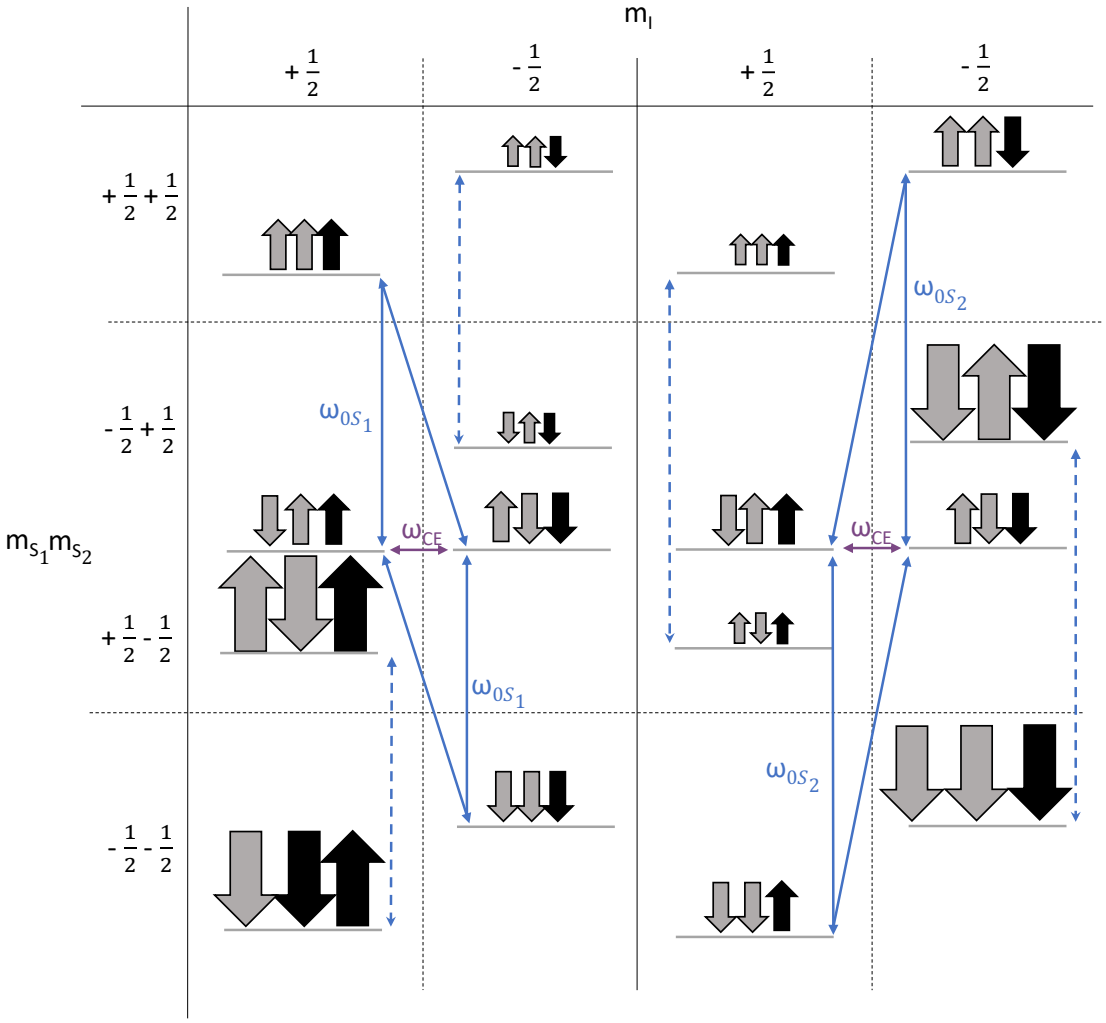

Figure 1.12: Triple spin mechanism during DNP
A schematic showing the split energy levels and their populations following DNP via a triple spin mechanism. For polarisation transfer to take place, microwave irradiation that is on-resonant with either the first or second electron is applied to the system and the nuclear Larmor frequency must match the difference in electron Larmor frequencies between the coupled electrons i.e. $\omega_I = |\omega_{0S_1} - \omega_{0S_2}|$. The transitions that occur upon satisfying this condition are indicated by the double-headed coloured arrows. The size of the single-headed arrows represents the relative population of each energy level at thermal equilibrium as dictated by the Boltzmann distribution. The electron and nuclear spins are represented by grey and black arrows, respectively.

The most efficient transfer of polarisation occurs when the nuclear Larmor frequency matches the difference in electron Larmor frequencies between the coupled electrons i.e. $\omega_I = |\omega_{S_1} - \omega_{S_2}|$. This takes place when there are degenerate energy levels which enables transitions between four of the split energy levels upon irradiation at a single common frequency.

The conventional description of the TM mechanism requires the introduction of the spin temperature formalism. Much of the discussion included here merges together concepts outlined in sources [14–16] and is aided by referral to Figure 1.13.

The spin system behind the TM mechanism can be categorised into three coupled reservoirs namely: the nuclear Zeeman reservoir, the electron Zeeman reservoir, and the electron non-Zeeman reservoir. The Zeeman reservoirs represent the average Zeeman energy arising from Zeeman interactions between the spins and the externally applied magnetic field. The other spin reservoir includes the contributions of energy from any other processes that occur such as the dipole interactions between electron spins. The interaction of the nuclear and electron spins with their surroundings is considered through the inclusion of a lattice reservoir with which the spin reservoirs are coupled via relaxation mechanisms.

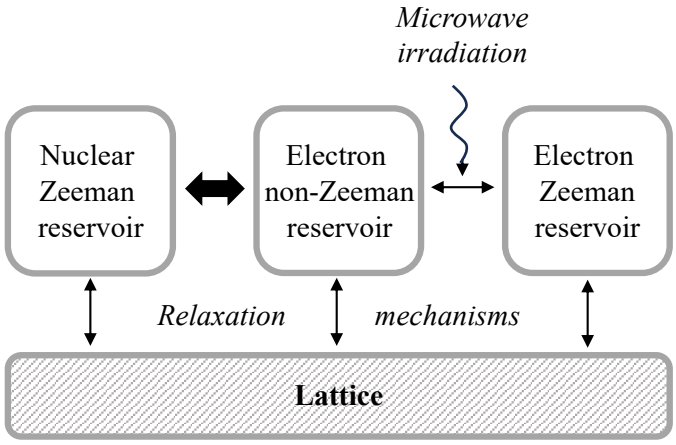

Figure 1.13: Spin reservoir model: Thermal Mixing
A schematic showing the spin reservoir model traditionally used for describing Thermal Mixing. The whole system comprises four coupled reservoirs namely: the nuclear Zeeman reservoir, the electron Zeeman reservoir, the electron non-Zeeman reservoir, and the lattice. The coupling between these reservoirs are indicated by the double-headed arrows. The larger arrow between the nuclear Zeeman and electron non-Zeeman reservoirs is to highlight the strength of this coupling compared to the others.

From the microwave irradiation applied during d-DNP, one of the electron transitions will be selectively driven leading to an absorption of either $\hbar\omega_{S_1}$ or $\hbar\omega_{S_2}$ and an increase in the energy of the electron Zeeman reservoir. Any remaining energy (ζ) is absorbed among the electron non-Zeeman reservoir. Let the microwaves be defined as:

$$\omega_{\mathrm{MW}} = \omega_S + \zeta \tag{1.40}$$

If ζ is negative/positive this leads to the cooling/heating of the electron non-Zeeman reservoir due to the emission/absorption of energy. For the case where $\zeta > 0$, the nuclear Zeeman reservoir is cooled due to its coupling with the electron non-Zeeman reservoir leading to an increase in the nuclear spin polarisation. Simultaneously, relaxation mechanisms drive for the reestablishment of the thermal polarisation levels.

The consideration of the CE and TM as separate mechanisms has been put down to them being extreme cases that satisfy distinct limits of a unified theory. From the descriptions above it is evident that the steps involved in leading up to the CE and TM mechanisms are the same. First, microwave irradiation is applied to the system and some of the electron spins (i.e. those which have a Larmor frequency that matches the frequency of the applied microwaves such that the resonance criteria is met) are partially saturated. Subsequently, due to coupling, this partial loss of polarisation spreads amongst other electron spins (i.e. spectral diffusion is induced). During either mechanism, the loss of electron polarisation and the resulting flip-flop of the electron spins induces the flip of the nuclear spin resulting in enhanced nuclear polarisation.

In the unified theory developed by Wenckebach *et al.*, the CE and TM are defined as being components of a single process that can occur simultaneously. Similar to the standalone TM model, using a spin temperature model, the energies associated with the two electrons and nuclear spin can be divided up into different reservoirs where the total energy of the electrons comprises contributions from the Zeeman effect and any spin-spin interactions (Figure 1.14).

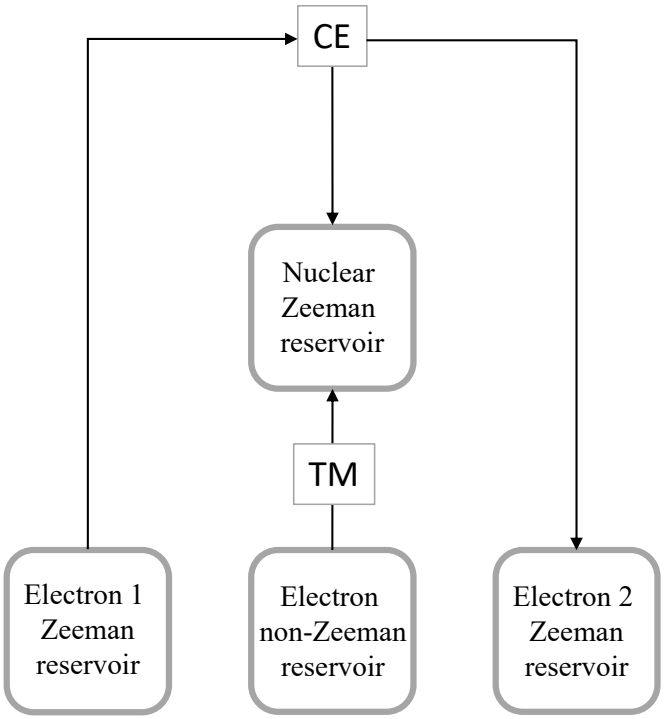

Figure 1.14: Spin reservoir model: Thermal Mixing and the Cross Effect
A schematic showing the flow of energy between different spin reservoirs. The Cross Effect corresponds to the transfer of energy from the electron Zeeman energy reservoirs to the nuclear spin reservoir whereas Thermal Mixing involves the transfer of energy from the electron non-Zeeman reservoir. These two mechanisms can occur simultaneously depending on the sample composition and the conditions of its environment.

The CE and TM are described by considering extreme cases of energy transfer[12, 13]. If the energy resulting from the nuclear Zeeman splitting is much greater than the energy resulting from the interaction between the two electron spins then the electron Zeeman energy reservoir will be the main source of energy to induce a change in the nuclear spin state. This partial flow of the Zeeman energy shared between the two electron spins to the nuclear spins was deemed to be the CE. Whereas if the interaction between the electron spins was on the same order of magnitude as the energy arising from the nuclear Zeeman energy then the non-Zeeman reservoir provides the required energy for the nuclear spin flip. Here, TM denotes the flow of electron non-Zeeman energy between the spins.

This model can also be extended to account for the large collection of spins that comprise d-DNP samples. Due to hyperfine interactions and the spatially varying electron density within a sample, a nuclear spin that neighbours an electron spin

will experience a different nuclear Larmor frequency than another nuclear spin that is located further away in the bulk of the sample. This leads to, different energies being required to flip the orientation of these nuclear spins and hence the need for different reservoirs in the spin reservoir model for large spin systems (Figure 1.15).

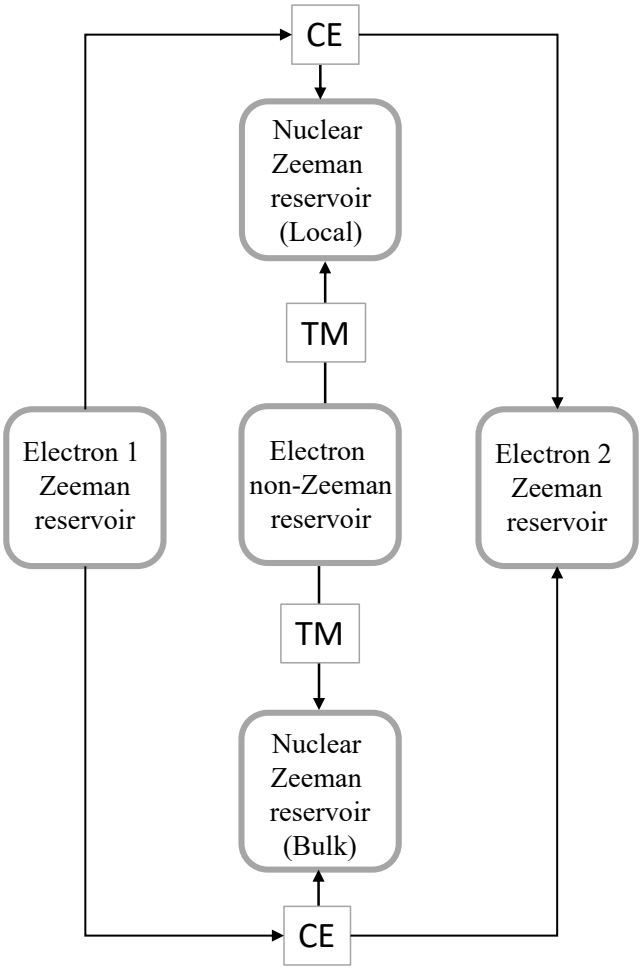

Figure 1.15: Spin reservoir model for large spin systems
A schematic showing the flow of energy between different spin reservoirs but modified to account for the large number of nuclear and electron spins contained within samples.

1.9.1.3 "Multi-spin" mechanisms

The SE, CE, and TM all require the close proximity of electron and nuclear spins for the transfer of polarisation and their descriptions typically focus on the involvement of one nuclear spin. In reality many nuclear spins are present within d-DNP samples and couplings between them exist. These couplings allow for a nuclear spin diffusion

mechanism which distributes the nuclear polarisation generated by the SE, CE, or TM amongst identical nuclear species in the bulk of the sample. The inability of nuclei closest to electron spins to take part in nuclear spin diffusion has been recognised and can be explained using the "spin diffusion barrier" model.

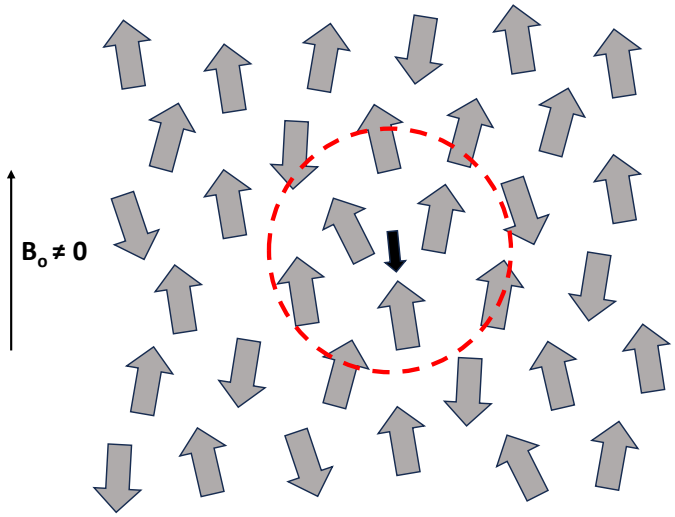

Figure 1.16: Spin diffusion barrier
A schematic of the spin diffusion barrier within which the diffusion constant describing nuclear spin diffusion is zero as a result of shifted nuclear Larmor frequencies.

Take a single electron surrounded by many nuclear spins (Figure 1.16). The nuclear Larmor frequency of the nuclear spins that are closest to the electron will be shifted in comparison to the Larmor frequency of those located at a greater distance from the electron due to them experiencing a strong dipolar field meaning nearby nuclei cannot therefore participate in the nuclear spin diffusion process[17]. The radius of the spin diffusion barrier remains a subject of debate and the mechanisms behind diffusion are not yet well understood[18]. There is general consensus, however, on the factors that can hamper or improve the efficiency of spin diffusion which is represented by the spin diffusion constant:

$$D_{\mathrm{SD}} = 0.15\frac{\mu\gamma^2\hbar}{4\pi a} \tag{1.41}$$

Equation 1.41 shows that the rate of polarisation transfer depends on the type of nuclear species and the distances between them (a)[16, 19]. For example, for

samples where nuclei are homogeneously spread throughout, nuclear spin diffusion is more efficient between ^{1}H nuclei than ^{15}N due to the large difference in gyromagnetic ratio. This discrepancy, however, forms the basis of another multi-spin polarisation transfer process called cross polarisation which can occur between nuclei of different species. Cross polarisation can be used for polarising nuclei that have low gyromagnetic ratios. The samples typically comprise the nuclei of interest embedded within a dilute proton system from which polarisation is transferred through the use of RF pulses.

It is important to note that electrons do in fact polarise multiple nuclei due to their relaxation rates being approximately > 1000 times greater than the nuclear spin relaxation rate. A rapid electron relaxation is desirable during d-DNP as it enables electrons to be "recycled" and take part in the polarisation of other nuclear spins with the aim of pumping nuclear spins into an ordered state at a greater rate than which nuclear spin relaxation occurs. In other words, the success of d-DNP lies in maximising the efficiency of polarisation transfer.

1.9.2 Measures of polarisation transfer efficiency

During d-DNP, relaxation processes concerning nuclear and electron spins concurrently take place and compete against the polarisation transfer mechanism(s) to return the system to a state of equilibrium. The efficiency with which electron polarisation is transferred during d-DNP is typically reported via constants extracted from the fittings of an integrated NMR signal that has been monitored over time. Such a collection of signals acquired during d-DNP is known as a build-up profile and the extracted constants are the aptly named build-up amplitude and build-up time. An improvement in the efficiency of polarisation transfer is indicated by an increase in build-up amplitude together with a decrease in the build-up time. The factors that influence the rate at which samples are polarised include the composition of the sample and its environmental conditions.

The very same factors are responsible for the rate at which samples lose their hyperpolarisation following d-DNP.

1.9.3 The translation from polariser to MR scanner

Upon the transfer of samples from the polariser to the MR scanner, samples are subjected to multiple changes in their environment. To be used clinically as a HCA, a sample first needs to be heated to a biological temperature and retain its polarisation as it undergoes a change of state from solid to liquid. This is made possible during the dissolution step of d-DNP where, following the irradiation with microwaves, the hyperpolarised sample is dissolved in a heated and pressurised solvent that has been injected within the sample space. It is during this process that the sample simultaneously takes on its final form as the HCA and is extracted from the polariser ready for intravenous use. The potential application of the HCA depends on the nuclear species within the sample.

Depending on the laboratory set up, samples can be exposed to large fluctuations in magnetic field strengths during their transfer between the polariser and MR scanner that can encourage relaxation processes. Other changes that occur regardless of the type of set up is the lower levels of thermal polarisation of both nuclear and electron spins (due to the transition from close to absolute zero to room temperature) and the sudden absence of microwave irradiation. For the same reason that electrons take on the role as polarisation agents during d-DNP, in the absence of microwave irradiation, they act as relaxation centres. Hence, due to the dominance of relaxation processes and the low levels of thermal polarisation, the signal enhancements achieved through hyperpolarisation are non-permanent and sensitivity levels return to the notoriously low levels associated with MRS/MRI.

In the same way that maximising the rate of polarisation transfer during d-DNP is desirable, so too is minimising the rate of polarisation relaxation during MR scanning and various optimisation strategies have been developed.

1.9.4 Current limitations and optimisation methods

Despite DNP being a relatively well established technique, the production of HCAs via d-DNP is comparatively new and few have been tested clinically.

The limited number of developed probes – which limits the types of clinically relevant information available – can be attributed to the set of criteria that their design must satisfy for their use to be practical and generate clinically relevant information. Whilst solubility in water, biocompatibility, and target selectivity are among some of the requirements, the level of polarisation generated and its lifetime has been attributed as the main obstacles. Not only are significant levels of nuclear polarisation needed to enable detectable signal enhancements following dissolution, but the duration the signal lasts for must be on the same order as the timescale of the activity or mechanism that the HCA was produced to elucidate. The non-recoverable nature of polarisation further adds to this challenge, however, there are various techniques that can be used at different stages of the DNP workflow to maximise the generation of polarisation and optimise its use[8].

Prior to DNP, aside from changes to the existing hardware and laboratory set-up (such as the microwave source and the magnetic field strength of the polariser) the factors relate mostly to the preparation of the sample, such as: isotope enrichment, an electron polarising agent (EPA), the addition of compounds to enable vitrification, sonication, and temperature[3, 20, 21]. During DNP optimisation, measures include the microwave parameters and pulse sequence readouts[22]. Lastly, post DNP, the choice and volume of dissolution solvent, sample transfer between the polariser and scanner, and pulse sequence can have an impact on how the polarisation is used and what it can be used for.

Such optimisation techniques are incorporated in the development of the different HCAs discussed within this thesis and are detailed further within the relevant chapters.

1.10 Motivation and overview

This thesis aims to address some of the main limitations in the preclinical development of HCAs through the incorporation of various optimisation techniques. These limitations — which include: long polarisation build-up times, short polarisation lifetimes, and low polarisation levels — impact the overall signal and imaging

window available during scans. As a result of these limitations, few HCAs have made it to the clinical trial stages of development. The clinical translation of a wider range of HCAs has the potential to enable access to different types of clinically relevant information.

Each chapter of this thesis focusses on the development of a HCA, each based on a different nucleus of interest. Chapter 3 details the partially unsuccessful development of a silicon nanoparticle HCA as a nanoparticle-based theragnostic agent. The attempt to generate radicals in situ, however, led to a more promising study into the hyperpolarisation of ^{13}C-alanine for use as an intracellular metabolic probe, the results of which are detailed within Chapter 4. Lastly, Chapter 5 features the investigation of ^{15}N-urea as a perfusion marker to replace the more widely used gadolinium-based contrast agents. Ultimately, the work detailed within this thesis contains optimisation strategies that are likely applicable to the development of other X-nuclei HCAs and was completed with a view to acquiring new information and widening the applications of hyperpolarised MRS/MRI.

No man ever steps in the same river twice...

— Heraclitus

2 Methods

Contents

2.1 Chapter overview 38
2.2 Dynamic Nuclear Polarisation 38
2.2.1 Apparatus 38
2.2.2 Sample preparation 40
2.2.2.1 ^{29}Si samples 40
2.2.2.2 ^{13}C samples 41
2.2.2.3 ^{15}N samples 42
2.2.2.4 Samples containing gadolinium 43
2.2.3 Signal generation and readout 43
2.2.4 Microwave frequency sweep profiles 45
2.2.5 Build-up profiles 47
2.2.6 Decay profiles 48
2.2.7 Determining polarisation levels 50
2.3 Magnetic Resonance Spectroscopy/Imaging 51
2.3.1 Apparatus 51
2.3.2 Sample preparation 52
2.3.3 Set-up and monitoring signal 52
2.4 Electron Paramagnetic Resonance 54
2.4.1 Apparatus 54
2.4.2 Sample preparation 56
2.4.3 Set-up and signal acquisition 56
2.5 X-ray diffraction 57
2.5.1 Apparatus 58
2.5.2 Sample preparation 58
2.6 Data processing and analysis 58

2.1 Chapter overview

An overview of the equipment and core methods used across multiple chapters are described here. The detailed methods for specific experiments are included within each relevant subsection of the corresponding chapter.

2.2 Dynamic Nuclear Polarisation

2.2.1 Apparatus

In Chapters 3 and 5, a prototype polariser (Oxford Instruments) was used to hyperpolarise silicon and nitrogen-based samples (Figure 2.1). The polariser operated at 3.35 T/<1.1 K and different tuning and matching (T&M) circuits were built to enable the real time monitoring of ^{29}Si and ^{15}N signals.



Figure 2.1: The prototype polariser
A photo of the prototype polariser in the Department of Physiology, Anatomy, and Genetics (University of Oxford).

In Chapter 4, the HyperSense (Oxford Instruments) and SpinAligner (Polarize) polarisers were used for the hyperpolarisation of carbon-based samples (Figures 2.2 and 2.3, respectively). The HyperSense operated at 3.35 T/<1.4 K and the

SpinAligner at 6.7 T/<1.3 K. Both polarisers were provided with a T&M circuit for monitoring ^{13}C signal.



Figure 2.2: The HyperSense
A photo of the HyperSense polariser in the Department of Physiology, Anatomy, and Genetics (University of Oxford).

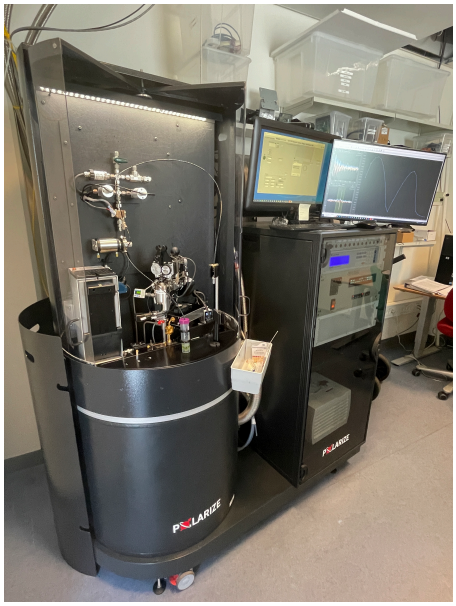

Figure 2.3: The SpinAligner
A photo of the SpinAligner polariser in the Magnetic Resonance Research Centre (Aarhus University Hospital).

The liquid state polarisation characteristics of samples in Chapter 4 were recorded at room temperature using a 1.4 T benchtop NMR spectrometer (Spinsolve 60^{ULTRA} Carbon, Magritek) shown in Figure 2.4.



Figure 2.4: The benchtop NMR spectrometer
A photo of the 1.4 T benchtop NMR spectrometer situated in the Magnetic Resonance Research Centre (Aarhus University Hospital).

2.2.2 Sample preparation

2.2.2.1 ^{29}Si samples

The different ^{29}Si-based samples prepared using silicon nanoparticles (SiNPs; US Nanomaterials) can be categorised into three main groups: samples where the SiNPs were used as received (hereafter referred to as "bare"); samples where the main source of unpaired electrons was an exogenous radical compound added to the mixture containing bare SiNPs; and samples where the SiNPs were subjected to ionising radiation. The sample preparation protocols for these samples are listed in order:

- Bare SiNPs: In an eppendorf, 130 μl of a 1:1 (v/v) mixture of Dimethylsulfoxide (DMSO; Sigma-Aldrich) and deuterium oxide (D_2O; Sigma-Aldrich) was pipetted onto 37 mg of SiNPs.

- SiNPs & exogenous radicals: 60 mM radical concentration stock solutions were made by dissolving the appropriate mass of radical in a 1:1 DMSO and D_2O (v/v) mixture. Aliquots of this stock solution were taken to make the 15 mM and 30 mM radical concentration stock solutions. For each sample, 130 μl of a stock solution was pipetted onto 37 mg of SiNPs in an eppendorf. The radicals used were TEMPO (Sigma-Aldrich) (MW = 156.25 g/mol), AH111501 Trityl (GE) (MW = 1595 g/mol) and their respective structural analogues: TEMPOL (Sigma-Aldrich) (MW = 172.25 g/mol) and OX063 Trityl (GE) (MW = 1427 g/mol).

- SiNPs & irradiation generated endogenous radicals: Dry SiNPs were irradiated using an ultra-high dose rate 6 MeV electron linear accelerator with doses ranging between 10 – 100 kGy. In an eppendorf, 130 μl of a 1:1 DMSO and D_2O (v/v) mixture was pipetted onto 37 mg of irradiated SiNPs.

Following preparation, all ^{29}Si sample mixtures were vortexed, sonicated, and pipetted into a PEEK sample cup ready for insertion into the polariser.

2.2.2.2 ^{13}C samples

Four main types of ^{13}C-based d-DNP samples were polarised, a ^{13}C-alanine sample that was subjected to ionising radiation and three samples which were used as control samples for comparison: an alanine preparation replicated from the literature[23], an alanine preparation developed within the Laustsen laboratory[1], and a pyruvate preparation.

The preparations of the ^{13}C samples were as follows:

- Dry [1-^{13}C]L-alanine powder (Sigma-Aldrich) was irradiated using an ultra-high dose rate 6 MeV electron linear accelerator. The dose of irradiation varied between 10 – 100 kGy. The irradiated powder was then used as the main component for various different samples that are detailed in the relevant subsections within Chapter 4.

[1]This sample preparation was developed by Mr. Nichlas Vous Christensen (Aarhus University)

- The preparation developed by Hu *et al.* comprised: 350 mg [1-^{13}C]L-alanine, 250 μl 18.94 M NaOH, 100 μl DMSO, 0.3 mM Dotarem gadolinium (Guerbet) and 15 mM OX063 Trityl (MW = 1427 g/mol)[23]. 100 μl of this mixture was pipetted into a sample cup.

- The alanine preparation developed within the Laustsen laboratory for the SpinAligner comprised: 1.276 g of [1-^{13}C]L-alanine mixed in 8 ml of water and 2 ml of 11.65 M HCl. This mixture was freeze-dried and approximately 1.512 g of alanine hydrochloride yielded. The alanine hydrochloride was then dissolved in 2.25 ml DMSO with the assistance of heating. 180 mg OX063 Trityl (MW = 1427 g/mol) was added leading to an approximately 38 mM radical concentration. 50 μl ($\sim$60 mg) of this mixture was pipetted into a sample cup.

- 14 M [1-^{13}C]-pyruvic acid was mixed with the appropriate mass of AH111501 Trityl (GE) (MW = 1595 g/mol) to achieve a 30 mM concentration. 18 μl of this mixture was pipetted into a sample cup.

2.2.2.3 ^{15}N samples

Two main types of ^{15}N-based d-DNP samples were prepared; sodium ^{15}N-nitrate samples were used as a control for comparison with $^{15}N_2$-urea samples.

The sample preparations were as follows:

- To make the sodium ^{15}N-nitrate DNP samples, 210.4 mg of a 7.5 M $Na^{15}NO_3$ stock solution was mixed with 64.6 mg of glycerol. Two 7.5 M $Na^{15}NO_3$ stock solutions were made, one with each solvent (D_2O or H_2O). The mixture was made into a 15 mM radical concentration stock solution by adding the appropriate mass of OX063 Trityl (MW = 1427 g/mol) to the total volume. 150 μl of sample was pipetted into a sample cup and the sample mass recorded.

- The $^{15}N_2$-urea sample comprised: 186.6 mg of a 0.4:0.6 glycerol:D_2O (w/w) or 0.4:0.6 glycerol:H_2O (w/w) mixture which was pipetted onto 70.9 mg of $^{15}N_2$-urea. The mixture was made into a 15 mM radical concentration stock

solution by adding the appropriate mass of OX063 Trityl (MW = 1427 g/mol) to the total volume. The difference in density between H_2O and D_2O was taken into consideration when determining the mass of radical to add. 150 μl of sample was pipetted into a sample cup and the sample mass recorded.

Further adjustments were made to the $^{15}N_2$-urea preparation during the course of its optimisation and the specific details are included within each relevant subsection in Chapter 5.

2.2.2.4 Samples containing gadolinium

Where samples required the addition of gadolinium, stock solutions of the solvents outlined above were modified. For example, a 1:25:25 (v/v/v) Dotarem (Guebert, France):DMSO:D_2O mixture was prepared to replace the 1:1 (v/v) DMSO:D_2O mixture. Other modified stock solutions included 1:50 (v/v) Dotarem (Guebert, France):D_2O and 1:50 (v/v) Dotarem:H_2O. The concentration of gadolinium in each of these stock solutions was 10 mMl^{-1}. The volume of gadolinium stock solution (v) added to a DNP sample was determined using Equation 2.2 and depended on the ratio between the concentration of the gadolinium stock solution (Equation 2.1), the desired molarity of gadolinium (x), and the volume of the sample (V).

$$r = \frac{10}{x} \tag{2.1}$$

$$v = \frac{V}{r} \tag{2.2}$$

2.2.3 Signal generation and readout

During DNP, the acquisition of signals follows the same principles as NMR/MRS whereby, as detailed in Section 1.7, the net magnetisation vector is flipped into the xy-plane by some angle (α) to induce a current in the detection coil and the resulting resonance is recorded. The flip angle (FA) of the net magnetisation vector following the application of an RF pulse of a specific width has to be found empirically for each T&M circuit. This is desirable to determine because each time the signal is

sampled some of the polarisation generated is lost. For example, if a 90° FA were to be applied to a hyperpolarised sample, a greater level of polarisation would be lost and it would take a longer time to recover compared to a pulse that induced a FA of 5°. Any polarisation that is used up during acquisitions can only be recovered by waiting whilst continuing the irradiation of the sample with microwaves. Hence, by having an estimate of the FA being delivered polarisation losses can be minimised.

For this, samples are first polarised and then, in the absence of microwave irradiation, a variable flip angle (VFA) scheme comprising RF pulses of various different widths (i.e. pulse widths or PW) are applied. An example of the data acquired for the calibration of the FA is shown in Figure 2.5.

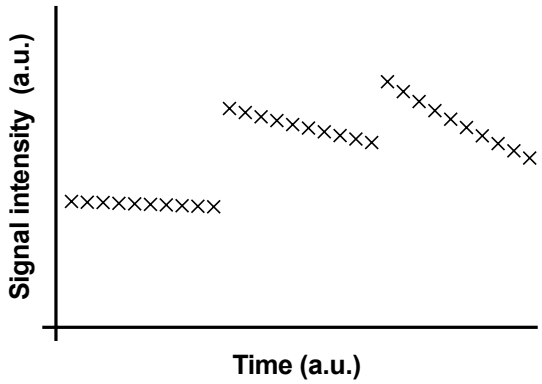

Figure 2.5: Example flip angle calibration data set
A simplified plot showing example data acquired for the calibration of the flip angle.

A VFA scheme is used due to both the delivered FA and the T_1 of the sample being unknown. A flip angle calibration factor (FA_c) can be extracted from the fit of such data and from that the flip angle (FA) can be determined:

$$\mathrm{Fit} = M_z(\sin(\mathrm{F}A)) = M_z(\sin(\mathrm{FA}_c \times \mathrm{PW})) = M_z(\sin(\mathrm{FA})) \tag{2.3}$$

where M_z is the longitudinal magnetisation along the z-axis. The relaxation of the magnetisation vector following such pulses is characterised by the spin-lattice relaxation time (T_1) which itself can be extracted by fitting M_{xy} to the same data using regression analysis.

$$M_{xy}(n) = M_0(n)\sin(\mathrm{FA}) \tag{2.4}$$

where $M_{xy}(n)$ is the transverse magnetisation for the nth acquisition, FA is the flip angle in degrees, and $M_0(n)$ is the initial magnetisation following the $(n-1)$ acquisition described by:

$$M_0(n) = M_z(n-1)e^{(\frac{-\mathrm{TR}}{T_1})} \tag{2.5}$$

and M_z is:

$$M_z(n) = M_0(n)\cos(\mathrm{FA}) \tag{2.6}$$

In this thesis, simple pulse acquire sequences were used to monitor the hyperpolarised signal (Figure 2.6). If signal averaging was required, the sequence was looped over a chosen repetition time (TR). Otherwise, a single RF pulse was delivered to the sample for each acquisition.

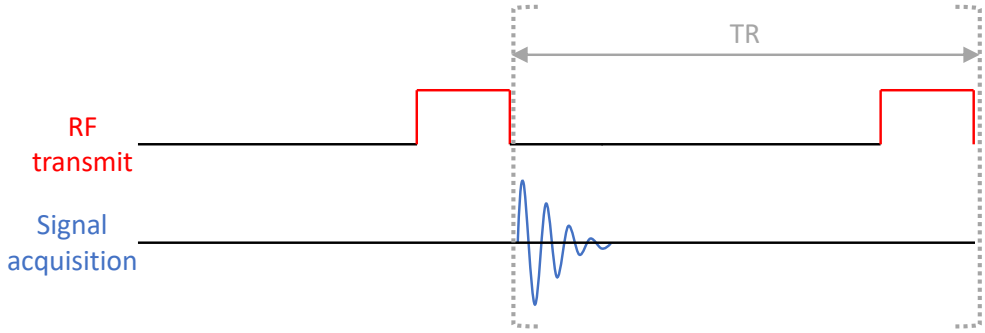

Figure 2.6: Pulse sequence diagram for hyperpolarised samples
A cartoon of the pulse acquire sequence used for monitoring polarisation build-up or decay from hyperpolarised samples. If signal averaging was used the sequence would be looped over a chosen TR.

2.2.4 Microwave frequency sweep profiles

A microwave frequency sweep forms the first key step of the DNP workflow and its purpose is to determine the optimal frequency at which to apply microwave irradiation for polarisation transfer to occur with the greatest efficiency. To obtain a microwave frequency sweep profile, microwave irradiation is applied for a predefined

amount of time at a set frequency after which any generated signal is acquired. The microwave frequency is then changed and this process is repeated until the optimal microwave frequency is determined by identifying the frequency at which the maximum signal amplitude was recorded.

The typical shape of a frequency sweep profile presents as NMR signal amplitudes that vary between different microwave frequencies and collectively hold an approximate resemblance to that of a sine curve. The two lobes arise from the microwave frequency satisfying a condition such as, for the solid effect, matching either the sum or difference of the electron and nuclear resonance frequencies. An example microwave frequency sweep profile is shown in Figure 2.7.

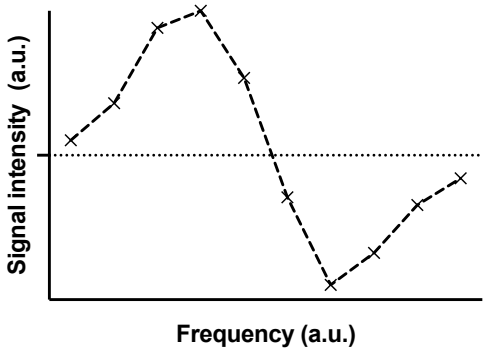

Figure 2.7: Example microwave frequency sweep profile
A simplified plot showing data acquired during a microwave frequency sweep as an example of a typical profile.

Due to handling new types of samples or samples that were notorious for requiring a long time to generate measurable signal, signal averaging was included as part of the microwave frequency sweep protocol. The number of frequency steps, width of the steps, range of frequencies covered, and the number of averages depended on each sample due to differences in their gyromagnetic ratios, distribution of paramagnetic centres, and the polarisation transfer mechanisms at play which affected the broadness of the sweep profile and the efficiency with which it could be generated.

2.2.5 Build-up profiles

Build-up profiles typically follow microwave frequency sweep profiles and are generated by continuously irradiating the sample at the optimal frequency determined from the microwave frequency sweep profile. These profiles comprise NMR signals from a nucleus of interest that have been acquired at different time points whilst microwave irradiation is being applied. The amplitudes of these signals are then plotted over time and can typically be fitted to a monoexponential or biexponential curve (Figure 2.8).

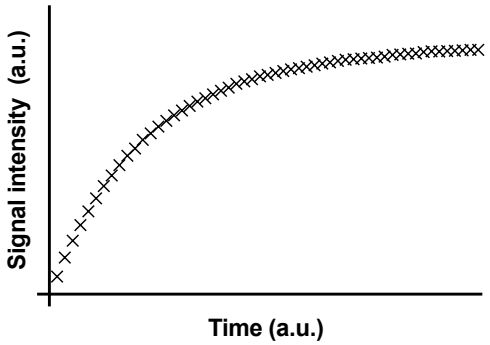

Figure 2.8: Example build-up profile
A simplified plot showing data acquired during the monitoring of polarisation build-up as an example of a typical build-up profile.

From the fitting of a build-up profile with either Equation 2.7 or 2.8 the build-up amplitude and build-up time constants can be extracted.

$$y = I\left(1 - \exp^{(\frac{-\text{time}}{T})}\right) \tag{2.7}$$

where I is the build-up amplitude and T is the build-up time. Or:

$$y = P\left(A(1 - e^{\frac{-\text{time}}{T}}) + (1 - A)(1 - e^{\frac{-\text{time}}{t}})\right) \tag{2.8}$$

where P is the build-up constant, A and $1 - A$ are the relative weightings of the fast and slow components of the polarisation transfer, and T and t are the fast and slow components of the build-up times.

These polarisation constants give an indication of the limiting level of polarisation that can be achieved with a sample under specific experimental conditions and the time required for this to be achieved.

2.2.6 Decay profiles

Immediately following the build-up profile, the decay of the generated polarisation in the absence of microwave irradiation can be monitored and the decay time constant can be extracted.

In Chapters 3 and 5, decay profiles were monitored whilst the sample was still within the polariser. For this, the microwave source was switched off and three sets of different PWs were applied to the system with each set having a greater PW than the previous set. The data was then corrected for the changes in the PW and the natural logarithm was taken to enable the extraction of the decay time constant using simple linear regression:

$$\ln(M_z) = \frac{1}{T_1}x + \ln(M_0) \tag{2.9}$$

The applied PWs and the TR depended on the sample type. An example decay profile is shown in Figure 2.9.

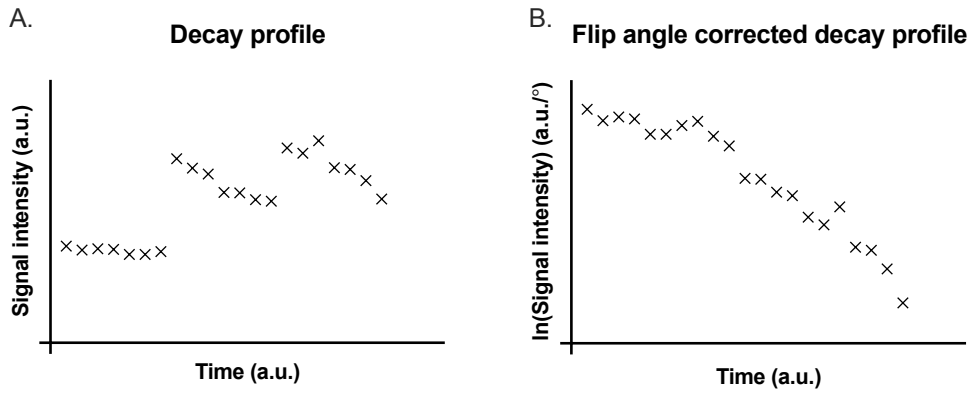

Figure 2.9: Example decay profile before and after correction
Simplified plots showing data acquired during the monitoring of polarisation decay as examples of a A) typical decay profile and B) its correction for the variable flip angle scheme.

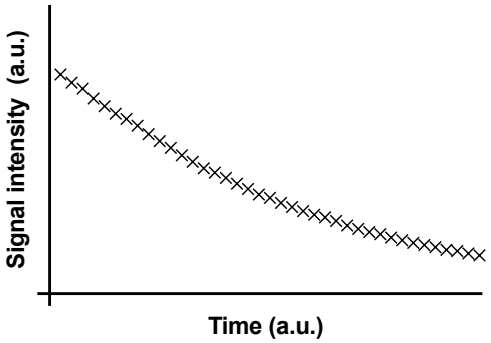

Figure 2.10: Example liquid state decay profile
A simplified plot showing data acquired during the monitoring of polarisation decay following dissolution as an example of a typical decay profile at room temperature.

For some samples, the decay profile was also recorded at room temperature and this required a similar procedure (Figure 2.10). The higher temperature of the sample, however, leads to a reduction in the nuclear T_1 relaxation time compared to that recorded at <1.4 K (i.e. prior to dissolution). Hence, a shorter TR was selected for these studies. Additionally, upon the loss of its hyperpolarisation, a thermal spectrum was acquired to enable the calculation of the level of polarisation generated. This was done by averaging spectra that had been acquired under Ernst angle conditions (Equation 2.10).

$$\theta_E = \arccos\left(e^{-\frac{\mathrm{TR}}{T_1}}\right) \tag{2.10}$$

The Ernst angle (θ_E) is the optimal flip angle to maximise the acquired signal and relies on the TR (which can be chosen) and the inherent nuclear T_1 relaxation time of the sample.

In Chapter 4, the SpinSolve (Figure 2.4) was used to monitor the decay of polarisation of alanine samples at room temperature and acquired thermal spectra following the addition of gadolinium to the sample in order to reduce the nuclear T_1 relaxation time of the sample and facilitate a greater number of averages in a shorter time frame.

2.2.7 Determining polarisation levels

The SpinSolve used in Chapter 4 (Figure 2.4) processed the decay profile and thermal spectrum to give a measure of the polarisation level at the point of the scan and also back calculated to the point of dissolution.

In Chapters 3 and 5, the polarisation levels were determined by processing the room temperature liquid state decay data through an in-house developed MATLAB script. In addition to the data file, the inputs for this script included the applied FA, the nuclear T_1 relaxation time, the SNR of the first acquired spectrum from the hyperpolarised sample, the SNR of the thermal spectrum, and the polarisation level at thermal equilibrium. The applied FAs were known from prior calibration on a phantom which allowed for the nuclear T_1 relaxation time to be extracted as described previously (Section 2.2.3). The SNRs were measured using VnmrJ (Agilent) and the thermal polarisation level for a sample was determined using:

$$P_{\text{th}} = \tanh\left(\frac{\hbar\gamma B}{2k_B T}\right) \tag{2.11}$$

From the SNRs and thermal polarisation level, the polarisation level at the point of dissolution was found:

$$P_{\text{hyp}} = P_{\text{th}}\left(\frac{M_{0(\text{hyp})}}{M_{0(\text{th})}}\right) \tag{2.12}$$

where,

$$M_{0(\text{hyp})} = \frac{\text{SNR}_{\text{hyp}}}{\sin(\alpha_{\text{hyp}})(1 - e^{\frac{-\text{TR}}{T_1}})} \tag{2.13}$$

and,

$$M_{0(\text{th})} = \frac{\text{SNR}_{\text{th}}\left(1 - e^{\frac{-\text{TR}}{T_1}}\right)\cos(\alpha_{\text{th}})}{\sqrt{n_{\text{avg}}}\sin(\alpha_{\text{th}})\left(1 - e^{\frac{-\text{TR}}{T_1}}\right)} \tag{2.14}$$

2.3 Magnetic Resonance Spectroscopy/Imaging

2.3.1 Apparatus

In Chapters 3 and 5, a preclinical scanner operating at 7 T (Varian/Agilent) was used to monitor the polarisation characteristics of HCAs at room temperature and for a proof of concept *in vivo* study (Figure 2.11).

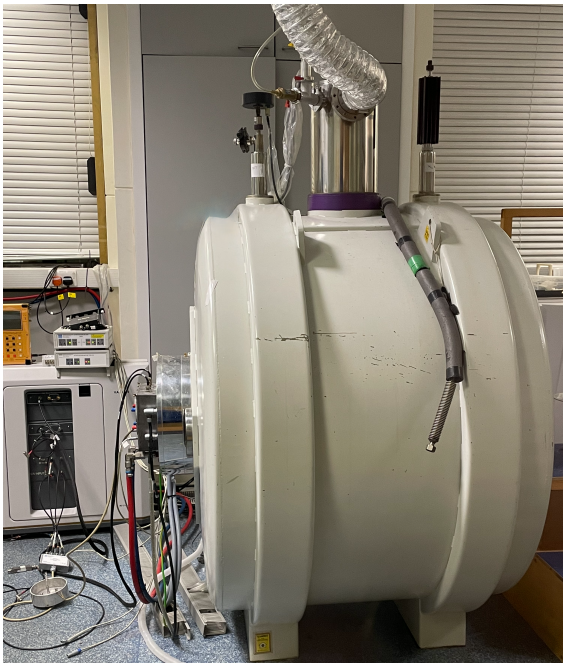

Figure 2.11: 7 T preclinical scanner
A photo of the 7 T preclinical scanner in the Department of Physiology, Anatomy, and Genetics (University of Oxford).

In Chapter 4, a clinical scanner operating at 3 T (GE MR750, GE Healthcare) situated in the Magnetic Resonance Research Centre (Aarhus University Hospital) was used for a proof of concept *in vivo* study (Figure 2.12).

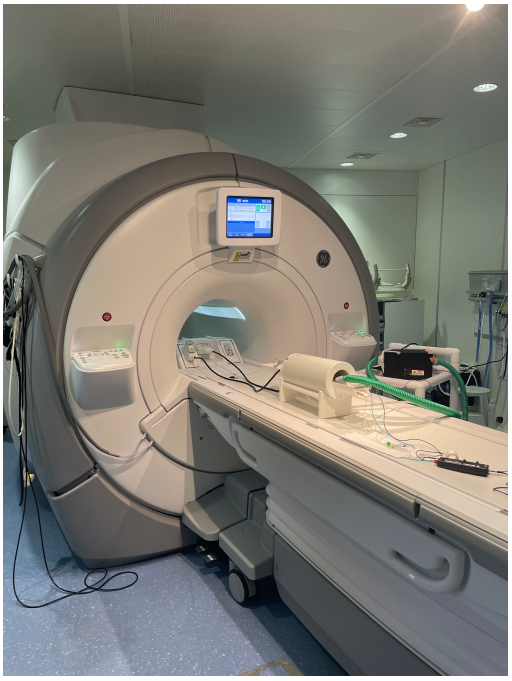

Figure 2.12: 3 T clinical scanner
A photo of the 3 T clinical scanner in the Magnetic Resonance Research Centre (Aarhus University Hospital).

2.3.2 Sample preparation

Details of the HCAs that were tested and the phantoms used for calibration are included in the relevant subsections within each chapter.

2.3.3 Set-up and monitoring signal

Prior to monitoring the polarisation characteristics of HCAs at room temperature with an MR scanner, the magnetic field of the scanner was shimmed and a FA/power calibration was conducted on a phantom.

Upon removal from the polariser, the polarisation of a HCA is non-renewable. Furthermore, its thermal polarisation level shifts due to changes in the sample environment and any polarisation that has been generated spontaneously begins to relax towards the new thermal equilibrium. Some polarisation is also used up with each acquisition and thus, it is imperative that the applied FA is determined from a non-hyperpolarised phantom to ensure the polarisation can be sampled as desired before it fully decays.

MR signals are recorded when the net magnetisation vector is tipped by some angle to enable its transverse components to induce a current in the detection coil. Greater FAs can be achieved either by increasing the PW of the RF pulses or their transmit power. The greatest signal is recorded when the net magnetisation is flipped fully into the xy-plane (i.e. a FA of 90°). Either side of the xy-plane, the magnitude of the transverse component of the net magnetisation vector is reduced. The transverse component is smallest or even negligible when the net magnetisation vector is aligned along the z-axis which can correspond to two scenarios: either no RF pulse has been applied, or a RF pulse corresponding to a FA that is a factor of 180° has been applied. Depending on the magnitude of the FA, the latter can lead to a fully inverted magnetisation vector (e.g. 180°, 540°, etc.) or its return to the original null point (e.g. 360°, 720°, etc.). For non-hyperpolarised samples, it follows that the recorded signal represents a sinusoidal function with respect to the FA of the net magnetisation vector. Yet, the shape of the FA calibration curve can become skewed if the TR is short in comparison to the T_1 due to the incomplete relaxation of the net magnetisation vector between acquisitions (Figure 2.13). For this reason, it is recommended to select a TR $> 5T_1$ and/or to record the calibration over the zero crossing of the sine curve due to the 180° acquisition being unaffected by the choice of TR. The PW required for any other FA can then be deduced from the PW that resulted in the 180° flip of the magnetisation vector. For a FA calibration, the transmit power of the RF pulse should be held constant whilst the PW is varied. Alternatively, a power calibration can be conducted by holding the PW constant and varying the transmit power. In the case of the Varian/Agilent console used in this thesis, the transmit power of the RF pulse is relative to a maximum of 100 W at 63 dB.

An estimate of the other relaxation constant T_2 can be found using the full width at half maximum (FWHM):

$$T_2 = \frac{1}{\pi \mathrm{FWHM}} \tag{2.15}$$

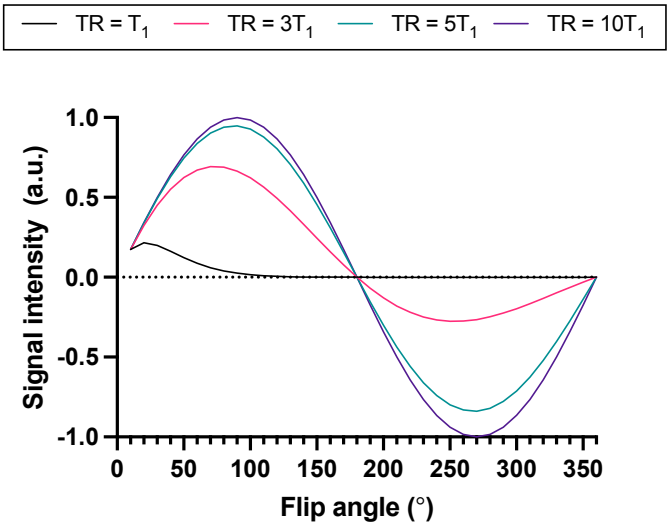

Figure 2.13: Flip angle calibration on a non-hyperpolarised phantom
Examples of the flip angle calibration curve for different choices of TR on a non-hyperpolarised sample. To calibrate the flip angle it is recommended that a TR of at least $5T_1$ is used and/or that the data set to be recorded such that the 180° flip is included due to it being unaffected by the choice of TR. The FAs and corresponding PWs can then be deduced.

From Equation 2.15, the narrower the spectral peaks recorded from a compound, the longer the T_2 and vice versa.

2.4 Electron Paramagnetic Resonance

2.4.1 Apparatus

An X-band continuous wave (CW) spectrometer (EMXmicro, Bruker BioSpin) was used to record EPR spectra at room temperature (Figure 2.14).

An X-band CW spectrometer (E680, Bruker BioSpin) was used to record EPR spectra at 5 K (Figure 2.15).

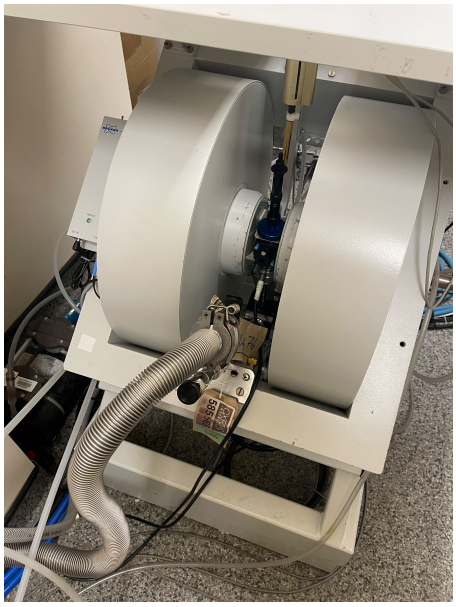

Figure 2.14: EMXmicro spectrometer
A photo of the spectrometer used to acquire EPR spectra at room temperature (Department of Chemistry, University of Oxford).

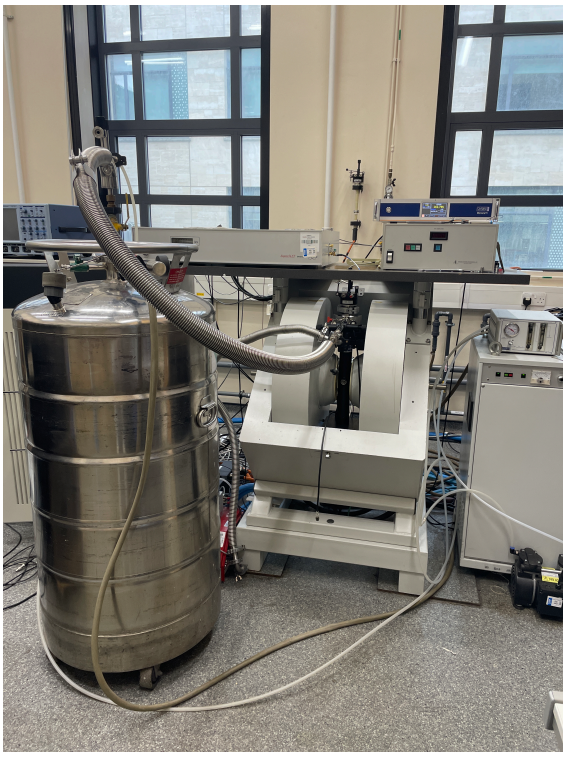

Figure 2.15: E680 spectrometer
A photo of the spectrometer used to acquire EPR spectra at 5 K (Department of Chemistry, University of Oxford).

2.4.2 Sample preparation

Magnesium Oxide (MgO) powder, a common standard reference in EPR, was used to account for changes in the magnetic field between experiments due to differences in sample positioning[24].

Samples that comprised dry powder were directly loaded into 4 mm thin wall quartz EPR tubes and their mass recorded. For repeated measurements, samples were rotated about their own axis by approximately $25-35°$. Liquid state samples were first loaded in 2 mm diameter capillary tubes which in turn were loaded into the EPR tubes. Details of the specific samples are included within the relevant subsections of Chapters 3 and 4.

2.4.3 Set-up and signal acquisition

Power dependence measurements were conducted on samples known to contain the greatest and lowest concentration of radical prior to obtaining EPR spectra and spin counts for all samples. This was to ensure that samples of the same type could be acquired using the same settings and directly compared (following a correction for differences in mass, baseline, and Q-factors). Measurements began on the sample containing the highest radical concentration and the gain setting adjusted in ± 6 dB steps. Spectra were inspected visually to determine if the intensity had doubled/halved with an increase/decrease in gain. The aim was to record spectra with the maximum possible power whilst avoiding the saturation of the detector. This setting was then applied to the sample containing the lowest concentration of radical to ensure its SNR was greater than that recorded from background measurements (e.g. an empty EPR tube or a solvent with no radical).

To ensure the signals were not artificially broadened, the modulation settings were varied on the same samples used for the power dependence measurements. Following this, the modulation amplitude was set to 1.2 G and modulation frequency to 100 kHz and these settings were held constant for all measurements on all the samples.

The scan range varied between different sample types due to differences in the broadness of their EPR spectra. Finally, in addition to the use of MgO to correct for differences in sample positioning, EPR tubes were marked to try and ensure the positioning of samples was reproducible.

2.5 X-ray diffraction

X-ray diffraction is a nondestructive technique used for characterising crystalline samples. The wavelength of X-rays is on the order of $0.01-10\,\text{nm}$ which is comparable to the distance between crystal planes; hence, when X-rays come into contact with planes of ordered atoms they scatter and constructive and destructive interference occurs. This produces a diffraction pattern from which characteristics such as crystal size and structure can be inferred. Known as Bragg's Law (described by Equation 2.16), constructive interference occurs when the angle of incidence of the X-rays equates to the angle of scattering or the difference in path length is equal to an integer number of wavelengths (Figure 2.16).

$$n\lambda = 2d\sin(\theta) \tag{2.16}$$

where n is an integer, λ is the wavelength, d is the spacing between crystal planes, and θ is the angle of incidence.

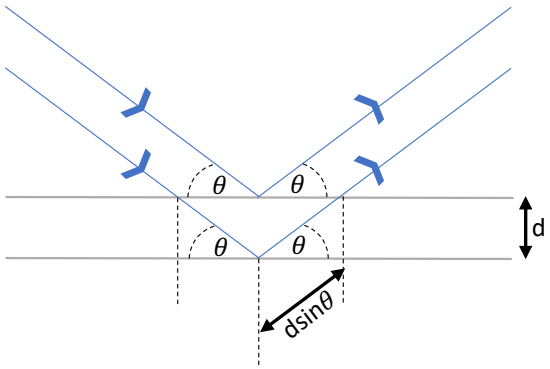

Figure 2.16: Derivation of Bragg's Law
A schematic demonstrating the derivation of Bragg's Law. The path difference between two incident X-rays is $2d\sin\theta$ and for constructive interference this path difference equates to an integer number of wavelengths.

2.5.1 Apparatus

XRD was conducted using copper plate (Cu-K) α X-rays, predominantly of wavelength 1.540 598 2 Å and 1.544 497 Å, in the diffractometer shown in Figure 2.17 (Empyrean, Malvern Panalytical).

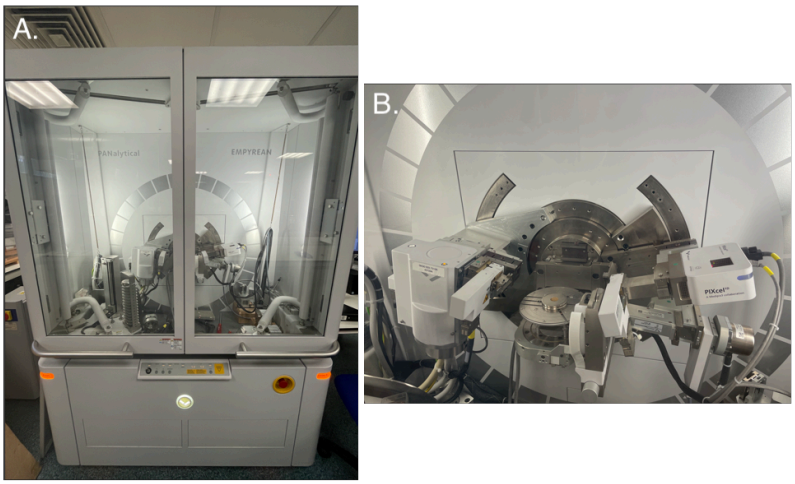

Figure 2.17: X-ray diffraction spectrometer
A) A photo of the X-ray diffraction spectrometer located at the Department of Materials (University of Oxford) and a B) close up.

2.5.2 Sample preparation

Samples were compacted using the accompanying sample holder to ensure the contents were prepared as flat and evenly as possible. Details of the specific samples are outlined in the relevant subsections of Chapters 3 and 4.

2.6 Data processing and analysis

The *in vitro* d-DNP data was processed using an in-house developed MATLAB script (*https://uk.mathworks.com/products/matlab.html*) where spectra were phased and integrated. For the extraction of the polarisation characteristics from the build-up and decay profiles and the polarisation levels, the integrated peaks were fitted according to the equations detailed in Subsections 2.2.5, 2.2.6, and 2.2.7. The exception to this was in Chapter 4 where the polarisation levels and liquid state nuclear T_1 relaxation times were automatically extracted from a benchtop NMR

spectrometer. In Chapter 3, the spectra acquired from SiNP samples were also apodised by an exponential function in the time domain to a width of 833 Hz. To enable direct comparisons across different SiNP sample types, the same level of apodisation was applied to each data set.

For the *in vivo* data in Chapter 4, MATLAB was used and for the *in vivo* data in Chapter 5 it was used in combination with jMRUI (*http://www.jmrui.eu/*), a software package developed for the processing of MRS data, and an in-house developed Python script (*https://docs.python.org/3/index.html*). Specific details can be found in the relevant subsections. The resulting MR images were viewed in Horos (*https://horosproject.org/about/*), a software package developed for the viewing of medical images.

To quantitatively compare the number of radicals between samples, spin counts were determined from EPR spectra using an in-house developed MATLAB script. The script incorporated baseline correction, normalised for differences in Q-factor, and integrated the recorded spectra to obtain a spin count. Figure 2.18 demonstrates the processing method for a representative EPR spectrum.

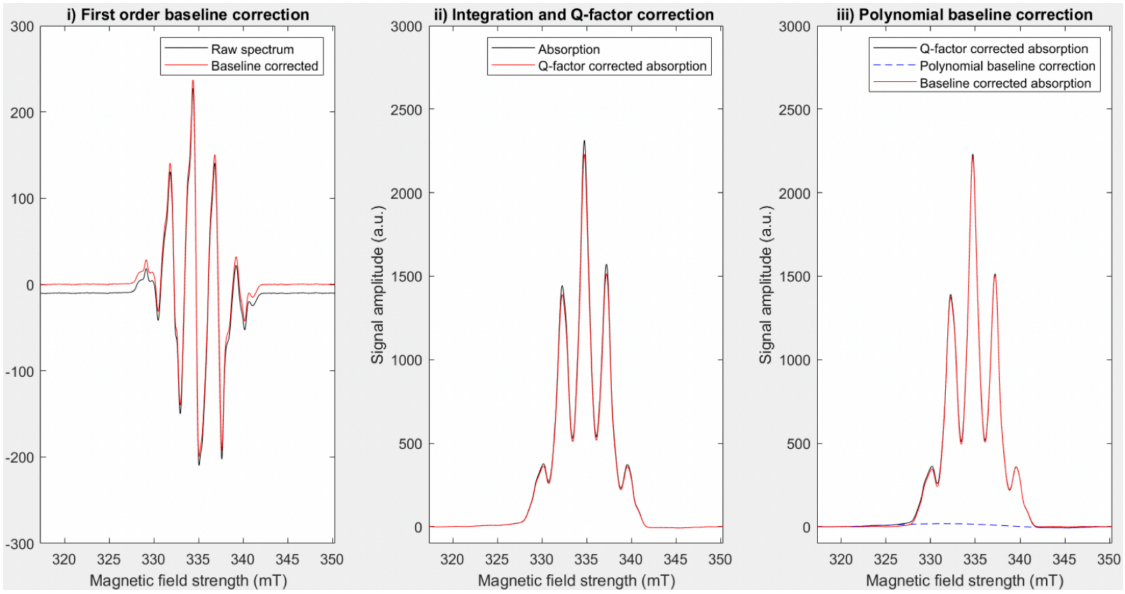

Figure 2.18: The process to obtain an EPR spin count
Plots showing the processing of a representative EPR spectrum using MATLAB. Each spectrum is corrected for i) baseline and ii) Q-factor. A spin count was then obtained from the iii) integration of the absorption spectrum.

The simulation of EPR spectra was conducted using EasySpin — a software package developed for simulation of spectra and their analysis — within MATLAB (*https://easyspin.org/*). Details of the software package and the inputs required from the user for simulations of CW spectra have previously been published[25, 26].

XRD spectra were automatically processed into text files by the software that was used to operate the diffractometer (Highscore+, Malvern Panalytical; *https://www.malvernpanalytical.com/en/products/category/software/x-ray-diffraction-software/highscore*).

Statistical tests were conducted where at least three independent repeats had been acquired. Normality and homegeneity of variance (homeodasticity) tests were performed in Prism 10 (GraphPad; *https://www.graphpad.com/features*) to assess for sample distribution. Accordingly, datasets were subjected to analysis using parametric or non-parametric tests.

In order to go on living, one must try to escape the death involved in perfectionism.

— Hannah Arendt

3

^{29}Si - Hyperpolarised Silicon Nanoparticles

Contents

3.1 Background 62
3.2 Chapter overview and aim 63
3.2.0.1 Prior to DNP 64
3.2.0.2 During DNP 64
3.2.0.3 Post DNP 64
3.3 ^{29}Si laboratory set-up 65
3.3.0.1 Background 65
3.3.1 Calibration of the ^{29}Si tuning-and-matching circuit . . . 66
3.3.1.1 Introduction 66
3.3.1.2 Methods 66
3.3.1.3 Results 67
3.3.1.4 Discussion 68
3.3.2 Microwave power optimisation 69
3.3.2.1 Introduction 69
3.3.2.2 Methods 70
3.3.2.3 Results 70
3.3.2.4 Discussion 71
3.3.3 Signal readout optimisation 72
3.3.3.1 Introduction 72
3.3.3.2 Methods 73
3.3.3.3 Results 75
3.3.3.4 Discussion 77
3.4 Silicon nanoparticle DNP 79
3.4.0.1 Background 79
3.4.1 Hyperpolarisation via intrinsic endogenous radicals . . . 79

3.4.1.1 Introduction 79
3.4.1.2 Methods 81
3.4.1.3 Results 82
3.4.1.4 Discussion 84
3.4.2 Hyperpolarisation via exogenous radicals 85
3.4.2.1 Introduction 85
3.4.2.2 Methods 88
3.4.2.3 Results 89
3.4.2.4 Discussion 97
3.4.3 Hyperpolarisation via irradiation generated radicals . . 100
3.4.3.1 Introduction 100
3.4.3.2 Methods 102
3.4.3.3 Results 104
3.4.3.4 Discussion 110
3.5 Beyond the polariser: using ^{29}Si polarisation 113
3.5.0.1 Background 113
3.5.0.2 Introduction 113
3.5.0.3 Methods 114
3.5.0.4 Results 116
3.5.0.5 Discussion 118
3.6 Conclusion 120

3.1 Background

The use of silicon particles as tracers for MRI was first proposed in 2008 following a study into the DNP properties of silicon microparticles (SiMPs)[27]. There have since been numerous studies utilising particles of various sizes ranging from nanoparticles (<100 nm) to microparticles (>100 nm). Initially, SiMPs showed greater polarisation enhancements and longer T_1 relaxation times and consequently, they were preferentially studied for the clinical translation of ^{29}Si-based HCAs. During preclinical studies, however, the signal recorded from SiMPs was found to remain concentrated at the sites of injection due to them causing blockages. One study, for example, conducted by Whiting *et al.* resorted to abdomen manipulation to help disperse larger particles[28]. Hence, focus shifted back to silicon nanoparticles (SiNPs) due to their greater mobility *in vivo* with the aim of finding ways to mimic the desirable polarisation characteristics offered by SiMPs.

This was first realised in 2017 when Kwiatkowski *et al.* achieved a signal enhancement of 12.6% using SiNPs with an average particle size (APS) of 55 ± 12 nm[29]. They also recorded a T_1 of 42 minutes at room temperature which was significantly longer than that recorded from other HCAs in preclinical development. For instance, the typical T_1 relaxation times recorded from ^{13}C metabolites — the most commonly studied samples in the field of d-DNP — are on the order of tens of seconds as opposed to tens of minutes[30]. The development of a long T_1 HCA (such as a SiNP-based HCA) could provide the opportunity for the imaging of slow biological processes and/or facilitate its transport without significant loss of polarisation[31].

In addition to their ability to retain polarisation, SiNPs exhibit many other properties that also have clinical relevance, such as: flexible surface chemistry, biocompatibility, and biodegradability *in vivo*[32]. Consequently, they are considered to have widespread clinical application potential as a theragnostic material, however, their development, thus far, has been limited mainly due to low signal enhancements following long DNP build-up times. For example, to achieve the signal enhancement of 12.6%, Kwiatkowski *et al.* polarised the SiNPs for 24 hours and, as part of a literature review, Pudakalakatti *et al.* published the first detailed DNP protocol for silicon particles in which they suggested the samples be polarised for approximately 18 hours[33]. Hence, for the clinical translation of SiNP HCAs to become a reality, greater signal enhancements must be achieved in shorter build-up times.

3.2 Chapter overview and aim

The overarching aim of the research described in this chapter was to address the main hurdle in the preclinical development of hyperpolarised SiNPs; low signal enhancements following lengthy polarisation build-up experiments. To tackle this, various optimisation strategies (listed below) were applied prior, during, and post

DNP. Although the actions taken post DNP would not directly affect the polarisation level and build-up time, these measures were taken in an attempt to ensure the efficient use of the generated polarisation.

3.2.0.1 Prior to DNP

The optimisation of the first stage involved:

- Adjustments to the existing laboratory set-up to enable monitoring of ^{29}Si NMR signal
- Development of ^{29}Si NMR signal readout sequences for the microwave frequency sweeps, polarisation build-up profiles, and polarisation decay profiles
- Development of a SiNP DNP protocol

3.2.0.2 During DNP

Different SiNP DNP sample preparations and their resulting polarisation characteristics were compared. The following features and their role in the polarisation of SiNPs were explored:

- Polarisation via intrinsic endogenous defects
- Optimisation of exogenous radical concentration and structure
- Generation of endogenous radicals and optimisation of their concentration

3.2.0.3 Post DNP

The optimisation of the final stage involved:

- Calibration and mapping of a ^{29}Si volume coil
- Development of a sample transfer protocol between the polariser and scanner

3.3 ^{29}Si laboratory set-up

3.3.0.1 Background

The existing laboratory set-up comprised: a polariser operating at 3.35 T/<1.4 K; a microwave source operating at 94.00 ± 0.25 GHz; and a tuning and matching (T&M) circuit that had been built for monitoring ^{13}C polarisation at approximately 36 MHz (Figure 3.1).

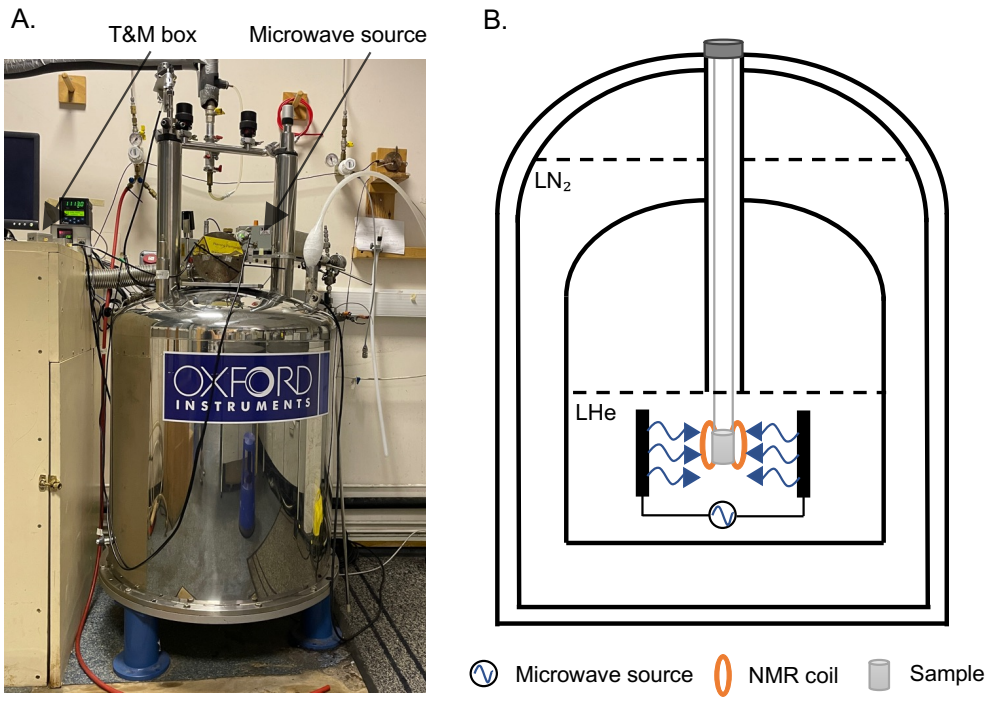

Figure 3.1: Laboratory set-up
A) The existing laboratory set-up comprised a polariser, a microwave source and a tuning and matching circuit. B) Schematic of a cross section of the polariser shows the environment samples are exposed to. When a sample is inserted, it experiences a magnetic field strength of 3.35 T, temperatures close to absolute zero (approximately 1 K), and microwave irradiation (approximately 94 GHz). To record signal from the sample, a single loop of wire that surrounds the sample space is used as an NMR coil. Due to the lack of capacitors in the NMR coil, its tune and match can be adjusted.

The nuclear Larmor frequency of ^{29}Si at 3.35 T is 28.3 MHz which was outside the frequency range of the existing T&M circuit therefore, ^{29}Si NMR signals would be filtered out with its use. Hence, the design and construction of a new T&M circuit was required in order to monitor ^{29}Si polarisation. Additionally, ^{13}C polarisation is relatively easy to monitor compared to ^{29}Si; large signal enhancements

are recorded following short d-DNP build-up times. Thus, the development of a new set-up and d-DNP protocol was also required.

3.3.1 Calibration of the ^{29}Si tuning-and-matching circuit

3.3.1.1 Introduction

To record signal, a NMR coil is located within the polariser (surrounding the sample space) and connects to the T&M circuit which is exterior to the polariser. This means the T&M circuit can be adjusted or different circuits can be connected to change the tune and match of the NMR coil and enable monitoring of different nuclei using the same polariser and NMR spectrometer.

The purpose of a T&M circuit is to maximise the power transmission of signals at a chosen frequency between the spectrometer and polariser and vice versa. The chosen frequency depends on the nucleus of interest within the sample and the magnetic field strength of the polariser i.e. the nuclear Larmor frequency.

T&M circuits work by transforming the impedance of the load (i.e. the NMR coil which is typically loaded) to match the impedance of the source (i.e. the spectrometer) which is typically at 50 Ω. A new T&M circuit had been constructed to monitor ^{29}Si polarisation but, to better understand the measurements that would be taken, it first had to be calibrated.

3.3.1.2 Methods

The calibration of the ^{29}Si T&M circuit involved determining the resulting flip angle (FA) after the application of a radio frequency (RF) pulse of a specific width. To find the conversion between the RF pulse width (PW) and the resulting FA, a SiNP sample was polarised at 94 GHz using a microwave power of 200 mW. After 45 minutes, the microwave source was switched off. Specifically, thirty pulses at three different PWs were applied (ten pulses each at 10 μs, 20 μs, and 30 μs) using a power of 61 dB and a TR of 1 s. A variable FA scheme was used due both the T_1 and FA being unknown and the loss of polarisation with each acquisition. A crusher

sequence was then applied to destroy any remaining polarisation and the process was repeated a further two times to acquire a total of three sets of calibration data.

A measure of the reflected power was obtained following the recording of the reflection coefficient (S_{11}) since:

$$S_{11} = 10 \log_{10} \frac{P_R}{P_I} \tag{3.1}$$

$$\Rightarrow \frac{P_R}{P_I} = 10^{\frac{S_{11}}{10}}, \tag{3.2}$$

where P_R and P_I are the reflected power and incident power, respectively.

For analysis, all spectra were passed through a MATLAB script where each spectrum was apodised, underwent baseline correction, and integrated to find the NMR signal intensity. The average NMR signal intensity at each acquisition was determined and plotted. This data was then fitted using Equation 2.3 and a FA calibration factor was extracted using regression analysis.

3.3.1.3 Results

The circuit was a LC-network which comprised two variable capacitors, one for tuning and one for matching, and a hand-wound inductor containing a ferrite choke (Figure 3.2). The reflection coefficient was measured to be -23.2 ± 0.1 dB which converted to less than 1% reflected power (Equation 3.2).

The FA calibration data is summarised in Figure 3.3 and the extracted FA calibration factor was $0.60 \pm 0.01\,^\circ/\mu$s at 61 dB. Hence, using the FA calibration factor, the applied PWs of 10 μs, 20 μs, and 30 μs corresponded to FAs of 6°, 12°, and 18°, respectively.

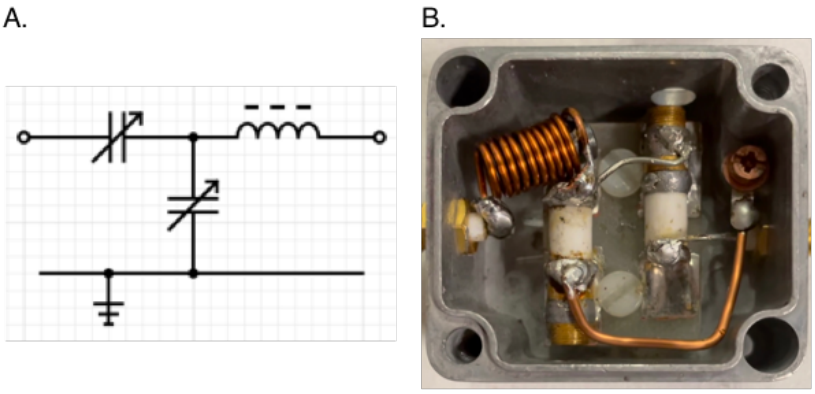

Figure 3.2: ^{29}Si tuning and matching circuit
A) The circuit diagram is shown. The circuit was a LC-network which comprised two variable capacitors (one for tuning and one for matching) and a hand-wound inductor which contained a ferrite choke. B) A photo of the built circuit is shown.

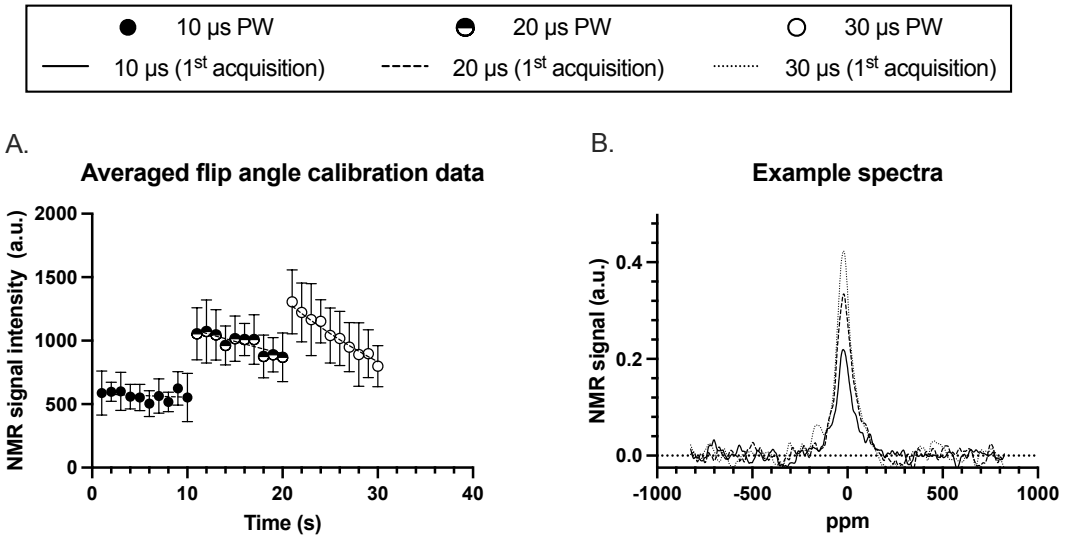

Figure 3.3: Flip angle calibration
A) The average of $n = 3$ flip angle calibrations for a polarised silicon nanoparticle sample is summarised in a dot plot. The average FA calibration factor extracted was $0.60 \pm 0.01\,^{\circ}/\mu$s. B) The first spectrum acquired with each PW is shown.

3.3.1.4 Discussion

The existing laboratory set up was optimised for monitoring ^{13}C NMR signal; thus, it required adapting to enable the monitoring of ^{29}Si NMR signal in the form of a ^{29}Si T&M circuit. The circuit was well tuned and matched at 28.3 MHz as less than 1% of the power was reflected. For the FA calibration, T_1 decay was considered as

part of the experimental design. The T_1 of polarised silicon samples have previously been measured to be on the order of tens of minutes at room temperature and hence, the TR was chosen to be much shorter (1 s) so that any contribution from T_1 relaxation at ∼1.4 K in the decay of polarisation would be negligible over the time scale of the experiment. Three different PWs were used so as to provide greater sensitivity to the applied FA. An average of three runs was used to determine the FA calibration factor, however, the accuracy in determining this constant could potentially have been improved by leaving the sample to polarise for longer which would likely have improved the SNR.

By using a dedicated T&M circuit, any changes to the build-up rate and/or build-up amplitude due to changes in the DNP protocol would now be easily observable. This information would be available in real time as opposed to transferring samples to an MR scanner after a build-up of approximately 18 hours (the recommended build-up duration reported in the literature) and recording the ^{29}Si NMR signal there instead[33].

3.3.2 Microwave power optimisation

3.3.2.1 Introduction

During d-DNP, samples are irradiated with microwaves to facilitate the transfer of electron polarisation to the nuclear spins (the various mechanisms by which this can happen are detailed in Section 1.9.1). Care must be taken whilst applying microwave irradiation, however, as sample heating can occur and impede on-going microscopic processes that aid polarisation. This is due to an increase in the rate of spin-lattice relaxation upon increases in sample temperature[22]. Thus, one obvious approach to increase the efficiency of polarisation generation would appear to be to reduce sample heating by operating at the lowest possible microwave power. Yet, whilst polarisation losses have been recorded following the use of higher microwave powers, significant enhancements can still be achieved and have been accompanied by a reduction in the build-up time[34]. This trade off was explored in the context of SiNP d-DNP to tackle the associated slow polarisation build-up rates.

3.3.2.2 Methods

A SiNP sample was polarised for 45 minutes at a set microwave power. Immediately following this, the microwave source was switched off and, using a PW of 10 μs, 256 acquisitions were recorded and averaged. This was repeated a further two times to achieve $n = 3$ and at each microwave power (0 mW, 10 mW, 25 mW, 50 mW, 100 mW, 150 mW, and 200 mW).

For analysis, all spectra were passed through a MATLAB script where each spectrum was apodised, underwent baseline correction, and integrated to find the NMR signal intensity. The build-up amplitudes and build-up times were extracted from the build-up profiles by fitting with a monoexponential (Equation 2.7).

3.3.2.3 Results

Between 0 – 100 mW, signal enhancements appeared to increase with increasing microwave power, however, using a microwave power greater than 100 mW appeared to have negligible effect on the signal enhancement (Figure 3.4A). Thus, 100 mW was determined to be the optimal microwave power.

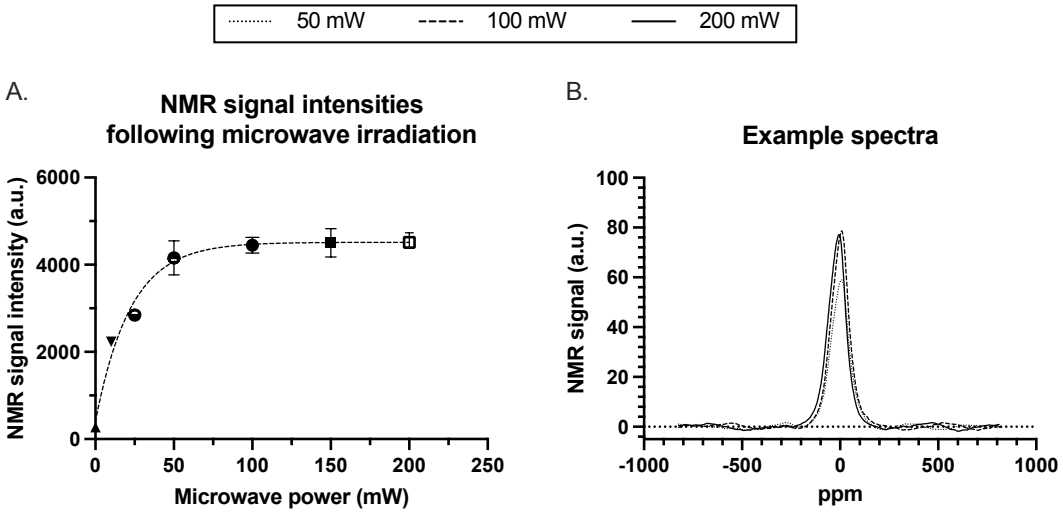

Figure 3.4: Microwave power
A) The NMR signal intensity achieved following irradiation at different microwave powers during polarisation build-up experiments are summarised as a dot plot ($n = 3$). Bars display mean ± SD. B) Example spectra from which NMR signal intensities were determined are shown. The optimal microwave power appeared to be 100 mW.

3.3.2.4 Discussion

The signal enhancements following DNP appeared to increase with increasing microwave power up until 100 mW and then plateaued. This relationship is characteristic of the competition between the Zeeman transition saturation and sample heating and has been observed in previous studies[35–37]. Over the range of microwave powers where the total signal enhancement plateaued, it is likely that full saturation of the selected electron transition occurred and the recorded polarisation would have been reliant upon fast spectral diffusion to engage a wider portion of the EPR spectrum. If the sample had been left to polarise for greater lengths of time at lower microwave powers, potentially the same or even greater signal enhancements than those recorded at higher microwave powers could have been achieved. Allowing extra time to achieve this signal, however, would not have tackled the issue of the slow build-up rates associated with SiNP DNP. Similarly, the converse (i.e. higher microwave powers used for shorter periods) might have led to greater signal enhancements. To investigate this, build-up profiles would need to be recorded at different microwave powers and the build-up times and amplitudes extracted and compared.

In terms of future experimental design, the choice of the number of averages could potentially be reconsidered so as to reduce any contribution of noise in the averaged NMR signal intensities. It must be noted that 256 was chosen to ensure measurable signal following relatively short periods of polarisation build-up to enable a reasonable number of experiments to be completed within each working day. It is possible, however, that the signal enhancements generated were used up in a fewer number of averages meaning noise may have been acquired and averaged into the final NMR signal intensities. Therefore, the true values of maximum possible NMR signal intensities recorded at each microwave power setting might vary from what has been plotted but ultimately, the choice of the optimal microwave power setting would remain the same. Thus, with the aim being to achieve the best possible SNR within the shortest time, whilst minimising

sample heating effects, it was concluded that the optimal microwave power for the polarisation of these SiNP samples was 100 mW.

3.3.3 Signal readout optimisation

3.3.3.1 Introduction

Following the calibration of the ^{29}Si T&M circuit and the optimisation of the microwave power, the sequence for signal readout during the recording of the microwave frequency sweeps and build-up profiles could be established. By optimising the signal readout sequence it would help ensure reasonable SNR could be achieved in as short an amount of time as possible and facilitate the full DNP protocol — i.e. the recording of a microwave frequency sweep, build-up profile, and decay profile for a SiNP sample — being completed within one working day (within 12 hours) as opposed to requiring 18 hours for the build-up alone.

The signal readout for the recording of the build-up and decay profiles is typically done using a single pulse that induces a small FA so as to use up as little of the generated polarisation as possible and minimise disturbance to the system. The purpose of the microwave frequency sweeps (to find the optimal microwave frequency), however, means that the polarisation enhancement generated at each microwave frequency is fully used up (i.e. crushed) prior to recording the enhancement at a different microwave frequency. In other words, it is only the microwave frequency that enabled the greatest polarisation enhancement in a given time that is of interest as opposed to what that polarisation enhancement was at that frequency. Thus, it is desirable to minimise the time required at each microwave frequency so the optimal microwave frequency can be found in as short a time as possible. This can be a challenge, however, for samples that exhibit long DNP build-up times such as SiNPs since measurable signal may not be generated within short time frames. Hence, the need for a signal readout sequence that maximises the SNR.

For any hyperpolarised sample, the greatest SNR during signal readout recorded after the application of a single RF pulse is with a PW corresponding to a 90° FA due to the net magnetisation having been flipped into the transverse plane. Ideally,

the RF pulse would be of a duration so short and applied at a high enough power such that T_2 decay during the pulse would be negligible and the full bandwidth of the ^{29}Si NMR spectra would be excited. However, due to the limited power of the RF amplifier used and the broad line width of ^{29}Si at low temperatures (due to the short T_2 in the solid state), this is not feasible.

For example, based on the FA calibration factor determined in Section 3.3.1.3, a 90° FA would be achieved using a PW of approximately 150 μs. The approximate bandwidth of such a pulse can be calculated using Equation 3.3.

$$\mathrm{BW} \approx \frac{1}{\mathrm{PW}} \approx \frac{1}{0.000150} \approx 6.7\,\mathrm{kHz} \tag{3.3}$$

Applying this pulse, and in the absence of line broadening, the FWHM of the ^{29}Si spectra was measured to be 3.5 kHz. Using Equation 2.15 the T_2 estimated from this spectra was approximately 91 μs.

$$T_2 = \frac{1}{\pi(3500)} = 90.9\,\mu\mathrm{s} \tag{3.4}$$

Hence, the T_2 decay would not be negligible during the application of a 150 μs pulse for a 90° FA. Therefore, an alternative signal readout sequence that was achievable within the limits of the existing hardware had to be found.

A common approach for improving the SNR of NMR spectra is the use of signal averaging. The number of RF pulses applied to a hyperpolarised sample, however, needs to be carefully considered due to the accelerated decay of polarisation with each acquisition. To this end, the maximum possible SNR recorded after varying the number of averages at different PWs was investigated.

3.3.3.2 Methods

To find the optimal number of averages and PW to use in the signal readout sequence, data was first generated using a Bloch simulation which then provided a starting point for the experimental parameters. The theory behind the Bloch simulation is detailed in Section 1.7.

For the acquisition of the experimental data, a SiNP sample was polarised for 20 minutes at 100 mW microwave power. Immediately following this, the microwave source was switched off and 256 acquisitions at a set PW were recorded. This process was repeated a further two times to achieve a total of three runs at each different PW. Within each run, the signal from each acquisition was then averaged together but only up until the point where maximum possible SNR was achieved (i.e. before noise from later acquisitions dominated and reduced the total SNR when averaged in). The number of acquisitions required for the SNR value to reach its maximum was noted for each run at each PW.

Tables 3.1 and 3.2 list the PWs and corresponding FAs – determined using the average FA calibration factor (Section 3.3.1.3) — used to acquire the simulated and experimental data, respectively.

Simulation	
Pulse width (μs)	Flip angle (°)
16.6	10
33.2	20
49.8	30
66.4	40
83	50
99.6	60
116.2	70
132.8	80
149.3	90

Table 3.1: Pulse widths and corresponding flip angles used in the Bloch simulation

Experimental	
Pulse width (μs)	Flip angle (°)
10	6
25	15
50	30
100	60

Table 3.2: Pulse widths and corresponding flip angles used in the experiments

3.3.3.3 Results

Examples of the experimental data that were acquired using PWs of 25 μs and 100 μs are shown in Figure 3.5 alongside example outputs from the Bloch simulation. Upon application of greater PWs, the polarised signal appeared to be used up at a faster rate (i.e. in fewer acquisitions) and this was observed both experimentally and by simulation (Figure 3.5A and B). Upon averaging these acquisitions, the resulting SNR appeared to depend on the number of acquisitions averaged together and also on the applied PW (Figure 3.5C and D).

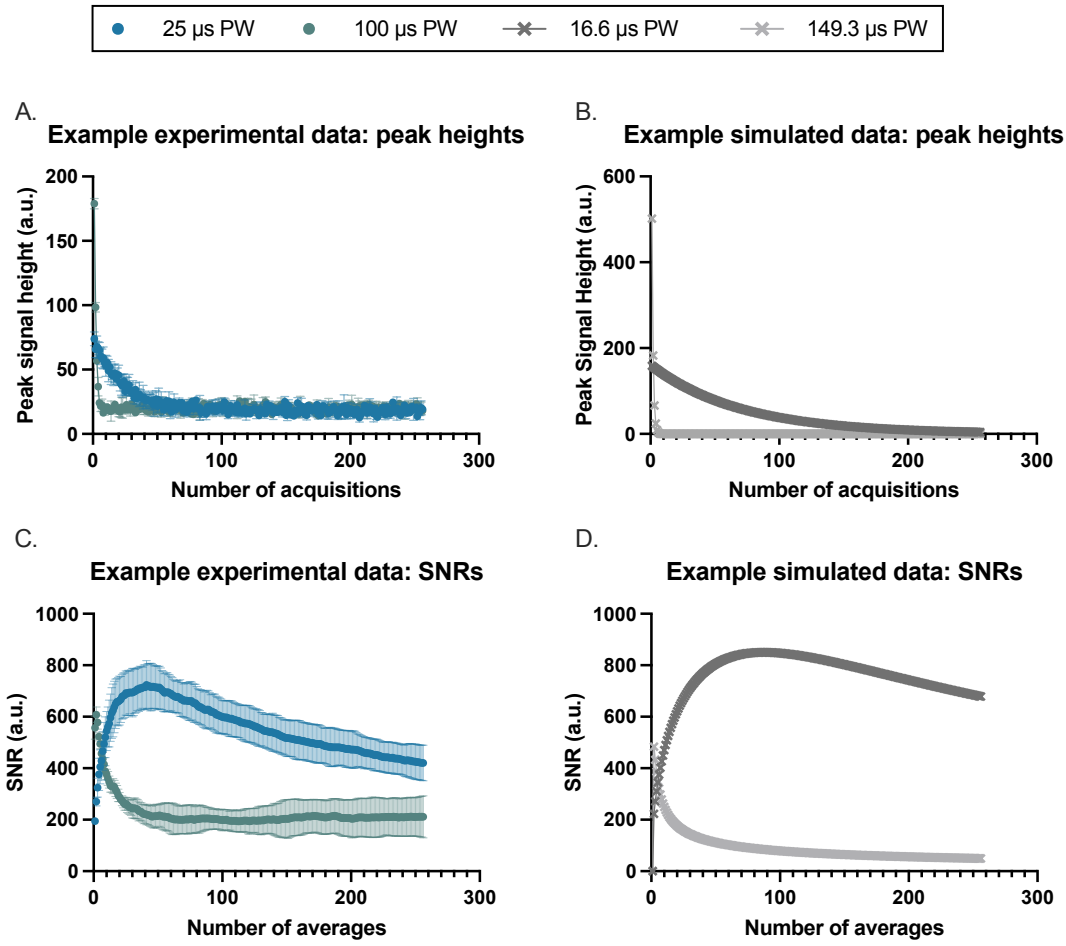

Figure 3.5: Example data from experiment and simulation
The polarised signal appeared to be used up at a faster rate upon application of greater PWs; this was observed both A) experimentally and by B) simulation. Upon averaging together these acquisitions, the resulting SNR appeared to depend on the number of acquisitions averaged together and on the applied PW (C and D). For the experimental data, the plots show the average of $n = 3$.

Overall, the experimental data appeared to be in agreement with the outputs of the Bloch simulation. The data acquired for all the explored PWs is summarised in Figure 3.6. Here, it can be seen that the number of averages required to achieve the maximum SNR appeared to decrease with increasing PW (Figure 3.6A). Specifically, there was a significant decrease in the optimal number of averages between signal readout sequences using PWs of 10 μs and 100 μs. Additionally, the SNR values appeared to decrease with increasing PW, however, no significant differences were identified (Figure 3.6B).

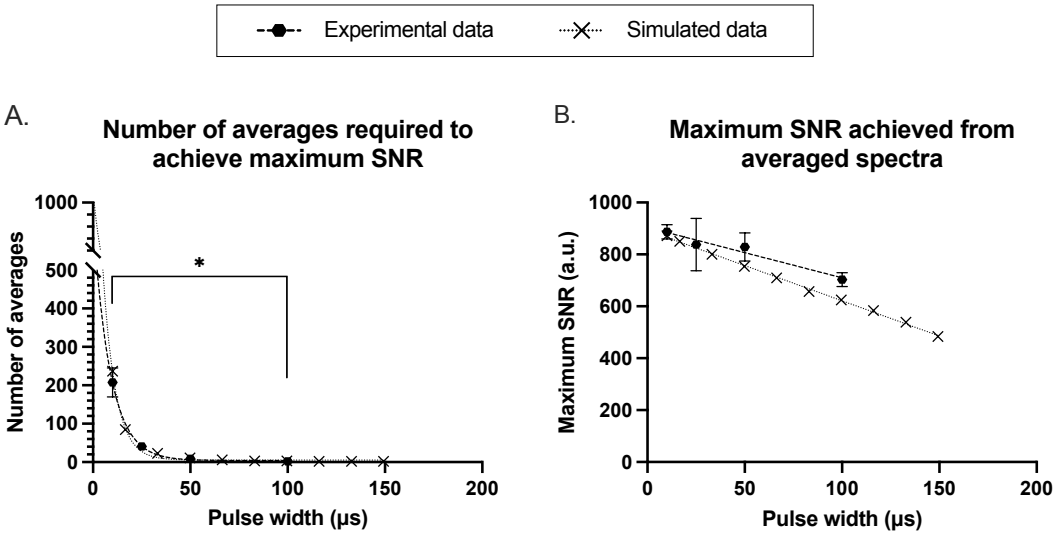

Figure 3.6: Optimisation of signal readout for different PWs
The full experimental data and simulation outputs are summarised as dot plots. Experimentally, in the absence of microwave irradiation, radio frequency pulses were repeatedly applied to polarised silicon nanoparticle samples. The total signal-to-noise ratio was calculated by averaging across acquisitions for each specific pulse width. A) The number of acquisitions averaged together to achieve the maximum possible signal-to-noise ratio appeared to decrease with increasing pulse width. B) The maximum signal-to-noise ratio value appeared to decrease with increasing pulse width. In both plots, the experimentally obtained data is the average of $n = 3$ and appears to be in agreement with the outputs of the Bloch simulation. Significance was calculated using a Holm-Šídák test. Significance is shown as * when $p < 0.05$.

To determine the optimal signal readout sequence, the maximum SNR was considered in combination with the time required to achieve it i.e. the duration of each sequence (Table 3.3). Thus, the 50 μs PW sequence was selected as — without a significant reduction in the maximum achievable SNR — it would enable

the acquisition to be completed in 1.01 s as opposed to the 23.4 s required for the 10 μs PW sequence.

Pulse width (μs)	Maximum SNR (a.u.)	Time to achieve maximum SNR (s)
10	887	23.4
25	838	4.61
50	829	1.01
100	703	0.225

Table 3.3: Summary of each signal readout sequence

3.3.3.4 Discussion

The optimal signal readout sequence available within the limits of the existing hardware was explored both experimentally and by simulation. Overall, the experimental results appeared to be in agreement with those generated by simulation. Compared to using a single 90° FA pulse, it appeared as though any of the four signal readout sequences explored experimentally would generate signals with greater SNR.

No significant differences amongst these SNR values were identified between the four signal readout options, however, the 50 μs PW sequence was selected to be optimal as it would enable the acquisition to be completed in 1.01 s as opposed to the 23.4 s required for the 10 μs PW sequence. Although this difference in duration would seem to be marginal in comparison to the minutes used in polarising the sample at each microwave frequency, the opportunity to save on time whilst having negligible effect on the maximum SNR was taken. Additionally, for the recording of the microwave frequency sweep profiles, the time the sample would be left to polarise at each frequency step would ideally be less than the 20 minutes used here.

For the recording of the build-up profiles, a 10 μs PW with no averages was deemed the most suitable readout sequence. Whilst the low FA may lead to difficulty in observing signal for the first few data points of the build-up (when SNR would be particularly low), due to the notoriously slow build-up rates and low signal enhancements of SiNP samples it was important to ensure the FAs and

number of FAs applied did not use up the polarisation at a rate faster than the rate of polarisation generation. Thus, this was thought to outweigh the possibility that the first few acquisitions may not have detectable signal. Nevertheless, after 20 minutes of polarisation, the first 10 μs pulse acquired in each experimental run resulted in signals with high enough SNR to be detected.

Finally, it must be noted that samples were left to polarise for a shorter period than that used in Section 3.3.2 where the effect of microwave power was explored. Hence, 100 mW might not have been the optimal power for this experimental design. Either the duration of the microwave irradiation should have remained the same, or the effect of its duration should have been explored further prior to the optimisation of the signal readout.

3.4 Silicon nanoparticle DNP

3.4.0.1 Background

The optimisation of SiNP polarisation during DNP is a critical step in the lead up to their use in *in vivo* studies due to the signal recorded during MR scans being limited by the signal enhancements generated within the polariser. Having set-up the laboratory for the assessment of DNP of ^{29}Si, efforts turned to finding the optimal sample preparation. The sample preparations that were explored can be sorted into three broad categories, each of which are discussed within their own subsection, namely: bare SiNPs; SiNPs and exogenous radicals; and SiNPs and irradiation generated endogenous radicals.

3.4.1 Hyperpolarisation via intrinsic endogenous radicals

3.4.1.1 Introduction

The extraordinarily long T_1 relaxation time exhibited by SiNPs has been attributed to: a low natural abundance of ^{29}Si (4.7 %); weak dipole-dipole interactions between dilute ^{29}Si nuclei; and particle structures that isolate these spins from thermal motions that drive relaxation[38].

The typical structure of a SiNP comprises a crystalline silicon core and a naturally occurring amorphous silicon dioxide (SiO_2) outer shell (Figure 3.7). There are a range of structural features, however, that can be introduced and finely tuned during synthesis to create intricate particle structures that offer additional benefits[1]. For example, multiple layers of different lattice structures can be used to create shells to prolong the T_1 relaxation time (which holds even under physiological conditions[40]) and/or pores that can provide the opportunity for drug-loading[41].

Regardless of how complex the SiNP structure is, the way in which they polarise during DNP is fundamentally the same. At a core-shell interface, due to structural

[1]There are numerous methods for the synthesis of SiNPs and consequently there are a wide range of SiNP structures and sizes available commercially. This diversity of choice is reflected in the varieties of particles used and reported in the literature which makes direct comparisons between studies an almost impossible task. A comprehensive discussion of all possible synthesis routes and resulting SiNP morphologies is beyond the scope of this work but can be found elsewhere (e.g. Huan and Shu-Qing[39])

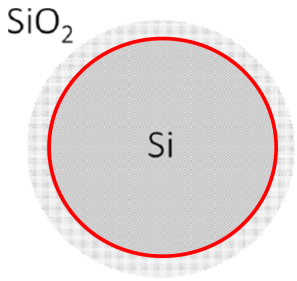

Figure 3.7: Typical structure of a silicon nanoparticle
The typical structure of a silcon nanoparticle comprises a crystalline silicon core and a naturally occurring amorphous silicon dioxide outer shell. At the core-shell interface, due to structural discontinuities, dangling bonds provide a source of free electrons which, during DNP, are used to directly transfer polarisation to neighbouring nuclei. The bulk of the particle is then polarised via nuclear spin diffusion. Figure adapted from Kwiakowski *et al*[42].

discontinuities, dangling bonds provide a source of free electrons. Upon microwave irradiation, polarisation is directly transferred from these electrons to neighbouring ^{29}Si nuclei[42]. Within the core of the particle there are few free electrons and hence, the nuclear spins located there rely upon nuclear spin diffusion to be polarised. Similarly, in the absence of microwave irradiation, the electrons at the interface undergo relaxation first, triggering the relaxation of neighbouring ^{29}Si nuclei, followed by those in the core, again via nuclear spin diffusion. Nuclear spin diffusion, however, is an inherently slow process and thus, the influence of structure on SiNP polarisation is a double edged sword; whilst it contributes to the desirable slow polarisation decay rates, it is also to blame for the slow rates of polarisation build-up.

In light of this, it is perhaps intuitive that particle size also has a part to play in the time it takes to achieve steady-state polarisation and the duration of polarisation retention. In general, the larger the particle, the greater the distance between the SiNP core and its surface, and thus, the greater the structure of the core whose order impedes the relaxation that originates at the disordered particle surface. Hence, the greater distance over which nuclear spin diffusion is the dominant polarisation/relaxation mechanism[43]. In other words, the smaller the particle, the shorter the polarisation build-up time and this pattern is mirrored in the T_1 relaxation times[44].

Thus, there has been growing interest in the implementation of methods to lengthen the T_1 relaxation time of SiNPs. One example is a study conducted by Atkins *et al.* where they developed a new synthesis method resulting in SiNPs that had "size adjusted" T_1 relaxation times. The SiNPs were synthesised by a metathesis reaction of sodium silicide with a silicon tetrachloride and, from those that were approximately 10 nm in diameter, they achieved a five-fold improvement in the T_1 relaxation time compared to those recorded from other commercially available SiNPs of similar size[45]. Kwiakowski *et al.* took a different approach that involved investigating the relationship between surface defect concentration, particle size, and polarisation characteristics between commercially available SiNPs that had been synthesised in different ways[42]. They found that ideally, the defect concentration should be tuned with respect to the particle size. For example, lower polarisation enhancements were recorded from SiNPs that exhibited higher surface defect concentrations, which was attributed to a reduction in polarisation transfer efficiency due to increased nuclear T_1 relaxation. SiNPs that had been synthesised via laser-assisted etching were found to exhibit the greatest polarisation levels and longest room temperature nuclear T_1 relaxation times.

Taking into account these findings, laser synthesised 30 – 50 nm polycrystalline SiNPs were sourced for this research which was conducted under comparable conditions to the vast majority of published work with d-DNP on glass-forming small molecules (i.e. at 3.35 T/94 GHz). Whilst it was expected that samples would polarise via the naturally occurring electrons located at the Si:SiO_2 interface and at structural defects within the polycrystalline structure, it was not known to what extent and how the resulting polarisation would compare to other HCAs in preclinical development.

3.4.1.2 Methods

Laser synthesised 30 – 50 nm SiNPs were commercially sourced from US Nanomaterials. In a 1.5 ml eppendorf tube, 130 μl of a 1:1 DMSO and D_2O mixture was pipetted onto 37 mg of bare (i.e. used as received) SiNPs.

Each sample was vortexed and sonicated until forming a liquid that could be pipetted into a sample cup. The sample cup was then inserted into the polariser where microwave frequency sweeps, build-up profiles, and decay profiles were recorded. The signal readout sequences optimised in Section 3.3.3 were used to record these and the step size for the microwave frequency sweep was 20 MHz. From the fits of the build-up and decay profiles, the build-up amplitudes, build-up times, and decay time constants were extracted. This was repeated for a total of three samples. The detailed ^{29}Si DNP protocol can be found in Section 2.2.

3.4.1.3 Results

The generation and decay of ^{29}Si NMR signal recorded from bare SiNP samples is summarised in Figure 3.8.

Among the three samples, the optimal microwave frequency was found to differ (Table 3.4) and from the averaged microwave frequency sweep profiles, there was no obvious peak in ^{29}Si NMR signal. As illustrated by the averaged build-up and decay profiles, an increase in ^{29}Si NMR signal intensity was recorded over time during DNP and, in the absence of microwave irradiation, the generated signal was found to decay over time. The extracted polarisation constants from these profiles were as follows: build-up amplitude = 11.2 ± 3.0 a.u./mg, build-up time = 4.6 ± 1.7 hours, decay time = 7.4 ± 1.1 hours.

Sample	Frequency (GHz)
1	93.78
2	93.80
3	93.84

Table 3.4: Bare SiNPs: Optimal microwave frequencies

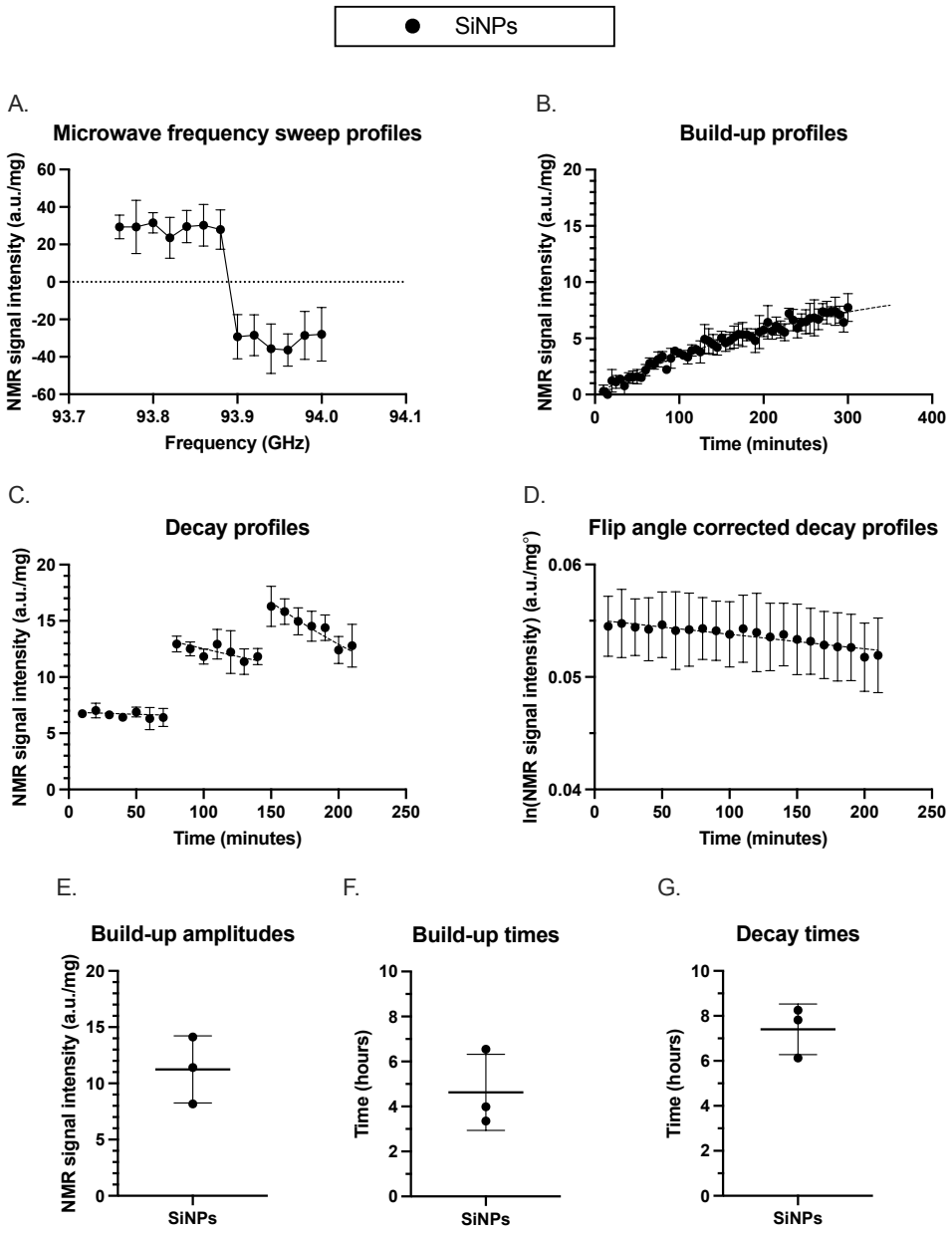

Figure 3.8: Samples polarised via naturally occurring endogenous radicals
The generation and decay of ^{29}Si polarisation recorded from bare silicon nanoparticle samples is summarised. ^{29}Si NMR signal was recorded at different microwave frequencies to generate A) microwave frequency sweeps. Following this, the ^{29}Si NMR signal was monitored whilst samples were continuously irradiated at the optimal frequency. This generated B) build-up profiles which showed an increase in NMR signal intensity over time. In the absence of microwave irradiation, the loss of ^{29}Si NMR signal was monitored in the solid state to generate C) decay profiles. The solid state decay data were corrected D) for pulse width and the natural logarithm was taken to enable the extraction of the decay time constant. The polarisation constants i.e. the E) build-up amplitudes, F) build-up times and, G) the solid state decay times are also shown. These data confirmed polarisation of ^{29}Si nuclei via naturally occurring endogenous radicals is feasible for these silicon nanoparticles. Dot plots show the average of $n = 3$. Bars display mean ± SD.

3.4.1.4 Discussion

The first observation from this work arose from the expectation that DNP samples of the same type have the same optimal microwave frequency due to the polarisation transfer mechanisms and their efficiencies being dependent on properties of the sample[46]. Here, different optimal microwave frequencies were recorded from the three "identical" samples. This discrepancy may have arisen due to low SNR following the acquisitions at each frequency step and/or as a consequence of the choice of frequency step size. In contrast to the work conducted in Section 3.3.3, where the signal readout sequence was optimised to maximise the SNR, the samples here were irradiated for five minutes at each frequency (as opposed to 20 minutes) and did not contain a polarising agent. Consequently, SiNP DNP samples polarising via intrinsic endogenous radicals would likely require longer build-up times at each step of the microwave frequency sweep to gain greater certainty that the optimal microwave frequency was selected for the monitoring each build-up profile. Alternatively, a smaller step size (e.g. 10 MHz) could have been adopted, however, this would have doubled the time required for the recording of the microwave frequency sweep.

For the build-up profiles, each sample was irradiated at its optimal microwave frequency i.e. at different frequencies. Nevertheless, the increase in ^{29}Si NMR signal intensity observed over time during continuous microwave irradiation, and the decay of this signal in the absence of the microwave irradiation, confirmed that the ^{29}Si nuclei within these SiNPs could be polarised via the naturally occurring endogenous radicals (Figure 3.8B and D). However, upon comparing the signal enhancements to those recorded from ^{13}C-pyruvate samples, it became evident that greater signal enhancements would be required for preclinical trials.

Another observation was that the build-up data was best fitted to monoexponential curves and not biexponential. Biexponential fittings of SiNP build-up and decay profiles have previously been reported and the two-step mechanism has been attributed to the SiNP structure[43]. In contrast to the ordered lattice structure of the core, the SiNP surface comprises a more disordered chemical environment in

which polarisation build-up and decay mechanisms are more efficient. One possible reason for a biexponential mechanism not being observed here is that the time resolution (acquisitions every five minutes) may not have have been sensitive to it; Thiessen *et al.* found the fast component to be on the order of minutes and the slow component to be on the order of hours[43]. An alternative reason would be the size of the SiNPs. As SiNPs increase in size, the distance between the nuceli within the core and the defects on the SiNP surface increases. For example, for SiMPs, Hu *et al.* hypothesised that the detectable signal remaining after a fast relaxation between the polariser and the scanner was due to ^{29}Si nuclei being located sufficiently far from relaxation centres resulting in a slow T_1 relaxation via spin diffusion[47]. The authors suggested that similar behaviour must occur in SiNPs, however, the shorter distance between the nuclear spins and relaxation centres may mean the "fast" relaxation component cannot be observed and that the "slow" component dominates.

Finally, it can be seen from the build-up profiles (Figure 3.8B) that the polarisation had not reached saturation prior to the microwaves being switched off. This is likely to affect the values of the extracted build-up polarisation constants (Figure 3.8E and F). However, the build-ups were not left to plateau due to the aim of this work being to achieve usable SiNP polarisation enhancements within a time period of one working day. To tackle low polarisation build-up rates, a method commonly used within the field of DNP is the addition of a polarising agent in the form of a stable organic exogenous radical species during sample preparation.

3.4.2 Hyperpolarisation via exogenous radicals

3.4.2.1 Introduction

An organic exogenous radical species is a molecule that has at least one unpaired electron[48]. The motivation behind adding these molecules to DNP samples is to improve the efficiency of polarisation transfer by increasing the number of electrons available to polarise nuclear spins. Here, the addition of radical species is explored

as a tool to improve the nuclear polarisation of the SiNPs and thus, achieve a SNR that would justify *in vivo* application.

At the time of writing, only one publication describing optimisation work with an exogenous radical for use in SiNP DNP could be found[2] and so this provided the starting point for this research. In the study, Hu *et al.* explored the effect of TEMPO concentration (0 – 120 mM) on the polarisation of silicon particles of various sizes (30 – 200 nm)[47]. For each particle size, the optimal TEMPO concentration was investigated but there did not appear to be a clear relationship between particle size, TEMPO concentration, and the maximum ^{29}Si signal enhancement. In general, the addition of TEMPO was found to improve the polarisation enhancements of the SiNPs and, whilst it appeared to shorten the T_1 relaxation time, the T_1 at room temperature was measured to be approximately 20 minutes. Therefore, it was hypothesised that greater signal enhancements would be achieved from our SiNP samples if TEMPO were added to the sample preparation.

This research was then taken a step further by considering the role of radical structure on the polarisation transfer mechanism(s) during DNP. So far, three polarisation transfer mechanisms are thought to occur during solid-state DNP, namely: the Solid Effect (SE), the Cross Effect (CE), and Thermal Mixing (TM), and the theory behind each of these is detailed in Section 1.9.1. During DNP, a combination of these mechanisms can occur and the relative contributions from each depends on: the radical concentration, the electron spin-lattice relaxation of the radical (T_{1e}), and the nuclear Larmor frequency and how it compares to the EPR linewidth of the radical[46]. Thus, the effect of using EPA/AH111501 (a narrow linewidth Trityl radical) was explored over a range of concentrations and compared to the effect of adding TEMPO (a broad linewidth Nitroxide radical). These two radicals are among the most commonly used during preclinical trials of HCAs and so were seen as representative radicals from the Trityl and Nitroxide families. Further to this, exploratory data using structurally analogous radicals to TEMPO and AH111501 were also acquired (TEMPOL and OX063, respectively).

[2] In contrast, there have been many studies conducted on silica nanoparticles.

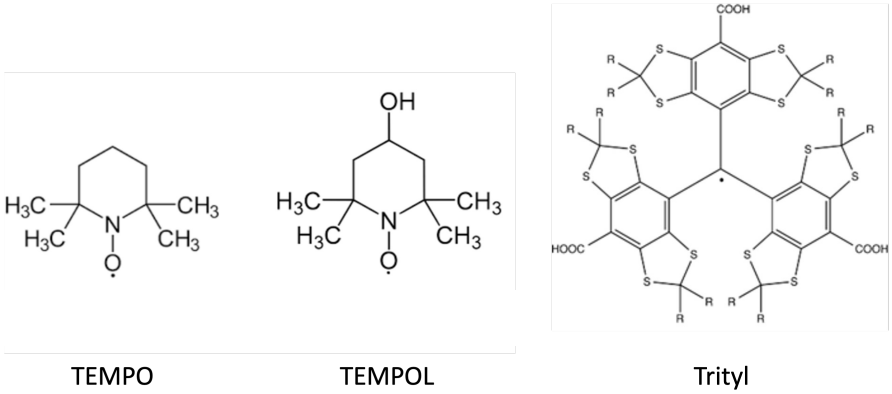

Figure 3.9: The selected radical species and their structures
The addition of radical species was explored as a tool in the optimisation of silicon nanoparticle polarisation. The effect of radical structure and concentration were assessed using: TEMPO and TEMPOL (from the Nitroxide family) and AH111501 and OX063 Trityl from the (Trityl family) where R=$CH_2CH_2OCH_3$ and R=CH_2CH_2OH, respectively.

From Figure 3.9, the differences in morphology between the Nitroxide and Trityl families is evident. In particular, the differences in their sizes provided an additional motivator for exploring structurally analogous radicals and their effect on SiNP polarisation. The "spin diffusion barrier" is a model that estimates the distance over which nuclei within the core of spherical particles can be directly polarised by radicals on their surface[49]. An estimate of the spin diffusion barrier radius (r_d) can be calculated using Equation 3.5 where S is the spin quantum number of the electron, γ_e and $\gamma(^{29}Si)$ are the gyromagnetic ratios of the electron and ^{29}Si nucleus, B_S is the Brillouin function for spin S, $\hbar$ is the reduced Planck constant, B_0 is the static magnetic field, k_b is the Boltzmann constant, and T is the temperature of the sample.

$$r_d \approx \left[2S\frac{\gamma_e}{\gamma(^{29}\mathrm{Si})}B_S\left(\frac{S\hbar\gamma_e B_0}{k_b T}\right)\right] \tag{3.5}$$

$$\text{where } B_S(x) = \frac{2S+1}{2S}\coth\left(\frac{2S+1}{2S}x\right) - \frac{1}{2S}\coth\left(\frac{1}{2S}x\right). \tag{3.6}$$

Based on this model, a more simplified approach termed the "penetration depth effect" was derived by Akbey *et al.* and is given by equation 3.7[50].

$$\frac{V_{\text{polarised}}}{V_{\text{nanoparticle}}} = \left[\frac{\frac{4}{3}\pi r^3 - \frac{4}{3}\pi(r-a)^3}{\frac{4}{3}\pi r^3}\right] \tag{3.7}$$

where a is the penetration depth and is found through fitting Equation 3.7 to experimental data. These two models are in principle the same, however, for the penetration depth model the size-dependent DNP enhancements must be known and the penetration depth has to be smaller than the radius of the particles. Regardless of the model, the number of radicals at the surface of a particle and the distance between the radicals and the core nuclei have been shown to be key factors in the efficiency of polarisation transfer between the electron and nuclear spin populations.

In conjunction with exogenous radicals, lanthanide metal chelates, such as those based on gadolinium ions (Gd^{3+}), are commonly added to DNP sample preparations to achieve further signal enhancements by altering the efficiency of polarisation transfer. Improvements of $50-100\,\%$ in polarisation have previously been recorded from samples containing Trityl radicals[51, 52]. These improvements have been ascribed to low concentrations of gadolinium reducing the electron spin-lattice relaxation time (T_{1e}) of the radical species but having no impact on the nuclear T_1 and thus, resulting in an increased rate at which electron polarisation can be transferred[53]. Gadolinium has seven unpaired electrons and so it has a large magnetic moment which it retains even when chelated. The addition of a commercially available and widely available form of chelated gadolinium formed the final step of this part of the research.

3.4.2.2 Methods

60 mM radical concentration stock solutions were made by dissolving the appropriate mass of radical in a 1:1 DMSO and D_2O mixture. Aliquots of this stock solution were taken to make 15 mM and 30 mM stock solutions. To make each DNP sample, 130 μl of stock solution was pipetted onto 37 mg of SiNPs. The radicals used were TEMPO (MW= 156.25 g/mol), AH111501 ("GE Trityl") (MW= 1595 g/mol) and their respective structural analogues: TEMPOL (MW= 172.25 g/mol) and OX063 Trityl (MW= 1427 g/mol).

For the addition of gadolinium, 14.5 μl of a 1:50 Dotarem (Guebert, France):D_2O stock solution was added to 130 μl of radical stock solution and 37 mg of SiNPs. This gave a final gadolinium concentration of 1 mM. See Section 2.2.2 for details on sample preparations that contained gadolinium.

Following preparation, all ^{29}Si sample mixtures were vortexed, sonicated, and pipetted into a PEEK sample cup ready for insertion into the polariser.

3.4.2.3 Results

The data recorded following the addition of 30 mM TEMPO is summarised in Figure 3.10. The first observed difference was that the optimal frequency for samples containing TEMPO could be easily identified from visual assessment of the resulting ^{29}Si NMR signal intensities (Figure 3.10A). Signal enhancements were also greater during the recording of the build-up profiles compared to samples that contained no radical (Figure 3.10B). Representative NMR spectra (Figure 3.10C and 3.10D) further demonstrate the differences in NMR signal intensity recorded after five hours of DNP. In the absence of microwave irradiation, samples containing TEMPO appeared to show a comparable ability to that of bare SiNP samples for polarisation retention in the solid-state (Figure 3.10F). Overall, the addition of 30 mM TEMPO appeared to aid the polarisation of the SiNPs.

Upon further investigation, the polarisation characteristics of SiNPs appeared to depend on the concentration of TEMPO (Figure 3.11). For example, samples containing 15 mM TEMPO had a significantly higher optimal frequency compared to samples that contained no radical (Figure 3.11A). Differences were also observed in the ^{29}Si NMR signal intensities recorded during polarisation build-ups (Figure 3.11B). Specifically, there was a significant reduction in the build-up amplitudes between samples that contained 30 mM and 60 mM TEMPO (Figure 3.11E). However, no significant differences in the rates of ^{29}Si NMR signal decay were found (Figure 3.11G). From the extracted polarisation constants, the addition of TEMPO appeared to increase the build-up amplitude, shorten the build-up time, and had little-to-no effect on the decay time.

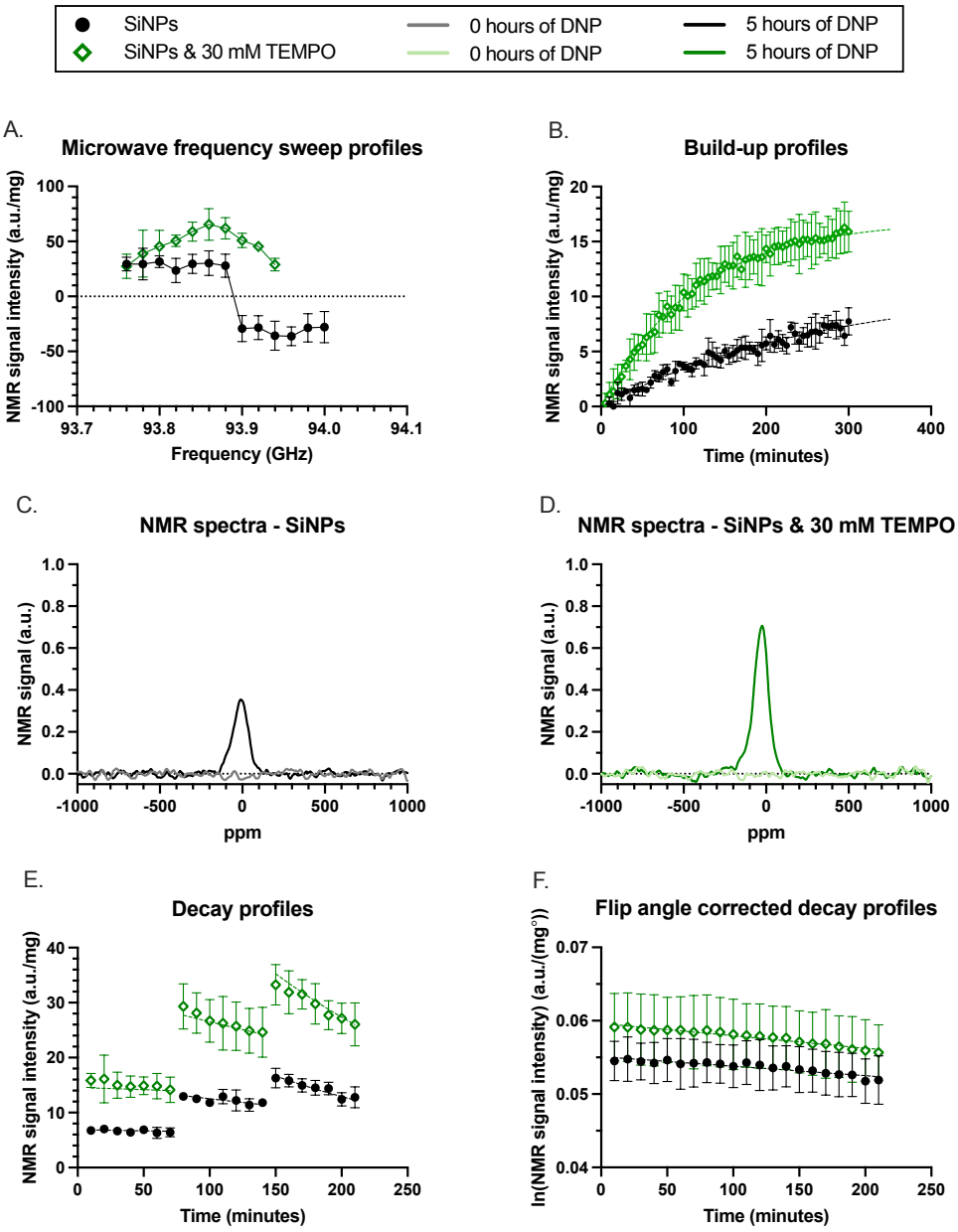

Figure 3.10: 30 mM TEMPO enhanced silicon nanoparticle polarisation
Differences in the ^{29}Si NMR signal intensities were recorded at different frequencies during the A) microwave frequency sweeps. These differences in ^{29}Si NMR signal intensity were also seen in the generated B) build-up profiles. Representative NMR spectra recorded before and after five hours of DNP for samples containing C) no radical and D) 30 mM TEMPO appeared to show greater signal enhancements from the latter. In the absence of microwave irradiation, the decay of ^{29}Si NMR signal was monitored over time to generate E) decay profiles which were subsequently F) corrected for increases in pulse width during signal readout. The ability for samples to retain their polarisation in the solid-state appeared to be preserved following the addition of 30 mM TEMPO. This data shows the potential of the TEMPO radical as a tool for the optimisation of silicon nanoparticle polarisation. Dot plots show the average of $n = 3$ samples. Bars display mean ± SD.

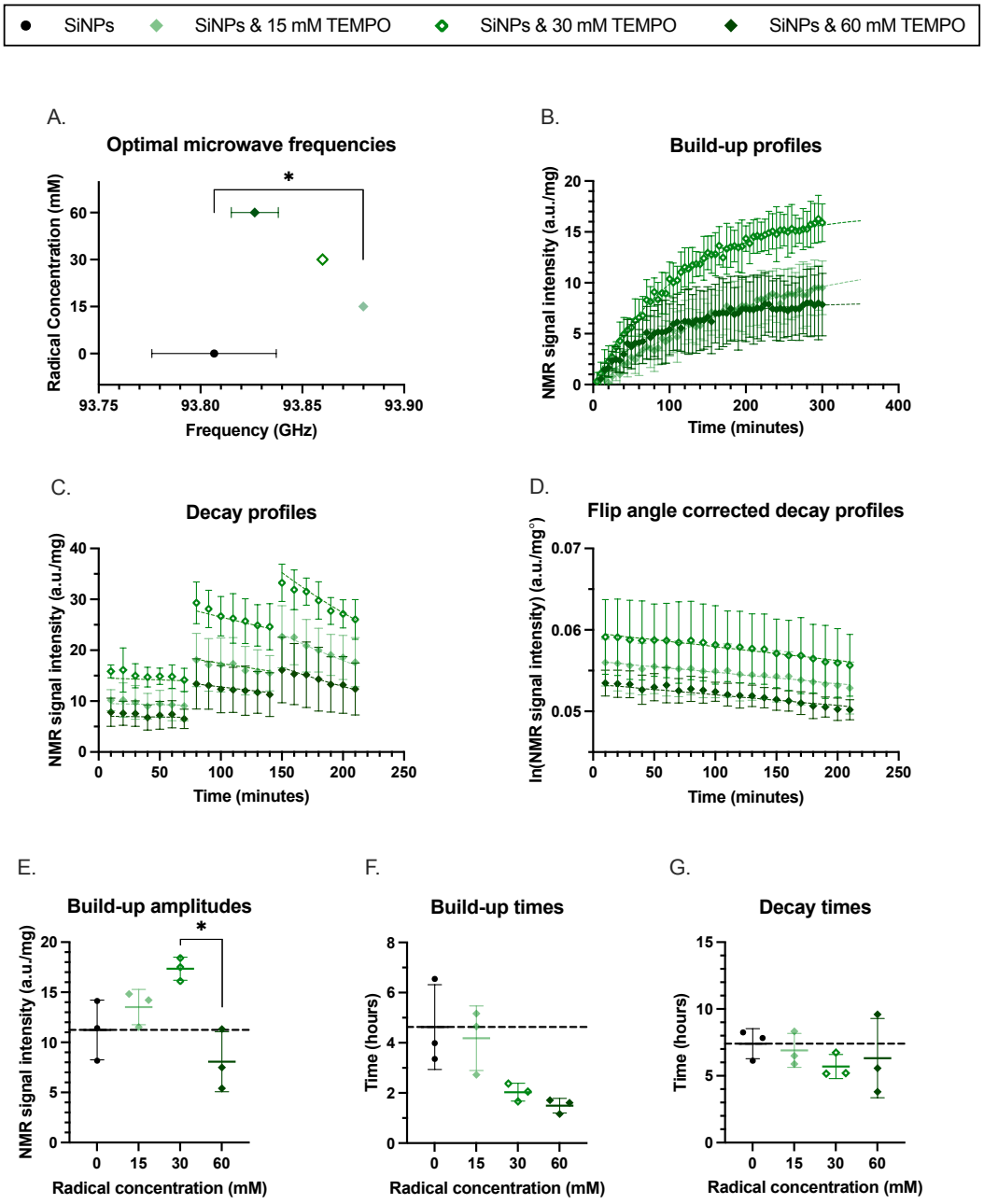

Figure 3.11: TEMPO concentration affected silicon nanoparticle polarisation Frequency sweeps were recorded to identify A) the optimal microwave frequencies for each sample; these appeared to decrease with increasing TEMPO concentration. The B) build-up profiles appeared to show differences in ^{29}Si NMR signal intensity recorded over time between the different sample types. No significant differences in the rate of ^{29}Si NMR signal decay were observed from the C) decay profiles which were D) corrected for changes in pulse width during signal readout. The extracted E) build-up amplitudes, F) build-up times, and G) decay times indicated 30 mM to be the optimal concentration of TEMPO for the polarisation of these silicon nanoparticles. Dot plots show the average of $n = 3$. Bars display mean ± SD. Significance was calculated using a Kruskal-Wallis test with Dunns multiple comparisons. Significance is shown as * when $p \leq 0.05$.

The mean and standard deviation of the polarisation constants for each sample type are detailed in Table 3.5 and would appear to show 30 mM as the optimal concentration of TEMPO for the polarisation of these SiNPs.

Concentration (mM)	Build-up amplitude (a.u./mg)	Build-up time (hours)	Decay time (hours)
0	11.2 ±3.0	4.6±1.7	7.4±1.1
15	13.5 ±1.8	4.2±1.3	6.9±1.3
30	17.3 ±1.2	2.0±0.4	5.7±0.9
60	8.07±3.0	1.5±0.3	6.3±3.0

Table 3.5: Polarisation constants: effect of TEMPO concentration

The effect of radical concentration on SiNP polarisation characteristics did not appear to be specific to the TEMPO radical (Figure 3.12). As observed with samples that contained TEMPO, upon increasing the concentration of AH111501, the optimal microwave frequency recorded during microwave frequency sweeps appeared to decrease (Figure 3.12A). There were also observable differences in ^{29}Si NMR signal intensity during the recording of polarisation build-up profiles (Figure 3.12B). Yet, as was seen with the TEMPO samples, no significant differences in the rates of ^{29}Si NMR signal decay were observed between samples that contained different AH111501 concentrations (Figure 3.12D). However, from the extracted polarisation constants, the addition of AH111501 appeared to decrease the build-up amplitude whilst shortening the build-up time, and had little-to-no effect on the decay time. At the highest AH111501 concentration (60 mM) the build-up amplitudes and build-up times were significantly reduced compared to samples that contained no radical. The mean and standard deviation of the polarisation constants for each sample type are detailed in Table 3.6.

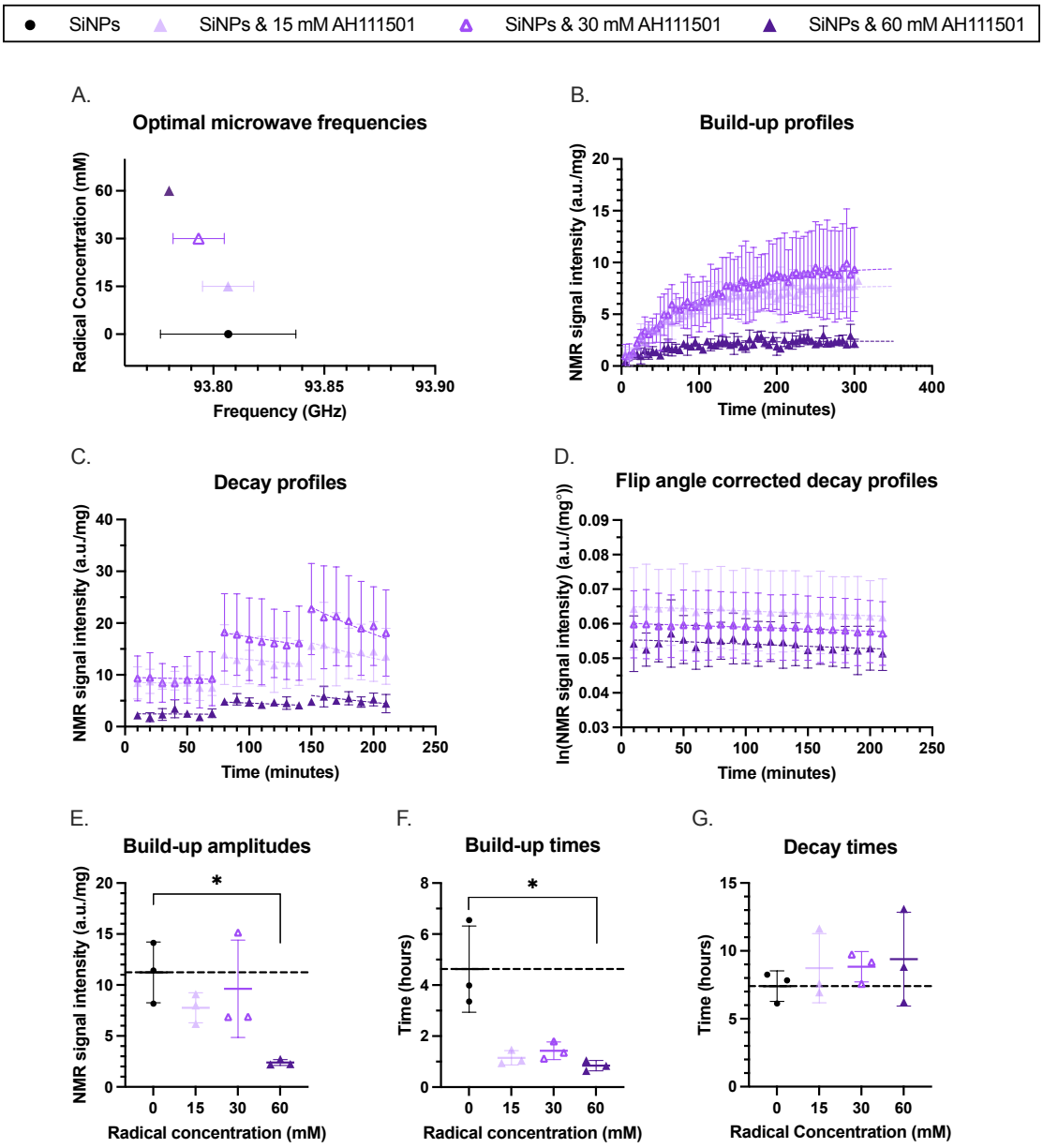

Figure 3.12: AH111501 hindered silicon nanoparticle polarisation
Frequency sweeps were recorded to identify A) the optimal microwave frequencies for each sample; these appeared to decrease with increasing AH111501 concentration. The B) build-up profiles appeared to show differences in ^{29}Si NMR signal intensity recorded over time between the different sample types. No significant differences in the rate of ^{29}Si NMR signal decay were observed from the C) decay profiles which were D) corrected for changes in pulse width during signal readout. The extracted E) build-up amplitudes, F) build-up times and, G) decay times appear to show the addition of AH111501 did not aid the polarisation of these silicon nanoparticles. Dot plots show the average of $n = 3$. Bars display mean ± SD. Significance was calculated using a Kruskal-Wallis test with Dunns multiple comparisons. Significance is shown as * when $p < 0.05$.

Concentration (mM)	Build-up amplitude (a.u./mg)	Build-up time (hours)	Decay time (hours)
0	11.2 ± 3.0	4.6 ± 1.7	7.4 ± 1.1
15	7.8 ± 1.5	1.2 ± 0.3	8.7 ± 2.5
30	9.6 ± 4.8	1.4 ± 0.3	8.8 ± 1.1
60	2.4 ± 0.3	0.8 ± 0.2	9.4 ± 3.5

Table 3.6: Polarisation constants: effect of AH111501 concentration

The addition of AH111501 did not improve the signal enhancement beyond that recorded from samples that contained no radical, however, it did appear to lead to a reduction in the build-up time. Therefore, if a reduction in build-up time was required, 15 mM would appear to be the optimal concentration of AH111501. Whilst 30 mM appeared to exhibit a greater build-up amplitude than the 15 mM sample, due to the toxicity of exogenous chemical radicals *in vivo* and their detrimental effect on the liquid state nuclear T_1 relaxation time, it is desirable to minimise the radical concentration wherever possible.

Although concentration-specific effects on SiNP polarisation were observed following the addition of either radical, differences were observed in the details of these effects (Figure 3.13). Firstly, the shape of the microwave frequency sweeps recorded from samples containing AH111501, whilst following a similar pattern, were narrower than those recorded from samples that contained TEMPO (Figure 3.13A). The full sweeps from AH111501 samples fitted within the positive lobes of the sweeps recorded from samples that contained TEMPO. As a result, the optimal microwave frequencies for AH111501 samples were consistently lower than those recorded from samples that contained TEMPO at the same concentration (Figure 3.13B). Further investigation into the role of radical structure led to the acquisition of EPR spectra of representative samples. A SiNP sample containing 30 mM AH111501 had an EPR linewidth that was approximately three times narrower than that recorded from a SiNP sample containing 30 mM TEMPO. Differences in EPR line shapes between the two samples were also observed (Figure 3.13C and D).

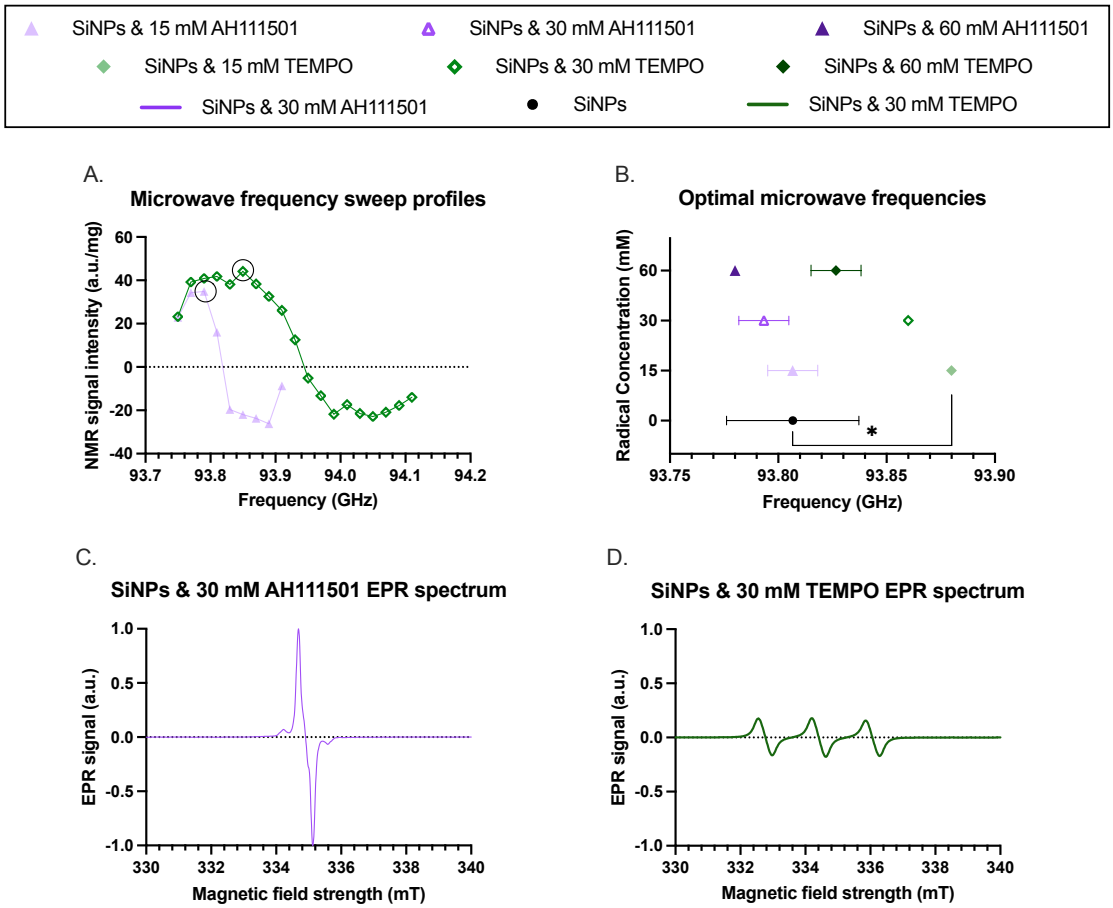

Figure 3.13: Radical-specific concentration-specific effects
Representative and summary data highlighting differences observed between polarised silicon nanoparticle samples containing radicals of different structure. Whilst the microwave frequency sweeps appeared to be similar in shape, the optimal frequencies recorded from them differed. Representative A) frequency sweep profiles recorded from samples containing either 15 mM AH111501 or 30 mM TEMPO are shown. The sample containing 15 mM AH111501 exhibited a narrower enhancement profile and peaked at a lower optimal frequency. A summary of the B) optimal frequencies appear to show radical-specific concentration effects. EPR spectra of each sample were recorded and differences in the EPR line widths and shapes were observed as shown by C) and D) representative EPR spectra (data normalised to AH111501). Dot plots show the average of $n = 3$. Bars display mean ± SD. Significance was calculated using a Kruskal-Wallis test with Dunns multiple comparisons. Significance is shown as * when $p < 0.05$.

Moreover, these radical-specific concentration-specific effects appeared to hold under the exploration of structurally-analogous radicals. The extracted polarisation constants (Figure 3.14) from samples containing OX063 Trityl and TEMPOL appeared to be in-line with those extracted from samples containing their structural analogues (AH111501 and TEMPO, respectively) at the same concentration. The

polarisation constants are detailed in Table 3.7.

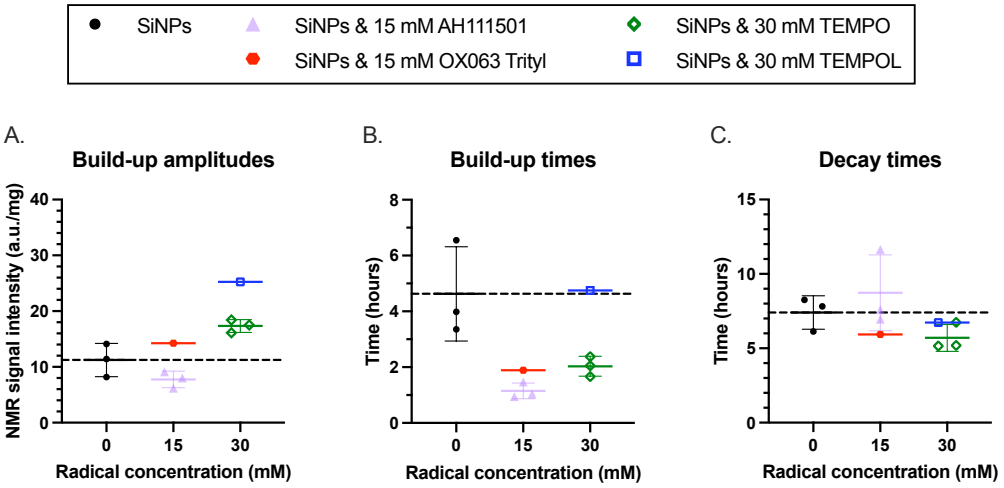

Figure 3.14: Structurally analogous radicals had similar effects on polarisation Dot plots summarising the polarisation constants extracted from samples containing structurally analogous radicals. Samples containing 15 mM OX063 Trityl ($n = 1$) and 30 mM TEMPOL ($n = 1$) were used as structural analogues for comparison to samples containing AH111501 ($n = 3$) and TEMPO ($n = 3$), respectively. From the A) build-up amplitudes, B) build-up times and, C) decay times, there appeared to be similar effects on the polarisation characteristics of silicon nanoparticles from using a structurally analogous radical. Bars display mean ± SD.

Radical species and concentration	Build-up amplitude (a.u./mg)	Build-up time (hours)	Decay time (hours)
15 mM OX063 Trityl	14.3	1.9	5.9
15 mM AH111501	7.8±1.5	1.2±0.3	8.7±2.5
30 mM TEMPOL	25.2	4.7	6.7
30 mM TEMPO	17.3 ±1.2	2.0±0.4	5.7±0.9

Table 3.7: Polarisation constants: structural analogues

The addition of 1 mM gadolinium in the form of Dotarem was explored with, the so far optimal sample preparation, a SiNP sample containing 30 mM TEMPO. However, there did not appear to be any further improvements in the polarisation of the SiNPs (Figure 3.15). Whilst the optimal microwave frequency appeared to remain the same, lower signal intensities were recorded at each frequency during the microwave frequency sweep and at each time point during the recording of the build-up profile (Figure 3.15A and B). The extracted build-up amplitude appeared

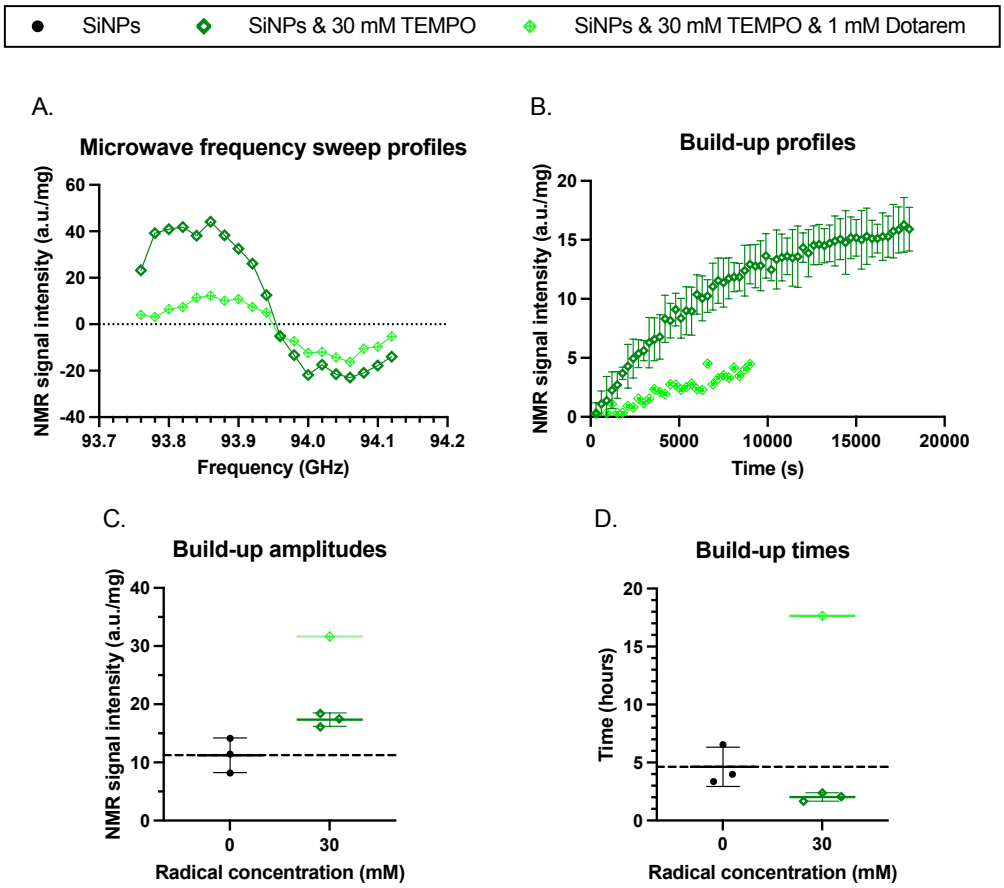

Figure 3.15: Gadolinium did not increase the efficiency of polarisation
The effect of adding gadolinium is summarised. Following the addition of 1 mM Dotarem to a silicon nanoparticle sample containing 30 mM TEMPO ($n = 1$), the optimal microwave frequency recorded during the A) microwave frequency sweep appeared to remain unchanged. However, lower signal intensities were recorded at each frequency of the sweep and at each time point of the B) build-up profile. The extrapolated C) build-up amplitude appeared to almost double upon the addition of gadolinium, yet the time to achieve such a signal intensity would appear to take approximately ten-fold longer. Bars display mean ± SD.

to almost double, yet the build-up time appeared to increase by approximately ten-fold (Figure 3.15 C and D).

3.4.2.4 Discussion

Among the few studies that have reported optimisation during this stage of the DNP workflow, the study conducted by Hu *et al.* — that took into account TEMPO concentration, SiNP size, and DNP duration — provided the inspiration behind the research conducted here. For the range of silicon particle sizes explored

(30 – 200 nm), they found the optimal concentration of TEMPO to be between 30 – 60 mM. For 30 nm particle samples specifically, the optimal TEMPO concentration was found to be 60 mM. At 60 mM, the build-up amplitude recorded from our SiNPs was significantly reduced compared to that recorded at 30 mM. Hence, the data presented here appeared to be more in agreement with the findings that Hu *et al.* reported for 70 nm particles. There are a couple of factors that could be behind this disparity. The first of which was the difference in core structures (polycrystalline vs. monocrystalline), however, the range of particle sizes comprising each sample is also likely to have played a part. The APS of the SiNPs used here was 30 – 50 nm, however, the commercial vendor describes the composition as approximately: 50% at 40 nm, 25% smaller than 40 nm, and 25% greater than 40 nm, with a small percentage of particles reaching 100 nm. A transmission electron microscopy (TEM) image of the 70 nm particles used by Hu *et al.* also showed a wide particle size distribution; the particles scaled between approximately 25 – 300 nm. These wide size distributions are encountered across the field and are a casualty of the current synthesis methods. The use of post synthesis methods, such as centrifugal filtration, is required to narrow these distributions, however, there is currently no gold standard approach. Ultimately, this data demonstrates the link between particle size and structure with SiNP polarisation efficiency, whilst also highlighting the "Goldilocks" effect of defect/radical concentrations within SiNP DNP samples.

Differences in the signal enhancements recorded from samples containing different exogenous radicals at the same concentration can likely be attributed to differences in the local environment that the free electron located on each radical molecule experiences. Firstly, the apparent magnetic field experienced by the free electron would affect its Larmor frequency and the difference between the nuclear and electron Larmor frequencies are known to play a role in the polarisation transfer mechanism(s) that take place during DNP. Hence, the polarisation transfer mechanism(s) could be different for these samples as a direct result of the exogenous radical structure. In addition to the structural environment of the free radical, the sizes of these molecules and the location of the free radical within them may

also affect their proximity to the nuclear spins at the SiNP surface and thus, the efficiency of direct polarisation transfer.

It must also be noted that, in addition to influencing the optimal microwave frequency, the choice of radical species would also have an effect on the optimal microwave power. The optimal power would depend on the dominant polarisation transfer mechanism and the T_{1e}. Investigating the microwave power for each sample in addition to the microwave frequency would add another dimension of complexity to the experimental design; recording this for each radical type (including those explored in the other subsections here) at each concentration was not feasible due to the limited availability of the equipment.

To investigate whether the differences in SiNP polarisation was due to the general structure used to categorise radical species or whether the differences were due to the structure of each specific radical, a pilot study was conducted using structurally analogous radicals. The data appeared to be in good agreement; the build-up amplitude appeared to increase with the addition of the Nitroxide radicals at 30 mM and the build-up time appeared to shorten with the addition of Trityl radicals at 15 mM. Hence, the general morphologies of these PAs appeared to have an effect which might be related to the number of radicals getting within a close enough distance to enable direct polarisation transfer to the ^{29}Si nuclei present at, or close to, the SiNP surface.

In an attempt to achieve greater signal enhancements from samples containing 30 mM TEMPO, an exploratory study into the addition of gadolinium was conducted, however, no improvement was observed. A potential reason for this might be that the concentration was too high and the presence of the unpaired electrons increased the rate of relaxation. The monitoring of ^{29}Si NMR intensity decay, the testing a range of gadolinium concentrations, and the recording of repeats may further elucidate this finding. Further to this, the benefit of gadolinium might be radical specific and hence, greater signal enhancements may have been generated from samples that contained a different radical. For example, Dotarem

has previously been found to significantly improve the signal enhancements from samples containing OX063 but not from samples containing AH111501[54].

Overall, these findings indicate that the addition of a Nitroxide radical, with careful consideration of its concentration, could give rise to an improvement in the DNP efficiency of SiNPs. However, it became apparent that the additional benefit provided by the presence of Nitroxide radicals within the SiNP DNP samples was insufficient for *in vivo* application and that greater signal enhancements would be needed.

3.4.3 Hyperpolarisation via irradiation generated radicals

3.4.3.1 Introduction

Whilst the addition of exogenous radicals is a well characterised technique in the field, their presence post-DNP is undesirable due to their potential toxicity *in vivo* and their relaxation effects which shorten polarisation lifetimes. In Section 3.4.1 it was shown, albeit with lower signal enhancements, that $30-50\,\text{nm}$ SiNPs could polarise via the naturally occurring endogenous defects at the Si:SiO_2 interface. Thus, it was hypothesised that if such defects were distributed throughout the SiNP structure, the DNP build-up time could be reduced.

Whilst the Si:SiO_2 interface has been extensively studied, the exact structure of the interface is still not fully known[55]. Three paramagnetic centers have been identified in Si:SiO_2 structures, namely; P_a, P_b, and P_c. These defects have been studied using EPR, however, their characterisation is still being debated and defined through the use of complementary techniques. P_b is the most studied defect and is characterised as a trivalent silicon atom with a dangling bond (Si[3]). This defect is: present at the Si:SiO_2 interface of silicon nanoparticles, observable at room temperature, and amphoteric. Out of the different charged states ($Si[3]^+$, $Si[3]^0$, and $Si[3]^-$), only $Si[3]^0$ is paramagnetic and hence observable in EPR spectra. The presence of the P_a and P_c defects is dependent upon the temperatures and pressures the material is exposed to (e.g. during synthesis or post-synthesis methods) and are not as well characterised as the P_b defect[56]. It is thought that

the P_a defect is due to the presence of a trapped electron and the P_c defect is due to a trapped vacancy or the presence of a foreign paramagnetic atom[57]. To generate and study these defects, various types of irradiation have been applied to silicon-based materials for decades. Hence, as an alternative method to the addition of exogenous radicals, the use of irradiation to generate these defects throughout the SiNP structure is explored in this section.

The use of irradiation-induced radicals as an alternative to exogenous radicals during DNP is not a new concept. In addition to electron and gamma irradiation[58, 59], alternative methods for radical generation have included: ultraviolet irradiation[60, 61] and electric discharge[62]. However, to our knowledge, none of these techniques have been applied to SiNPs. Out of the variety of techniques, electron irradiation was the most attractive starting point due to the ability of electrons to displace host atoms without creating impurities. This displacement of the lattice atoms in silicon materials means that the primary defects[3] produced upon irradiation damage are vacancies and interstitials[64]. These defects are formed in pairs (known as Frenkel pairs) and the differences between them is summarised in Figure 3.16. A vacancy defect is where an atom is missing from its typical position in the lattice site whereas an interstitial defect is where an atom occupies an interatomic space at odds with the regular pattern of the lattice.

These defects can then recombine if the temperature of the material is increased or they can diffuse through the lattice and become trapped by other impurities or defects[64]. With the use of cryogenic temperatures for DNP, it was hypothesised that electron irradiation-induced defects in SiNPs could be used as endogenous radicals for the polarisation of SiNPs.

[3]A complete overview of the defects present in silicon is beyond the scope of this work and as Newman states: "such a 'book' would now have to consist of several large volumes because of the amount of material to be covered"[63]. Such defects include, but are not limited to: isolated impurity atoms; isolated lattice defects (vacancies or interstitials); aggregates of two or more impurity atoms; and aggregates of two or more intrinsic defects (e.g. divacancies). It is important to note that these defects can co-exist i.e. they are by no means independent.

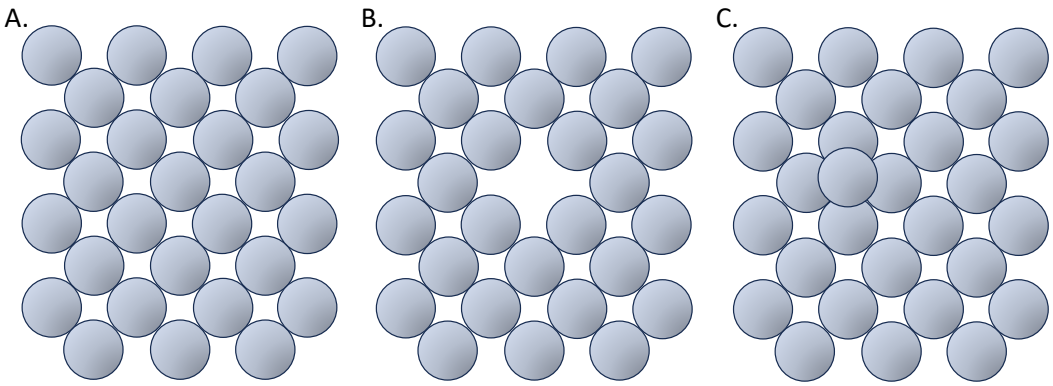

Figure 3.16: Vacancies and interstitials
Diagrams showing the primary defects that occur following irradiation damage in silicon materials. The regular pattern of the lattice and idealised structure is shown in A). A vacancy defect B) is where an atom is missing from where it would typical be present in the lattice site whereas an interstitial defect C) is where an atom occupies interatomic space outwith the regular pattern of the lattice.

3.4.3.2 Methods

An ultra-high dose rate 6 MeV linear particle accelerator (LinAc) was used with the aim of creating radical damage within the bulk of the SiNPs[4].A sample holder compatible with the existing LinAc set-up was designed in parts using CAD software (SOLIDWORKS; *https://www.solidworks.com/*) and these designs were given to the University of Oxford Physics Department's Research Workshop for manufacture. Dry SiNPs were placed in one side of the sample holder and dry alanine powder was placed in the other side to act as a dosimeter. The volume of each sample space was ∼3.8 cm^3 which enabled ∼300 mg of SiNP to be irradiated at once. The sample holder was flipped 180° halfway through each irradiation in an attempt to make the irradiation exposure more homogeneous throughout the entire volume of the samples. Both SiNP and alanine samples were irradiated between 10 – 100 kGy every 10 kGy.

A slider (BSR2080SL, IKO Nippon Thompson) was also incorporated into the design to facilitate reproducible positioning within the electron beam (e-beam).

The irradiated samples were studied by DNP, EPR, and X-ray diffraction (XRD):

[4]The LinAc was operated by Professor Kristoffer Petersson and Dr Iain Tullis.

- For DNP, 130 μl of a 1:1 DMSO and D_2O mixture was pipetted onto 37 mg of irradiated SiNPs in an eppendorf. Each sample was vortexed and sonicated until forming a liquid that could be pipetted into a sample cup. The sample cup was then inserted into the polariser where microwave frequency sweeps, build-up profiles, and decay profiles were recorded. The signal readout sequences optimised in Section 3.3.3 were used to record these. From the fits of the build-up and decay profiles, the build-up amplitudes, build-up times, and decay time constants were extracted. The detailed ^{29}Si DNP protocol can be found in Section 2.2.

- EPR was conducted using an X-band continuous wave spectrometer at room temperature. Dry irradiated SiNPs were loaded into EPR tubes and the mass of each sample was noted. EPR spectra were recorded for each sample and integrated using an in-house MATLAB script to find the corresponding spin counts. These spin counts were corrected for the mass of each sample. The full EPR protocol and data analysis is detailed in Section 2.4.

- For XRD, the samples comprised loose powder – either used as received (non-irradiated) or irradiated at 100 kGy – that was compacted into a round sample holder which was placed at the centre of the diffractometer (see inset of Figure 3.17).

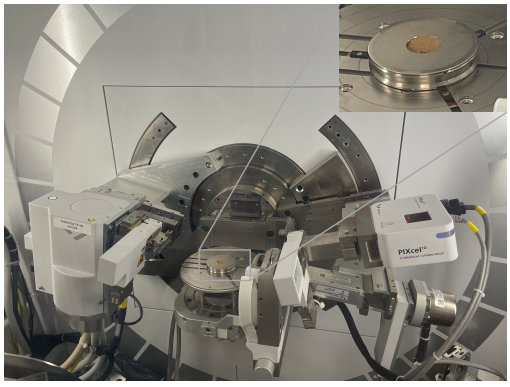

Figure 3.17: X-ray diffraction diffractometer
Photograph of X-ray diffraction spectrometer with inset showing a magnified view of the sample holder containing loose SiNPs.

The effect of sample density on how the dose was absorbed by the samples was also explored. For this, the irradiation set up was replicated using a Geant4-based Architecture for Medicine-Oriented Simulation (GAMOS)[5]. SiNP samples with densities of 0.05 g/cm^3, 0.5 g/cm^3, and 5 g/cm^3 under irradiation of a 100 kGy dose electron beam were simulated using a Monte Carlo simulation framework which included details of the known physical interactions between an e-beam and different matter and the imported CAD geometry of the sample holder. Following the simulation, a pellet maker was designed and constructed. The pellet maker was used in conjunction with a three tonne manual hydraulic press. SiNPs that had been made into pellets were gently crumbled back into loose powder following irradiation. As done for the loose powder samples, the powder originating from irradiated pellets was studied by EPR and XRD.

3.4.3.3 Results

A sample holder for the irradiation of the SiNPs was designed to be compatible with the existing LinAc set up. CAD software generated designs for the sample holder are shown in Figure 3.18. When assembled and tested with the existing set up, a linear slide and stoppers were incorporated into the design to ensure precise and reproducible positioning within the electron beam (Figure 3.19).

The polarisation constants extracted from the build-up and decay profiles of the irradiated SiNP samples are summarised in Figure 3.20. There appeared to be a reduction in the build-up amplitudes, a reduction in the build-up times, and an increase in the decay times compared to non-irradiated SiNP samples. A significant reduction in the build-up amplitude was found at 50 kGy.

X-ray diffraction (XRD) spectra appeared to show no significant change to the structural composition of the SiNPs upon irradiation (Figure 3.21). SiNPs irradiated at 100 kGy appeared to show similar amorphosity as shown by the presence of the amorphous hump. Similar proportions of crystallinity were also observed in background subtracted XRD spectra compared to non-irradiated SiNPs.

[5]Associate Professor Jack Miller ran Geant4 on a supercomputer.

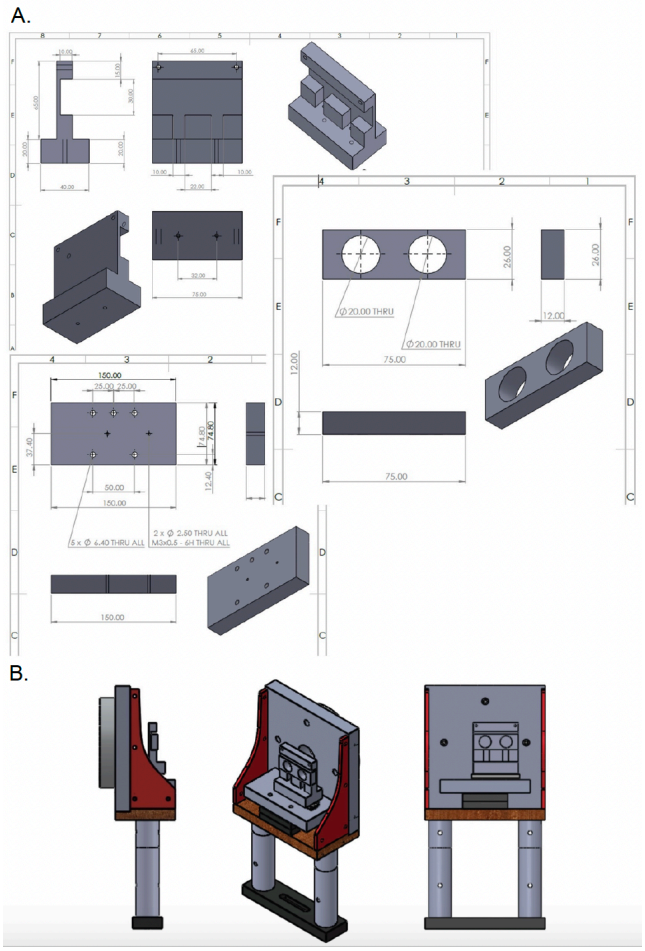

Figure 3.18: Design of sample holder compatible with existing set-up
A) CAD software designs of individual parts for assembly. B) CAD software designs for a sample holder compatible with the existing LinAc set up.

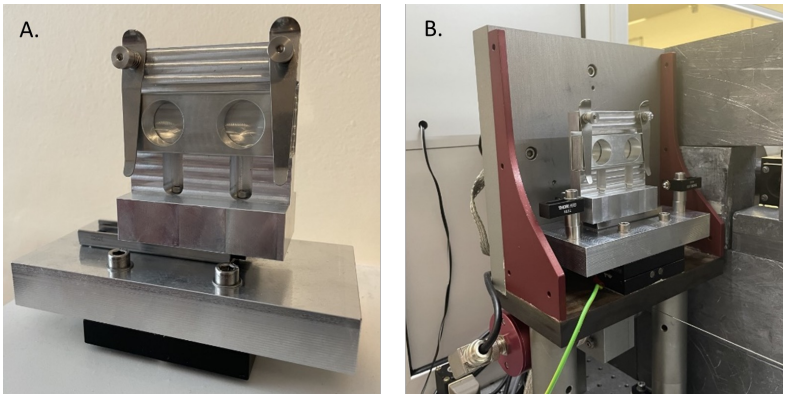

Figure 3.19: LinAc sample holder
A) The assembled sample holder based off CAD software designs is shown. B) Additions to the final design included: a stainless steel linear slide (commercially sourced) and stoppers for the reproducible positioning of samples within the LinAc beam.

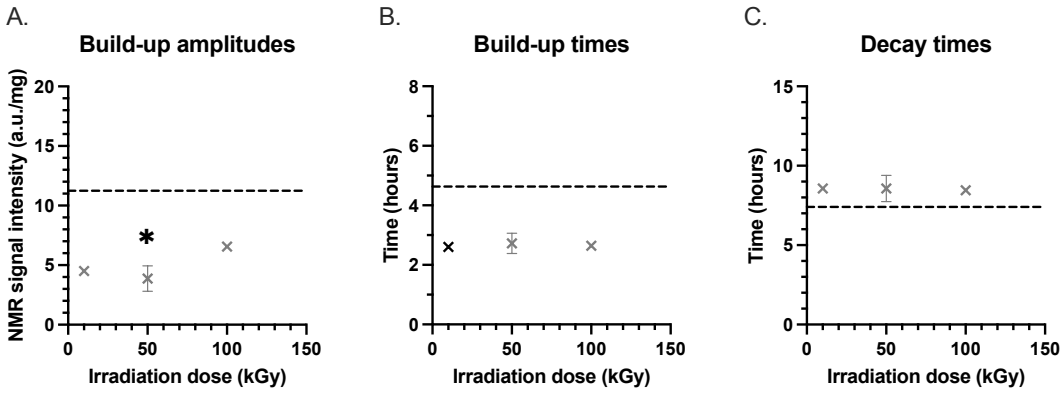

Figure 3.20: Irradiation hindered silicon nanoparticle polarisation
The polarisation constants extracted from samples irradiated with 6 MeV electrons at different irradiation doses are summarised as dot plots. There appeared to be a reduction in A) the build-up amplitudes, a reduction in B) the build-up times, and an increase in C) the decay times compared to non-irradiated silicon nanoparticle samples. The mean polarisation constant for non-irradiated SiNP samples is indicated by the dotted line. For 10 kGy and 100 kGy samples $n = 1$ and for 50 kGy samples $n = 3$. The bar displays mean ± SD. Significance was calculated using an unequal variance t-test. Significance is shown as * when $p \leq 0.05$.

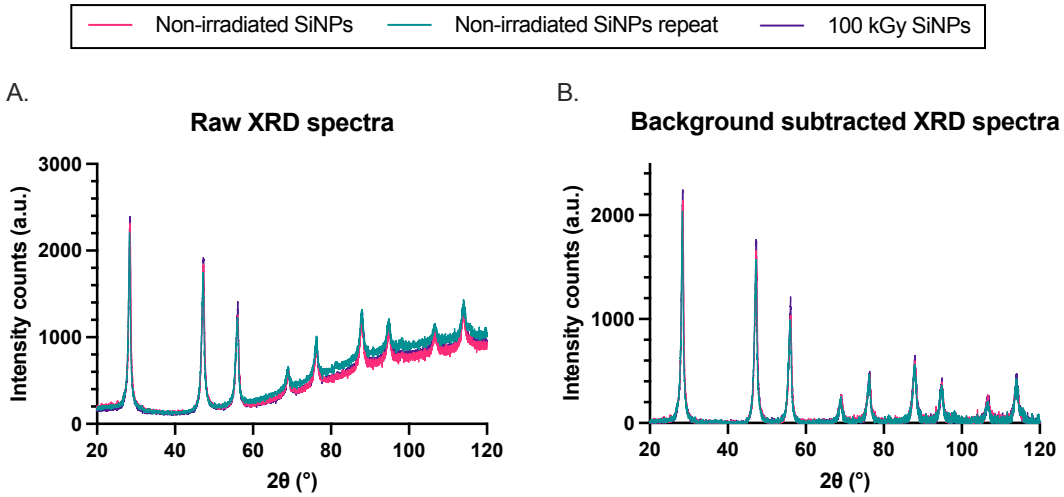

Figure 3.21: Irradiation had little-to-no effect on particle structure
X-ray diffraction spectra exploring the effect of irradiation on the structure of silicon nanoparticle samples are shown. Silicon nanoparticles irradiated at 100 kGy ($n = 1$) appeared to show similar amorphosity as shown by the amorphous hump in the A) raw X-ray diffraction spectra. Similar proportions of crystallinity were also observed as shown by the peak heights in the B) background subtracted X-ray diffraction spectra compared to silicon nanoparticles that had not been irradiated ($n = 2$). These data would suggest irradiation has little-to-no effect on the structure of silicon nanoparticles.

To elucidate these findings, a GAMOS simulation was conducted from which an increase in the number particle interactions was found upon increased SiNP sample density (Figure 3.22). Hence, a pellet maker was designed and constructed. Comprising of four pieces (Figure 3.23A) the pellet maker was used in conjunction with a manual three tonne hydraulic press (Figure 3.23B). Pellets were successfully made and remained intact whilst being transported. An example pellet and its placement within the LinAc sample holder is shown in Figure 3.23.

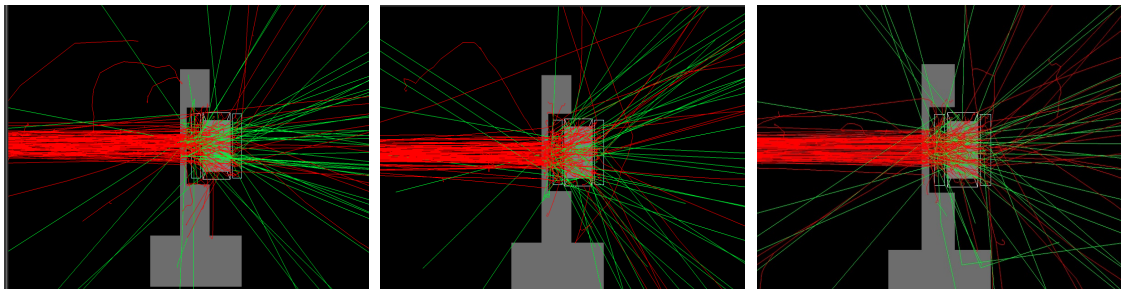

Figure 3.22: More particle interactions predicted with greater sample density The irradiation set up was replicated in a GAMOS simulation. The outputs of the simulation showed a greater number of particle interaction events upon increasing the density of the SiNP samples under irradiation of a 100 kGy dose electron beam. From left to right, the sample density was: 0.05 g/cm^3, 0.5 g/cm^3, and 5 g/cm^3.

Upon increasing the density of the SiNP sample being loaded into the LinAc sample holder, lower spin counts appeared to be recorded during EPR (Figure 3.24), however, no significant differences were found following a paired t-test (p=0.09). Pellet making also appeared to increase the crystallinity of SiNP samples (Figure 3.25); no amorphous hump was detected from SiNP powder that had been made into a pellet.

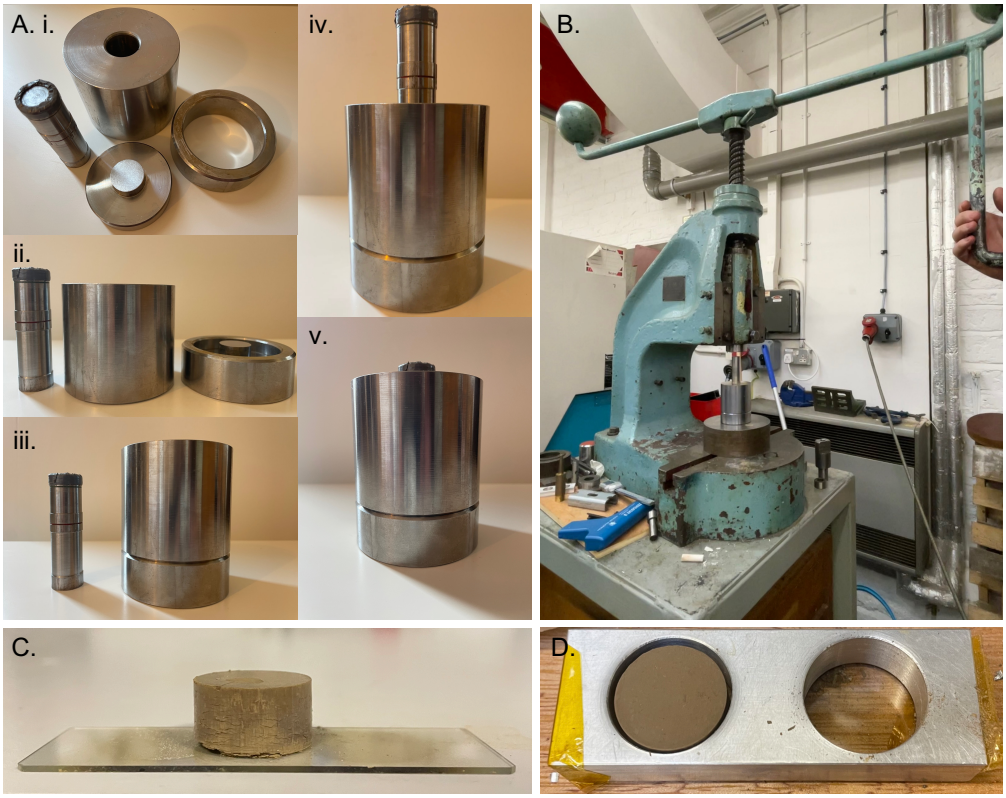

Figure 3.23: Pellet maker
The stages of assembly for the pellet maker are shown in A). The pellet maker was used in conjunction with a manual three tonne hydraulic press B). An example pellet is shown in C) and in D) the pellet is in the sample holder for the LinAc.

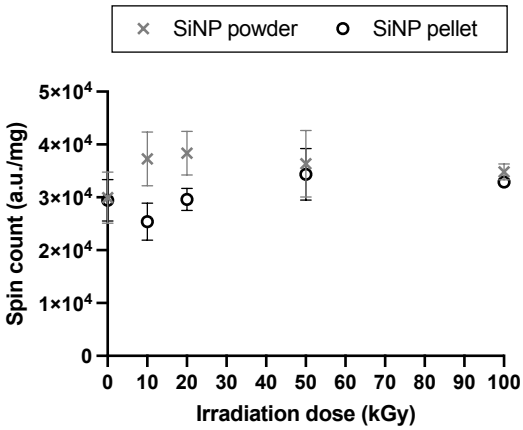

Figure 3.24: Increased sample density lowered the spin count
The EPR spin counts recorded from silicon nanoparticle samples following 6 MeV electron irradiation at different irradiation doses and at two different densities are summarised. Irradiated samples comprising silicon nanoparticle powder that had been compressed into pellets ($n = 3$) appeared to have lower spin counts than samples that comprised loose powder ($n = 3$). Bars display mean ± SD.

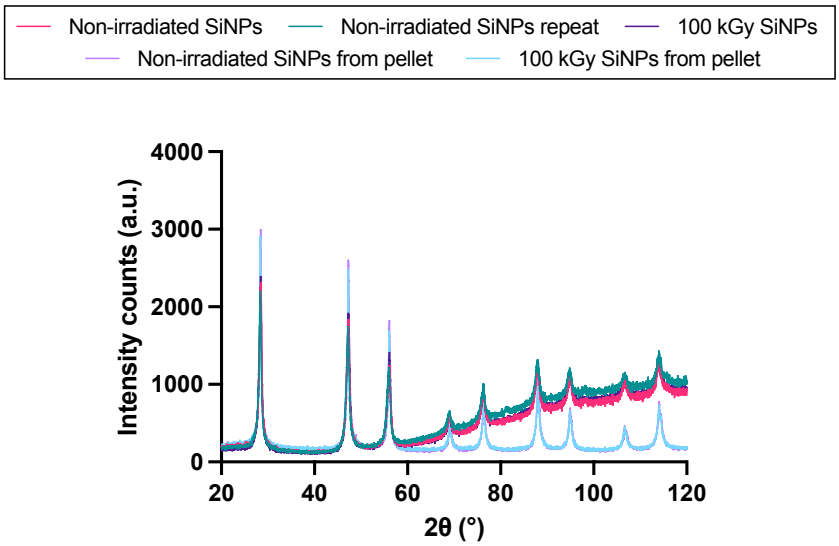

Figure 3.25: Pellet making increased the crystallinity of silicon nanoparticles Raw X-ray diffraction spectra exploring the effect of increased sample density for the irradiation of silicon nanoparticles are shown. Spectra recorded from silicon nanoparticles originating from samples that had been compressed into a pellet appeared to show no amorphous hump. There also appeared to be little-to-no difference between the spectra recorded from powder derived from pellets before ($n = 1$) and after irradiation ($n = 1$). These data appeared to show an increase in crystallinity due to sample compression into pellets prior to irradiation.

3.4.3.4 Discussion

There appeared to be a trend of lower signal enhancements following the DNP of samples that contained irradiated SiNPs compared to those that contained non-irradiated SiNPs. Repeats were recorded with one of the irradiated powders (50 kGy) and a significant reduction in the build-up amplitude was found. No repeats were conducted using 10 kGy and 100 kGy as it was thought that there was sufficient evidence to suggest that irradiation did not lead to improvements in signal enhancement.

The importance of electron concentration in the polarisation of SiNPs had already been established through the experiments conducted with exogenous radicals (Section 3.4.2) and hence, a potential reason for this finding was that the concentration of defects generated throughout the SiNPs may have been too low or too high. For example, in work that focused on endogenous radical concentrations, Kwiakowski *et al.* recorded lower polarisation enhancements from SiNPs with high surface defect concentrations[42]. There were, however, no significant differences between the spin counts recorded from the non-irradiated samples and irradiated samples which suggested that defects had not been generated and distributed throughout the SiNP structure as had been expected.

Two other potential reasons for low signal enhancements were: loss of the SiO_2 surface leading to the disruption of the Si:SiO_2 interface upon irradiation and/or instability of the generated defects. The former has been observed in other studies where high energy electron irradiation on Si:SiO_2 structures[65] was investigated but appears to have been ruled out as the main mechanism taking place here due to the acquisition of XRD spectra. No significant differences between XRD patterns recorded from non-irradiated and irradiated samples were found. Indeed, the greatest difference appears to have been recorded between the non-irradiated sample and a repeat. The presence of the amorphous hump in spectra originating from both non-irradiated and irradiated powder would suggest that irradiation did not lead to significant structural changes to the SiO_2 surface and that the interface remained intact. The positions of the peaks were found to be the same among

all spectra. Small variations in the heights of the peaks were recorded which could be due to the large variability in particle sizes contained within samples. The diameter of the crystalline core increases with increasing particle size and thus, larger particles would have had greater contributions to the XRD signal. Additionally, the mass of each XRD sample was not recorded but is likely to have been a factor. In terms of the latter potential reason, defects were perhaps generated but had short lifetimes due to the temperature the SiNP samples reached during irradiation and their storage at room temperature. The stability of vacancy-defect pairs in silicon materials as a function of temperature has previously been summarised and it has been shown that the temperature at which they become mobile depends on the defect and charge[64]. In general, single vacancies become mobile at temperatures below 273 K whereas other defects, such as the divacancy, are stable at room temperature and beyond[66, 67]. The temperatures to which the SiNP samples reached during irradiation with the LinAC were unknown but would have increased with increasing irradiation dose. To reduce sample heating during irradiation, either the irradiations could have taken place over longer time frames or, a cold finger could have been incorporated into the LinAc sample holder design. With this addition to the set up, if defects (of whichever form) had been generated, they could potentially have been preserved.

Currently, the only approach known to generate isolated vacancies and interstitials is irradiation with an electron beam at $1-3$ MeV conducted at cryogenic temperatures[64]. An alternative and hypothetical approach could be irradiating the SiNPs through the use of cryogenic TEM. If the energy of the incident electron beam is greater than the energy required for displacement, interstitial defects can form. For example, if during TEM the accelerating voltage of the electron beam is around 200 kV, structural damage in crystalline silicon has been observed[68]. TEM can be conducted with a wide range of beam energies and hence, if carried out at cryogenic temperatures, any resulting defects could potentially be preserved. SiNP samples could subsequently be stored in liquid helium prior to their use in DNP. One of the limitations to this hypothetical approach, however, could be

low sample throughput. This approach was not tested due to restrictions on the sample types allowed for the required microscope.

Lastly, the hypothesis that greater sample density would lead to an increase in the number of collisions between incoming electrons and the SiNPs was backed up by simulation. However, no increase in the EPR spin count was recorded, instead, there appeared to be a trend for reduced spin count at each irradiation dose. The difference in the XRD spectra between pellet and powder samples is perhaps due to the process of the pellet making as opposed to irradiation. No amorphous hump was observed from the powder originating from the non-irradiated pellet nor from the 100 kGy irradiated pellet. This could potentially have arisen as a result of disruption to the Si:SiO_2 interface which could be confirmed through the use of scanning transmission electron microscopy, for example[69]. It was not feasible, however, to acquire such data. Due to the known importance of the Si:SiO_2 interface in the polarisation of SiNPs, no DNP data was acquired from the pellet samples.

3.5 Beyond the polariser: using ^{29}Si polarisation

3.5.0.1 Background

Following on from the optimisation work conducted in Sections 3.3.3 and 3.4.2, the ability of the samples to retain polarisation following their removal from the polariser was explored. Just as the laboratory required a new set up for the assessment of ^{29}Si DNP, a new set up and protocol had to be developed for assessing the polarisation of the SiNPs at room temperature in the laboratory MR scanner. Following this, a proof of concept study was conducted.

3.5.0.2 Introduction

In order to observe the hyperpolarised signal in the MR scanner, a ^{29}Si/^{1}H volume coil would be used which first needed to be calibrated. The calibration involved establishing the relationship between the PW and FA, before subsequently mapping the B_1 field.

Inhomogeneities in the B_1 field strength affect the FA experienced by nuclear spins and ultimately makes quantitative comparisons of signals obtained from different voxels in NMR spectroscopy difficult. A map showing the spatial distribution of the B_1 field strength across the volume of a coil enables the signal intensity to be corrected for and made uniform across images. One method for B_1 field mapping is the Double Angle (DA) method which requires a minimum of two images[70].

To investigate the polarisation of the SiNP samples at room temperature a proof of concept study in which all previous optimisations were put into practice was conducted.

The liquid state polarisation is typically calculated by comparing the SNRs of the hyperpolarised and the thermal signals. Among the few studies that investigate hyperpolarised SiNP DNP samples at room temperature, no measurements of the liquid state polarisation have been reported and studies typically only report the liquid state T_1. Previous polarisation levels have been reported in the solid state. For example, Kwiatkowski *et al.* reported a polarisation of 12.6% by comparing

the solid state hyperpolarised signal to a thermal spectrum acquired from a liquid state sample comprising 99% ^{29}Si labelled silicon. Also in the solid state, Shimon *et al.* took an alternative approach — albeit during a study involving SiMPs — where they defined the signal enhancement as comparing the integrated intensity of signals with and without microwave irradiation[71].

Due to the long T_1 of SiNP samples at room temperature, the best approach for acquiring their thermal spectrum would be to average together spectra that had been acquired under Ernst angle conditions:

$$\theta_E = \arccos\left(e^{-\frac{\mathrm{TR}}{T_1}}\right) \tag{3.8}$$

The Ernst angle (θ_E) is the optimal flip angle to maximise non-hyperpolarised signal in the least amount of time when acquiring many averages. The Ernst angle relies on the TR (which can be chosen) and the inherent T_1 of the sample. The other option for acquiring thermal spectra would be to average signals each of which would be acquired with a time resolution equating to 3-5 times the T_1. For example, if the T_1 of a SiNP sample were 20 minutes, signals would be acquired every 1-1.5 hours. Hence, by making use of the Ernst angle method a greater number of spectra can be acquired in a shorter time, ultimately reducing the time required to acquire a thermal spectrum.

3.5.0.3 Methods

For the calibration of the ^{29}Si/^{1}H volume coil (RAPID Biomedical, Rimpar), a 2 ml eppendorf of Tetramethylsilane (TMS) was placed at the centre of the coil which itself was placed inside a 7 T horizontal-bore preclinical scanner.

The T_1 of the TMS phantom was found using an inversion recovery (IR) sequence and by fitting the data to Equation 3.9:

$$M_z(\mathrm{TI}) = A\left(1 - 2e^{\frac{-\mathrm{TI}}{T_1}} + e^{\frac{-\mathrm{TR}}{T_1}}\right) \tag{3.9}$$

where M_z(TI) is the longitudinal magnetisation prior to the acquisition, A is a constant, TI is the inversion time (i.e. the time between applying the 180° pulse

and acquiring the signal), T_1 is the liquid state nuclear T_1 relaxation time of the sample, and TR is the repetition time. Six TIs were used, the durations of which doubled between each measurement (1.83 s, 3.66 s, 7.32 s, 14.64 s, 29.28 s, and 58.56 s), and a TR of one minute.

For the power calibration, pulses with increasing PW were applied using a TR of 44 s and four averages at 55 dB. The data were fitted using Equation 2.3 from which the FA calibration factor was extracted.

The B_1 of the $^{29}Si/^{1}H$ volume coil was then mapped using the DA method. This required the magnitude data from two images, one acquired at FA α and the other at 2α (Equations 3.10 and 3.11):

$$M_1 = M_0 \sin(\alpha) \tag{3.10}$$

$$M_2 = M_0 \sin(2\alpha) \tag{3.11}$$

where M_0 is the magnitude of the magnetisation at thermal equilibrium. The ratio of the two magnitudes was found (Equation 3.12) and thus, the magnetic field strength calculated for each pixel (Equation 3.13).

$$r = \frac{M_1}{M_2} = \frac{1}{2\cos(\alpha)} \tag{3.12}$$

$$B_1 = \frac{r}{\gamma \times 10^4} \tag{3.13}$$

Images were recorded using FAs of 30°, 60°, 90°, 120°, and 180° for a Gradient Echo Multi Slice (GEMS) sequence and the data was processed using an in-house MATLAB script (ver. R2018a). The five images were summed and used to generated a mask for the map. The ratio of the signal intensity from the images generated with 30° and 60° FAs were used to find the B_1.

For DNP, a SiNP sample with 30 mM TEMPO was prepared as described previously. The sample was inserted into the polariser and a build-up monitored. After five hours, the microwave source was switched off and a "dry" dissolution conducted. A "dry" dissolution consisted of the removal of the sample cup from

the polariser and its placement into a 3D printed sample holder which was slotted into the ^{29}Si/^{1}H volume coil[6]. The volume coil was then inserted into the bore of a 7 T Varian/Agilent preclinical MR scanner.



Figure 3.26: "Dry" dissolution set up
Photos showing the "dry" dissolution set up. The set up consisted of the placement of the sample cup into a 3D printed sample holder which kept the sample upright within the volume coil. The ^{29}Si/^{1}H volume coil was then inserted into the bore of a 7 T Varian/Agilent preclinical MR scanner.

The decay of polarisation was monitored by applying RF pulses corresponding to a FA of approximately 10° every 30 seconds for one hour. The data was fitted to extract the liquid state T_1 of the sample using equations (2.4), (2.5), and (2.6).

Based on the liquid state T_1 measurement, a thermal scan was conducted using 50,000 averages, a TR of 1 s, and the Ernst angle. Two further one hour thermal scans were acquired at a narrower spectral width using 3600 averages, a TR of 1 s, and the Ernst angle. One of these was acquired with the sample and the other with the sample removed.

3.5.0.4 Results

The ^{29}Si/^{1}H volume coil calibration data is shown in Figure 3.27. The T_1 extracted from the IR sequence was 20.8 s. The FA calibration factor extracted from the power calibration curve was 1.39 °/μs and was used to determine the PWs for subsequent scans including the B_1 field map.

[6]The 3D printing of the sample holder was conducted by Dr. Aaron Axford (Tyler group)

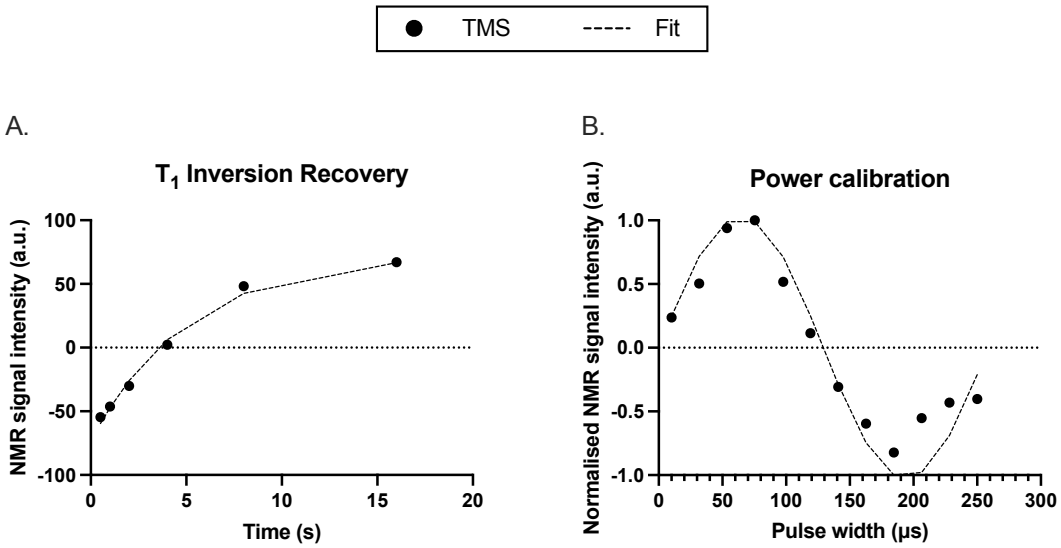

Figure 3.27: Calibration of the ^{29}Si/^{1}H volume coil
The flip angle calibration factor was extracted from the fit of the curve and was found to be 1.39 °/μs. This calibration determined the pulse widths used in subsequent scans.

The B_1 field map of the ^{29}Si/^{1}H volume coil is shown in Figure 3.28. The inset scale shows the ratio of the signal between the images acquired with the 30° and 60° FAs.

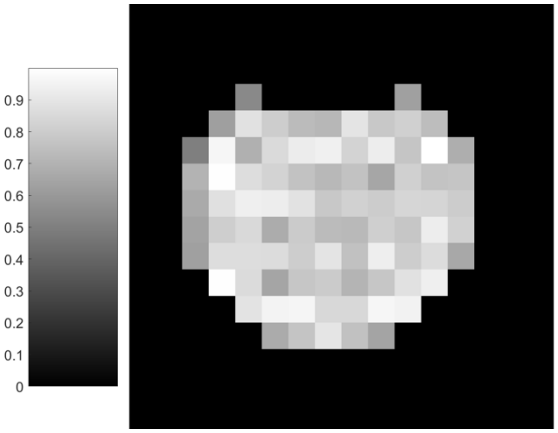

Figure 3.28: B_1 map of the ^{29}Si volume coil
The B_1 field map of the ^{29}Si/^{1}H volume coil was recorded using the Double Angle Method on a 1.5 ml Eppendorf filled with Tetramethylsilane. The inset scale shows the ratio of the signal acquired between the 30° and 60° FAs.

The data from a proof-of-principle "dry" dissolution is shown in Figure 3.29. First, the build-up profile was acquired which showed an increase in ^{29}Si NMR signal intensity over time (Figure 3.29A). The decay of polarisation at room tem-

perature was subsequently monitored using the MR scanner and the ^{29}Si NMR signal intensity was found to decrease over time (Figure 3.29B). The extracted liquid state T_1 from this data was 32.5 minutes. Thermal spectra were acquired and there appeared to be little-to-no difference in the spectra acquired with and without a sample present.

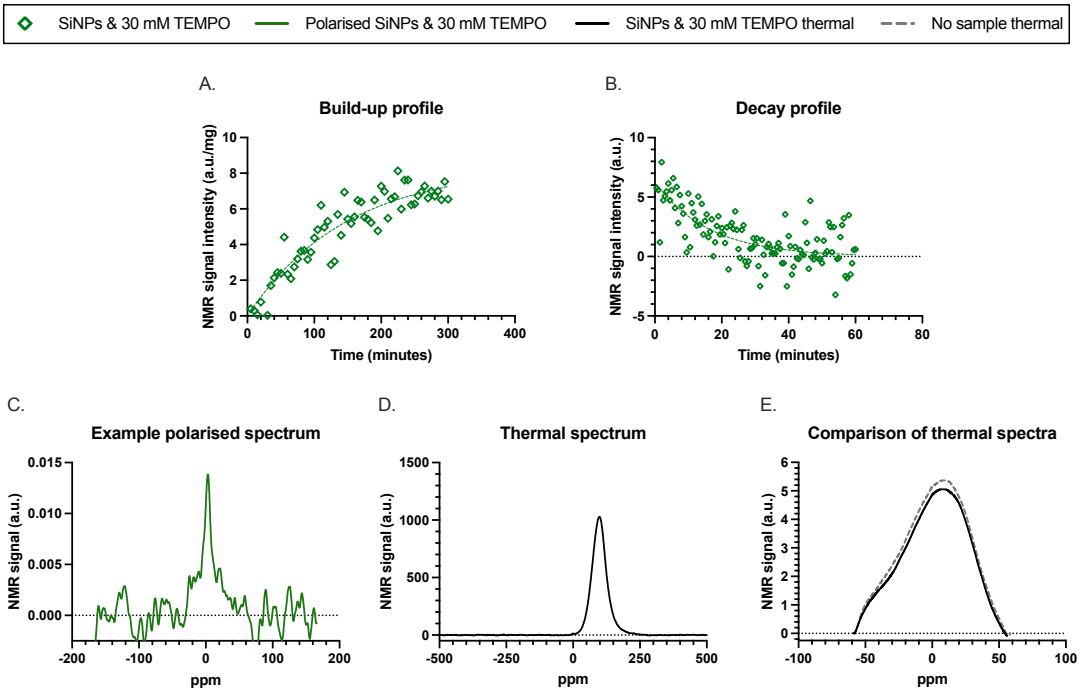

Figure 3.29: Liquid state polarisation
The data recorded from a proof of concept dry dissolution are summarised. A) The build-up profile shows an increase in ^{29}Si NMR signal over time. The sample cup was removed from the polariser and inserted into the centre of a volume coil which itself was inserted into the bore of a 7 T magnet. B) The decay of polarisation at room temperature was subsequently monitored. The extracted liquid state T_1 was 32.5 minutes. C) The first spectrum recorded from the polarised liquid state sample is shown as an example. D) Using the Ernst angle, a thermal spectrum was acquired but the polarisation level could not be determined due to E) signal from the fibreglass in the system obscuring any thermal signal originating from the SiNP sample.

3.5.0.5 Discussion

The optimisation work conducted throughout this chapter was brought together here in an attempt to measure the liquid state polarisation of a SiNP sample at room temperature.

First the volume coil was calibrated using a TMS phantom and the T_1 extracted from the IR sequence was used to inform the choice of TR for the power calibration. Typically, a TR of 3-5 times the T_1 should be used to ensure the magnetisation vector has fully relaxed between pulses. If the magnetisation has not fully relaxed between pulses, the power calibration curve can appeared skewed. Here, the TR used was only 2-3 times the T_1, however, the shape of the power calibration appeared to fit well to a sine curve and was not visibly skewed. Additionally, the 180° FA was reached which, as it is unaffected by the choice of TR, was used to check the value of the extracted FA calibration factor.

In determining the B_1 field map, the chosen FAs were 30° and 60° due to these lower FAs being less likely affected if the FA calibration had been affected by the choice of TR. The B_1 field appeared to be relatively homogeneous throughout the volume of the coil and for the purposes of this proof of concept study, it seemed reasonable that the SiNP sample cup be placed in the center of the coil and no corrections be applied to the subsequent data.

Following DNP, the "dry" dissolution approach was adopted due to the non-Newtonian nature of SiNP DNP samples and difficulties injecting such a fluid. It must be acknowledged that the sample was still partially frozen upon insertion into the bore of the scanner, however, having observed the defrosting of previous samples, it would have returned to the liquid state within a matter of minutes. Due to this time scale being short in comparison to the time spent monitoring the decay of polarisation, the term "liquid state" was still applied. Whilst the thermal spectra were acquired under Ernst angle conditions, the polarisation level could not be determined due to signal from the fibreglass in the system obscuring any thermal signal from the SiNPs. The polarisation level was not estimated using the alternative approaches reported in literature as there was no record of signal enhancements from the SiNP samples following five hours in the polariser with no microwave irradiation. Nevertheless, this proof of concept study showed detectable polarised signal from a SiNP sample following five hours of DNP. The optimisations adopted from the work conducted earlier in this chapter resulted in a three-fold

reduction in the time used for monitoring the polarisation build-up and a room temperature T_1 measurement that was in line with literature values (reported between five – ten minutes [45], approximately 20 minutes [47] and 42 minutes [29]).

3.6 Conclusion

For the clinical potential of SiNPs in hyperpolarised MRI to be realised, efforts must first focus on their preclinical development, where progress has been hindered partly due to the recording of low signal enhancements following long DNP build-up times. Furthermore, the optimisation of SiNP DNP should not simply include strategies to apply during DNP, but those that encompass the whole workflow. Here, the strategies that contributed to increasing the signal enhancement and reducing the time required for the d-DNP protocol were: the optimisation of the microwave power to maximise efficiency of the polarisation transfer mechanism and minimise sample heating effects; the development of a specific signal readout sequence for the microwave frequency sweep profile to ensure maximum SNR was achieved in the shortest available time; the addition of an exogenous chemical radical species; and the tuning of the radical concentration depending on the selected exogenous chemical radical species. Incorporating all of the optimisations, polarised signal from a SiNP sample containing 30 mM TEMPO was detected following a five hour build-up and the liquid state T_1 at room temperature was 32.5 minutes. The d-DNP protocol for SiNPs established here enables the full workflow to be completed within a single working day; something that is not feasible with current published guidelines. This increased throughput would ensure compatibility with polarisers that operate on a 12-hour duty cycle, for example, thereby increasing the accessibility of this sample type for future *in vivo* applications.

Aprender a dudar es aprender a pensar

To learn to doubt is to learn to think

— Octavio Paz

4

^{13}C - Hyperpolarised Alanine

Contents

4.1 Background 122
4.2 Chapter overview 124
4.3 Chapter aims 124
4.4 Generation of nonpersistent radicals for DNP 125
4.4.1 Irradiation-induced endogenous radicals 125
4.4.1.1 Introduction 125
4.4.1.2 Methods 127
4.4.1.3 Results 128
4.4.1.4 Discussion 130
4.4.2 Hyperpolarisation via endogenous radicals 132
4.4.2.1 Introduction 132
4.4.2.2 Methods 132
4.4.2.3 Results 133
4.4.2.4 Discussion 140
4.5 Microwave modulation during DNP 142
4.5.0.1 Introduction 142
4.5.0.2 Methods 142
4.5.0.3 Results 144
4.5.0.4 Discussion 154
4.6 *In vivo* study of metabolism 156
4.6.0.1 Introduction 156
4.6.0.2 Methods 156
4.6.0.3 Results 158
4.6.0.4 Discussion 165
4.7 Conclusion 167

4.1 Background

Since the development of d-DNP, its application has predominantly been in the production of hyperpolarised probes for studies of metabolism in *in vitro* and *in vivo* systems[53]. Hyperpolarised metabolic probes enable real time, non-invasive monitoring of metabolic pathways from which biomarkers for various pathologies can be detected. Such probes have primarily been based on metabolites labelled with ^{13}C[30]. Currently, the most widely used hyperpolarised metabolic probe is ^{13}C-pyruvate due to its position at a key intersection of metabolic pathways and its superior hyperpolarisation characteristics compared to other ^{13}C-labelled compounds. However, the suitability of ^{13}C-pyruvate for determining a metric commonly used for intracellular metabolism — the ^{13}C-lactate/^{13}C-pyruvate ratio — has been called into question. In 2011, upon switching the injectable substrate from ^{13}C-pyruvate to ^{13}C-alanine, Hu *et al.* recorded more than a ten-fold increase in the ^{13}C-lactate/^{13}C-pyruvate ratio[23]. The authors suggested this difference was due to the uptake of ^{13}C-pyruvate being limited by perfusion and its flux through monocarboxylate tranporters (MCTs) during the acquisition window. An incomplete uptake of ^{13}C-pyruvate would mean contributions from an extracellular ^{13}C-pyruvate pool in the measured ^{13}C-pyruvate signal. Furthermore, any extracellular ^{13}C-pyruvate present in plasma can be converted into ^{13}C-lactate by red blood cells that contain lactate dehydrogenase (LDH); leading to an "extracellular" ^{13}C-lactate pool[72]. Signals arising from intracellular and extracellular pools cannot be easily distinguished in hyperpolarised MR and hence the proposed use of ^{13}C-alanine for determining the ^{13}C-lactate/^{13}C-pyruvate ratio. For ^{13}C-alanine to be converted into ^{13}C-pyruvate, and subsequently ^{13}C-lactate, it must first be exposed to the intracellular enzyme alanine transaminase (ALT). Thus, the ^{13}C-pyruvate signal detected following the injection of ^{13}C-alanine would be intracellular in origin (Figure 4.1).

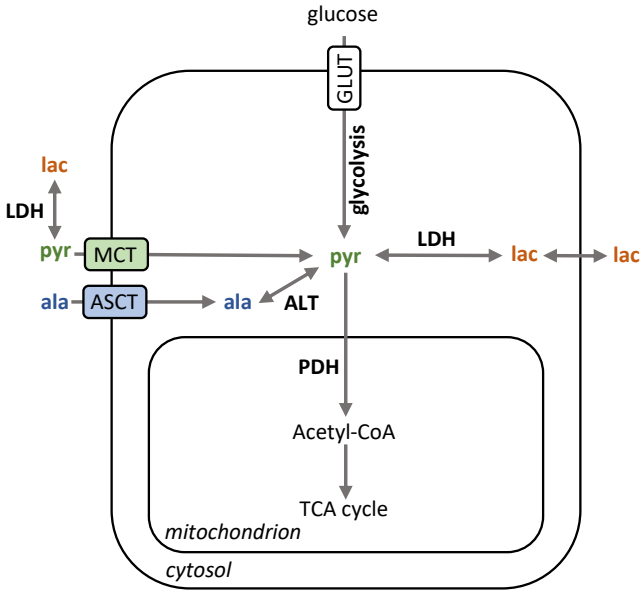

Figure 4.1: Alanine and pyruvate uptake
The uptake of ^{13}C-pyruvate is limited by perfusion and flux through monocarboxylate tranporters (MCTs). An incomplete uptake of ^{13}C-pyruvate would result in an extracellular ^{13}C-pyruvate pool that would contribute to ^{13}C-pyruvate signal. Signals arising from intracellular and extracellular pools cannot be easily distinguished in hyperpolarised MR and hence the posit of using ^{13}C-alanine as the injectable substrate for determining intracellular metrics that rely on pyruvate and lactate measurements.

For ^{13}C-alanine to be adopted as a HCA for routine clinical use, the signal enhancements and nuclear T_1 relaxation time must at least be comparable to those of hyperpolarised ^{13}C-pyruvate. Most metabolites have a very short T_1 (<60 s) due to their molecular structure. Non-protonated carbons retain signal for longer than protonated carbons yet, very few metabolites contain these types of functional groups[73]. The structures of non-enriched and ^{13}C-enriched alanine are shown in Figure 4.2.

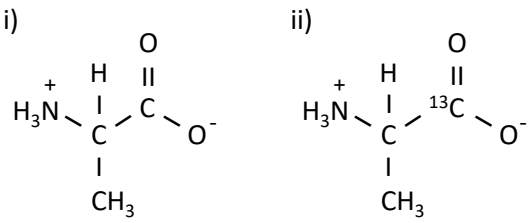

Figure 4.2: L-alanine molecular structure
Molecular structure of i) non-enriched L-alanine and ii) [1-^{13}C]L-alanine.

One strategy for lengthening the nuclear T_1 relaxation time is to remove the presence of exogenous radical species that have been added prior to d-DNP to act as polarisation centres as, following d-DNP, they also act as relaxation centres. Their removal is typically done during dissolution by filtration, however, this is only possible with certain radicals (e.g. AH111501) and not with others (e.g. OX063 Trityl). An emerging alternative is to generate nonpersistent free radicals in situ that recombine during the dissolution step of DNP. One such example is the ultraviolet irradiation of frozen pellet samples first conducted by Capozzi *et al.*[60]. The generation of radicals upon exposure to irradiation has been extensively studied in many different compounds using various sources, however, their application in DNP is relatively new.

4.2 Chapter overview

In Chapter 3, non-enriched (NE) L-alanine was used as a dosimeter to confirm that SiNP samples had been exposed to electron beam (e-beam) irradiation. This work is developed further in the present chapter by investigating the generation of radicals following the e-beam irradiation of [1-^{13}C]L-alanine and their characterisation to determine their suitability as a nonpersistent polarising agent for d-DNP.

4.3 Chapter aims

The following aims were addressed:

- Generate endogenous radicals in [1-^{13}C]L-alanine using e-beam irradiation
- Monitor and optimise DNP signal enhancement
- Conduct a proof of concept study to quantify intracellular pyruvate levels

4.4 Generation of nonpersistent radicals for DNP

4.4.1 Irradiation-induced endogenous radicals

4.4.1.1 Introduction

Alanine is one of the most abundant amino acids in the human body and is mostly known for its anaeplerotic role to prevent glycolytic decay[74]. The glucose-alanine or "Cahill" cycle involves the synthesis of alanine by the action of aminotransferase (ALT) within skeletal muscle cells in response to high glucose demands. Following its release into the blood stream its circulation culminates in its uptake in the liver where it is recycled as a precursor for glucose synthesis[75]. The interest in using [1-^{13}C]L-alanine as a hyperpolarised traceable compound of metabolism in health and disease arises from its spin exchange with pyruvate which is an intermediate for different metabolic pathways and the potential it offers for a more accurate measure of intracellular metabolism than that provided by current methods.

Alanine has often been reported in the literature alongside lactate as a metabolic product of a ^{13}C-labelled pyruvate substrate and as such, it has seldom been the main focus of metabolic studies conducted by d-DNP. Conversely, in the field of dosimetry, alanine has been extensively studied by EPR due to its use as a solid state dosimeter for monitoring high dose irradiations. Radiation effects on alanine were first reported in 1955 by Gordy *et al.* during a study into the EPR spectra of amino acids following their irradiation with X-rays and, in 1962, Bradshaw *et al.* demonstrated the first use of alanine as a dosimeter[76, 77]. As part of the 1983 "high-dose standardisation and intercomparison programme", the International Atomic Energy Agency (IAEA) approved the use of alanine as a reference dosimeter for measurements in the high dose regime (5 – 100 kGy)[78].

There are a number of factors that make alanine a gold standard dosimeter: the number of endogenous radicals generated is linearly proportional to the irradiation dose that alanine is exposed to; the aversion of the resulting radicals to recombine (unlike the ions generated in ionisation chambers); and its suitability for X-ray, gamma, neutron, and e-beam applications[79–81]. Additionally, the radicals

generated in alanine exhibit high stability compared to other dosimeters yet, the loss of radicals has been shown to occur following prolonged exposure to light and moisture[82]. The nonpersistent nature of these radicals in the presence of moisture could, however, be a desirable property in the setting of d-DNP. If irradiation generated radicals could be repurposed to hyperpolarise [1-^{13}C]L-alanine, there would be no need for filtering samples during dissolution. This method could also potentially lead to the extension of the nuclear T_1 relaxation time during sample transfer between the polariser and MR scanner and facilitate the generation of a radical concentration that was tuneable with irradiation dose whilst remaining independent of toxicity concerns. A further benefit would be the simultaneous sterilisation of samples which addresses an integral part of the preparation of d-DNP samples for clinical use. Indeed, e-beam irradiation can sterilise samples within seconds whereas the conventional method used for sterilisation (gamma irradiation) can require days[83].

Although the generation of radicals following the irradiation of alanine crystals has been studied for decades, the characterisation of these radicals has yet to be finalised. During early EPR studies only one radical species was thought to occur[84]. Named the "stable alanine radical" (SAR) its resonance is a result of the deamination of the protonated alanine anion (Figure 4.3i). In subsequent studies, evidence of two other radical species — R2 and R3 — was found. R2 was first characterised by Sagstuen *et al.* using a combination of continuous and pulsed EPR techniques and spectral simulations[85]. Its spectra is thought to arise following oxidation leading to the abstraction of the proton on the central carbon (Figure 4.3ii). Whilst also thought to be a product of oxidation, in contrast, R3 remains experimentally elusive and current evidence suggests it takes on multiple forms (Figure 4.3iii)[86].

Consequently, the EPR spectrum recorded from irradiated alanine is a combination of the different spectra that arise from each radical species. From spectral simulations, estimates for the relative occurrence of R1, R2, and R3 are approximately 0.55-0.60 : 0.30-0.35 : 0.05-0.10[84, 87].

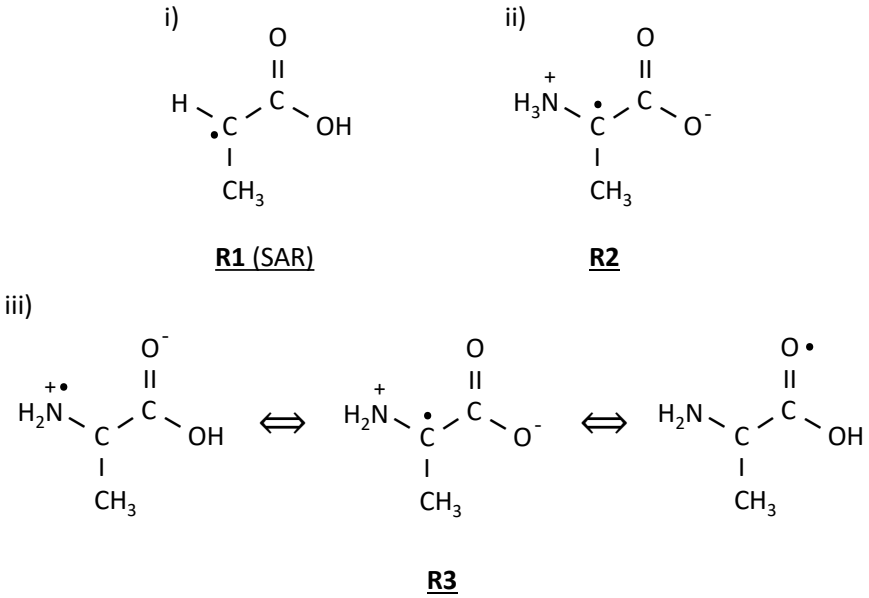

Figure 4.3: L-alanine irradiation-induced radical species
The different radical species formed following the irradiation of alanine. i) The stable alanine radical (SAR) or R1 whose EPR spectra arises as a result of the deamination of the protonated alanine anion. ii) R2 forms following the loss of a proton on the central carbon. iii) R3 is hypothesised to have various different forms and a detailed EPR spectrum has yet to be experimentally obtained.

No prior research could be found to confirm if these fractional contributions are upheld when alanine is enriched with ^{13}C, much less if radicals are generated and retained following irradiation damage. To this end, the research into irradiation generated radicals for the hyperpolarisation of alanine commenced with the investigation of radical generation in [1-^{13}C]L-alanine and the effect of irradiation dose.

4.4.1.2 Methods

Non-enriched (NE) and ^{13}C-enriched L-alanine powder samples were irradiated over a range of different doses using an ultra-high dose rate 6 MeV electron linear accelerator.

It is possible for electron irradiation to induce radioactivity in materials[88]. Thus, immediately following the production of the first irradiated alanine samples (both NE and ^{13}C-enriched), a Geiger counter was used to check for radioactivity.

CW EPR (Bruker, EMXmicro) was used to obtain EPR spectra at room temperature. The different samples included: dry NE L-alanine powder, dry ^{13}C-

enriched L-alanine powder, and solutions comprising different concentrations of TEMPO (10 – 100 mM) dissolved in a 1:1 DMSO and D_2O mixture. Dry powder samples were loaded directly into 4 mm thin wall quartz EPR tubes and their mass recorded. Samples were rotated about their own axis by approximately 25–35° between repeats. Liquid state samples were first loaded in 2 mm diameter capillary tubes which in turn were loaded into the EPR tubes. MATLAB was used to obtain spin counts from the EPR spectra and the simulation of EPR spectra was conducted using EasySpin.

4.4.1.3 Results

First and foremost, no induced radioactivity was detected from the irradiated NE and ^{13}C-enriched L-alanine powder samples and hence, they were deemed safe to work with.

The data from exploring the generation of irradiation induced radicals in NE and ^{13}C-enriched L-alanine powder samples is summarised in Figure 4.4. Representative EPR spectra recorded from NE L-alanine powder samples irradiated at different doses showed differences in signal amplitude (Figure 4.4A). The spin counts obtained from integrating these spectra appeared to be dose-dependent as the spin count increased with increasing irradiation dose between 10 – 70 kGy (Figure 4.4B). Furthermore, within this dose range, the spin count following each 10 kGy increment in dose was found to be approximately equivalent to increasing the concentration of the exogenous radical species TEMPO in 10 mM increments. Beyond 70 kGy, the generation of endogenous radicals appeared to reach saturation. The EPR spectra of irradiated [1-^{13}C]L-alanine powder samples confirmed the generation of radicals in ^{13}C-enriched alanine upon e-beam irradiation. The line shape was found to be more complex than that recorded from the NE samples and was attributed to the presence of hyperfine interactions between the ^{13}C nuclei and the generated radical species (Figure 4.4C). Comparable spin counts to the NE samples were obtained from the ^{13}C-enriched samples at 30 kGy, 50 kGy, 70 kGy, and 100 kGy (Figure 4.4D).

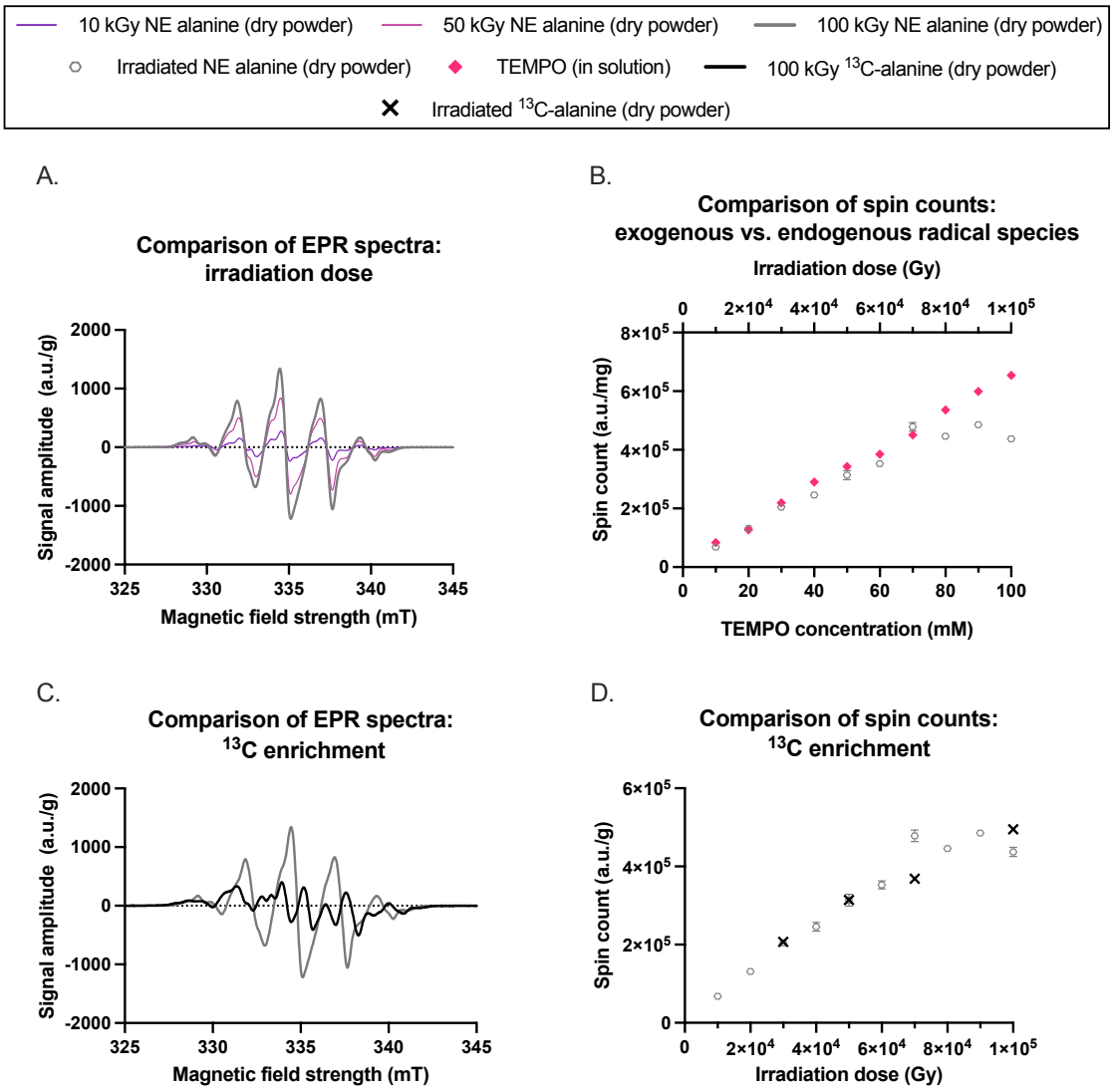

Figure 4.4: Confirmation of endogenous radical generation
EPR spectra and spin counts generated from non-enriched and ^{13}C-enriched L-alanine samples irradiated with an electron beam. A) Differences in the EPR signal were recorded from non-enriched L-alanine samples that had been irradiated at different doses. B) To an extent, the effect of irradiation on the spin count appeared to be dose-dependent. Between 10 – 70 kGy, each additional 10 kGy dose of irradiation appeared to be approximately equivalent to adding 10 mM of the exogenous radical TEMPO to the DNP sample preparation. C) Differences in EPR line shapes between non-enriched and enriched samples was attributed to the hyperfine interaction. D) An increase in spin count with irradiation dose was also recorded from irradiated [1-^{13}C]L-alanine powder. This data provided confirmation that endogenous radicals were generated within [1-^{13}C]L-alanine powder upon irradiation with 6 MeV electrons.

The EPR line shape recorded from irradiated NE samples matched that reported in the literature and could be well fitted by simulating only the SAR species using the g-tensor and hyperfine interaction constants previously reported by Sagstuen *et al.* (Figure 4.5A)[85]. At the time of writing, no reports of these constants could be found for describing the line shape of irradiated ^{13}C-alanine. Nevertheless, an adequate fit was simulated with the principal values of the hyperfine tensor set to [21.1679; 2.4736; 85.7337] MHz and using Euler angles of [4.9476; 1.4290; 2.7288] rad (Figure 4.5B).

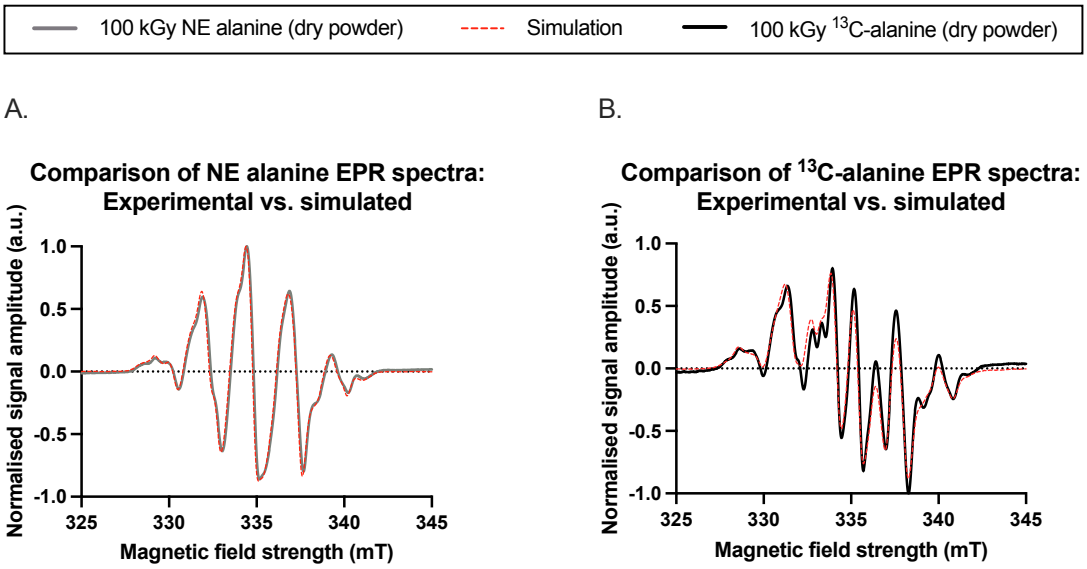

Figure 4.5: Simulations of EPR spectra
Comparisons of experimentally obtained and simulation generated EPR spectra for A) 100 kGy non-enriched L-alanine dry powder and B) 100 kGy [1-^{13}C]L-alanine dry powder. The non-enriched spectrum was simulated using previously published values for the g-tensor and hyperfine interaction constants for the stable alanine radical species (R1).

4.4.1.4 Discussion

As expected from the extensive studies reported in the literature regarding the use of NE alanine as a dosimeter, the e-beam irradiation of NE L-alanine resulted in the generation of radicals. Specifically, there appeared to be a dose-dependent effect that was visible in the EPR spectra, and consequently their spin counts, between 10 – 70 kGy. These dose-dependent changes also seemed to be reflected in the EPR spectra and spin counts recorded from the ^{13}C-enriched samples. It is

not fully understood why the spin counts appeared to saturate above 70 kGy when alanine powder has been approved for dosimeter use for a dose range of 5 – 100 kGy. One possible explanation could be a limited penetration depth of the e-beam. To maximise the homogeneity of irradiation exposure, however, the sample holder was flipped halfway through the irradiation procedure. Nevertheless, perhaps crystals located at the centre of the holder were still not fully exposed to the irradiation.

The representative EPR spectrum of a 100 kGy NE alanine sample appeared to be fairly well characterised by the simulation of the SAR species alone. This result is expected to apply to all the NE irradiated samples as, although changes in the linewidth and signal amplitude were observed following changes in irradiation dose, there were no visually obvious changes to the EPR line shape. This finding was in agreement with a study which found no dose-dependence on the ratio of alanine radical species generated by alpha or gamma irradiation[89].

A reasonable fitting of the EPR spectrum obtained from a 100 kGy ^{13}C-alanine sample was also achieved, albeit to a lesser extent owing in part to its increased complexity arising from the hyperfine interaction. Comparing the EPR line shape to those of the different identified radical species, it would seem possible that the ^{13}C-enriched alanine samples might have had greater contributions from the R2 and R3 species compared to the NE samples. Increases of up to $\sim$60% in the occurrence of R2 and R3 have previously been reported following the heating of samples[86]. For each dose, enriched samples were irradiated for the same duration as the NE samples, however, it is possible that there were differences in the dimensions of the crystals. The ^{13}C-enriched crystals were visually smaller which might have led to a decrease in scattering and thus an increase in sample heating[90]. To confirm this as a contributing factor, more in depth simulations with use of a supercomputer would be required and the dimensions of both types of crystals (NE and enriched) would need to be estimated and compared by microscopy.

4.4.2 Hyperpolarisation via endogenous radicals

4.4.2.1 Introduction

Following the successful generation of radicals within [1-^{13}C]L-alanine powder samples with e-beam irradiation, their use as a polarising agent during DNP was investigated. For this, multiple DNP sample preparations utilising irradiated alanine were explored including a comparison to the exogenous radical based [1-^{13}C]L-alanine preparation developed by Hu *et al.*[23].

4.4.2.2 Methods

In addition to irradiated alanine samples, a control sample comprising non-irradiated alanine and an exogenous radical species as the source of polarising agent was tested. The control sample was a "liquid state" sample preparation based on the protocol outlined by Hu *et al.*: 350 mg [1-^{13}C]L-alanine (Sigma Aldrich), 250 μl 18.94 M NaOH, 100 μl DMSO, 15 mM OX063 Trityl and 0.3 mM Dotarem gadolinium (Guerbet). The replacement of OX063 Trityl with irradiated [1-^{13}C]L-alanine was also explored using d-DNP. A sample which comprised a combination of irradiation generated radicals and OX063 Trityl was explored solely for the purpose of recording a spin count via EPR and not as a sample for d-DNP.

[1-^{13}C]L-alanine was irradiated using an ultra-high dose rate 6 MeV electron linear accelerator. "Solid state" samples were also prepared and comprised solely irradiated [1-^{13}C]L-alanine powder with a frozen glycerol "plug" on top. These plugs were made by pipetting droplets of glycerol into liquid nitrogen. Another sample preparation comprised irradiated [1-^{13}C]L-alanine powder mixed in anhydrous glycerol at room temperature.

The different sample types are summarised in Table 4.1.

Each sample was pipetted into a small PEEK sample cup and inserted into a HyperSense polariser (Oxford Instruments, Abingdon, UK) at <1.4 K (3.35 T/94 GHz) for DNP. Microwave frequency sweeps were acquired for each sample between 93.75 – 94.195 GHz in 5 MHz steps with a two minute build-up per frequency step. The microwave power was held constant at 100 mW for all microwave frequency

Sample	Description	Radical source	State
1.	Based on protocol by Hu *et al.*	OX063 Trityl	Liquid
2.	Based on protocol by Hu *et al.*	Irradiation	Liquid
3.	Based on protocol by Hu *et al.*	Both	Liquid
4.	[1-^{13}C]L-alanine powder with glycerol plug	Irradiation	Solid
5.	[1-^{13}C]L-alanine powder and glycerol mix	Irradiation	"Solid"

Table 4.1: Summary of different alanine samples

sweeps and build-ups. The build-up of polarisation was subsequently monitored at the peak frequency of the microwave frequency sweep every three minutes using a low flip-angle readout. The acquired spectra were analysed using an in-house developed MATLAB script and normalised for the mass of [1-^{13}C]L-alanine.

CW EPR (EMXmicro and E680, Bruker) was used to obtain EPR spectra and spin counts at room temperature and at 5 K. A longitudinal study into the stability of the alanine radical species was also conducted. For this, EPR spin counts were recorded on the same day as their irradiation and then two weeks, four weeks, and 16 weeks post irradiation. Dry powder samples were prepared directly in the EPR tubes and rotated about their own axis by approximately 25 – 35° between repeats. The data generated from dry powder samples was corrected for the mass of alanine. Samples containing glycerol were prepared as stock solutions which were used to fill haematocrit tubes which themselves were inserted into the EPR tubes. Spin counts from glycerol containing samples were not corrected for alanine mass due to difficulty in accurately determining the quantity of alanine that had been taken up in each haematocrit tube. Instead, the ratio of spin counts were taken at each time point.

X-ray diffraction (XRD) (Malvern Panalytical) was used to gain an understanding of the structure of the samples being inserted for DNP. XRD samples comprised NE-alanine dry powder or NE-alanine mixed with glycerol.

4.4.2.3 Results

When prepared in the liquid state, compared to samples containing the exogenous radical OX063 Trityl as the source of radicals, little-to-no signal enhancement was

recorded from irradiated [1-^{13}C]L-alanine samples (Figure 4.6A). Signal enhancements were, however, recorded from irradiated [1-^{13}C]L-alanine prepared in the solid-state (Figure 4.6B). Greater signal enhancement appeared to be recorded from samples containing [1-^{13}C]L-alanine irradiated at 100 kGy compared to the sample irradiated at 10 kGy. A further improvement on these signal enhancements was achieved by mixing irradiated [1-^{13}C]L-alanine powder with glycerol. Nevertheless, the greatest signal enhancement remained that recorded from the OX063 Trityl radical sample preparation replicated from the literature (Figure 4.6C). Unexpectedly, the highest spin count was recorded from a sample consisting of 100 kGy irradiated [1-^{13}C]L-alanine mixed with glycerol (Figure 4.6D).

There were no visible differences in EPR line shape and width between dry [1-^{13}C]L-alanine samples and [1-^{13}C]L-alanine mixed with glycerol (Figure 4.7A and B) but differences were observed between endogenous and exogenous radical species. For example, the line width of 30 kGy irradiated [1-^{13}C]L-alanine was approximately seven and three times wider than that recorded from 15 mM OX063 Trityl and 15 mM TEMPO, respectively (Figure 4.7C and D). Spectra recorded from irradiated alanine radical species exhibited greater line widths than either of the exogenous radical species over a range of concentrations (Figure 4.7E).

A longitudinal study appeared to show greater stability in the spin counts of NE alanine powder compared to ^{13}C-enriched powder over a 16 week period (Figure 4.8A and B). Specifically, there appeared to be greater overlap of the mean spin counts recorded from ^{13}C-enriched samples between different irradiation dose conditions. This observation appeared to hold when the ^{13}C-enriched powder was stored in glycerol over the same time frame. Notably, however, there was no clear relationship between changes in spin count and duration of storage.

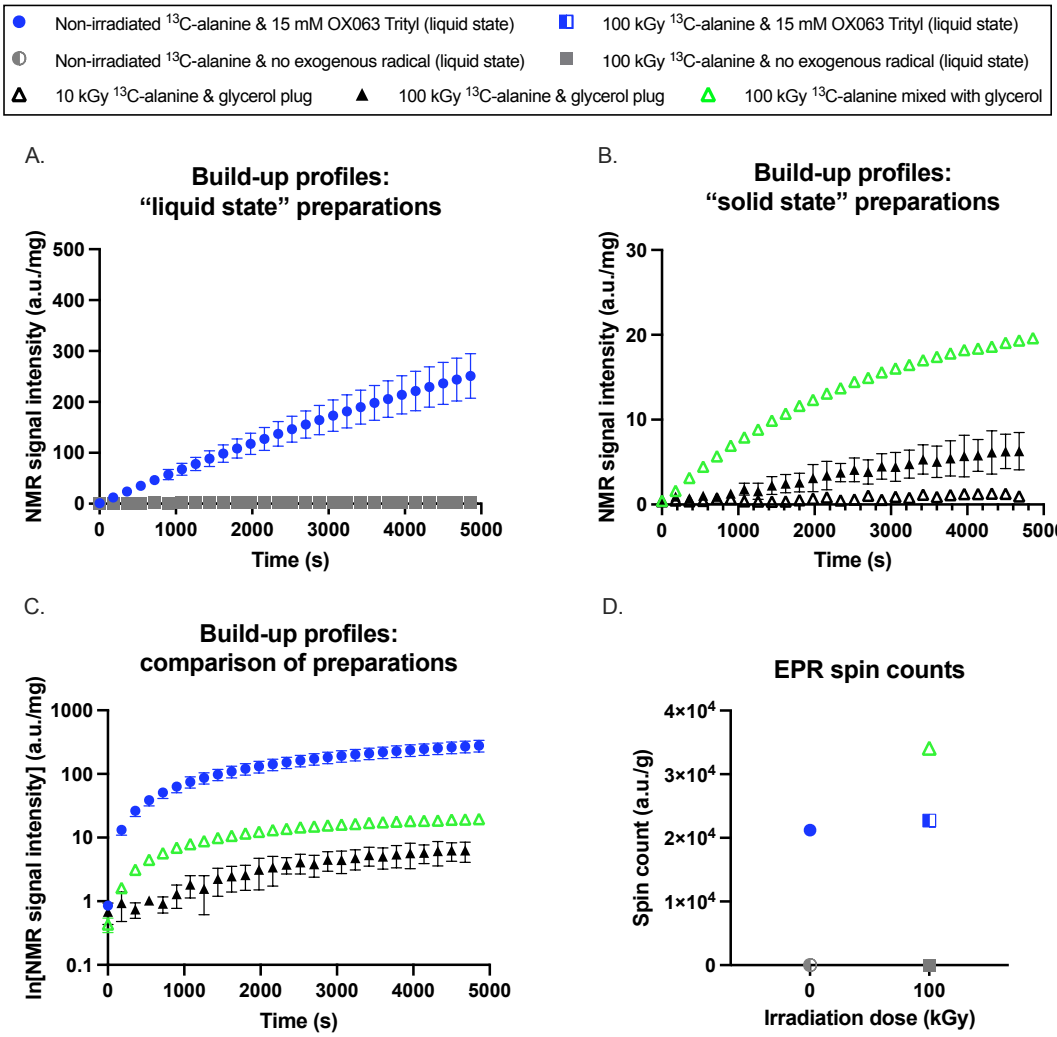

Figure 4.6: ^{13}C-alanine DNP sample preparation optimisation at 3.35 T
A) Build-up profiles recorded from literature-based sample preparations. The two sample types differed in their source of polarising agent; irradiated [1-^{13}C]L-alanine ($n = 1$) provided little-to-no signal enhancement compared to samples containing the exogenous radical OX063 Trityl ($n = 3$). B) Build-up profiles recorded from [1-^{13}C]L-alanine dry powder irradiated at 10 kGy or 100 kGy doses kept in position by a frozen glycerol "plug" and a 100 kGy [1-^{13}C]L-alanine and glycerol mixture. Compared to the sample irradiated at 10 kGy ($n = 1$), greater signal enhancement appeared to be recorded from the samples irradiated at 100 kGy ($n = 3$). Further improvement was recorded when the powder was dispersed within glycerol as opposed to the viscous liquid acting as a plug ($n = 3$). C) The generated signal enhancement did not reach the level recorded from the liquid-state sample preparation replicated from the literature. D) In the liquid state, only radicals from the exogenous radical compound appeared to contribute to the spin count and the greatest spin count was recorded from the 100 kGy [1-^{13}C]L-alanine and glycerol mixture.

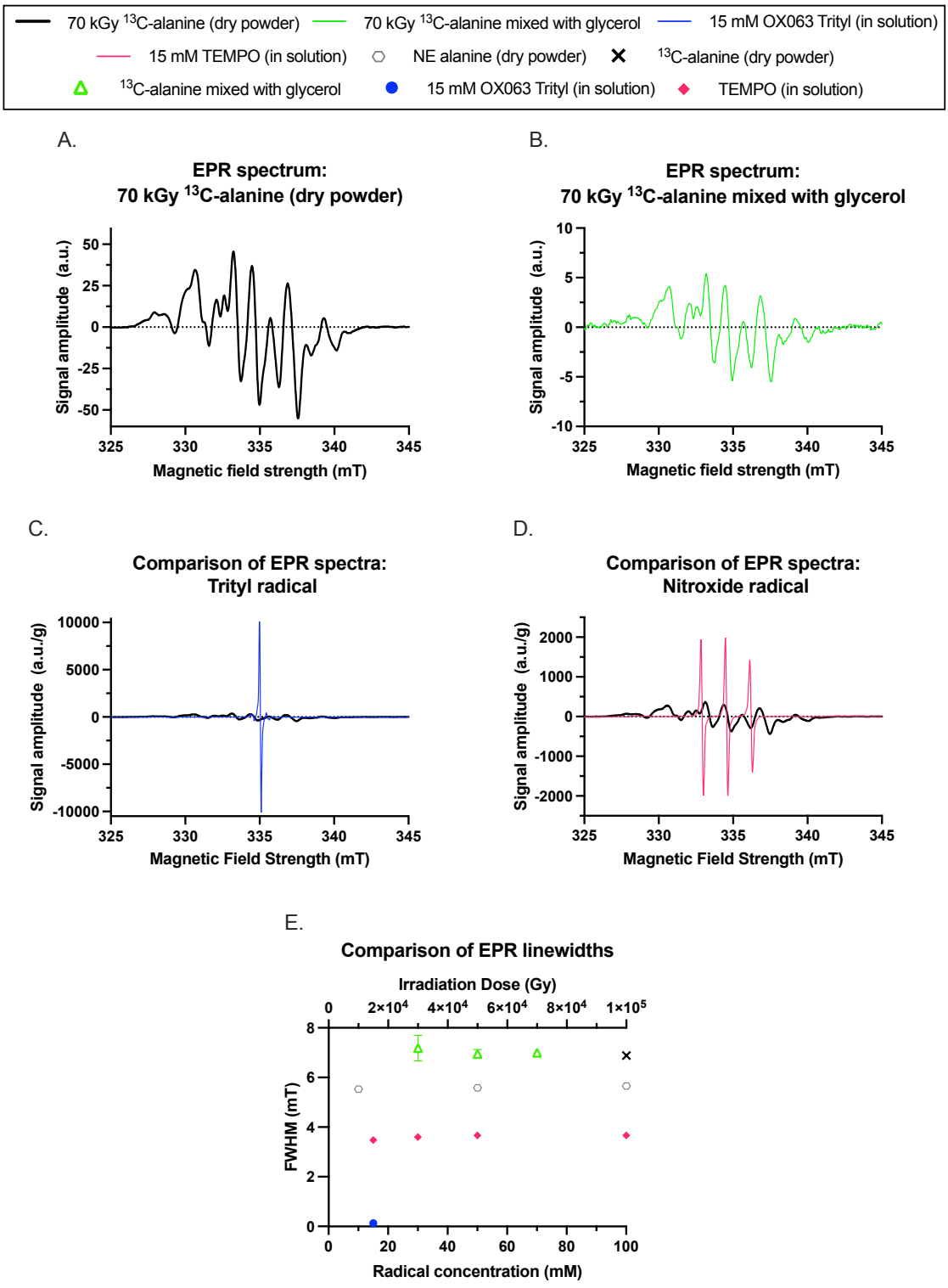

Figure 4.7: Comparison of exogenous and endogenous radical EPR spectra Comparison of EPR line shapes and widths between 70 kGy irradiated [1-^{13}C]L-alanine and B) 70 kGy irradiated [1-^{13}C]L-alanine mixed in glycerol, C) 15 mM OX063 Trityl and, D) 15 mM TEMPO. E) Irradiated samples exhibited greater line widths than either of the exogenous radical species over a range of concentrations.

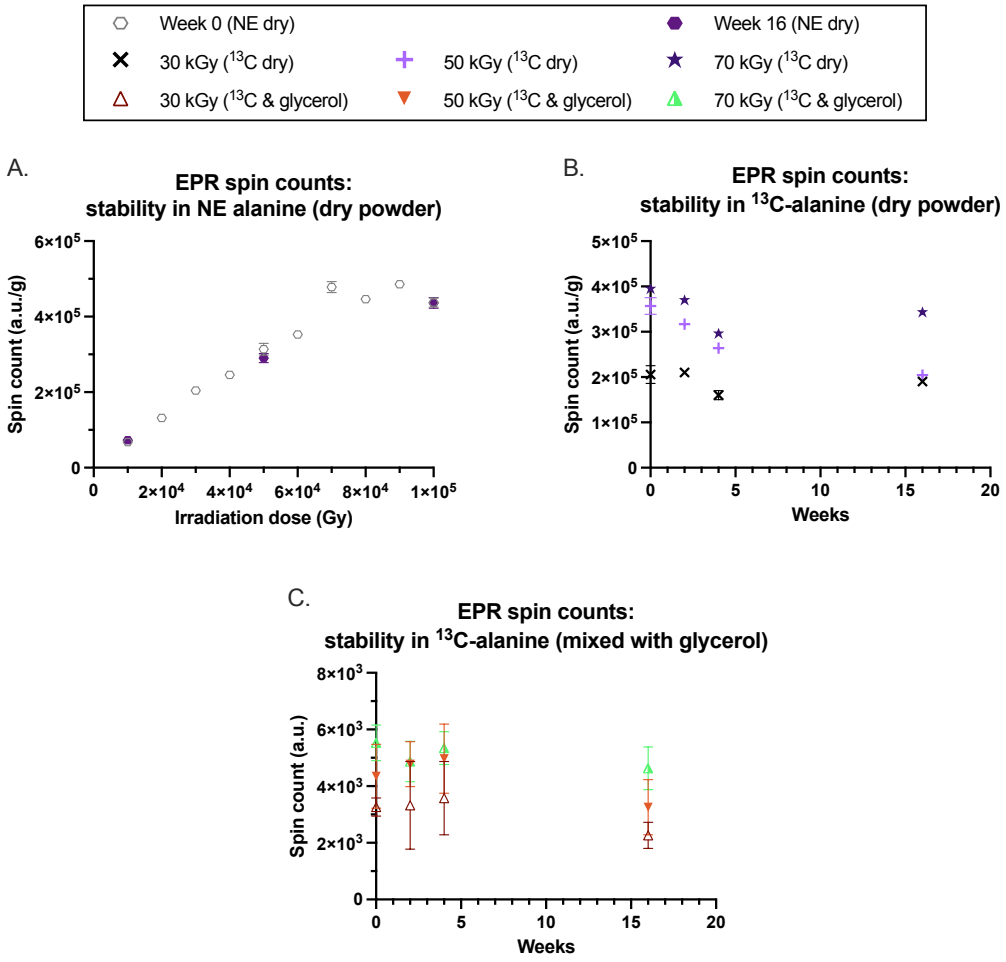

Figure 4.8: Stability of endogenous radicals
Comparison of EPR spin counts from A) non-enriched alanine powder, B) [1-^{13}C]L-alanine powder, and C) [1-^{13}C]L-alanine mixed in glycerol. Between the dry powder samples, greater stability appeared to be recorded from the non-enriched samples. Changes in spin counts did not appear to be consistent with increased duration of storage.

To ensure that the room temperature EPR data were representative, the d-DNP sample environment was replicated as far as was possible through the use of cryogenic EPR. The absorption spectra recorded from [1-^{13}C]L-alanine powder mixed with glycerol and a repeat measurement taken following the 90° rotation of the sample appeared to show slight differences in signal amplitude (Figure 4.9A). Any difference in the spectra was not as easily observed in the first derivatives of the absorption spectra which exhibited the same line shape as observed at room temperature (Figure 4.9B). The EPR spectrum recorded from a "liquid state" non-irradiated [1-^{13}C]L-alanine sample where the source of polarising agent

was the OX063 Trityl radical also showed a similar line shape as that recorded previously (Figure 4.9C).

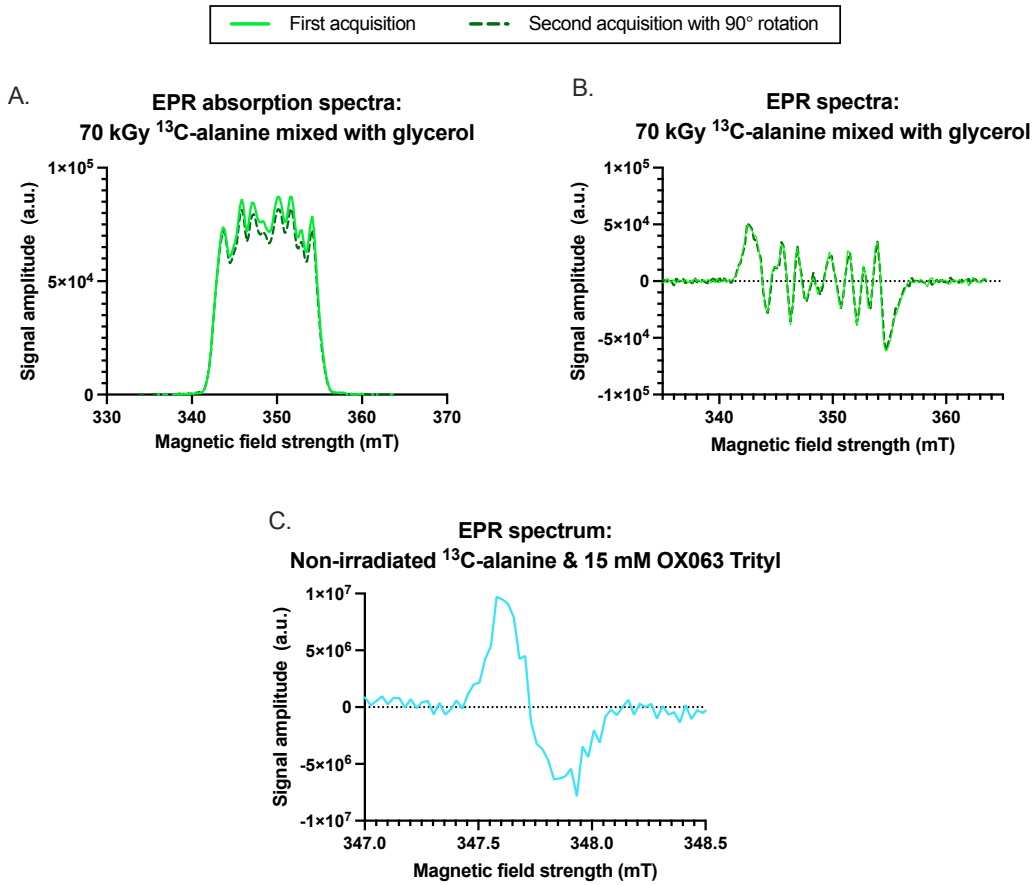

Figure 4.9: Cryogenic EPR spectra
EPR data recorded at 5 K. The A) absorption spectra and B) first derivative recorded from [1-^{13}C]L-alanine powder mixed with glycerol and a repeat measurement taken following the 90° rotation of the sample. The signal amplitude appeared to differ between the two measurements. C) The EPR spectrum recorded from a "liquid state" non-irradiated [1-^{13}C]L-alanine sample where the source of polarising agent was the OX063 Trityl radical.

X-ray diffraction spectra recorded from NE alanine powder mixed with glycerol exhibited peaks that matched those recorded from dry NE alanine powder (Figure 4.10). This data appeared to suggest that alanine does not fully dissolve in glycerol.

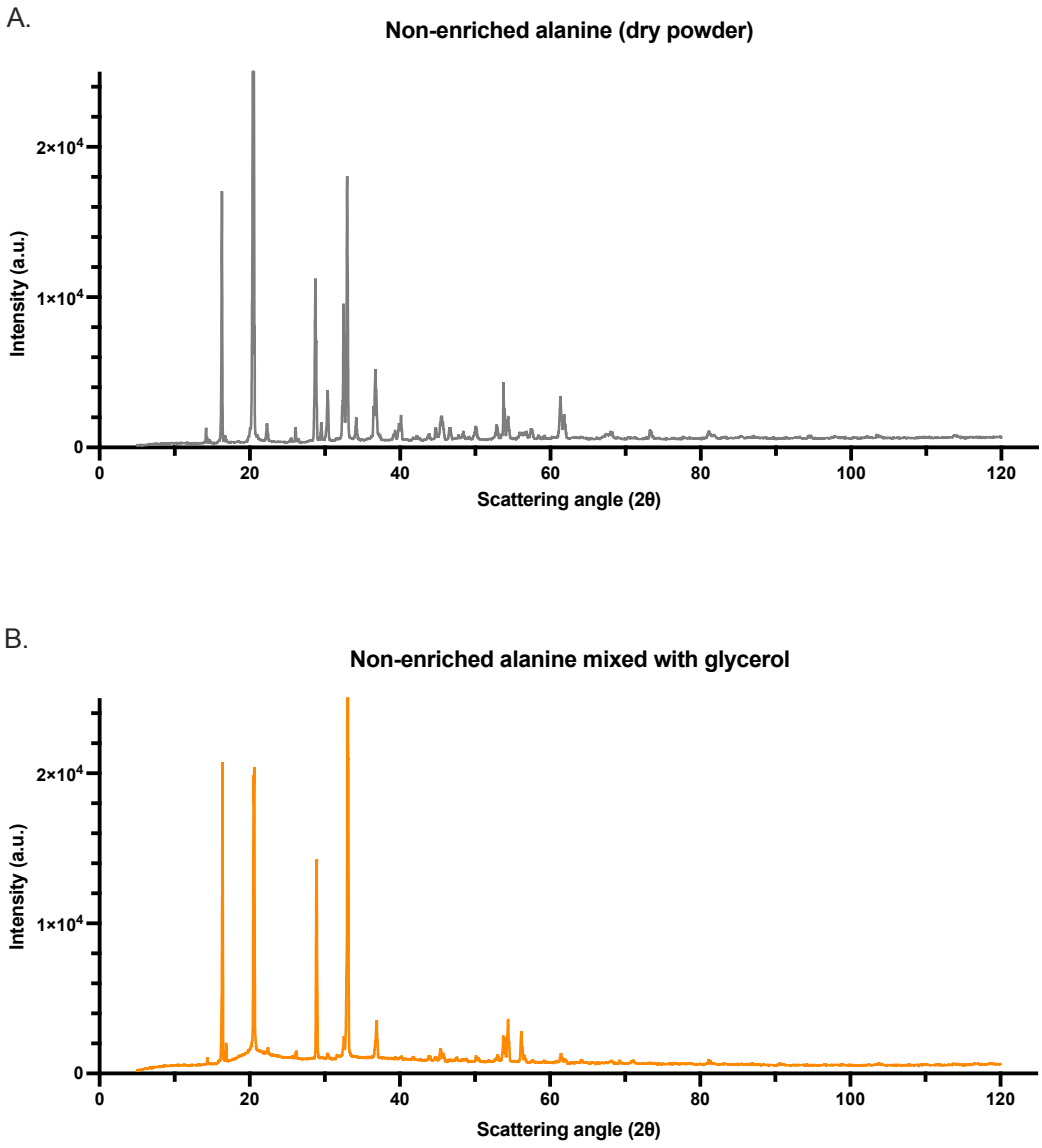

Figure 4.10: X-ray diffraction spectra
X-ray diffraction spectra recorded from A) dry NE alanine powder and B) NE alanine powder mixed with glycerol. Comparing the spectra, due to the presence of diffraction peaks in both, it appears as though the alanine does not fully dissolve in glycerol.

4.4.2.4 Discussion

This data showed the potential for [1-^{13}C]L-alanine to be polarised at 3.35 T via radicals generated in situ by ionising radiation. Of the irradiated sample preparations trialled here, ^{13}C signal enhancements were only recorded from those prepared in the "solid state". This finding, and that of zero spin counts from irradiated alanine liquid state samples, is in agreement with the literature where irradiation generated radicals in non-enriched alanine rapidly recombine when exposed to moisture. Reflecting their short recombination time, the endogenous radicals did not appear to polarise [1-^{13}C]L-alanine DNP samples, nor contribute to the spin count when prepared in the liquid state. Thus, the endogenous radicals generated are nonpersistent which could prove to be a useful feature for d-DNP by removing the need for a radical filtration step and might even lead to the prolongation of the nuclear T_1 following dissolution compared to the use of chemically stabilised radicals. Furthermore, the quenching of the irradiation generated radicals upon dissolution offers a flexibility of solvent choice that is not currently provided by their exogenous counterparts.

Another sample preparation that could have been explored as a control sample was a non-irradiated [1-^{13}C]L-alanine powder and glycerol mix with OX063 Trityl. This was not done as samples containing OX063 Trityl have undergone optimisations by many users in the field and hence, the liquid state preparation developed by Hu *et al.* was seen as a fairer comparison.

The greatest signal enhancements and spin count among the irradiated sample types were recorded from the samples comprising 100 kGy irradiated alanine powder mixed with glycerol. The increase in EPR spin count compared to the liquid state literature-based preparations suggests either the endogenous radical concentration is unfavourably high — encouraging polarisation decay — or that only a fraction of the irradiation generated radicals are contributing to the polarisation of [1-^{13}C]L-alanine. The CW microwave DNP scheme used here is perhaps interacting with

only a proportion of the spins present in the wide EPR line shape. The incorporation of microwave frequency modulation may enable the saturation of a larger number of EPR transitions by engaging a larger fraction of the electron population.

The irradiation induced radicals appeared to be relatively stable over a 16 week period whether stored as a dry powder or mixed with glycerol. Notably, the variability in spin counts was not found to be significant nor correlate with the duration of storage for each sample. One possible source for the observed changes in spin count between measurements could be the preferential ordering of alanine crystals. To be more sensitive to this effect, a goniometer could have been employed to assist the rotation of samples at small angle intervals with greater precision and the mean spin counts from a full rotation could have been compared. Instead, the results outlined here were generated following the manual rotation of samples to enable approximately three or four measurements within one full rotation. X-ray diffraction was also implemented to provide insight into the structure of crystal-based samples. The presence of diffraction peaks in the glycerol containing sample indicated that alanine crystals do not fully dissolve in glycerol which could result in the preferential ordering of crystals and affect how polarisation is transferred throughout the whole DNP sample.

4.5 Microwave modulation during DNP

4.5.0.1 Introduction

The modulation of the microwave irradiation during d-DNP has typically been applied to samples containing broad line width radicals, such as TEMPO, to improve the efficiency of polarisation transfer by engaging a larger fraction of the electron population. Previous benefits from its incorporation into the d-DNP protocol include a reduction in the required radical concentration, the extracted build-up times, and microwave power, to generate optimal levels of polarisation[91]. Following the findings detailed in Section 4.4.2, in particular, regarding the EPR line width and shape of the irradiation induced radicals, the modulation of microwave irradiation during d-DNP was hypothesised to aid the hyperpolarisation of irradiated [1-^{13}C]L-alanine samples.

4.5.0.2 Methods

The work described in this section was carried out at the Magnetic Resonance Research Centre, Aarhus University on the SpinAligner polariser (Polarize, Denmark) due to it having an inbuilt microwave modulation feature. Microwave modulation was not an available feature on the polariser systems at Oxford University.

The magnetic field strength of the SpinAligner was 6.7 T and four different microwave settings were available: Continuous wave (CW), CW with microwave modulation, Pulse modulation (PM), and PM with microwave modulation. In the previous subsections, the microwave irradiation was applied continuously at a single frequency 4.11A). When applying microwave modulation, the amplitude and frequency of the modulation (AM and FM, respectively) can be selected by the user. AM is the chosen range of frequencies around a centre frequency whereas FM is the rate at which this range of frequencies is applied (Figure 4.11B). PM is simply the microwaves being applied at a single frequency in pulsed bursts to the sample (Figure 4.11C). Microwave modulation can also be applied in conjunction with PM where the full range of amplitudes is covered during the time frame of a single pulse (Figure 4.11D).

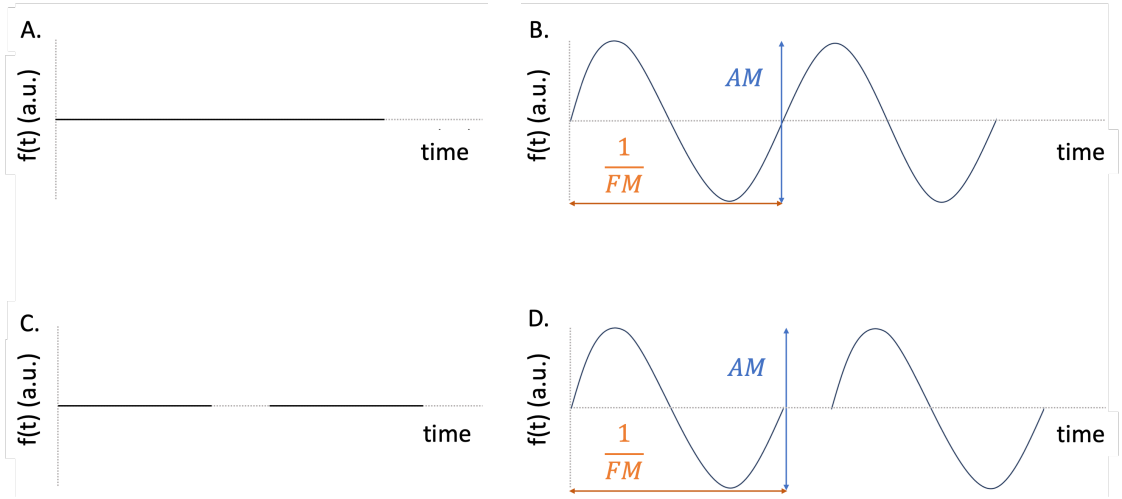

Figure 4.11: SpinAligner microwave settings
A schematic of the four microwave settings available on the SpinAligner system. A) The continuous wave setting involves the application of microwave irradiation at a single frequency. B) Continuous wave in conjunction with microwave modulation is the application of microwave irradiation symmetrically around a chosen centre frequency. AM is the amplitude modulation and refers to the chosen range of frequencies around a centre frequency. FM is the frequency modulation which determines the rate at which the AM is covered. C) Pulse modulation is where microwaves are applied at a single frequency but they are repetitively switched on and off. D) Pulse modulation with microwave modulation is the modulation of the amplitude and frequency of the microwaves occurring within the time frame of a single pulse.

Following initial tests of the various modulation schemes, microwave modulation was applied with PM over a range of amplitudes at different rates to find the optimal AM and FM setting. The optimal irradiation generated radical concentration was also sought. For this, 50 mg of 30 kGy, 50 kGy, or 70 kGy irradiated [1-^{13}C]L-alanine was mixed with 100 mg anhydrous glycerol directly in the sample cup.

The microwave frequency sweep profiles were acquired using 32 averages, PWs of 2 μs, and a TR of 30 s for irradiated samples or a TR of 10 s for all other sample types. The range of frequencies explored varied between different sample types due to differences in the widths of their profiles, however, the step size of 5 MHz was held constant across all sample types. The build-up profiles were acquired using 2 μs PWs with a TR of 60 s at 20 mW power and no averaging for all sample types. The transmission power of the pulses was 32 dB. To extract the polarisation constants, the build-up profiles were fitted to a bi-exponential function (Equation 2.8).

4.5.0.3 Results

Following the insertion of a sample comprising 70 kGy ^{13}C-alanine mixed with glycerol, each of the microwave operating settings were tested. All four frequency sweeps exhibited a single positive lobe but a shoulder was observed during PM and the PM with microwave modulation setting (Figure 4.12). Greater signal enhancements were achieved using PM compared to CW or CW with microwave modulation. PM in conjunction with microwave modulation appeared to further enhance the signal. As a starting point, the settings used for the AM and FM were those used and optimised for pyruvate samples by the Laustsen laboratory (30 MHz AM and 5 kHz FM).

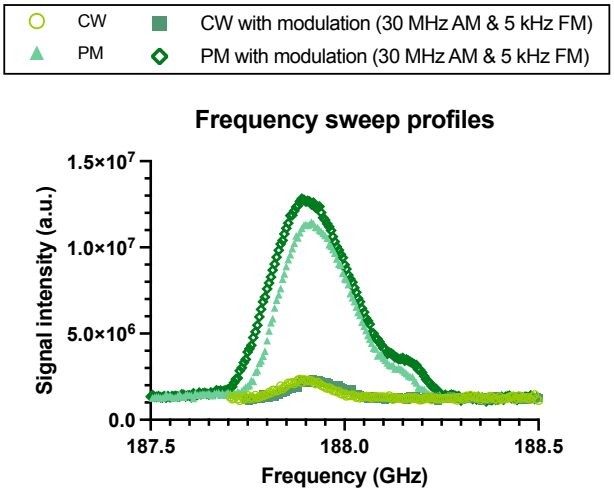

Figure 4.12: Initial testing of the microwave settings
The four microwave source settings were tested on the same sample comprising 70 kGy irradiated ^{13}C-alanine mixed with glycerol. All frequency sweep profiles exhibited the same shape; a single positive lobe. The greatest signal enhancement was achieved using the microwaves in the PM setting in conjunction with amplitude and frequency modulation at 30 MHz and 5 kHz, respectively.

Prior to testing different AMs and FMs to find the optimal combination, a comparison of samples irradiated at different doses was recorded using PM. The data acquired from samples irradiated at 30 kGy, 50 kGy, and 70 kGy is summarised in Figure 4.13. During the recording of the microwave frequency sweeps, a second lobe was recorded from the 30 kGy and 50 kGy samples. The height of the second lobe appeared to decrease with increasing radical concentration and was not visible

in the sweep recorded from the 70 kGy sample. In contrast, the height of the first lobe appeared to increase with increased radical concentration (Figure 4.13A). The effect of irradiation dose did not appear to be reflected in the build-up profiles to the same extent as the microwave frequency sweep profiles (Figure 4.13B). The extracted build-up constant appeared to increase with irradiation dose (Figure 4.13C). The relative weightings of the D) fast and E) slow components of the build-up amplitude appeared to show a dominance of the fast component but also an increasing dependence on the slow component with increasing irradiation dose. The F) fast component of the build-up time for each sample was on the order of tens of seconds and the extracted G) slow components were on the order of hours. With increasing irradiation dose, the fast component of the build-up time appeared to decrease and the slow component appeared to increase. Out of the three irradiation doses tested, this data indicated 70 kGy to be the optimum sample.

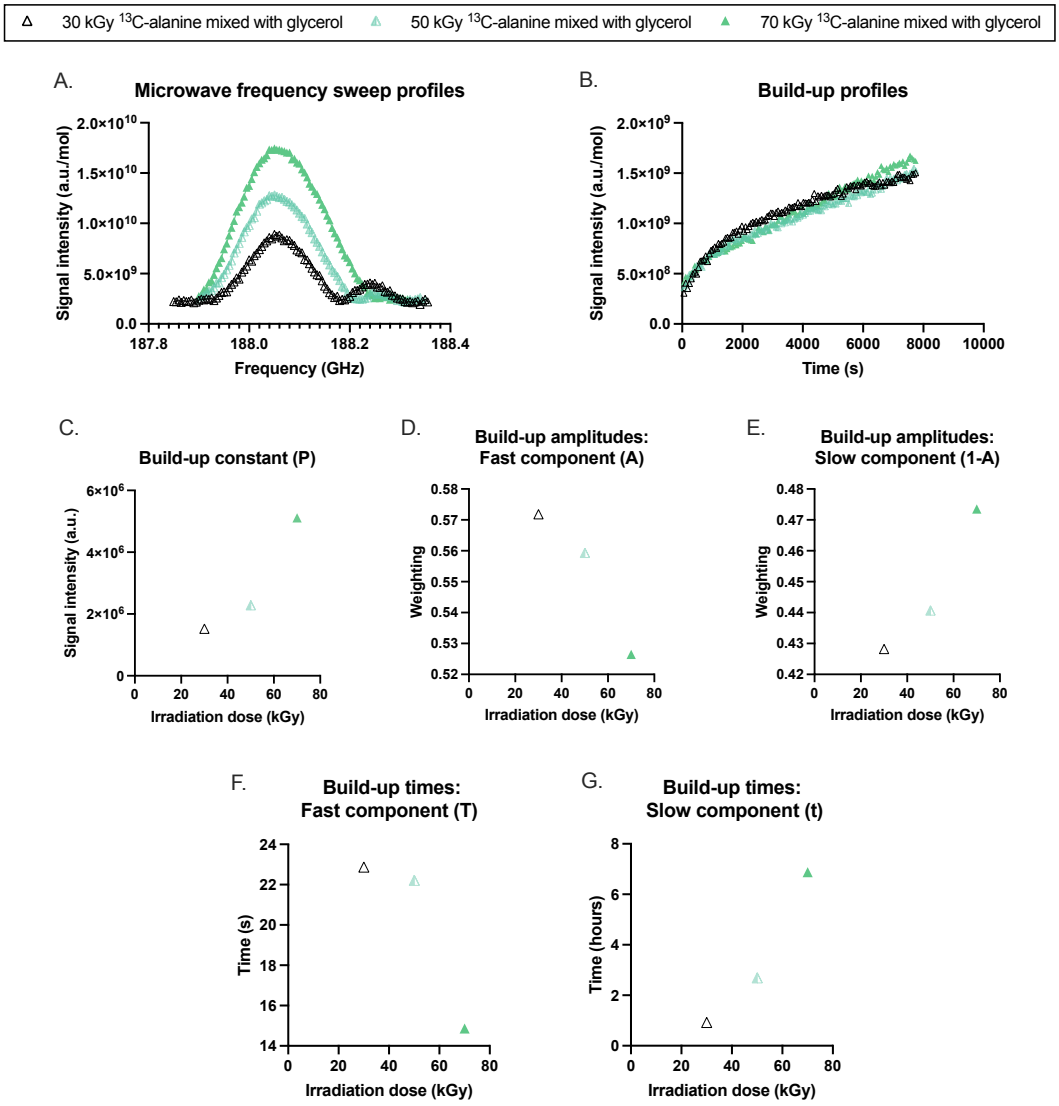

Figure 4.13: Comparison of irradiation dose
A) Microwave frequency sweep profiles for samples irradiated at 30 kGy, 50 kGy, and 70 kGy. A second lobe was recorded from 30 kGy and 50 kGy samples and its height appeared to decrease with increasing radical concentration. This second lobe was not visible in the sweep recorded from the 70 kGy sample. In contrast, the height of the first lobe appeared to increase with increasing radical concentration. B) Build-up profiles recorded following the microwave frequency sweeps. The effect of irradiation dose did not appear to be reflected in the build-up profiles to the same extent as the microwave frequency sweep profiles. C) The extracted build-up constant appeared to increase with an increase in irradiation dose. The relative weightings of the D) fast and E) slow components of the build-up amplitude appeared to show a dominance of the fast component but also an increasing dependence on the slow component with increasing irradiation dose. The F) fast component of the build-up time was on the order of tens of seconds and the G) slow component was on the order of hours. With increasing irradiation dose, the fast component of the build-up time appeared to decrease and the slow component appeared to increase.

As a starting point for the optimisation of the microwave modulation settings, the AM was fixed to 100 MHz and different FMs were explored: 1 Hz, 100 Hz, 1 kHz, 10 kHz (Figure 4.14A). Following the integral of the final spectrum from each build-up, the greatest value was recorded following the 100 Hz FM setting (Figure 4.14C). Hence, the FM was fixed at 100 Hz and the AM setting was explored at 25 MHz and 50 MHz (Figure 4.14B). The greatest integral from the final spectrum was obtained from the combination of 25 MHz AM with 100 Hz FM (Figure 4.14D). An improvement in signal enhancement appeared to be observed between microwave frequency sweep profiles following the adjustment of the microwave settings to 25 MHz AM with 100 Hz FM compared to the use of the preset combination of 30 MHz AM with 5 kHz FM (Figure 4.14E). The build-up polarisation constants extracted from each build-up profile are summarised in Figure 4.15 and Table 4.2.

In agreement with the data summarised in Figure 4.14, the greatest build-up constant was extracted following the application of the microwaves with 25 MHz AM at a rate of 100 Hz.

AM (MHz)	FM (Hz)	Build-up Amp: P (a.u.)	Build-up time: T (s)	Build-up time: t (hours)
100	1	1970000	16.9	0.59
100	100	1890000	76.9	0.47
100	1000	1460000	275.9	0.84
100	10000	1520000	254.6	0.84
25	100	3210000	31.6	0.52
50	100	3050000	43.3	0.53

Table 4.2: Polarisation constants: effect of modulation

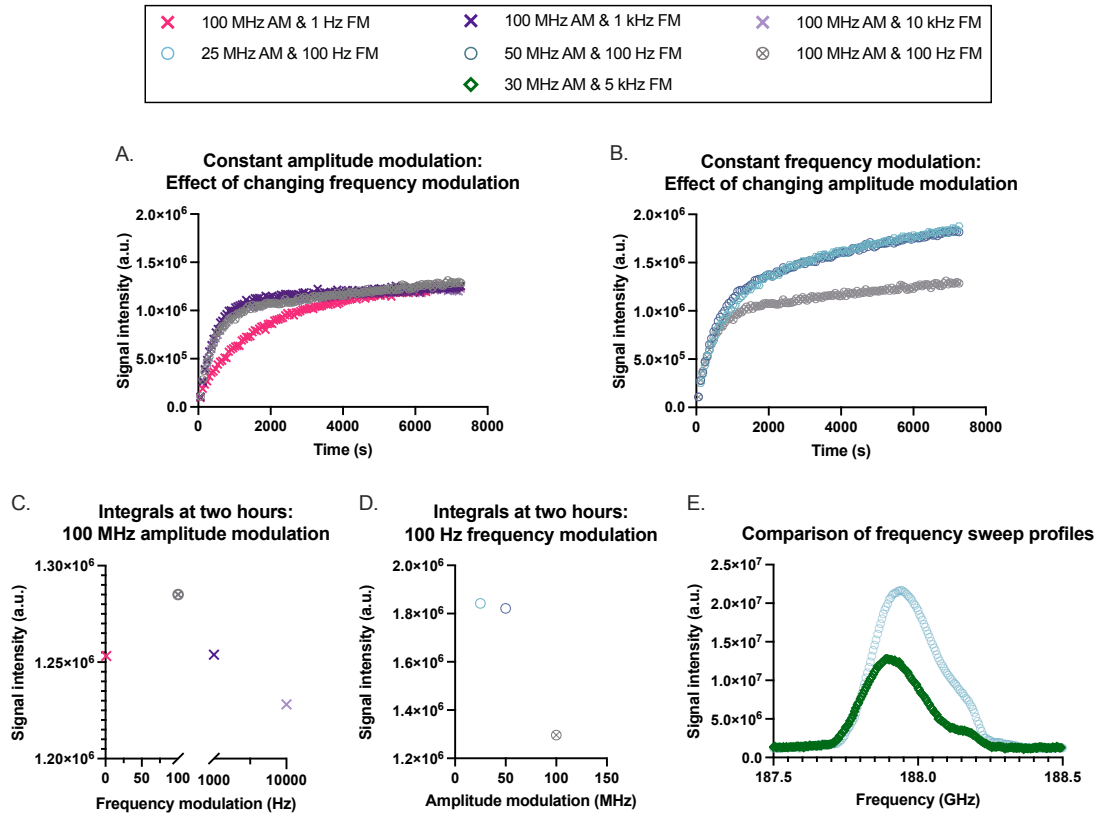

Figure 4.14: Optimisation of modulation
A) The amplitude modulation was initially fixed to 100 MHz and the frequency modulation set to 1 Hz, 100 Hz, 1 kHz, 10 kHz. B) The FM was then fixed at 100 Hz and the AM setting settings explored 25 MHz and 50 MHz. C) The greatest integral of the spectrum acquired at two hours was recorded following the 100 Hz FM setting. D) Holding the FM constant at 100 Hz, the greatest integral was recorded when the AM was set to 25 MHz. E) An improvement in signal enhancement appeared to be observed between microwave frequency sweep profiles following the adjustment of the microwave settings to 25 MHz AM with 100 Hz FM compared to the use of the preset combination of 30 MHz AM with 5 kHz FM.

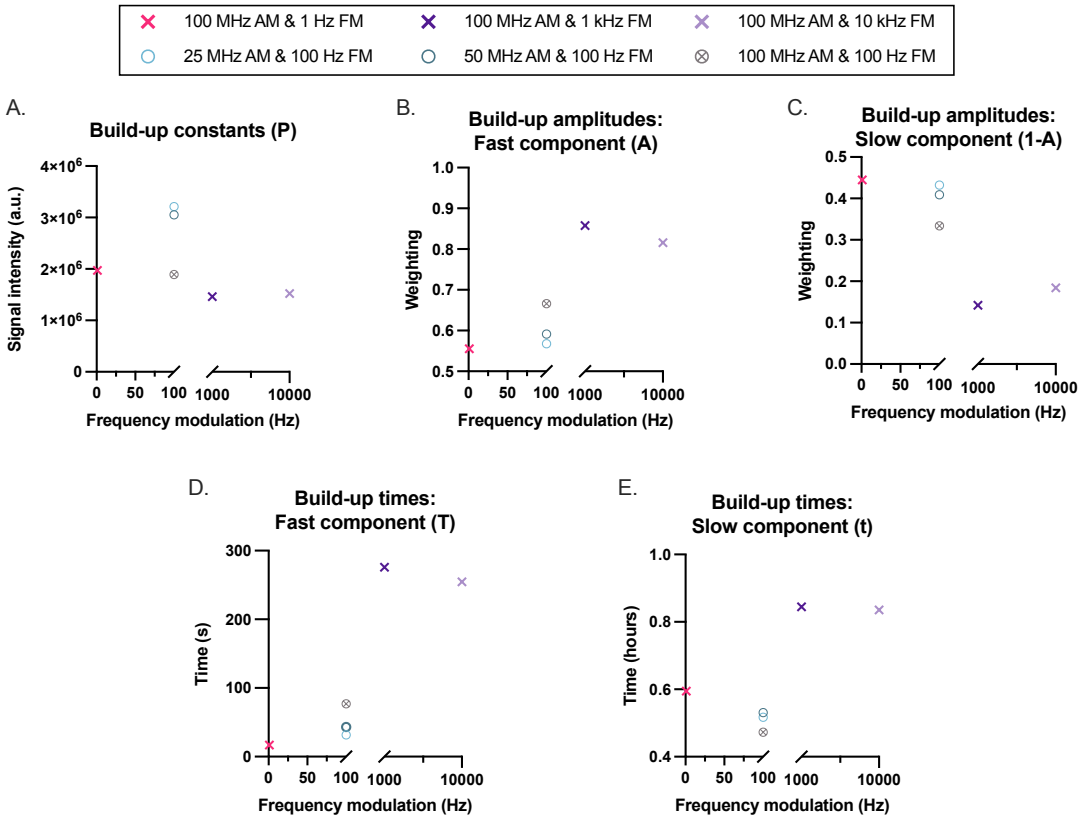

Figure 4.15: The effect of AM and FM on the polarisation constants
Comparison of the A) the build-up constant, B) fast component of the build-up amplitude, C) slow component of the build-up amplitude, D) fast component of the build-up time, and E) slow component of the build-up time. The greatest build-up constant was extracted following the application of the microwaves with 25 MHz AM at a rate of 100 Hz.

Further optimisation of the FM setting was conducted during a second trip to the Laustsen laboratory in an attempt to improve the generated signal enhancement. The microwave frequency sweep profiles recorded following the adjustment of the FM setting (whilst the AM was held constant at 25 MHz) appeared to show greater enhancement with a FM of 1 kHz but a reduction in the enhancement at 10 kHz (Figure 4.16A). The build-up profiles were recorded at the peak frequency obtained from each microwave frequency sweep (Figure 4.16B). The extracted polarisation build-up constants also appeared to indicate that 25 MHz AM with FM of 1 kHz facilitated the greatest signal enhancement (Figure 4.16C, D, E, F, & G). These constants are also summarised in Table 4.3.

AM (MHz)	FM (Hz)	Build-up Amp: P (a.u.)	Build-up time: T (s)	Build-up time: t (hours)
25	100	1850000	138.8	0.93
25	1000	5170000	14.8	6.96
25	10000	2520000	50.1	1.95

Table 4.3: Polarisation constants: further optimsiation of modulation

Further repeats were acquired using the 25 MHz AM and 1 kHz FM setting. Comparisons of the microwave frequency sweep profiles showed large variability (Figure 4.17A). This observation was also reflected in the subsequent build-up profiles (Figure 4.17B). Notably, some of the extracted solid state polarisation constants (Figure 4.17 C, D, E, and F) overlapped with those extracted for combinations of the AM and FM settings previously explored in Figure 4.14.

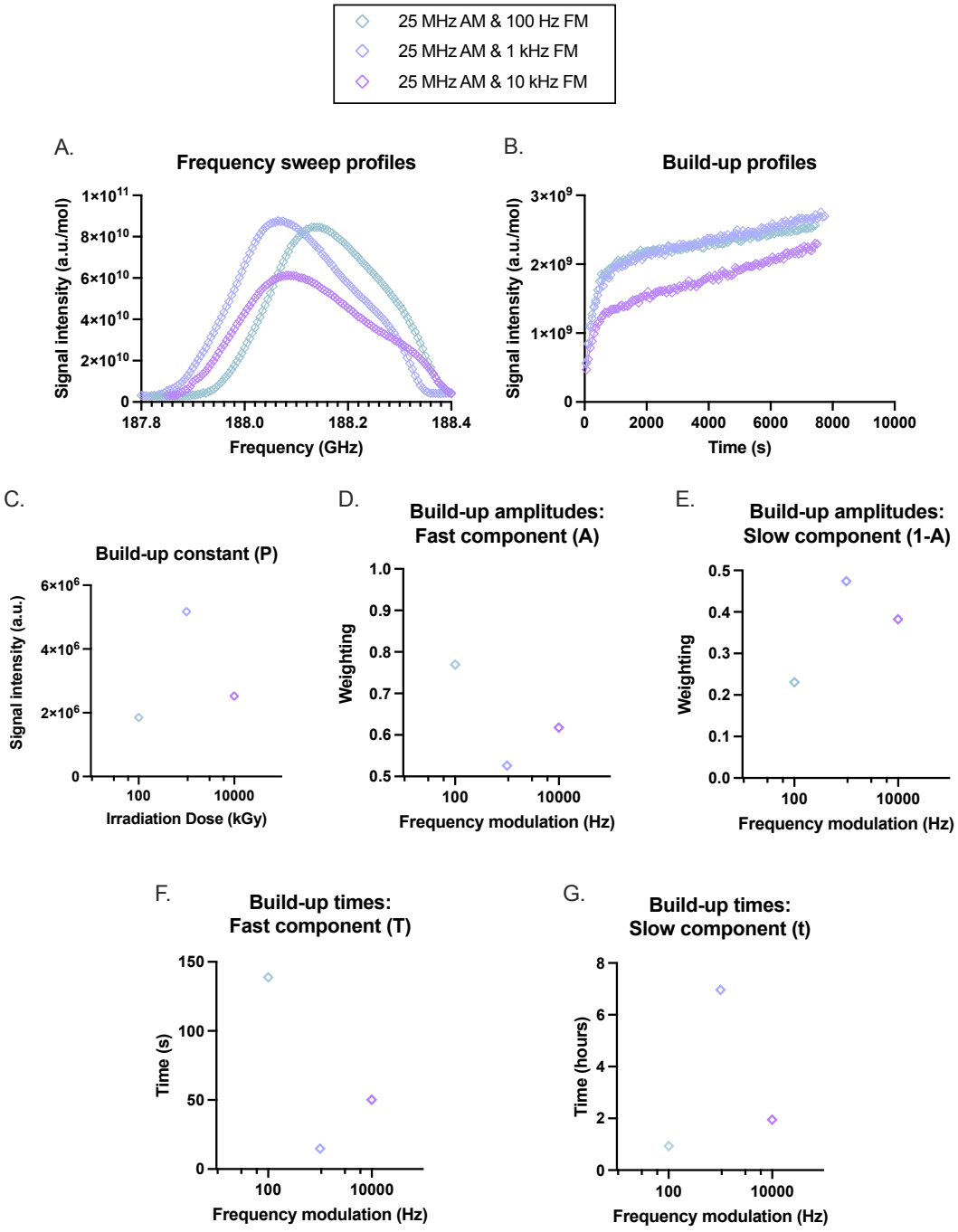

Figure 4.16: Comparison of frequency modulation settings at 25 MHz AM A) Microwave frequency sweep profiles recorded following the adjustment of the frequency modulation setting whilst the amplitude modulation was held constant at 25 MHz. B) Subsequent build-up profiles appeared to suggest either 100 Hz or 1 kHz as the optimal choice for the frequency modulation whereas a reduction in the enhancement was observed whilst using 10 kHz. The extracted polarisation constants, particularly the build-up constant, appeared to indicate 25 MHz AM with a FM of 1 kHz as the optimal setting.

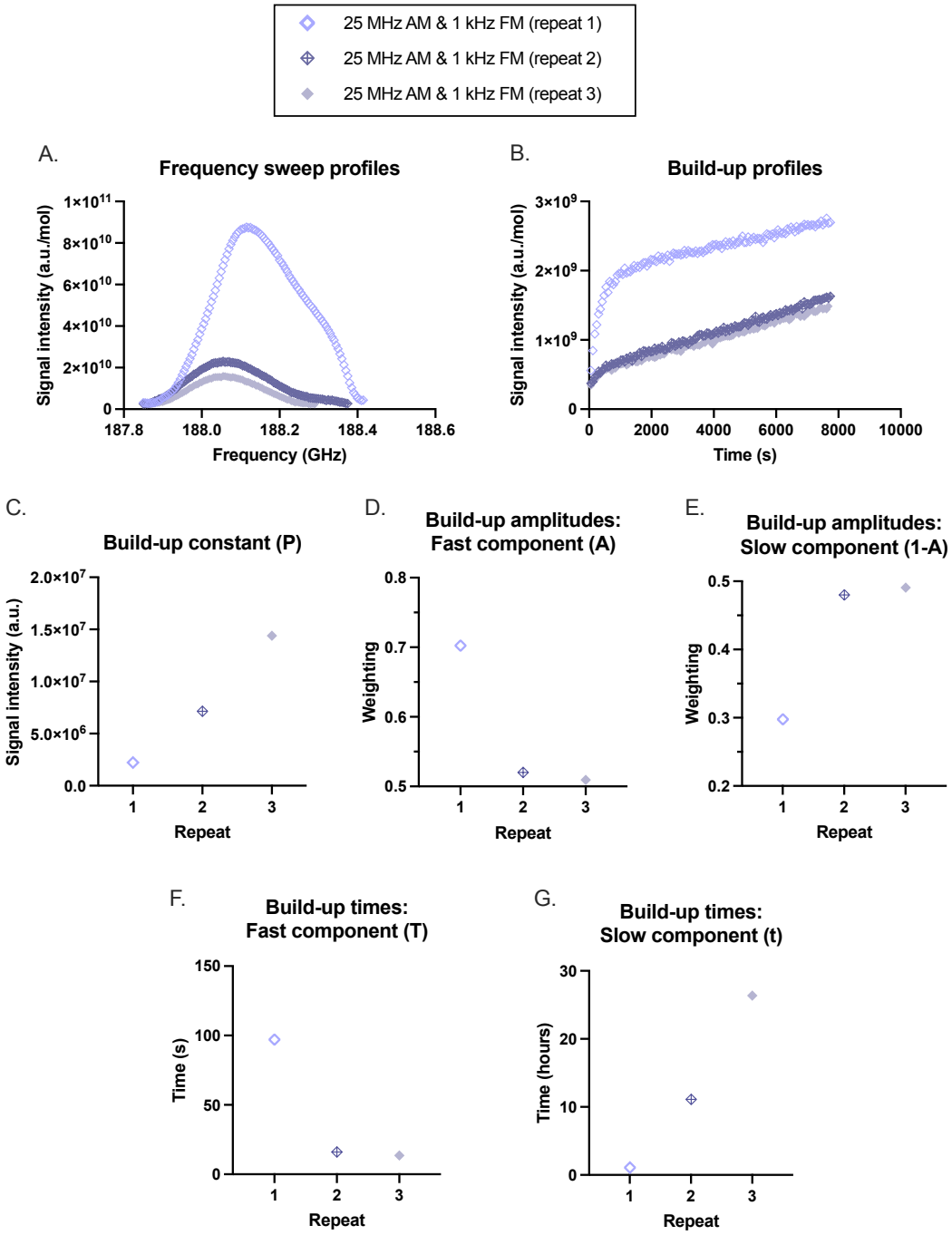

Figure 4.17: Repeats: solid state data
A) Comparisons between repeats of the microwave frequency sweep profiles acquired using 25 MHz AM and 1 kHz FM. Two out of the three repeats appeared to show similar levels of signal enhancement as that achieved with no microwave modulation. This observation was also reflected in the subsequent B) build-up profiles. The extracted polarisation constants C), D), E), & F) showed large variability between repeats.

This variability was also observed in the liquid state polarisation decay data acquired at room temperature following dissolution (Figure 4.18A). The extracted liquid state nuclear T_1 relaxation times ($67.3 \pm 10.9\,\mathrm{s}$) and polarisation levels — both at the point of dissolution ($7.6 \pm 2.6\,\%$) and scan ($3.0 \pm 1.1\,\%$) — were deemed suitable for an *in vivo* trial (Figure 4.18B, C, and D).

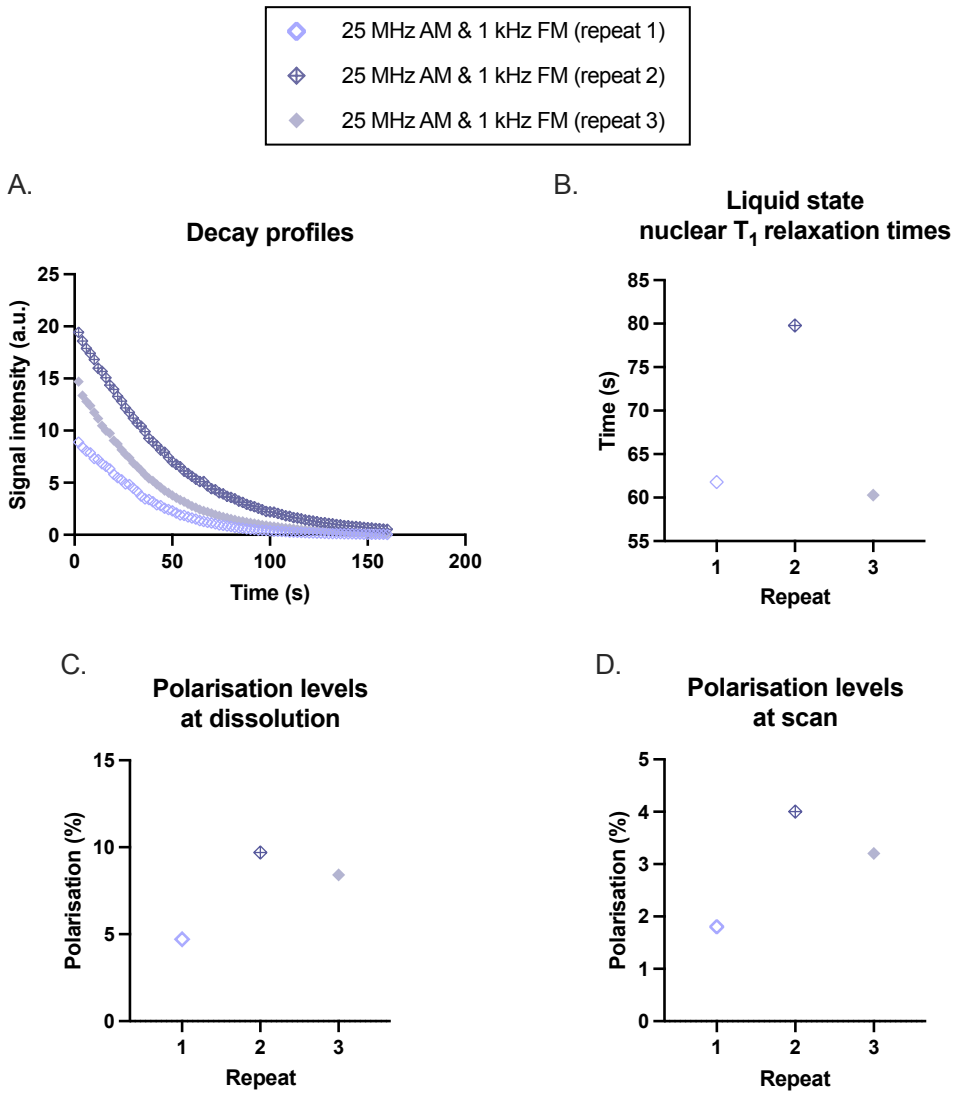

Figure 4.18: Repeats: liquid state data
A) The liquid state polarisation decay data acquired at room temperature following dissolution. B) The extracted liquid state nuclear T_1 relaxation times and C) & D) polarisation levels were deemed suitable for an *in vivo* trial.

4.5.0.4 Discussion

This data showed the feasibility of modulation to improve the signal enhancements generated from irradiated [1-^{13}C]L-alanine samples during d-DNP. The use of PM instead of CW was seen as an important contributing factor and likely helped to reduce sample heating.

The extraction of the build-up polarisation constants from this preliminary data did not lead to the identification of a definite optimal microwave setting for generating polarisation via endogenous irradiation generated radicals. Instead, out of the range of settings tested, the AM and FM combination that gave the best signal enhancement (25 MHz AM and 1 kHz FM) was selected for subsequent experiments. The improvements recorded following the AM being set to 25 MHz or 50 MHz compared to 100 MHz was in agreement with previous literature in the context of the nuclear Larmor frequency of ^{13}C at 6.7 T (71.7 MHz) where the optimal AM is expected to be smaller than the nuclear Larmor frequency[92]. For the optimal setting to be determined, repeats at each of the different settings would be required. Due to time constraints and the use of a polariser that belonged to another laboratory, repeats were not recorded at all of the tested microwave settings. Among the repeats that were recorded, the extent of variability that was observed could not be fully accounted for and hence repeated measurements on a control sample such as pyruvate would be required to ensure the equipment itself was not a contributing factor.

The effects of irradiation dose and microwave modulation settings were most pronounced during the recording of the microwave frequency sweeps which was likely due to the dominance of the fast build-up components during the 30 s build-up at each frequency step.

Further improvement could have perhaps been achieved if the [1-^{13}C]L-alanine had also been directly deuterated. Lumata *et al.* previously demonstrated this for samples where the source of polarising agent was a broad line width radical; deuteration resulted in a narrowing of the EPR spectrum due to a reduction

in the hyperfine coupling and a 2–3 fold improvement observed in the nuclear polarisation levels[93].

Irrespective of this, the extracted liquid state nuclear T_1 relaxation times and polarisation levels suggested that, following d-DNP, e-beam irradiated alanine samples are suitable for *in vivo* imaging.

4.6 *In vivo* study of metabolism

4.6.0.1 Introduction

Changes in the kinetics and/or ratios of metabolites are typically used as a biomarker to identify a pathological state[94]. As discussed previously (Section 4.1), [1-^{13}C]L-alanine has the potential to enable a more accurate measurement of intracellular pyruvate and lactate levels if selected as the injected substrate for hyperpolarised MR. Here, a proof of concept *in vivo* study was conducted with healthy rats to test the irradiated alanine preparation and the optimised DNP protocol (detailed in Section 4.5).

4.6.0.2 Methods

The work described in this section is a continuation of the work summarised in Section 4.5 and was also carried out at the Magnetic Resonance Research Centre, Aarhus University.

Prior to the work detailed in this section, a [1-^{13}C]L-alanine preparation developed by Hu *et al.* had been used as a control sample. The team at Aarhus Univeristy, however, had developed and optimised a different alanine preparation for use on their polariser that operated at a higher magnetic field strength. This preparation was selected as a more appropriate control for the subsequent *in vivo* proof of concept study.

Two different alanine-based samples were tested *in vivo*:

1. 1.276 g of [1-^{13}C]L-alanine was mixed in 8 ml of water and 2 ml of 11.65 M HCl. This mixture was freeze-dried and approximately 1.512 g of alanine hydrochloride yielded. The alanine hydrochloride was then dissolved in 2.25 ml DMSO with the assistance of heating. 180 mg OX063 Trityl was added leading to approximately 38 mM radical concentration. 50 μl (∼60 mg) of this mixture was pipetted into a sample cup and inserted into the polariser. 2.5 ml of buffer (with NaOH for neutralising pH) was used for dissolution.[1]

[1]This sample preparation was developed and prepared by Mr. Nichlas Vous Christensen (Aarhus Univeristy, Aarhus)

2. 50 mg 70 kGy irradiated alanine mixed in 100 mg anhydrous glycerol directly in the sample cup. For dissolution, the sample was dissolved in 5.5 g of D_2O.

The former preparation was selected as a control sample as it comprised non-irradiated alanine and an exogenous radical species as the source of polarising agent and had been previously optimised on the SpinAligner.

In addition, a pyruvate sample was used as a control for the polarisation characteristics due to it being the standard choice of HCA for metabolic studies. The preparation for this sample comprised a 14 M [1-^{13}C]-pyruvic acid stock solution with the appropriate mass of AH111501 ("GE Trityl", MW = 1595 g/mol) to achieve a 30 mM radical concentration. 18 μl of this mixture was pipetted into a sample cup and the sample dissolution was conducted using 3 ml of buffer.

Based on previous optimisation work and the use of a narrow line width radical, the polariser was set to PM with no microwave modulation for the non-irradiated samples and, for the irradiated sample preparation, microwave modulation was applied over a range of 25 MHz (AM) at a rate of 1 kHz (FM). The microwave frequency sweep profiles were acquired using 32 averages, PWs of 2 μs, and a TR of 10 s for non-irradiated samples or a TR of 30 s for irradiated samples. The range of frequencies explored varied between different sample types due to differences in the widths of their profiles, however, the step size of 5 MHz was held constant across all sample types. The build-up profiles were acquired using 2 μs PWs with a TR of 60 s at 20 mW power and no averaging for all sample types. The transmission power of the pulses was 32 dB.

Two healthy male Sprague-Dawley rats were injected with one shot of each hyperpolarised sample via a tail vein catheter. The time between each injection was approximately two hours. The respiratory rate and body temperature of each rat was monitored whilst the rats were under anaesthesia and scanned using a dual-tuned ^{13}C/^{1}H volume rat coil in conjunction with a 3 T system (GE MR750, GE

Healthcare). One rat was scanned using a slice-selective spectroscopic acquisition and the other was imaged using a 2D MR Spectroscopic Imaging (MRSI) sequence[2].

Prior to these scans, a urea phantom was used to calibrate the applied FAs and proton anatomical images were acquired for reference. For the slice-selective spectroscopic acquisition (80 mm slice thickness to include the whole abdomen of the rat), 1 ml of the hyperpolarised sample was injected over ∼5 s and the scan started upon the start of the injection. A 30° FA was applied with a TR of 3 s for a total of 5 minutes (100 time points). For the MRSI (16 × 16 matrix), 1 ml of the hyperpolarised substrate was injected over ∼5 s and the scan started upon the start of the injection. A 15° FA was applied with a TR of 64 ms for a total of 2 minutes (8 time points and ∼16 s per time point).

The liquid state polarisation characteristics of all the sample types were also recorded at room temperature using a 1.4 T benchtop NMR spectrometer (Spinsolve 60^{ULTRA} Carbon, Magritek). The pH levels of the samples were digitally recorded.

For analysis, spectral fitting and quantification was conducted with AMARES using in-house MATLAB scripts (OXSA, [95]), in an attempt to quantify the heights of any metabolite peaks and observe spatial localisation in their production (e.g. in the kidney).

4.6.0.3 Results

Representative solid state polarisation data is shown in Figure 4.19 and the liquid state data in Figure 4.20. The microwave frequency sweep profiles recorded from samples containing the exogenous radical species appeared to exhibit two lobes whereas, as seen previously, only a single lobe was observed from the irradiated alanine samples (Figure 4.19A). Large differences in the limiting signal enhancements appeared to be recorded during the course of the build-up profiles (Figure 4.19B). The exogenous radical samples were best fitted to a monoexponential whilst the irradiation induced radical samples appeared to exhibit a biexponential profile.

[2]This data was acquired in collaboration with: Dr. Esben Søvsø Szocska Hansen who operated the MR scanner and Dr. Lotte Bonde Bertelsen who handled the imaging subjects.

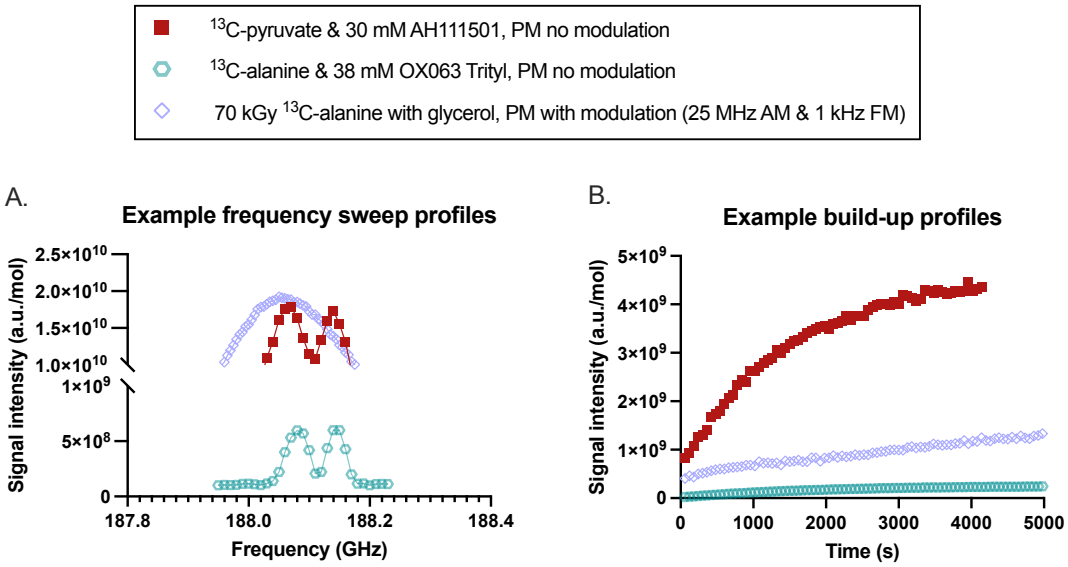

Figure 4.19: Comparison of exogenous and endogenous radicals: solid state Representative microwave frequency sweeps and build-up profiles to compare the signal enhancements generated from samples polarised via exogenous and endogenous radicals. A) Microwave frequency sweep profiles recorded from samples containing exogenous radical species appeared similar in shape where two lobes were observed ($n = 3$). As seen previously, a single lobe was observed from the irradiated alanine samples. Its peak appeared to be comparable to the peak signal intensity recorded from the pyruvate sample. The similarity in signal enhancement did not appear to translate beyond the 30 s time period used for recording each point of the microwave frequency sweep as large differences in the limiting signal enhancements appeared to be recorded during the course of the B) build-up profiles. The exogenous radical samples were best fitted to a monoexponential whereas the irradiation induced radical samples appeared to exhibit a biexponential profile.

The greatest signal enhancement was recorded from the pyruvate sample and this was also reflected in the decay profiles recorded at room temperature (Figure 4.19B and Figure 4.20A). The extracted nuclear T_1 relaxation times appeared to show a prolongation of the T_1 of alanine following the use of irradiation generated radicals whilst also appearing to achieve comparable polarisation levels (Figure 4.20B, C, & D). Approximately half the polarisation level was lost for all samples between the point of dissolution and the start of the scan.

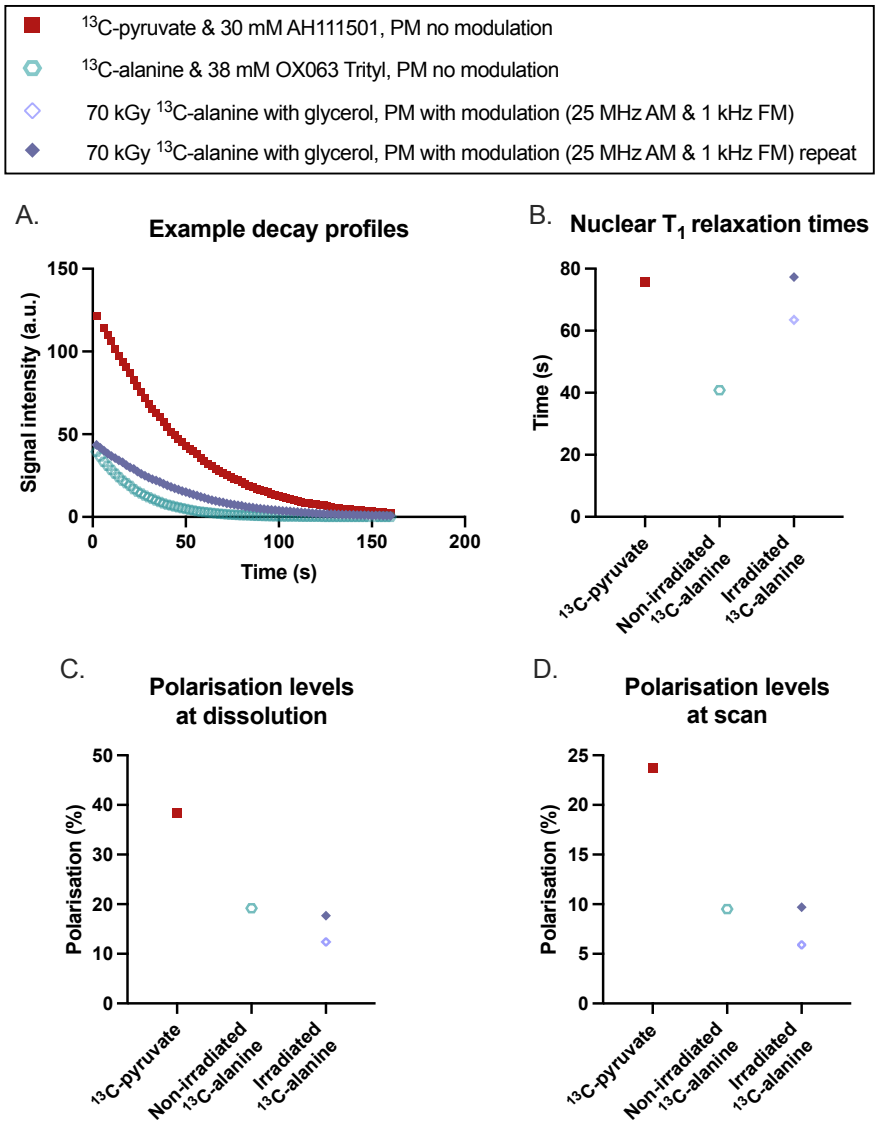

Figure 4.20: Comparison of exogenous and endogenous radicals: liquid state Representative liquid state data recorded at room temperature to compare the polarisation decay, liquid state nuclear T_1 relaxation times, and the polarisation levels between samples polarised via exogenous and endogenous radicals. A) Decay profiles recorded at room temperature appeared to show that the greatest signal enhancement was recorded from the pyruvate sample which was in agreement with the build-up profiles. B) The extracted nuclear T_1 relaxation times appeared to show a prolongation of the T_1 of alanine following the use of irradiation generated radicals whilst also appearing to achieve comparable C) & D) polarisation levels.

Figures 4.21 and 4.22 explore the spectra acquired following the separate tail vein injections of the hyperpolarised ^{13}C-alanine samples into the first rat. Figure 4.21A and B depict the spectra at all time points for the non-irradiated and 70 kGy

irradiated samples, respectively. During the initial time points, greater signal appeared to be recorded from the irradiated sample. Additionally, the first two spectra acquired from the non-irradiated alanine exhibited a phase shift. For this reason, when taking the sum of the spectra, all but the first three time points were summed for both the non-irradiated and irradiated alanine samples (Figure 4.21C and D). The sum of these spectra appeared to result in small peaks either side of the ^{13}C-alanine signal, the positions of which corresponded with the chemical shift values reported in the literature for ^{13}C-lactate and ^{13}C-pyruvate (183 ppm and 171 ppm, respectively)[96].

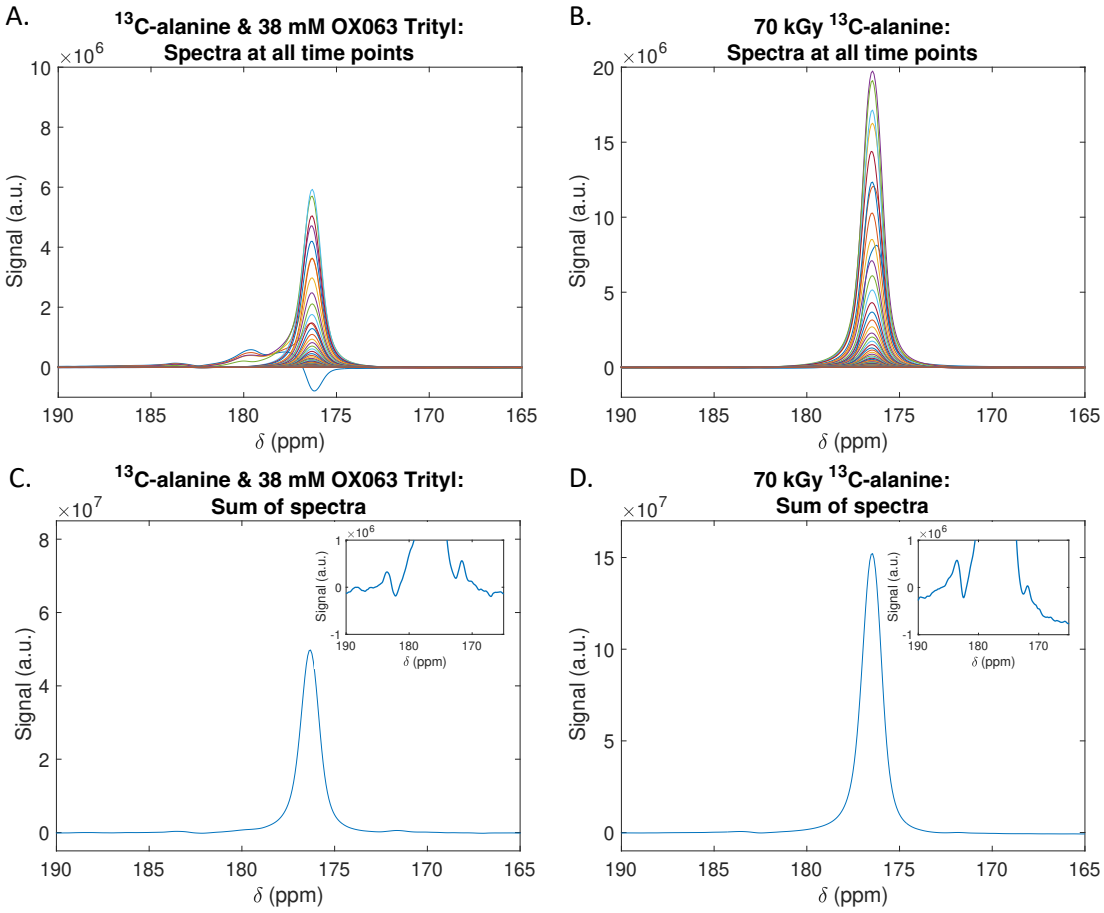

Figure 4.21: Comparison of exogenous and endogenous radicals: 2D spectra The spectra at all time points for the A) non-irradiated and B) 70 kGy irradiated samples are shown. During the initial time points, greater signal appeared to be recorded from the irradiated sample. The sum of all but the first three time points for the C) non-irradiated sample and D) 70 kGy irradiated sample appear to show small peaks either side of the ^{13}C-alanine signal. Each inset shows the same plot but with a truncated y-axis.

The presence of these metabolite peaks can be seen more clearly in the 3D representation of the spectra (Figure4.22). The results from the spectral fitting of this data is summarised in Figure 4.23. In both cases, for scaling, the signal recorded from the alanine peak was reduced by a factor of 10.

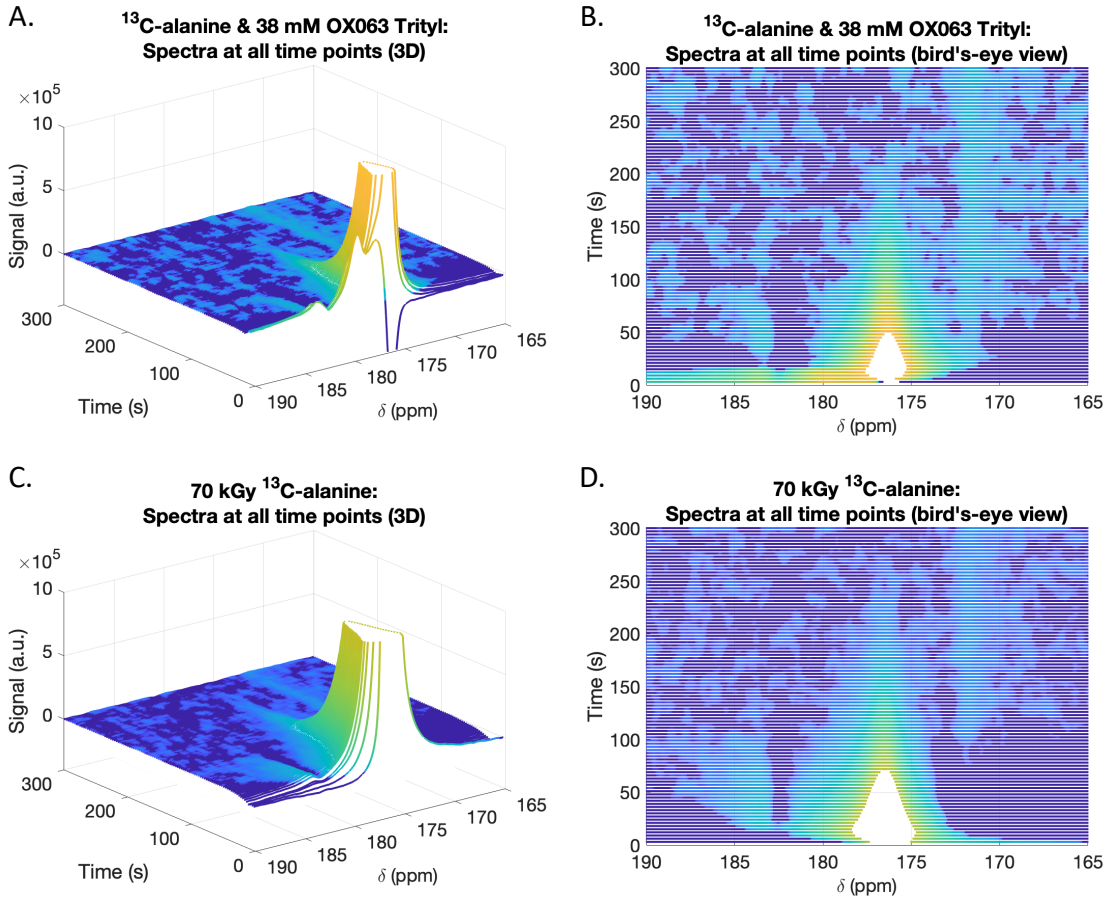

Figure 4.22: Comparison of exogenous and endogenous radicals: 3D spectra The 3D representations of the spectra recorded from the A) non-irradiated and C) irradiated samples are shown from two different views. Other metabolites appeared to be detected and can most easily be seen in plots B) and D) for the non-irradiated and irradiated samples, respectively. Due to their position on the chemical shift scale, these signals could have potentially arisen from the presence of ^{13}C-lactate and ^{13}C-pyruvate.

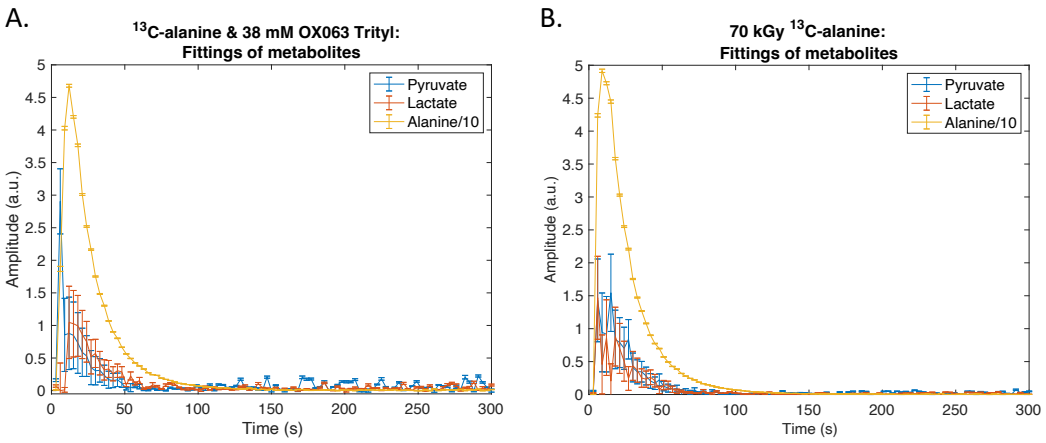

Figure 4.23: SPSP: Metabolite fittings
The amplitudes extracted from the spectral fitting of the A) non-irradiated and B) 70 kGy irradiated data is summarised. In both cases, for scaling, the signal recorded from the ^{13}C-alanine peak was reduced by a factor of 10.

The administration of hyperpolarised alanine samples into the second rat was imaged using MRSI and the data is summarised in Figure 4.24. The MRSI data was overlaid onto a proton image acquired in the axial plane for anatomical reference (Figure 4.24A). The signal recorded at each time point from the non-irradiated and 70 kGy irradiated samples appeared to show the perfusion of ^{13}C-alanine into the kidneys (Figure 4.24B and C). Due to an artefact (potentially caused by flow or a receiver gain overload) present in the plotting of the first time point, the signal peak heights from the second and third time points were summed to generate a map of the distribution of ^{13}C-alanine, ^{13}C-lactate, and ^{13}C-pyruvate (Figure 4.24D, E, and F).

The pH levels of the injected alanine samples were also measured and are summarised in Table 4.4.

Sample	pH
70 kGy ^{13}C-alanine	6.89
^{13}C-alanine & 38 mM OX063 Trityl	7.11

Table 4.4: pH of samples injected *in vivo*

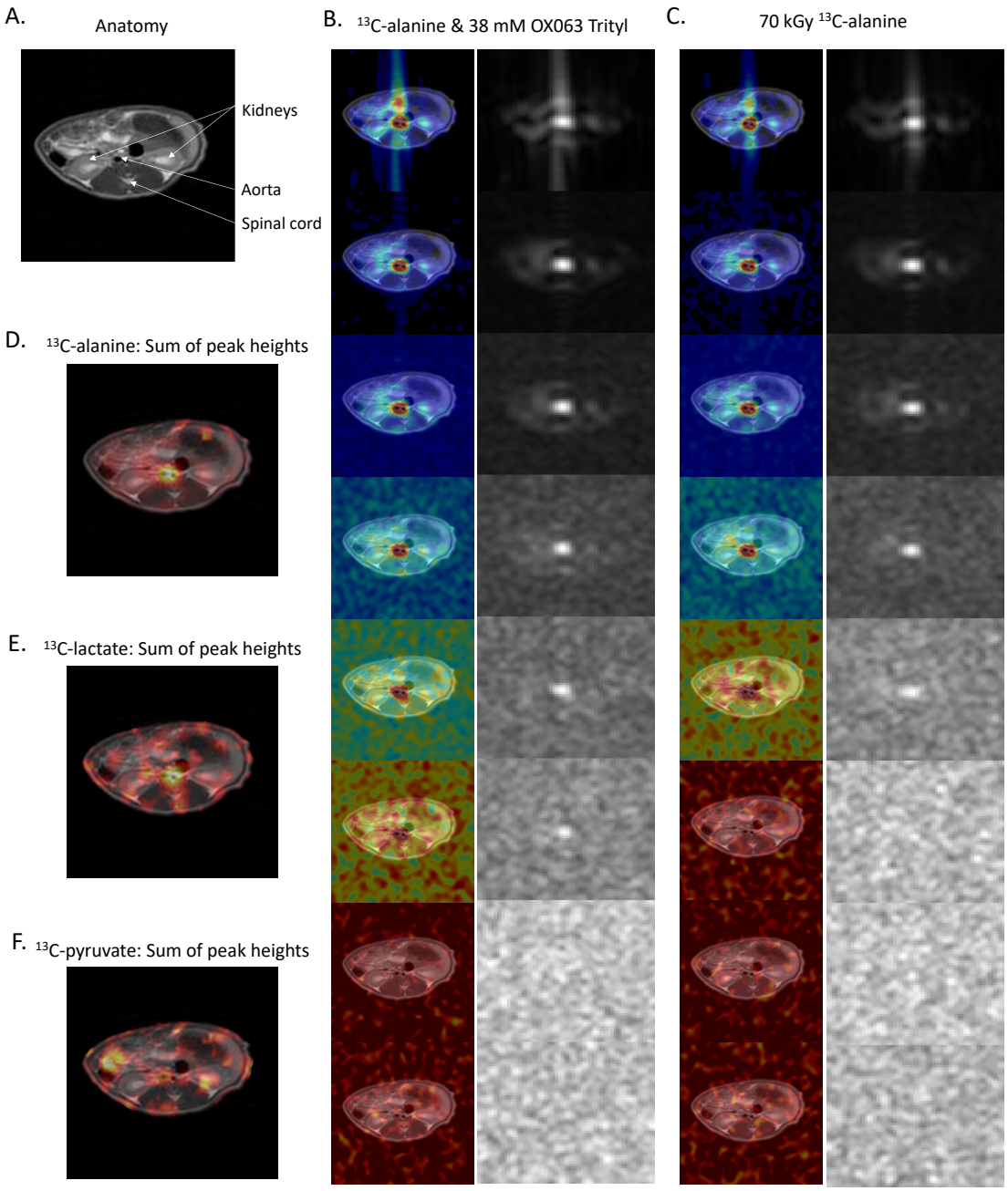

Figure 4.24: Comparison of exogenous and endogenous radicals: MRSI
A) A proton image acquired in the axial plane for anatomical reference. The ^{13}C-alanine signal recorded at each time point from the B) non-irradiated and C) 70 kGy irradiated samples indicating the distribution of ^{13}C-alanine *in vivo*. Two versions are shown where one is overlaid with the anatomical image for reference. Following the summation of the second and third time points, maps of the peak height of D) ^{13}C-alanine, E) ^{13}C-lactate, and F) ^{13}C-pyruvate were generated.

4.6.0.4 Discussion

The *in vivo* administration of an alanine HCA polarised via radicals generated by e-beam irradiation was demonstrated for the first time. The injection of hyperpolarised [1-^{13}C]-alanine into a healthy rat model has previously been investigated by Hu *et al.* where a liquid state polarisation of 12.6% at the point of dissolution and an *in vitro* T_1 of 41.5 s was recorded at 3 T[23]. Here, the hyperpolarisation of alanine using irradiation induced radicals generated comparable results; polarisation levels of 12.4% and 17.7% were recorded at the point of dissolution and the extracted nuclear T_1 relaxation times were 63.5 s and 77.3 s at 1.4 T. A nuclear T_1 measurement from one of the non-irradiated alanine samples was unsuccessful due to there not being enough volume of dissoluted sample for both the *in vivo* and *in vitro* experiments and hence, the *in vivo* scan was prioritised. The nuclear T_1 value that was extracted was 40.8 s which suggests a potential prolongation of the nuclear T_1 relaxation time following the use of irradiation generated radicals due to their quenching upon dissolution. The dissolution media, however, was different for these two sample types. The 70 kGy alanine samples might have benefited from the deuteration of its media which could potentially have led to further improvement in the relaxation properties of the liquid state samples. The pH of the irradiated alanine samples of approximately 7 is within the optimal pH range for the bolus dosing of substrates *in vivo* and was also within the pH range of 6.7–8 established by quality control criteria for a previous clinical study[97, 98].

Overall, the spectra acquired from the slice-selective spectroscopic scans from both samples showed a large peak at the expected frequency for alanine which decayed over time. The spectra acquired from the irradiated alanine sample during the slice-selective spectroscopic scan appeared to have approximately double the peak height even though a lower polarisation level was recorded compared to the non-irradiated alanine sample that was later injected into the same rat. This can partially be explained by a difference in timings between the dissolution and the start of the MR scan — it took 28 s and 25 s for the non-irradiated and irradiated alanine samples, respectively — in conjunction with a potentially shorter nuclear T_1

relaxation time as suggested by the *in vitro* data. As the relationship between T_1 relaxation and magnetic field strength is non-linear, this observation could also potentially be due to differences in the T_1 in the absence of a high magnetic field strength in areas outside the polariser and NMR benchtop spectrometer[99]. The transport of samples between the polariser and MR scanner included regions outwith the 5 gauss lines whereas the transport of the samples between the polariser and benchtop NMR spectrometer took place within the same room. Thus, the current nuclear T_1 relaxation time measurements may not have been sensitive to this. To investigate the effect of sample transport to another room, nuclear T_1 relaxation measurements could be taken at different intervals from different aliquots with each aliquot having been exposed to a low magnetic field strength for different time intervals. Additionally, there was no obvious cause for the phase shift of the first two spectra acquired from the non-irradiated alanine sample and thus, it is suspected to be flow related. Lastly, there also appeared to be a detection of ^{13}C-lactate and ^{13}C-pyruvate, however, the quantification of metabolite ratios was unsuccessful due to low SNR which resulted in difficulty in fitting the spectra. Specifically, upon running the purpose written MATLAB script, the pyruvate peaks could not be identified even when fitting with constraints.

In terms of the MRSI data, there was no difference in the time taken for the dissolution process preceding each scan; both HCAs were injected 33 s after the dissolution was started. It was noted that, in both cases, downstream metabolite production from ^{13}C-alanine was relatively minimal in the healthy anaesthetised animal, and not much metabolism was visible, however, the distribution of ^{13}C-alanine itself approximately mirrored the gross anatomy of the rat, as might be expected if it were acting solely as a perfusion agent.

As this was the first study using [1-^{13}C]-alanine polarised via irradiation induced radicals it was not known if the signal would be detectable *in vivo*. Hence, the FAs and TRs for both the slice-selective spectroscopic and MRSI scans had been chosen to give the best possible chance of detection of ^{13}C-alanine. Having now demonstrated the feasibility of using such samples *in vivo*, a smaller FA could be

employed in future studies to preserve the ^{13}C polarisation and potentially lead to greater ^{13}C-lactate and ^{13}C-pyruvate signals.

4.7 Conclusion

This work demonstrated the feasibility of hyperpolarising [1-^{13}C]L-alanine via radicals generated in situ by high energy electron irradiation and spectra were recorded both *in vitro* and *in vivo*. Ultimately, further investigation is required to elucidate the polarisation transfer mechanism(s) underlying these results. Nevertheless, this method of generating persistent radicals in the solid state could potentially be used for the polarisation of other solid agents whilst — due to the simple sample composition and the nonpersistent nature of the radicals in solution — removing the need for filtering samples during dissolution and potentially facilitating the prolongation of the liquid state nuclear T_1 relaxation time at room temperature. Additionally, this method offers flexibility with regards to the radical concentration as adjustments to irradiation dose can be easily made during the irradiation procedure, during which samples are simultaneously sterilised. The clinical application potential of hyperpolarised [1-^{13}C]L-alanine is vast as its use would be synonymous to that of [1-^{13}C]-pyruvate which is currently undergoing clinical translation[100–102].

This is a bit of a hellish thing to do FYI but obviously needs doing

— Jack J. J. J Miller

5

^{15}N - Hyperpolarised Urea

Contents

5.1 Background 169
5.2 Chapter overview 171
5.3 Chapter aims 172
5.4 Tuning and matching circuit 172
5.4.0.1 Background 172
5.4.0.2 Introduction 172
5.4.0.3 Methods 173
5.4.0.4 Results 174
5.4.0.5 Discussion 175
5.5 Sample optimisation 177
5.5.0.1 Background 177
5.5.1 Solvent 177
5.5.1.1 Introduction 177
5.5.1.2 Methods 178
5.5.1.3 Results 179
5.5.1.4 Discussion 181
5.5.2 Radical 182
5.5.2.1 Introduction 182
5.5.2.2 Methods 182
5.5.2.3 Results 183
5.5.2.4 Discussion 184
5.5.3 Concentration of gadolinium 186
5.5.3.1 Introduction 186
5.5.3.2 Methods 186
5.5.3.3 Results 187
5.5.3.4 Discussion 188
5.5.4 Glassing matrix 189
5.5.4.1 Introduction 189

5.5.4.2 Methods . . . 189
5.5.4.3 Results . . . 190
5.5.4.4 Discussion . . . 192
5.5.5 Dual-labelling . . . 192
5.5.5.1 Introduction . . . 192
5.5.5.2 Methods . . . 193
5.5.5.3 Results . . . 193
5.5.5.4 Discussion . . . 195
5.6 Liquid-state polarisation . . . 196
5.6.0.1 Background . . . 196
5.6.0.2 Introduction . . . 196
5.6.0.3 Methods . . . 196
5.6.0.4 Results . . . 199
5.6.0.5 Discussion . . . 203
5.7 *In vivo* study of perfusion . . . 204
5.7.0.1 Background . . . 204
5.7.0.2 Introduction . . . 204
5.7.0.3 Methods . . . 205
5.7.0.4 Results . . . 207
5.7.0.5 Discussion . . . 214
5.8 Conclusion . . . 214

5.1 Background

The research described within this final results chapter explores the development and application of a hyperpolarised perfusion agent. Similar to the assessment of metabolism, the assessment of tissue perfusion properties — that is, how fluid flows in the body to a tissue of interest — can inform patient treatment planning. Clinically, the measurement of perfusion is typically done using nuclear imaging techniques involving the use of a radioactive tracer such as $H_2{}^{15}O$, or by the administration of lanthanide metal chelates, predominantly gadolinium based, via the administration of a bolus during contrast-enhanced MR imaging. Whilst there is the obvious disadvantage of radioactivity associated with the former, concerns have been raised following observations of gadolinium deposits in patient tissue [103]. Using MRI, there are alternative approaches such as Arterial Spin Labeling (ASL) techniques for which an exogenous contrast bolus is not required yet, these have mostly been used as research tools and have not been as readily adopted

into the clinic primarily due to comparably lower SNR[104]. Low SNR leads to longer acquisition times and hence, an increased sensitivity to patient motion. Much research has been focused on reducing this through the development of new acquisition schemes and the incorporation of post-processing methods but the clinical application of ASL remains predominantly constrained to the brain[105].

One known adverse effect of the administration of gadolinium is nephrogenic systemic fibrosis. This condition can be fatal and has been observed in patients with renal failure who cannot clear gadolinium-based contrast agents (GBCAs) efficiently[106]. Consequences arising from deposits and prolonged exposure to gadolinium in other tissues have not been reported but the accumulation of the Gd^{3+} ion has been shown to occur regardless of normal renal function[107, 108]. Furthermore, the extent of accumulation appears to depend on the structure of the gadolinium chelate; Tweedle *et al.* found that chelates with a macrocyclic structure released fewer Gd^{3+} ions than linear chelates[109]. There is, however, some evidence to suggest that the detection of gadolinium in the brain following an MR scan does not necessarily identify a gadolinium deposit. Rather, the presence of GBCAs in the glymphatic pathway could be due to their clearance from the brain, a process that was shown to take up to six months in rodent studies[110]. Nevertheless, the differences observed following administration of different GBCAs and the mounting evidence of gadolinium deposits within extracranial tissue has prompted reviews by different medical regulation bodies. Notably, the European Medicines Agency recommended the restriction of three GBCAs and the suspension of authorisation for others[111]. Despite there being no current evidence to suggest that the deposits lead to impaired function of the host tissue, their impact over the average human lifespan is still to be assessed. There are also concerns regarding the release of Gd^{3+} ions and the impact this could have on the environment[112]. With millions of scans taking place worldwide every year, there is demand for the development of alternative tracers that are non-toxic and metal-free. Among those proposed, hyperpolarised non-metabolic compounds are attractive candidates.

To date, the majority of research involving hyperpolarised MR for perfusion measurements has been conducted with ^{13}C-urea HCAs. The feasibility of ^{13}C-urea in delivering perfusion measurements comparable to gadolinium-enhanced imaging has previously been demonstrated in a cardiac imaging study conducted by Fuetterer *et al.*[113]. The T_1 relaxation times of ^{13}C-labelled compounds, however, are notoriously short (∼60 s) in comparison with the time scale of many physiological processes[114]. Another metabolically inactive HCA known as HP001 (bis-1,1-(hydroxymethyl)-[1-^{13}C]cyclopropane-d_8) was engineered to have a long nuclear T_1 relaxation time (∼95 s ex vivo and ∼32 s *in vivo*) yet, urea-based HCAs have retained greater interest due to the ability to co-polarise with pyruvate for the simultaneous assessment of perfusion and metabolism[115, 116]. Moreover, there are fewer toxicity concerns surrounding urea due to its natural occurrence within the human body and an LD_{50} of (∼8.5 g/kg) in rats. Hyperpolarised water is an alternative endogenous compound but it suffers from a rapid nuclear T_1 relaxation time (∼5 s)[117].

One method found to lengthen the T_1 relaxation time of ^{13}C-urea is dual-labelling with ^{15}N[118]. This finding, among other factors, has drawn interest to the use of single-labelled $^{15}N_2$-urea as a perfusion marker instead. Such factors include: the ability to label each urea molecule with two ^{15}N nuclei as opposed to one ^{13}C, and the comparably long room temperature T_1 relaxation times (200 – 800 s) recorded from ^{15}N nuclei in a variety of compounds[119]. In general, the T_1 relaxation times of ^{15}N nuclei are typically longer than those recorded from ^{13}C nuclei[120]. Despite this, the preclinical development of $^{15}N_2$-urea (and other ^{15}N-labelled HCAs) has been limited due, in part, to the inability to monitor ^{15}N solid-state polarisation and low sensitivity caused by the low gyromagnetic ratio of ^{15}N[121].

5.2 Chapter overview

This chapter focuses on the development of $^{15}N_2$-urea as a hyperpolarised perfusion agent and seeks to address the current limitations impeding its clinical

translation, culminating in a proof of concept study where the optimised set-up was tested *in vivo*.

5.3 Chapter aims

The following aims were addressed:

- Directly monitor ^{15}N NMR signal during DNP
- Optimise the solid state polarisation of $^{15}N_2$-urea
- Record the liquid state polarisation of a $^{15}N_2$-urea sample
- Use ^{15}N hyperpolarised MR imaging to assess perfusion in a model of stroke

5.4 Tuning and matching circuit

5.4.0.1 Background

Having a means to directly measure ^{15}N polarisation would likely accelerate the preclinical development of ^{15}N probes as it would allow for dynamic information relating to the build-up rate and/or build-up amplitude in response to changes in the DNP protocol to be more readily observed. This could be done by using a tuning and matching (T&M) circuit connected to a polariser. Hence, to monitor ^{15}N polarisation during DNP, a T&M circuit was designed and constructed.

5.4.0.2 Introduction

There are different types of T&M circuits which vary in their complexity, however, for DNP applications often a simple network, such as a L-network, T-network, or π-network is suitable. The rationale behind using one of these circuits includes the availability of capacitors at large discrete values of capacitance that minimises the parasitic element inherently possessed by all electrical components[122].

Here, a low pass π-network was selected and designed at the nuclear Larmor frequency of ^{15}N at 3.35 T (14.5 MHz). LC circuits, such as that used for the ^{29}Si T&M circuit, are more versatile and can be adapted for different frequency

responses but a low-pass π-network was selected for the ^{15}N T&M circuit to enable the fewest losses. Additionally, the availability of the ^{29}Si and ^{13}C T&M circuits designed at higher frequencies meant there was less need for an adaptable frequency response feature.

5.4.0.3 Methods

First, the complex impedance of the NMR coil within the polariser (i.e. the load impedance) was measured using a network analyser and plotted on a Smith chart. A path was then mapped out, starting from the load impedance, to the centre of the Smith chart which represents a reflection coefficient of zero (i.e. matched impedance with the source). The route of the path was partially predetermined by the choice of circuit and the distance between the load impedance and circles of constant reactance and resistance. A low pass pi-network comprises a capacitor in parallel, an inductor in series, and another capacitor in parallel. Thus, the trace could be split into three sections where each section corresponded to a component of the circuit. The lengths of each section could then be converted into capacitive reactances (X_C) or an inductive reactance (X_L) using equation 5.1.

$$X_C/X_L = \Delta X \cdot 50\,\Omega = \frac{1}{\Delta B \cdot 50\,\Omega} \tag{5.1}$$

Here, ΔX corresponds to the change in reactance and ΔB corresponds to the change in susceptance of a component. The value of the constant arises from the desire to take the complex load impedance (the impedance of the NMR coil within the polariser) and transform it into the system impedance (the characteristic impedance of both commonly-used transmission lines and the Varian console) of $50\,\Omega$.

From the capacitive and inductive reactances, the value of each circuit component (i.e. capacictors and inductor) was computed using Equations 5.2 or 5.3.

$$C = \frac{1}{2\pi f X_C} = \frac{1}{\omega X_C} \tag{5.2}$$

$$L = \frac{X_L}{2\pi f} = \frac{X_L}{\omega} \tag{5.3}$$

Finally, using the network analyser, the effect of transmission line lengths were taken into account and the reflection coefficient (S_{11}) recorded. A measure of the reflected power was then obtained using Equation 3.2.

To find the conversion between the RF PW and the resulting FA, each sample was polarised for 60 minutes and then, in the absence of microwave irradiation, a series of increasing PWs (10 μs, 20 μs, and 30 μs) were applied at a transmit power of 55 dB. The resulting spectra were passed through a MATLAB script where each spectrum was apodised, underwent baseline correction, and integrated to find the NMR signal intensity. The average NMR signal intensity at each acquisition was determined and plotted. This data was then fitted using Equation (2.3) and a FA calibration factor was extracted using regression analysis.

5.4.0.4 Results

The complex impedance of the coil within the polariser measured at 14.45 MHz (the nuclear Larmor frequency of ^{15}N at 3.35 T) was $(10 + 74i)\Omega$. The trace from this load impedance to the centre of the Smith chart, the circuit diagram, and a photo of the constructed circuit are shown in Figure 5.1.

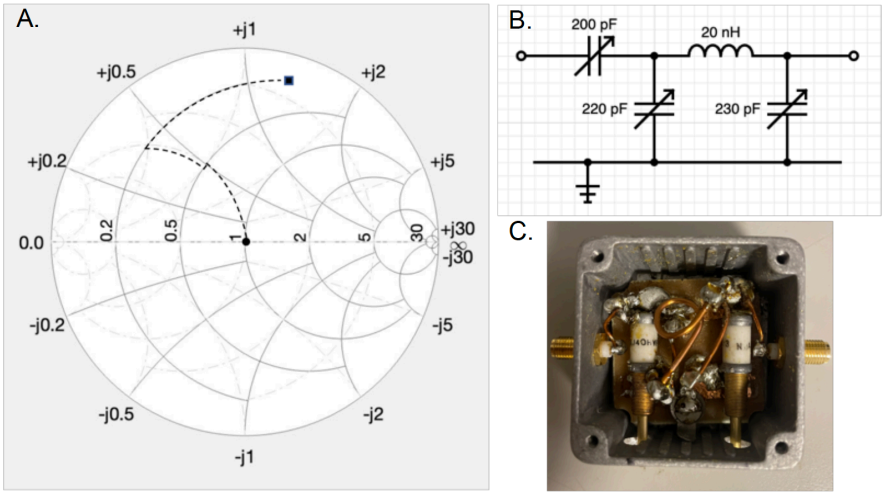

Figure 5.1: Smith chart trace
A) The complex impedance of the coil within the polariser (measured at 14.45 MHz) was plotted on the Smith chart (black square) and a trace was mapped to the centre of the Smith chart. The trace followed a path that enabled the design of a low pass pi-network. The circuit design and the corresponding constructed circuit are shown in B) and C), respectively.

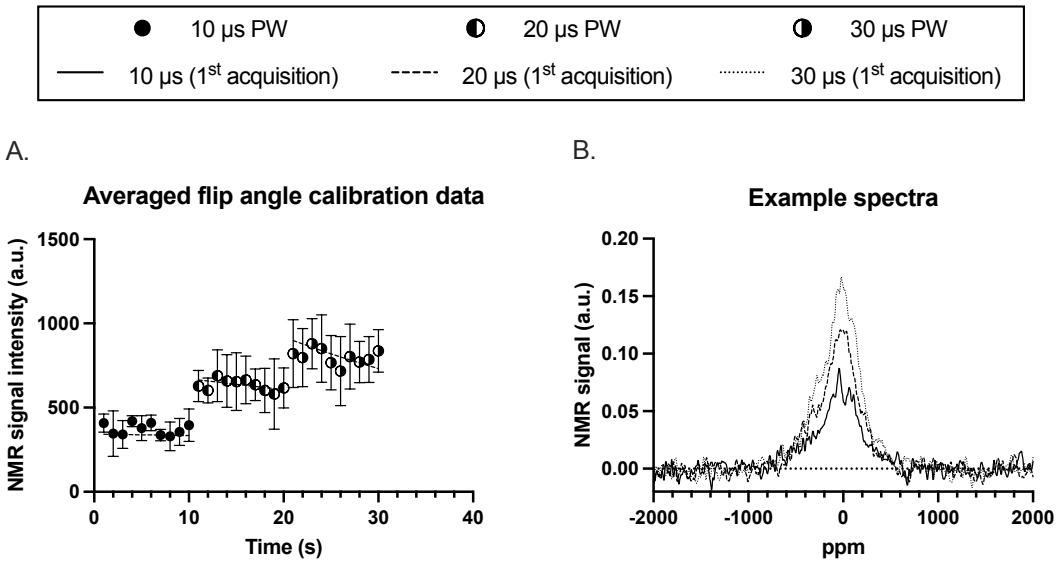

Figure 5.2: Flip angle calibration
A) The average of $n = 3$ flip angle calibrations for a polarised urea sample is summarised as a dot plot. To find the conversion between the radio frequency pulse width and the resulting flip angle, each sample was polarised for 60 minutes and then, in the absence of microwave irradiation, a series of increasing pulse widths (10 μs, 20 μs, and 30 μs) were applied. The average flip angle calibration factor was extracted using regression analysis and found to be $0.40 \pm 0.03\,^\circ/\mu$s at 55 dB. Dot plot shows the average of $n = 3$. Bars display mean ± SD. B) The first spectra acquired with each PW are shown.

The reflection coefficient of the constructed circuit was measured to be -26.0 ± 0.1 dB, comparable to that recorded from the ^{29}Si T&M circuit (-23.2 ± 0.1 dB). Using Equation 3.2 this converted to less than 1% reflected power. The flip angle calibration for a polarised $^{15}N_2$-urea sample is summarised in Figure 5.2. The extracted FA calibration factor was found to be $0.40 \pm 0.03\,^\circ/\mu$s at 55 dB.

5.4.0.5 Discussion

A T&M circuit optimised for recording ^{15}N signal was designed and built to facilitate the direct monitoring of ^{15}N solid state polarisation. Consequently, any changes to the build-up rate and/or build-up amplitude in response to changes in the DNP protocol would be more readily observed. This information could not be directly inferred from transferring samples to the MR scanner and recording the ^{15}N NMR signal there instead. Additionally, large losses of polarisation can occur during sample transfer and these losses can occur at different rates for

different samples.

An important consideration in designing a T&M circuit that is remote to the load (as was the case here) is the losses due to the transmission line. Here, two transmission lines were required: the first measured approximately 0.6 m from the T&M circuit to the insert of the polariser, and the second measured approximately 20 m which connected the T&M circuit to the spectrometer console. This set up is inefficient as losses can occur due to resistance along the coaxial cables, however, the polariser could not be moved closer to the spectrometer console or vice versa. Nevertheless, the circuit was well tuned and matched as the reflection coefficient converted to less than 1% reflected power. Furthermore, having the T&M circuit positioned exterior to the polariser enabled the circuit to be swapped for other T&M circuits which allowed for other nuclei be monitored as was done for each of the chapters of this thesis.

5.5 Sample optimisation

5.5.0.1 Background

Following the detection of ^{15}N polarisation using the custom designed and constructed T&M circuit, work focused on finding the optimal sample preparation for $^{15}N_2$-urea. For this, the factors considered were: the solvent, radical, glassing matrix, gadolinium content, and isotope labelling. Each of these factors forms its own subsection within this section.

5.5.1 Solvent

5.5.1.1 Introduction

It has previously been reported that deuteration prolongs the T_1 relaxation of ^{15}N sites through lowering the number of dipole-dipole interactions between NMR active nuclei[120]. This can be achieved either through direct deuteration of the ^{15}N nuclei and their neighbouring sites or by exploiting the exchangeable properties of labile protons in solvents by dissolving the compound in D_2O[123]. Thus, to test the effect of deuteration on the polarisation of $^{15}N_2$-urea, $^{15}N_2$-urea samples were prepared using either H_2O or D_2O as the solvent. The phenomenon of the hydrogen-deuterium exchange has been extensively studied and reported for non-enriched amino groups using mass spectroscopy and occurs due to the presence of a lone pair of electrons in the nitrogen atom[124]. Hence, when prepared in a D_2O-based mixture, it was hypothesised that the protons on the ^{15}N nuclei of a urea molecule would be preferentially exchanged for deuterons. Additionally, to test whether any change in the build-up amplitude or build-up rate was due to the direct binding of deuterons to the ^{15}N site, the same experiments were repeated using sodium ^{15}N-nitrate; a compound which has no labile protons available for deuteration (Figure 5.3).

A decrease in the rate of T_1 relaxation was expected upon preparing $^{15}N_2$-urea samples in D_2O as the strength of dipolar coupling (D) between two nuclei is proportional to their respective gyromagnetic ratios (γ_i and γ_j) [125]:

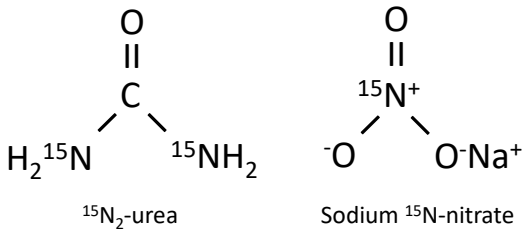

Figure 5.3: ^{15}N compounds and their structures
The effect of deuteration was explored as a tool in the optimisation of $^{15}N_2$-urea polarisation. Samples were prepared using either H_2O or D_2O as the solvent. The effect was assessed using sodium ^{15}N-nitrate as a control molecule as it has no labile protons available for deuteration.

$$D_{i,j} = -\frac{3\gamma_i\gamma_j\hbar\mu_0}{8\pi^2R^3}\cos^2(\theta) - \frac{1}{3} \tag{5.4}$$

where $\hbar$ is the reduced Planck's constant, μ_0 is the vacuum permeability constant, R is the distance between the nuclei, and θ is the angle of the vector between the two nuclei with respect to the direction of the external magnetic field vector. The gyromagnetic ratio of a proton (42.5 MHz/T) is approximately six times greater than that of the deuteron (6.5 MHz/T). Hence, hydrogen-deuterium exchange would lead to a reduction in dipolar coupling and, as it is the dominant relaxation pathway, the lengthening of the nuclear T_1 relaxation time.

5.5.1.2 Methods

Two different $^{15}N_2$-urea samples were prepared, one with H_2O as the solvent and the other with D_2O. Two ^{15}N-sodium nitrate samples were also prepared this way.

To make the $^{15}N_2$-urea DNP samples, 186.6 mg of a 0.4:0.6 glycerol:D_2O (w/w) or 0.4:0.6 glycerol:H_2O (w/w) mixture was pipetted onto 70.9 mg of $^{15}N_2$-urea. The difference in densities between H_2O and D_2O was taken into consideration when determining the mass of radical to add. The mixture was made into a 15 mM radical concentration stock solution by adding the appropriate mass of OX063 Trityl (MW = 1427 g/mol) to the total volume.

To make the sodium ^{15}N-nitrate DNP samples, 210.4 mg of a 7.5 M $Na^{15}NO_3$ stock solution was mixed with 64.6 mg of glycerol. Two 7.5 M $Na^{15}NO_3$ stock

solutions were made, one with each solvent (D_2O or H_2O). The mixture was made into a 15 mM radical concentration stock solution by adding the appropriate mass of OX063 Trityl to the total volume.

For either sample preparation, 150 μl of the final mixture was pipetted into a sample cup and the sample mass recorded.

The optimal microwave frequencies for monitoring polarisation build-up were identified from the microwave frequency sweep profiles for each sample. The samples were then irradiated for at least 90 minutes at their respective optimal microwave frequency. The build-up of polarisation at this frequency was monitored every 5 minutes using a PW of 5 μs at 55 dB (equivalent to a 2° FA).

For analysis, all spectra were passed through a MATLAB script where each spectrum underwent baseline correction and was integrated to find the NMR signal intensity. The build-up amplitudes and build-up times were extracted from the build-up profiles by fitting with a monoexponential (Equation 2.7). All the data was corrected for the concentration of each ^{15}N compound, sample mass, and the number of ^{15}N nuclei.

5.5.1.3 Results

The results are summarised in Figure 5.4. The microwave frequency sweep profiles recorded from the $^{15}N_2$-urea and sodium ^{15}N-nitrate samples were found to be similar in shape and had the same optimal microwave frequencies (Figure 5.4A and B). For both ^{15}N-labelled compounds, the optimal microwave frequency appeared to shift by ~10 MHz when D_2O was used as the solvent. An increase in NMR signal intensity with time was recorded for all samples during the monitoring of the build-up profiles (Figure 5.4C and D). The polarisation constants extracted from the build-up profiles (Figure 5.4E and F) are summarised in Table 5.1. A significant increase in the build-up amplitude was recorded from $^{15}N_2$-urea samples containing D_2O compared to those containing H_2O ($p=0.0195$). In contrast, no significant change in the build-up amplitude of sodium ^{15}N-nitrate samples was recorded.

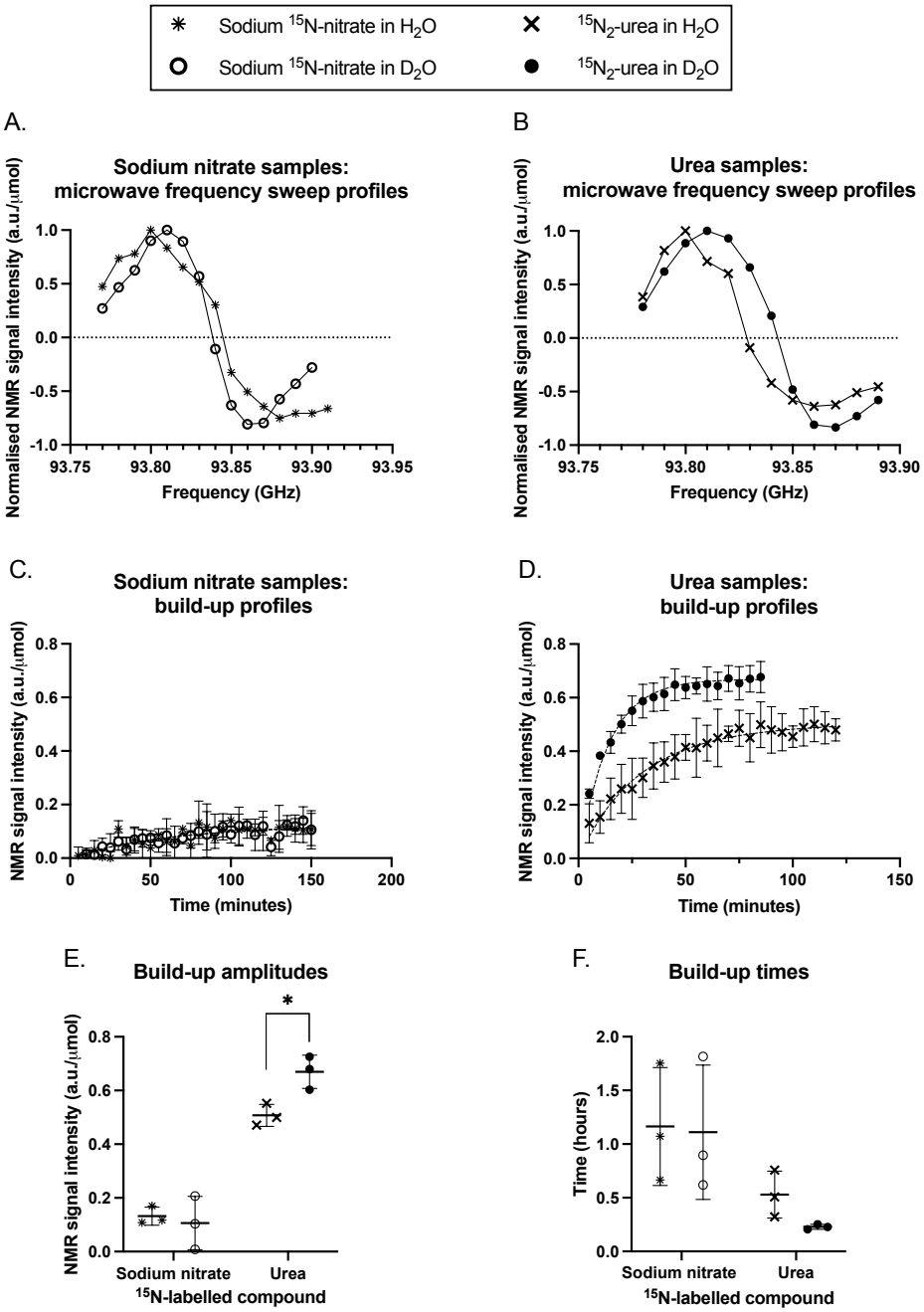

Figure 5.4: Effect of deuteration
The frequency sweep profiles from A) urea and B) sodium nitrate samples were found to be similar in shape. The build-up profiles C) and D) showed an increase in NMR signal intensity over time for all samples. A significant increase in the build-up amplitude (E) was recorded when D_2O was used as the solvent for the urea samples (p=0.0195) whilst no significance in the build-up amplitudes of sodium ^{15}N-nitrate samples was found. No significant effect on the build-up times were recorded (F). Significance was calculated using a two-sample unequal variance t-test. Significance is shown as * when $p \leq 0.05$. Dot plots show the average of $n = 3$. Bars display mean ± SD.

Sample	Build-up amplitude (a.u./μmol)	Build-up time (hours)
$^{15}N_2$-urea with H_2O	0.51 ± 0.04	0.53 ± 0.22
$^{15}N_2$-urea with D_2O	0.67 ± 0.06	0.23 ± 0.02
Sodium $^{15}N_2$-nitrate with H_2O	0.13 ± 0.03	1.16 ± 0.55
Sodium $^{15}N_2$-nitrate with D_2O	0.13 ± 0.07	1.11 ± 0.63

Table 5.1: Polarisation constants: effect of solvent

5.5.1.4 Discussion

The use of D_2O appeared to improve the polarisation characteristics of $^{15}N_2$-urea samples compared to H_2O. Significantly greater signal enhancements were recorded from samples containing D_2O and the build-up time appeared to reduce. To elucidate whether this improvement was due to the direct binding of deuterons to the ^{15}N site or due to the presence of deuterons within the glassing matrix solution, the same data was acquired using sodium ^{15}N-nitrate samples. As hypothesised and in agreement with the literature, no significant change in the ^{15}N polarisation of sodium ^{15}N-nitrate was recorded upon use of D_2O[126]. Thus, the improvement recorded from the $^{15}N_2$-urea samples was attributed to the direct deuteration upon proton exchange of the ^{15}N site as opposed to the nearby deuterons within the glassing matrix solution.

Further improvements to the build-up amplitude could potentially have been recorded following the perdeuteration of $^{15}N_2$-urea samples. For example, with ^{15}N-choline, both Sarkar *et al.* and Kumagai *et al.* recorded a two-fold increase in the ^{15}N spin lattice relaxation time when the solvent and the carbon nuclei were perdeuterated compared to non deuterated samples that relied on the exchange of the protons through the deuterated solvent[127, 128]. Perdeuterated $^{15}N_2$-urea, however, was not commercially available. Thus, future optimisation should consider the preparation of such a compound through repeated freeze drying as done by Houliston *et al.*[129].

Another consideration was that the glycerol used in the sample preparation of the $^{15}N_2$-urea samples was itself not perdeuterated and thus, its protons might

in some way dilute the potential direct deuteration effect. This was henceforth investigated and the data is summarised within this section (Subsection 5.5.4).

Prior to this, the focus of this optimisation work turned to the choice of radical.

5.5.2 Radical

5.5.2.1 Introduction

As previously described and shown within this thesis (Chapter 3, Section 3.4.2), the choice of radical can influence the polarisation transfer mechanism that takes place during DNP and thus, the efficiency of DNP. As part of these different transfer mechanisms, DNP may be performed either directly or indirectly. The latter refers to the situation where there is an intermediate step in the polarisation process; another nuclei, such as ^{1}H, is first polarised and its polarisation is subsequently transferred to the nucleus of interest which typically has a lower gyromagnetic ratio[130]. Indirect DNP is most commonly employed as it has the advantage of generating large levels of polarisation amongst nuclei that are "more easily" polarised. That is, nuclei that exhibit large gyromagnetic ratios, are present in large concentrations, and, hence, form strongly coupled nuclear spin networks[131]. There are situations, however, where it is advantageous to use direct DNP, for example, it can be performed in the absence of ^{1}H nuclei. For nuclei with low gyromagnetic ratios such as ^{13}C and ^{15}N, direct DNP has typically been achieved through utilising narrow line width radicals to facilitate polarisation transfer[119].

Due to the improvement in ^{15}N polarisation recorded from $^{15}N_2$-urea samples following deuteration (Subsection 5.5.1), the direct polarisation of $^{15}N_2$-urea with structurally analogous Trityl radicals was explored here. The Trityl radicals of choice were OX063 and AH111501.

5.5.2.2 Methods

The work detailed here builds upon the optimisation work carried out in the previous subsection. For a detailed description of the sample preparation, DNP protocol, and data analysis refer to Subsection 5.5.1.2.

$^{15}N_2$-urea samples were made using the D_2O-based glassing matrix and a trace amount of gadolinium (1.3 mM) was included as part of the sample preparation. For this, 25 μl of a 1:50 Dotarem:D_2O mixture was added. This mixture was then made into a 15 mM radical concentration stock solution by dissolving the appropriate mass of radical to the total volume. The radicals used were OX063 Trityl (MW = 1427 g/mol) and its structural analogue AH111501 ("GE Trityl") (MW = 1595 g/mol). 150 μl of stock solution was pipetted into a sample cup, the sample mass recorded, and then inserted into the polariser.

5.5.2.3 Results

The results are summarised in Figure 5.5. Visually, signal enhancements appear to have been generated from samples containing the AH111501 radical compared to OX063 (Figure 5.5B). The shape of the microwave frequency sweep profiles appeared to be similar between the two sample types but the optimal microwave frequency was 10 MHz lower for samples that contained AH111501 (Figure 5.5A). An increase in NMR signal intensity over time was recorded from all samples during the monitoring of the build-up profiles (Figure 5.5B). Significant increases in the build-up amplitudes (Figure 5.5C) and build-up times (Figure 5.5D) were recorded from samples containing the AH111501 radical compared to samples containing OX063 ($p = 0.0121$ and $p = 0.0452$, respectively). This data appears to suggest that ^{15}N nuclei polarisation is affected by the choice of radical, even amongst those that are structurally analogous. The polarisation constants extracted from the build-up profiles are summarised in Table 5.2.

Sample	Build-up amplitude (a.u./μmol)	Build-up time (hours)
$^{15}N_2$-urea with OX063	0.67 ± 0.06	0.23 ± 0.02
$^{15}N_2$-urea with AH111501	1.62 ± 0.22	0.75 ± 0.20

Table 5.2: Polarisation constants: effect of radical choice

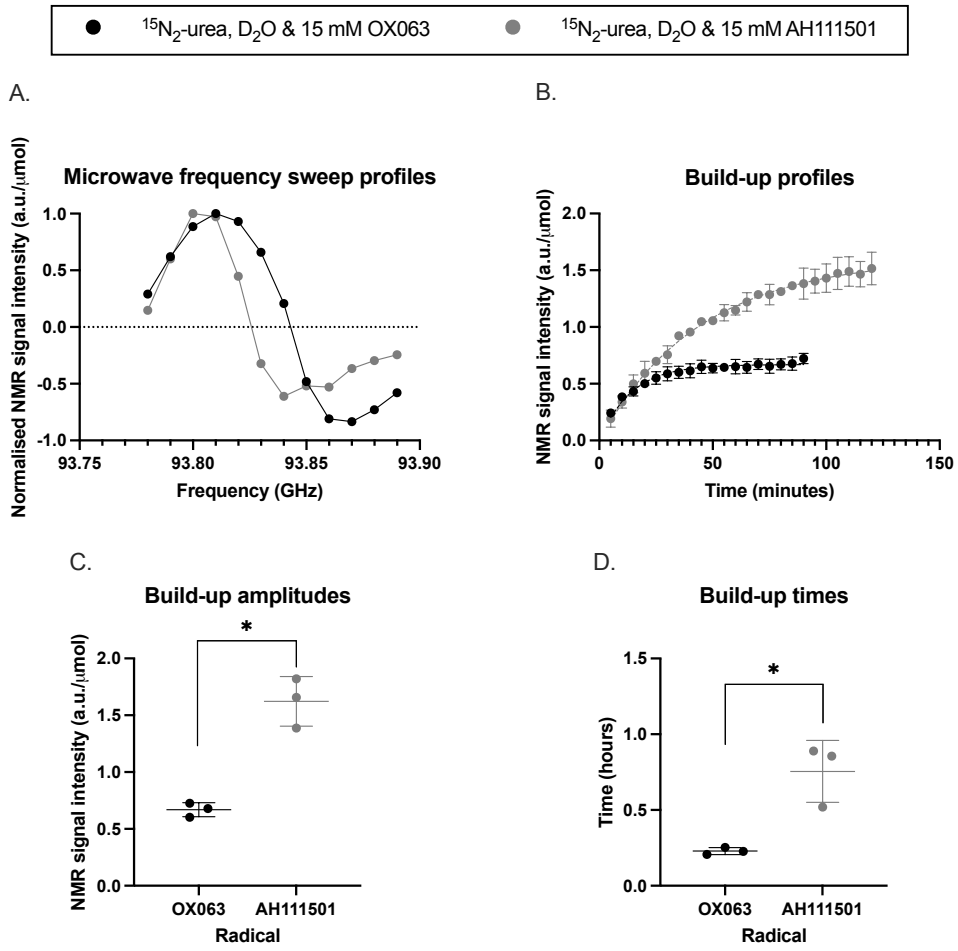

Figure 5.5: Effect of radical choice
The effect of radical choice in the generation of ^{15}N polarisation is summarised. As shown by A) representative microwave frequency sweep profiles, the shape of the profiles appeared similar between the two sample types but the optimal microwave frequency differed by 10 MHz. The build-up profiles B) showed an increase in NMR signal intensity over time for all samples. A significant increase in the C) build-up amplitude and D) build-up time was recorded from samples containing the AH111501 radical compared to those that contained OX063 (p=0.012 and p=0.045, respectively). Significance was calculated using a two-sample unequal variance t-test. Significance is shown as * when $p \leq 0.05$. Dot plots show the average of $n = 3$. Bars display mean ± SD.

5.5.2.4 Discussion

Significant differences in the polarisation characteristics between the two sample types were recorded. The reason behind the observed differences remains unclear, yet one potential explanation might be the differences in solubility between the two radicals. AH111501 is methylated OX063 (also known as OX063Me) and, in medicinal chemistry, methylation of a compound typically reduces its solubil-

ity[132]. Further investigation, however, is required to determine whether this plays a factor or not.

Another factor for investigation that was not explored here is the concentration of the exogenous radical compounds. The concentration of 15 mM was chosen as it has previously been shown to be the optimal concentration of these Trityl radicals for the d-DNP of [1-^{13}C]pyruvic acid and ^{13}C-urea samples at 3.35 T [3, 133]. Radical concentration is directly proportional to the EPR line width of the radical and, how this compares to the nuclear Larmor frequency, plays a role in polarisation transfer mechanism taking place during DNP[133]. The nuclear Larmor frequency of ^{13}C is more than double that of ^{15}N and hence, lower Trityl concentrations might have led to greater signal enhancements in a shorter time. Nevertheless, other studies directly polarising ^{15}N-labelled compounds with Trityl radicals also appear to use 15 mM concentrations at 3.35 T [120, 123, 128, 134, 135].

Greater signal enhancements might also have be achieved through using indirect DNP and broad line width radicals, such as those from the Nitroxide family.

Of the studies conducted using ^{15}N-based HCAs, both Trityl and Nitroxide radicals have been explored and — at the time of writing — all bar one generated modest polarisation enhancements (approximately 4%). The study that reported a significant improvement on these results was conducted by Milani *et al.* who recorded polarisations of 17-25% from various ^{15}N-labelled compounds (23% from $^{15}N_2$-urea) at room temperature using 50 mM TEMPOL[119]. To achieve this, however, a novel cross polarisation DNP probe was constructed which enabled simultaneous monitoring of ^{1}H and ^{15}N nuclei and an accompanying dedicated pulse sequence had to be applied. Furthermore, Sarkar *et al.* who used TEMPO to polarise ^{15}N-choline achieved a lower polarisation enhancements of 3.3%.

Finally, it must be noted that the signal enhancements generated here likely benefited from the presence of a trace amount of gadolinium (1.3 mM). The effect of incorporating this into the sample preparation was investigated next.

5.5.3 Concentration of gadolinium

5.5.3.1 Introduction

The overall aim of this work was to develop an alternative method for the measurement of perfusion that was less toxic than current methods i.e. through the use of a nonradioactive tracer that contained less or no gadolinium than that administered in clinical MR scans. Whilst researching methods to improve ^{15}N polarisation signal enhancements, the addition of trace amounts of gadolinium was reported to lead to significant improvements when used in conjunction with a Trityl radical. The proposed mechanism for this is a reduction in the electron spin-lattice relaxation time (T_{1e}) of the radical but with no effect on the nuclear spin-lattice relaxation time (T_1)[51]. During a clinical MR scan, if administering a GBCA, the concentration of gadolinium is on the order of $5-10$ mM[136]. Here, the effect of adding $0.7-1.9$ mM on the polarisation of $^{15}N_2$-urea was explored.

5.5.3.2 Methods

The work detailed here builds upon the optimisation work carried out in the previous subsections. For a detailed description of the sample preparation, DNP protocol, and data analysis refer to Subsection 5.5.1.2.

The basis of each sample comprised $^{15}N_2$-urea in the D_2O-based glassing matrix and 15 mM AH111501. The volume of the mixture was taken into account when determining the volume of Dotarem to add. Three 1:50 Dotarem:D_2O mixtures were made, each with a different concentration of gadolinium (0.7 mM, 1.3 mM, and 1.9 mM). The appropriate volume of a 1:50 Dotarem:D_2O mixture was added to the existing mixture. A fourth sample type that contained no Dotarem was also made. For each sample, 150 μl of stock solution was pipetted into a sample cup, the sample mass recorded, and then inserted into the polariser.

5.5.3.3 Results

The results are summarised in Figure 5.6. The shape of the microwave frequency sweep profiles appeared similar between the different sample types with the exception of the sample containing 0.7 mM gadolinium (Figure 5.6A). The optimal microwave frequencies appeared to differ, however, there was no clear link between this and the concentration of gadolinium (Figure 5.6B). The build-up profiles showed an increase in NMR signal intensity over time for all samples (Figure 5.6C). From the build-up amplitudes, the addition of gadolinium to the sample preparation appeared to aid ^{15}N polarisation (Figure 5.6D) and, from the build-up times (Figure 5.6E), a significant reduction was recorded between samples that contained no gadolinium and those that contained 1.9 mM (p=0.0395). The polarisation constants extracted from the build-up profiles are summarised in Table 5.3. This data would appear to suggest the addition of gadolinium leads to overall improvements in signal enhancement as has commonly been reported at 3.35 T.

Sample	Build-up amplitude (a.u./μmol)	Build-up time (hours)
$^{15}N_2$-urea with 0 mM gadolinium	0.40 ± 0.22	2.18 ± 1.95
$^{15}N_2$-urea with 0.7 mM gadolinium	1.50 ± 0.24	0.77 ± 0.34
$^{15}N_2$-urea with 1.3 mM gadolinium	1.62 ± 0.22	0.75 ± 0.20
$^{15}N_2$-urea with 1.9 mM gadolinium	1.43 ± 0.14	0.47 ± 0.01

Table 5.3: Polarisation constants: effect of gadolinium concentration

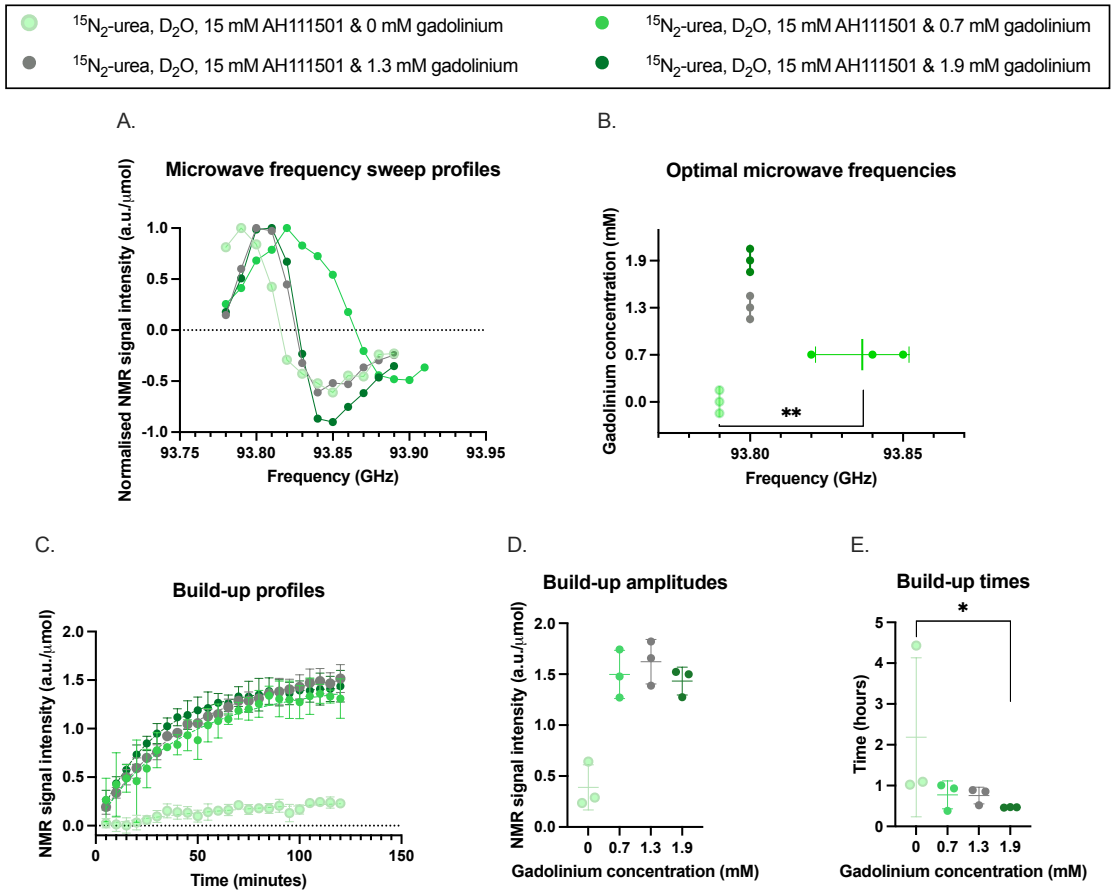

Figure 5.6: Effect of gadolinium concentration
The effect of gadolinium concentration in the generation of ^{15}N polarisation is summarised. A) As shown by representative microwave frequency sweep profiles, the shape of the profiles appeared similar between the different sample types. B) The optimal microwave frequency appeared to differ, however, there was no clear link between this and the concentration of gadolinium. C) The build-up profiles showed an increase in NMR signal intensity over time for all samples. From the D) build-up amplitudes, the addition of gadolinium to the sample preparation appeared to aid ^{15}N polarisation. From the E) build-up times, a significant reduction in the build-up time was recorded between samples that contained no gadolinium and those that contained 1.9 mM (p=0.0395). Significance was calculated using a Kruskal-Wallis test with Dunns multiple comparisons. Significance is shown as * when $p \leq 0.05$. Dot plots show the average of $n = 3$. Bars display mean ± SD.

5.5.3.4 Discussion

The optimal sample preparation was determined to be that which contained 1.3 mM Dotarem as this appeared to lead to an increase in signal enhancement and reduction in the build-up time. Although comparable polarisation characteristics were

extracted from the build-up profiles of the 0.7 mM Dotarem samples, there was no obvious source for the variability in the recorded optimal microwave frequency from the microwave frequency sweep profiles. By selecting the 1.3 mM Dotarem sample type for further study, the high consistency of the optimal microwave frequency opens the possibility for the future removal of the microwave frequency profile from the DNP protocol. The time saved from this could either be used for extending the duration of the polarisation build-up, or enable increased sample throughput by reducing the time required for the full DNP workflow.

Whilst the HCA would ideally contain no gadolinium, the concentrations used here would be further diluted prior to injection due to the dissolution step resulting in an overall reduction in gadolinium concentration compared to current clinical MR scans where 5 – 10 mM is administered[136]. Additionally, the signal enhancements generated from samples containing no gadolinium were likely too low for *in vivo* application and thus, the 1.3 mM samples were taken forward for further preclinical development.

5.5.4 Glassing matrix

5.5.4.1 Introduction

In Section 5.5.1, the potential for nondeuterated glycerol (used as part of the glassing matrix solution) to hamper the benefits provided by deuteration of the solvent was discussed. Here, the effect of full deuteration of the glassing matrix on the hyperpolarisation of $^{15}N_2$-urea is investigated.

5.5.4.2 Methods

The work detailed here builds upon the optimisation work carried out in the previous subsections. For a detailed description of the sample preparation, DNP protocol, and data analysis refer to Subsection 5.5.1.2.

$^{15}N_2$-urea samples with a glassing matrix comprising either a 0.4:0.6 glycerol:D_2O (w/w) or 0.4:0.6 glycerol-d8:D_2O (w/w) mixture were made with 15 mM AH111501. Taking into account the differences in densities in the glassing matrix solutions,

the appropriate volume of a 1:50 Dotarem:D_2O (v/v) mixture was added for a gadolinium concentration of 1.3 mM. For each sample, 150 μl of stock solution was pipetted into a sample cup, the sample mass recorded, and then inserted into the polariser.

5.5.4.3 Results

The results are summarised in Figure 5.7. The microwave frequency sweep profiles appeared similar in shape between the two sample types (Figure 5.7A). The optimal microwave frequency recorded from samples containing the deuterated glycerol samples, however, appeared to be 10 MHz higher. An increase in NMR signal intensity over time was recorded for all samples during the monitoring of the build-up profiles (Figure 5.7B). No significant differences in the build-up amplitudes or build-up times were recorded (Figure 5.7C and D). This data appears to show that full deuteration of the glassing matrix does not aid the polarisation of ^{15}N-urea beyond that achieved through direct deuteration of the ^{15}N-sites provided by the use of D_2O.

Sample	Build-up amplitude (a.u./μmol)	Build-up time (hours)
$^{15}N_2$-urea with glycerol	1.62 ± 0.22	0.75 ± 0.20
$^{15}N_2$-urea with glycerol-d_8	1.42 ± 0.19	1.37 ± 0.54

Table 5.4: Polarisation constants: effect of deuterated glycerol

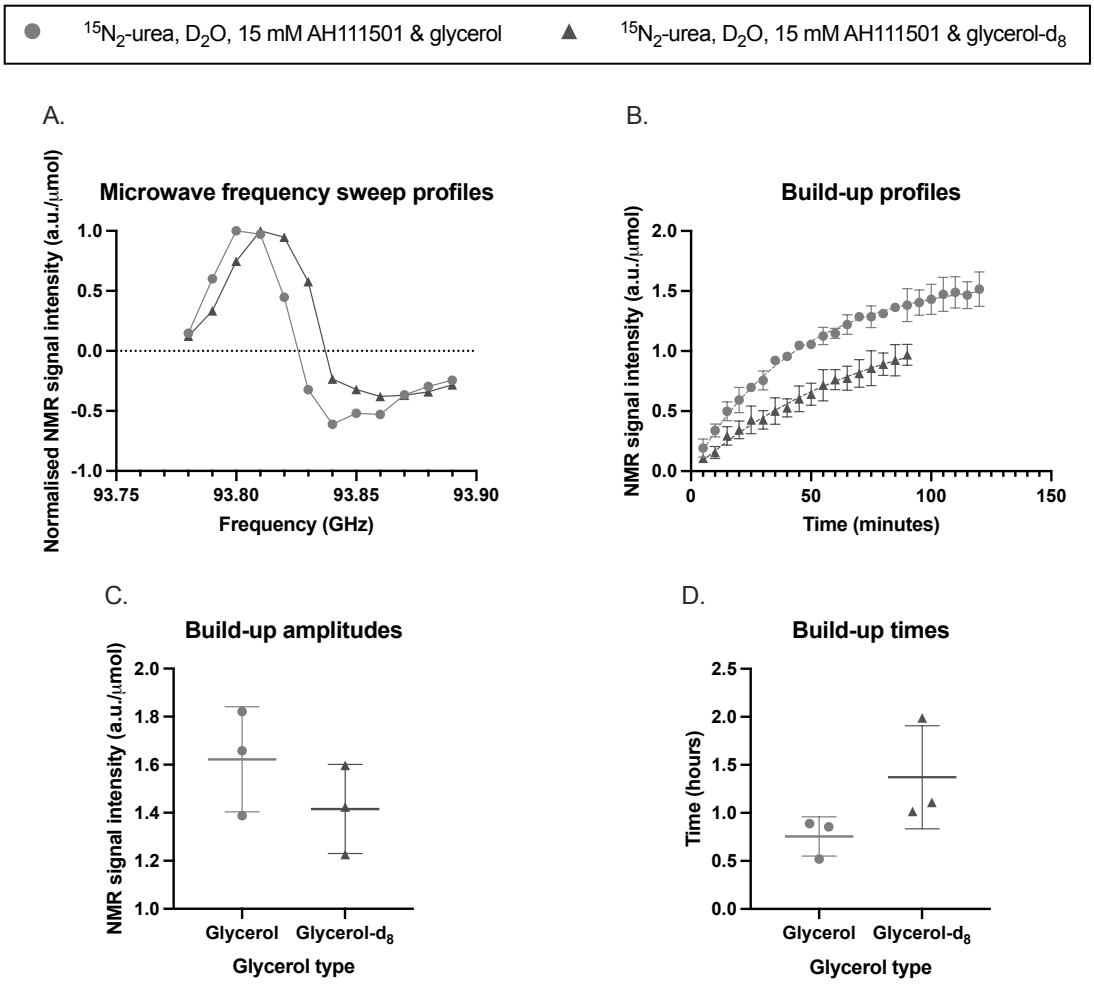

Figure 5.7: Effect of glycerol deuteration
The effect of deuteration of the whole glassing matrix in the generation of ^{15}N polarisation is summarised. As illustrated by A) representative microwave frequency sweep profiles, the shape of the profiles appeared similar between the two sample types, however, the optimal microwave frequency appeared to differ by 10 MHz. The build-up profiles B) showed an increase in NMR signal intensity over time for all samples. No significant differences in the C) build-up amplitudes or D) build-up times were recorded. Significance was calculated using a two-sample unequal variance t-test. Significance is shown as * when $p \leq 0.05$. Dot plots show the average of $n = 3$. Bars display mean ± SD.

5.5.4.4 Discussion

No significant differences between samples that contained fully deuterated glassing matrices and those that contained only a deuterated solvent were observed. In general, greater signal enhancements appeared to be recorded from samples that did not contain deuterated glycerol. Additionally, the use of glycerol-d8 appeared to lead to longer build-up times.

As part of this optimisation work, other glassing matrix compositions could have been explored. The glassing matrix composition used here (0.4:0.6 glycerol:D_2O) was based on the commonly used glassing matrix composition (also known as "DNP juice") comprising 60% glycerol-d8, 30% D_2O, and 10% H_2O but was altered to 40% D_2O due to the reported effects of deuteration on the T_1 of ^{15}N-labelled compounds. Additionally, a similar composition comprising only glycerol and D_2O had been reported in the literature for a $^{15}N_2$-urea sample[121].

5.5.5 Dual-labelling

5.5.5.1 Introduction

An inability to detect ^{15}N solid-state NMR signal within commercial polarisers means that many studies either do not report ^{15}N polarisation build-up or use ^{13}C-labelled compounds as markers of polarisation. For example, Gamliel *et al.* opted for using ^{13}C and ^{15}N dual-labelled urea with the former acting as a marker for ^{15}N polarisation[135]. Yet, to our knowledge, no study has investigated whether ^{13}C polarisation is an appropriate indicator of ^{15}N polarisation. Specifically, the optimal microwave frequency for ^{13}C might not be the optimal microwave frequency for the build-up of ^{15}N polarisation and the build-up rates between these two nuclei might differ. To date, one study reported using a T&M circuit to enable the monitoring of ^{15}N polarisation and different build-up rates between $^{15}N_2$-urea and $^{15}N_2$,^{13}C-urea monitored on ^{15}N were reported[137]. Using the custom T&M circuit built here, the suitability of ^{13}C as a marker for ^{15}N polarisation was investigated and the presence of ^{13}C on the polarisation characteristics of urea was also explored.

5.5.5.2 Methods

The work detailed here builds upon the optimisation work carried out in the previous subsections. For a detailed description of the sample preparation, DNP protocol, and data analysis refer to Subsection 5.5.1.2.

To make each DNP sample, 186.6 mg of a 0.4:0.6 glycerol:D_2O (w/w) mixture was pipetted onto 70.9 mg of $^{15}N_2$,^{13}C-urea or $^{15}N_2$-urea. The volume increase was taken into account when determining the volume of Dotarem to add for a final gadolinium concentration of 1.3 mM. Similarly, the appropriate mass of AH111501 ("GE Trityl") (MW = 1595 g/mol) was added to this mixture for a final radical concentration of 15 mM. For each sample, 150 μl of stock solution was pipetted into a sample cup, the sample mass recorded, and then inserted into the polariser.

5.5.5.3 Results

The results are summarised in Figure 5.8. The shapes of the microwave frequency sweep profiles appeared to be similar between the different sample types (Figure 5.8A). The optimal microwave frequency for the dual-labelled urea when monitored on ^{15}N was recorded to be 10 MHz higher than the other optimal microwave frequencies. The NMR signal intensity increased over time for all samples (Figure 5.8B and C) and greater signal enhancements appeared to be recorded whilst monitoring ^{15}N polarisation from single-labelled samples compared to the dual-labelled samples. No significant differences were identified, however, from the build-up amplitudes extracted from the build-up profiles whilst monitoring on ^{15}N. Yet, the build-up times were significantly reduced when urea was monitored on single labelled urea compared to dual-labelled. The polarisation constants extracted from the build-up profiles are summarised in Table 5.5 where they are also compared to the polarisation constants extracted from single-labelled samples.

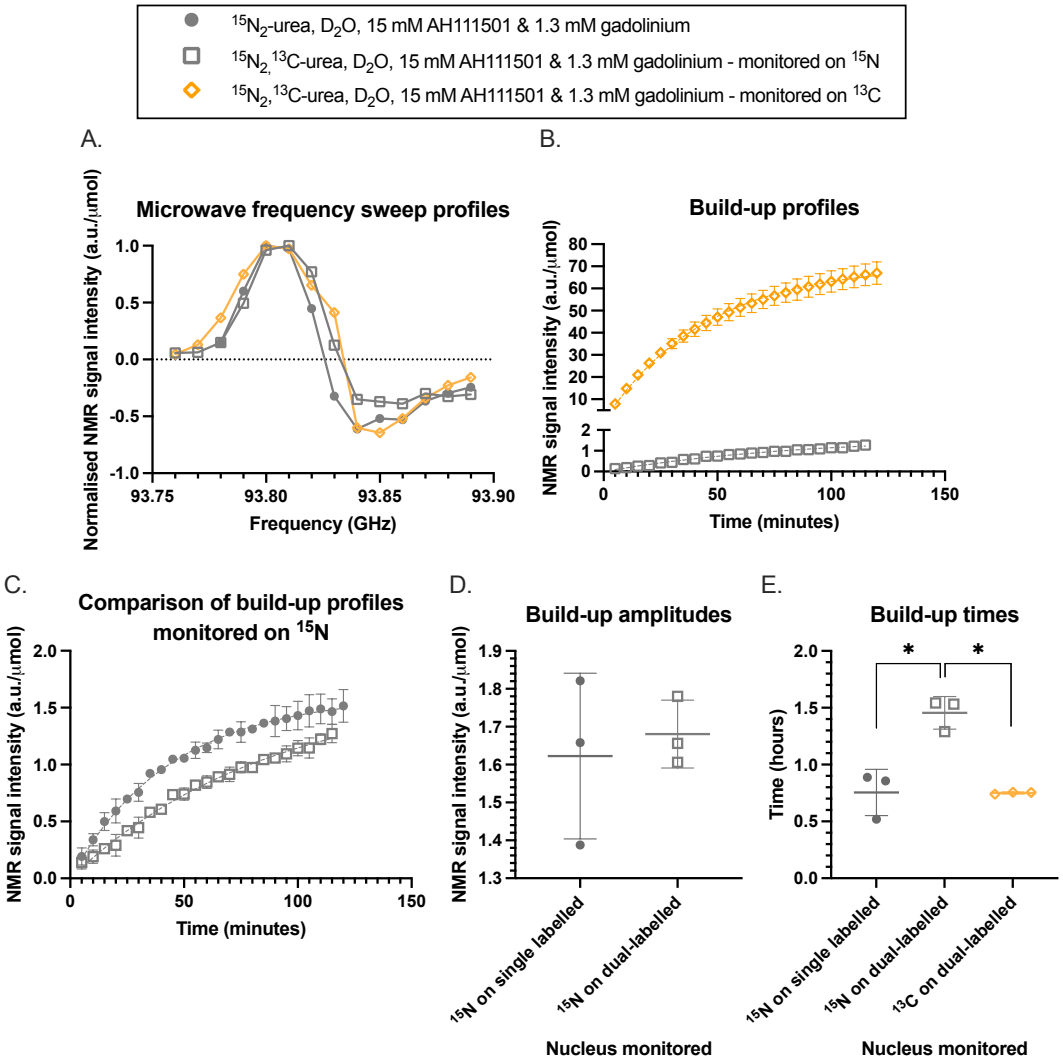

Figure 5.8: Effect of dual-labelling
The effect of dual-labelling is summarised by dot plots. As shown by A) representative microwave frequency sweep profiles the shapes of the profiles appeared to be similar between the different sample types. The optimal microwave frequency was the same for the single labelled urea and for the dual-labelled urea when monitored on ^{13}C. When monitored on ^{15}N the optimal microwave frequency was found to be 10 MHz higher. B) & C) The build-up profiles showed an increase in NMR signal intensity over time for all samples. D) No significant differences were identified between the build-up amplitudes extracted whilst monitoring on ^{15}N. E) From the build-up times, a significant reduction in the build-up time was recorded between single and dual-labelled samples when monitored on ^{15}N and between the ^{15}N and ^{13}C nuclei on dual-labelled samples. Significance was calculated using an unequal variance t-test. Significance is shown as * when $p \leq 0.05$. Dot plots show the average of $n = 3$. Bars display mean ± SD.

Sample	Build-up amplitude (a.u./μmol)	Build-up time (hours)
$^{15}N_2$-urea monitored on $^{15}N_2$	1.62 ± 0.22	0.75 ± 0.20
$^{15}N_2$,^{13}C-urea monitored on $^{15}N_2$	1.68 ± 0.09	1.46 ± 0.14
$^{15}N_2$,^{13}C-urea monitored on ^{13}C	70.8 ± 5.60	0.75 ± 0.01

Table 5.5: Polarisation constants: effect of dual-labelling

5.5.5.4 Discussion

This data would appear to suggest that the polarisation monitored on ^{13}C is an appropriate marker of ^{15}N polarisation for urea HCAs. The optimal microwave frequency when monitoring ^{13}C polarisation matched that recorded when monitoring the single labelled sample on ^{15}N. Furthermore, this frequency appeared to be only 10 MHz lower than the optimal recorded when monitoring $^{15}N_2$,^{13}C-urea on ^{15}N, however, repeats would be required to determine if there was a difference between the optimal microwave frequencies and to rule out experimental noise as a contributing factor. From the polarisation constants extracted from the build-up profiles recorded when monitoring on ^{15}N, the build-up amplitudes were within one standard deviation of each other, however, the build-up time for the dual-labelled sample was almost double that recorded from the single-labelled sample. This would appear to suggest that the presence of ^{13}C does not benefit the build-up efficiency of ^{15}N polarisation in $^{15}N_2$,^{13}C-urea samples. Thus, if ^{15}N is the nucleus of interest, using single-labelled urea would appear to generate similar signal enhancements but in approximately half the time. This data is in disagreement with the study published by Ferrari *et al.* who reported build-up times of 2140 ± 391 s and 3358 ± 425 s for $^{15}N_2$,^{13}C-urea and $^{15}N_2$-urea, respectively[137]. Potential reasons for this discrepancy could include differences in magnetic field strengths and sample preparation, such as the solvent.

5.6 Liquid-state polarisation

5.6.0.1 Background

Following on from the optimisation work conducted in Section 5.5, the liquid state polarisation level and ability of the samples to retain polarisation following their removal from the polariser was explored. As no ^{15}N polarisation measurements had previously been conducted on-site, a new set up and protocol had to be developed. The results from this work would then infer the feasibility of *in vivo* application.

5.6.0.2 Introduction

Whilst desirably long T_1 relaxation times have been recorded from ^{15}N-based HCAs in the liquid-state, these have been accompanied by low polarisation enhancements. For instance, 1% polarisation was recorded from sodium ^{15}N-nitrate samples following d-DNP and was reported by Gamliel *et al.* to be in good agreement with reports of other ^{15}N-labelled compounds where polarisation levels of approximately 3–10% were achieved[126, 127, 138, 139]. Yet, further optimisation of such probes has been justified by the aim of addressing concerns regarding the safety profile of GBCAs and the prospect of little-to-no background signal *in vivo*.

An estimation of the liquid-state polarisation can be determined by first calculating the thermal polarisation (Equation 2.11) and comparing the SNR recorded from the hyperpolarised and thermal signals recorded from the same sample (Equation 2.12). Here, the liquid state polarisation level and T_1 relaxation time at room temperature of the optimal sample preparation (determined in Section 5.5) was explored.

5.6.0.3 Methods

Due to the long T_1 of ^{15}N samples (200 – 800 s) at room temperature, the coil calibration and the acquisition of the thermal spectrum were conducted using the same methods as those followed in Chapter 3, Section 3.5[119]. That is, the Double Angle (DA) method was used for the coil mapping and the thermal was acquired under Ernst angle conditions.

Two coils were used to observe the hyperpolarised ^{15}N signal in the MR scanner; a ^{15}N/^{1}H volume coil for transmitting the RF pulses to the sample and a ^{15}N surface coil to receive the signal from the sample. The set up of transmitting on a volume coil and receiving on a surface coil is a well established paradigm in the field of MR. The set up of receiving on the same volume coil is also often performed preclinically. The calibration of the volume coil — to establish the relationship between the PW and FA — was completed prior to mapping the B_1 field.

To make a phantom for the calibration of the volume coil (Rapid Biomedical, Rimpar, Germany), a 15 ml centrifuge ("Falcon") tube was partially filled with agar to reduce the volume to 10 ml. The rest of the phantom comprised a 6 M solution of sodium ^{15}N-nitrate in double-distilled water (dd-H_2O) mixed with 100 μl Dotarem. The surface coil was taped to the phantom and was placed at the centre of the coil which itself was placed within the ^{15}N/^{1}H volume coil. This set up was then positioned at the isocentre of the 7 T horizontal-bore preclinical scanner.

The T_1 of the sodium ^{15}N-nitrate phantom was found using an IR sequence with a TR of 30 s between the excitation and the next inversion, 1 average, 90° FA at 52.9 dB, a 180° FA at 58.9 dB, and by fitting the data to Equation (3.9). Six TIs were used, the durations of which doubled between each measurement, starting with 0.875 s (0.875 s, 1.75 s, 3.5 s, 7 s, 14 s, 28 s). For the power calibration, pulses with increasing PW were applied using a TR of 30 s and four averages at 56 dB. The data was fitted using Equation (2.3) from which the FA calibration factor was extracted.

The B_1 of the volume and surface coil combination was then mapped using the DA method. Images were recorded using a Gradient Echo Multi Slice (GEMS) sequence with FAs of 65° and 130°. ^{1}H and ^{15}N images in the axial and sagittal planes were acquired to generate maps for both orientations. In the axial plane, 128 averages (16 minutes per average) at 51.7 dB were acquired for both FAs. The same was acquired in the sagittal plane but for 115 averages. The images were processed using a MATLAB script (ver. R2023a). ^{1}H images (real) were used to create a mask to locate pixels of interest in the ^{15}N images. From these pixels, an estimate of the mean ^{15}N signal recorded from the phantom could be determined.

For each map, a SNR threshold was generated by using the mean ^{15}N signal and the mean noise determined from the corners of one of the real images. This mask was then applied to the other image and the ratio of the signal intensity from the images was used to find the B_1 map for that plane.

To make each DNP sample, 186.6 mg of a 0.4:0.6 glycerol:D_2O (w/w) mixture was pipetted onto 70.9 mg of $^{15}N_2$-urea. The volume of this mixture was taken into account when determining the volume Dotarem to add. For a gadolinium concentration of 1.3 mM, 25 μl of a 1:50 Dotarem:D_2O (v/v) mixture was added. This was made into a 15 mM radical concentration stock solution by dissolving the appropriate mass of OX063 Trityl (MW = 1427 g/mol) or AH111501 ("GE Trityl") (MW = 1595 g/mol) to the total volume. 150 μl of stock solution was pipetted into a sample cup, the sample mass recorded, and then inserted into the polariser.

Samples were irradiated at 93.8 GHz having been identified as the optimal microwave frequency for this sample type from the work conducted in Section 5.5. The samples were irradiated for at least 90 minutes and the build-up of polarisation was monitored every 5 minutes using a 5 μs PW at 55 dB (equivalent to a 2° FA).

Prior to the dissolution, the container used to collect the HCA during a dissolution was heated to 70 °C in a water bath. The incorporation of this step was due to a previous finding by Harris *et al.* where the nuclear T_1 relaxation time of ^{15}N-urea was found to more than double upon increasing the temperature of the sample from physiological temperatures to over 65 °C following dissolution[138]. 4 ml of D_2O was pressurised and heated in a "dissolution stick" which was then inserted into the sample space of the polariser. The resulting HCA was collected from the heated container and injected into a syringe placed at the isocentre of the scanner. Polarised signal was recorded using the ^{1}H,^{15}N volume coil. PWs corresponding to 10°, 20°, and 30° were applied (six pulses of each) with a TR of 10 s at 56 dB. The liquid-state T_1 was extracted from the polarisation decay curve and informed the Ernst angle (Equation 2.10).

Thermal spectra were acquired by applying a PW corresponding to the Ernst angle at 56 dB, using a TR of 1 s, and 54,000 averages which took a total of 15 hours.

For analysis, all spectra were passed through a MATLAB script where each spectrum underwent baseline correction and was integrated to find the NMR signal intensity. The build-up amplitudes and build-up times were extracted from the build-up profiles by fitting with a monoexponential (Equation 2.7). The polarisation levels were estimated using a MATLAB script which compared the SNR of polarised and thermal spectra from each sample. All the data was corrected for the concentration of $^{15}N_2$-urea, sample mass, and the number of ^{15}N nuclei.

5.6.0.4 Results

The coil calibration data is shown in Figure 5.9. The T_1 extracted from the IR sequence was 6.99 s. The FA calibration factor extracted from the power calibration curve was 0.17 °/μs at at 56 dB transmit power.

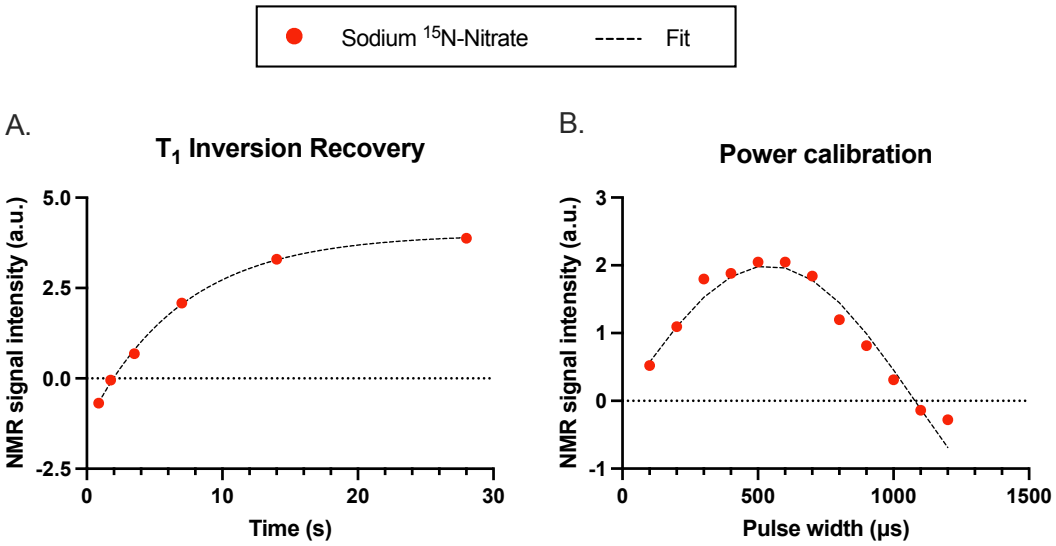

Figure 5.9: Calibration of the $^{15}N/^{1}H$ coil set-up
A) The T_1 extracted from the IR sequence was 6.99 s. B) The flip angle calibration factor extracted from the fit of the power calibration curve and was found to be 0.17 °/μs

The B_1 field ratio map of the $^{15}N/^{1}H$ coil set-up in the axial and sagittal plane is shown in Figure 5.10. The inset scale shows the ratio of the signal between the images acquired with the 65° and 130° FA.

Prior to each dissolution, a power calibration of the $^{15}N/^{1}H$ volume coil was conducted on the sodium ^{15}N-nitrate phantom. The extracted calibration factor

was found to change following each measurement. A visual representation of the instability of these measurements is shown in Figure 5.11. This was thought to be due to an interaction between the volume and surface coils and so a decision was made to repeat the liquid state polarisation measurements and use the $^{15}N/^{1}H$ volume coil as the transmit and receive coil instead.

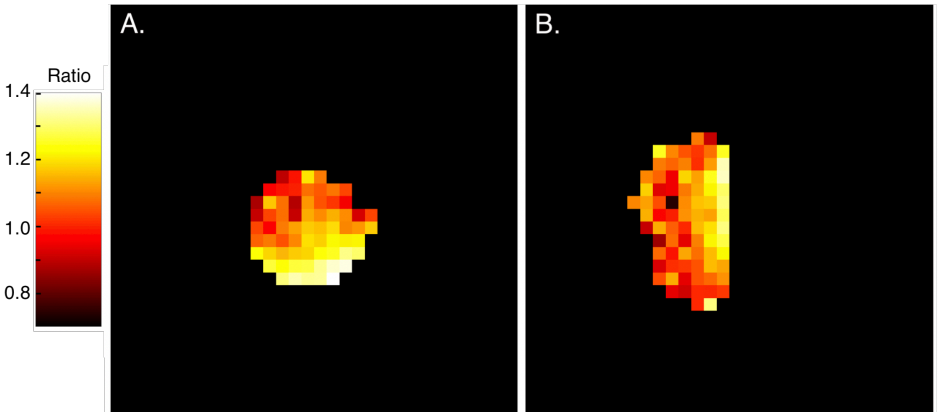

Figure 5.10: B_1 ratio map of the ^{15}N surface coil
The B_1 field ratio maps of the $^{15}N/^{1}H$ surface coil recorded using the Double Angle Method on a sodium ^{15}N-nitrate phantom are shown in A) the axial plane and B) the sagittal plane. The inset scale shows the ratio of signal acquired between the 65° and 130° FA.

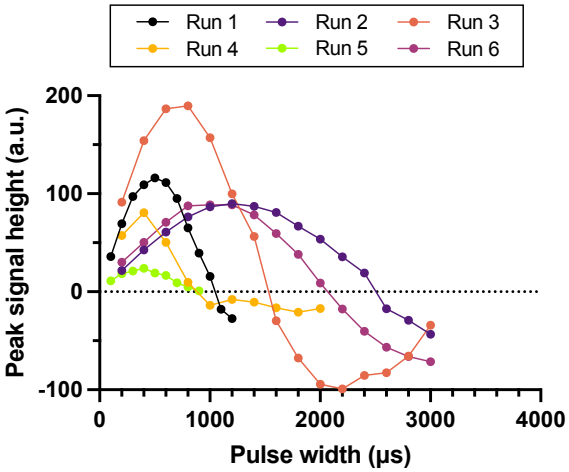

Figure 5.11: Surface coil power calibrations
Power calibrations of the surface coil recorded on different days are plotted. The variability in the extracted FA calibration factor suggested the joint volume/surface coil set-up was unstable. Henceforth, the $^{15}N/^{1}H$ volume coil as the receive coil instead.

The liquid state polarisation data acquired using the $^{15}N/^{1}H$ volume coil is summarised in Figure 5.12. The main difference in the polarised signals recorded over time from samples containing OX063 and AH111501 Trityl radicals was the range in NMR signal intensities (Figure 5.12A and B). Whilst the mean signal appears to be relatively similar between the two sample types there is a greater spread in values from samples that contained the OX063 Trityl radical. Representative NMR spectra taken from the first acquisition of the polarised samples and from the thermal measurements are also shown (Figure 5.12C and D). The thermal spectra were undersampled and hence, a smaller sampling interval should have been used. There were no significant differences in the levels of polarisation, liquid state nuclear T_1s, nor pH measurements determined for each sample type (Figure 5.12E, F, and G).

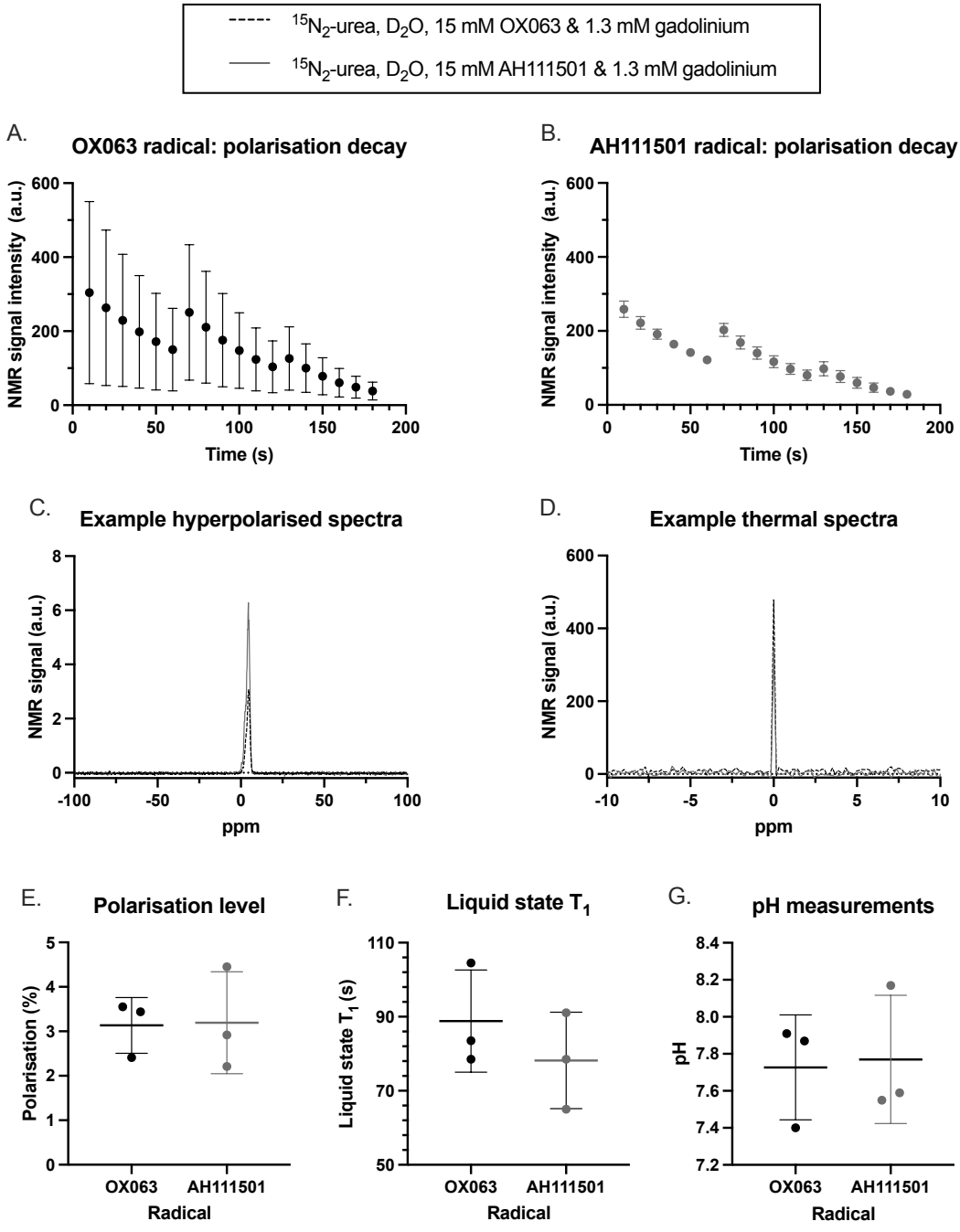

Figure 5.12: Liquid state ^{15}N polarisation
Data recorded from the ^{15}N liquid state measurements of hyperpolarised ^{15}N-urea samples is summarised. The mean signal recorded over time from samples containing A) OX063 Trityl and B) AH111501 Trityl appear similar yet, a greater spread in values was recorded from OX063 Trityl samples. Representative NMR spectra taken from C) the first acquisition of the polarised samples and from D) the thermal measurements are also shown. There were no significant differences in the E) levels of polarisation, F) liquid state nuclear T_1s, nor in the F) pH measurements determined for each sample type. Dot plot shows the average of $n = 3$. Bars display mean ± SD.

5.6.0.5 Discussion

Polarisation levels of approximately 3% were recorded from both $^{15}N_2$-urea sample types at room temperature following dissolution. It must be acknowledged, however, that the thermal spectra were undersampled and this likely will have affected the determination of the polarisation levels. The measurements for the thermal spectra could not be repeated due to the limited availability of the equipment.

Whilst the levels of polarisation enhancements that were determined were low in comparison to those expected and reported from ^{13}C-labelled compounds (where enhancements of 20% are typically measured), it is generally accepted that lower enhancements are achieved with ^{15}N nuclei due to differences in their gyromagnetic ratios[134]. For polarisation enhancements that are comparable to the levels reported from ^{13}C-labelled compounds, it appears as though following the typical dissolution-DNP set up is insufficient; the only study where polarisation levels of approximately 20% were generated from ^{15}N-labelled compounds involved hardware modifications and a custom pulse sequence[119].

Nevertheless, such modest levels of polarisation have previously been applied in *in vivo* studies and there was sufficient signal available for detection[140]. Hence, in addition to the extracted liquid state nuclear T_1s that were comparable, if not greater, than that typically recorded from ^{13}C-pyruvate and the results of the pH measurements that are within the accepted range for *in vivo* bolus dosing, it was proposed that the feasibility of the $^{15}N_2$-urea HCA optimised here for *in vivo* application was ready for testing[97].

5.7 *In vivo* study of perfusion

5.7.0.1 Background

The feasibility of *in vivo* application was demonstrated for both the HCAs tested in Section 5.6. The sample preparation containing AH111501 Trityl was taken forward for a proof of concept study to investigate perfusion in a stroke model. For comparison, perfusion data was also acquired using the current gold standard approach for contrast-enhanced MR, Dynamic Susceptibility Contrast (DSC) imaging.

5.7.0.2 Introduction

The rationale for imaging perfusion is to discern if oxygen, nutrients, and potentially medicines can be delivered to diseased tissue which can then be used to inform a patient treatment plan[141]. Previous clinical applications of perfusion MRI include: oncology for the assessment of brain tumours; cardiology to diagnose ischemic cardiomyopathy; and neurology in the context of degenerative diseases and following a stroke[142–145]. The most commonly used technique in neuro MRI is DSC which involves the intravenous administration of a GBCA followed by rapid T_2-weighted imaging[146]. The concept behind DSC is that, as the bolus is transported through the vasculature, the presence of gadolinium induces the paramagnetic relaxation of nearby tissue. The dephasing of T_2 (or $T_2{}^*$) results in a drop in MR signal intensity recorded from the surrounding tissue. From monitoring this signal over time, different parameters can be extracted from the fit of the data with a gamma-variate curve. Common parameters used to quantify perfusion include: the area under the curve (AUC), the mean transit time (MTT), the blood flow index (BFI), the time to peak (T_p), and the peak amplitude (Y_p). These parameters and the profile of a gamma variate curve are depicted in Figure 5.13. The BFI can be found using:

$$\mathrm{BFI} = \frac{\mathrm{AUC}}{\mathrm{MTT}} \tag{5.5}$$

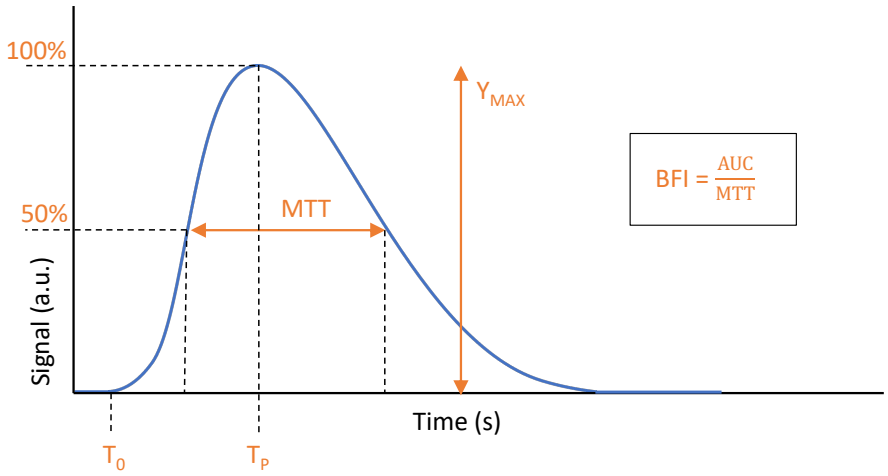

Figure 5.13: Gamma-variate curve profile
Common parameters used to quantify perfusion — the area under the curve (AUC), the mean transit time (MTT), the blood flow index (BFI), the time to peak (T_p), and the peak amplitude (Y_p) — and how they are extracted from perfusion data.

Due to the health and environmental concerns surrounding the use of GBCAs (detailed in Section 5.1), HCAs have been identified as a potential alternative for perfusion measurements using MR whereby hyperpolarised signal from a nucleus of interest is monitored over time. In addition to lower concentrations of gadolinium, another benefit that hyperpolarised MR perfusion imaging has to offer over DSC (and other imaging modalities) is that the concentration of the tracer and its level of polarisation is directly proportional to the recorded signal[147]. Here, ^{15}N spectroscopy were recorded in healthy and stroke model rat brains following intravenous injection of the optimised ^{15}N-urea preparation and the data compared to that generated using DSC MR.

5.7.0.3 Methods

All *in vivo* scanning conformed to institutional guidelines and were approved by the United Kingdom Home Office Animal Ethics Review Committee. Six male Wistar rats were used and split into two groups of three - one group to act as the healthy controls and the other to be imaged three days post stroke induced by endothelin-1 injection[1]. Endothelin-1 is a vasoconstrictive peptide and thus,

[1]The endothelin-1 injections were performed by Dr Yvonne Couch, Radcliffe Department of Medicine (University of Oxford)

causes temporary restriction of blood flow at the site of its injection. Since its development, endothelin-1 injection has frequently been used as an *in vivo* model of subcortical ischemic stroke in rodents[148–150]. The rats were housed together in their groups on a 12 hour day/night cycle and had free access to food and water.

Prior to scanning, each rat was placed into an anesthetic induction box where they were exposed to a gas mix of 60:40% O_2:N_2O with gas ratios equating to a total of 2 litres per minute combined with 2.5% isoflurane. Once under anesthesia, each rat was weighed and then transferred to a heat mat to be tail veined. The rat was then transferred to a home built imaging cradle which was inserted into a 7 T preclinical scanner and the isoflurane was reduced to 2%. A localiser was run using a $^{1}H/^{15}N$ volume coil to ensure the rat was at isocentre. Each rat underwent a hyperpolarised MR perfusion scan and a subsequent DSC scan. During both scans, the body temperature and respiratory rate were monitored.

For the hyperpolarised ^{15}N perfusion scans, $^{15}N_2$-urea samples containing 15 mM AH111501 and 1.3 mM gadolinium were prepared as previously described (Subsection 5.6.0.3). Slice selective spectroscopy was used for which two slices of 10 mm thickness were visually positioned, one over each hemisphere of the brain, such that in the stroke model one of the slices covered the endothelin-1 injection site to obtain ipsilateral and contralateral data. The HCA was injected into the tail vein and, using the $^{1}H/^{15}N$ volume coil, ^{15}N signal was monitored within each slice using 1 average and a TR of 0.5 s such that acquisitions alternated between each hemisphere so they were sampled every second.

For the planning of the DSC scans, a ^{1}H surface coil was secured over the head of each rat and T_2 weighted images acquired for 16 slices using a 1 mm slice thickness, four averages, and a TR of 2 s. Then, similar to the ^{15}N perfusion scan, a slice was positioned through the region where a stroke lesion had been observed on the T_2 weighted image. The tail vein was preloaded with 200 μl gadolinium (Dotarem) and was injected using a 300 μl saline flush following 20 baseline acquisitions.

For analysis, the hyperpolarised ^{15}N spectra were passed through jMRUI where they were separated into ipsilateral and contralateral spectra. The signal amplitudes output from the AMARES analysis package were then used as inputs in a python script where they were fitted using the gamma-variate function and the perfusion parameters extracted (Figure 5.13). All the hyperpolarised data was corrected for the concentration of $^{15}N_2$-urea, sample mass, and the number of ^{15}N nuclei. The DSC data was also processed using in-house python script and analysed using an in-house MATLAB script where perfusion parameters were extracted from regions of interest.

5.7.0.4 Results

Figure 5.14 shows, for each hemisphere in each healthy rat model, the appearance of ^{15}N signal and its subsequent decay. There were no visual differences between the profiles acquired from each hemisphere nor any significant differences between the extracted parameters (Figure 5.15).

Hyperpolarised ^{15}N signal was quantifiable in all the stroke model imaging subjects but there were no consistent visual differences between the contralateral and ipsilateral slices (Figure 5.16). Similarly, there were no significant differences between the extracted perfusion parameters recorded from the two hemispheres (Figure 5.17). The injection of endothelin-1 was expected to result in local ischemia and hence, the ratio of the perfusion parameters extracted from the left and right hemispheres within each model were taken and plotted for comparison (Figure 5.18). Again, no significant differences were recorded.

Examples of the proton-based images acquired from the stroke model three days post endothelin-1 injection is shown in Figure 5.19A. As an example of a perfusion parameter map generated following the processing of the data, a corresponding map of the blood flow is also shown (Figure 5.19B).

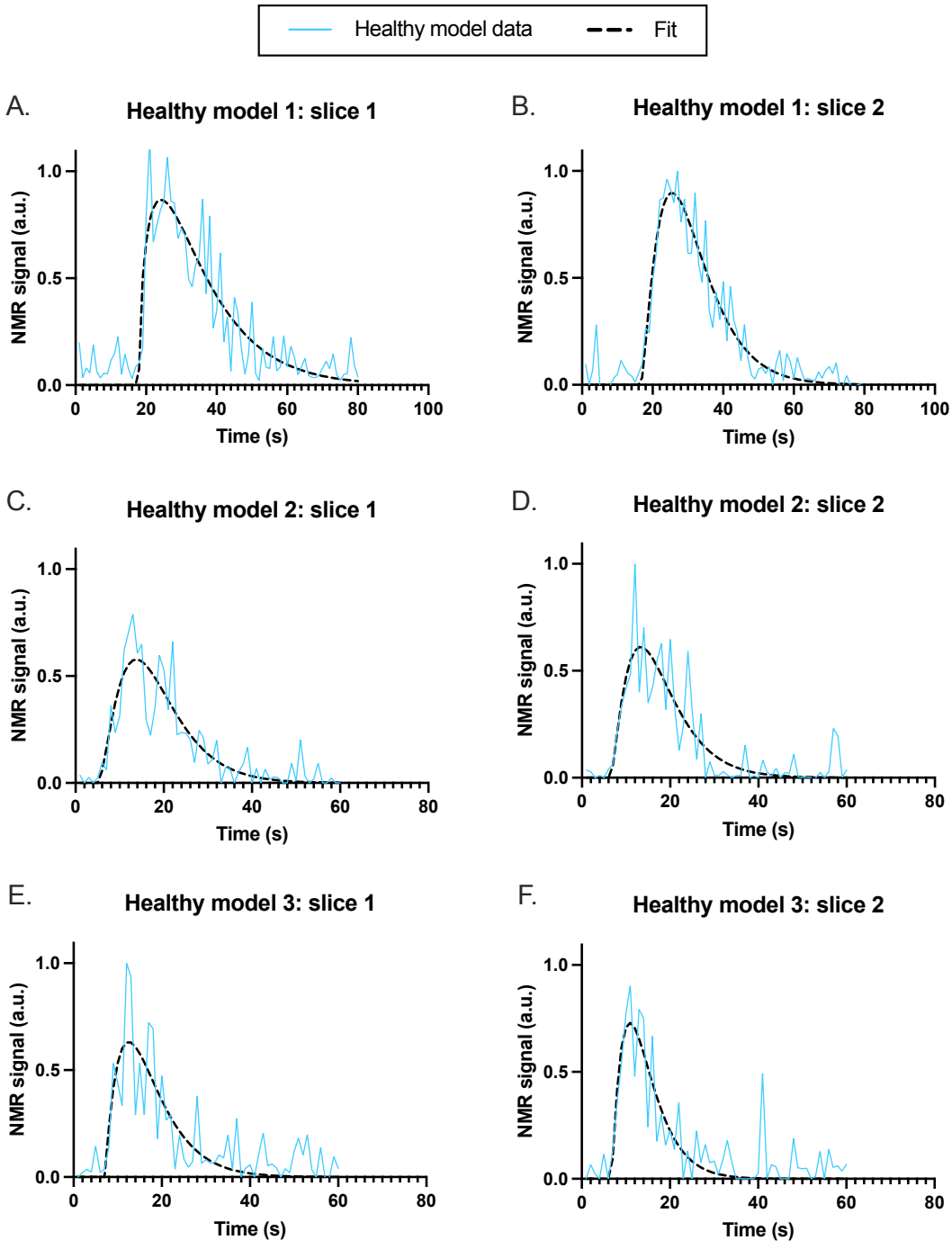

Figure 5.14: ^{15}N vascular traces: healthy models
^{15}N hyperpolarised data recorded from the healthy models ($n = 3$). For each model, data from the two slices are fitted to the gamma variate function.

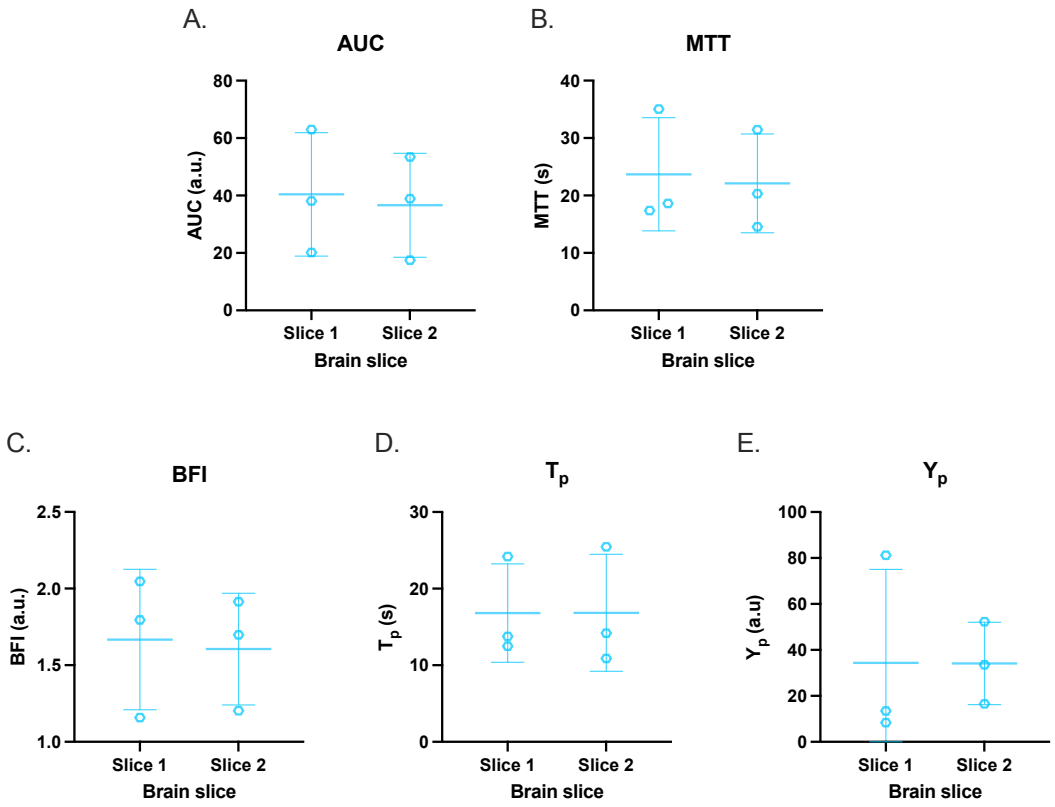

Figure 5.15: Vascular tracer parameters: healthy models
Dot plots summarising the extracted perfusion parameters from each hemisphere of the brain from the healthy models ($n = 3$) following administration of hyperpolarised $^{15}N_2$-urea. No significant differences between the extracted parameters were found.

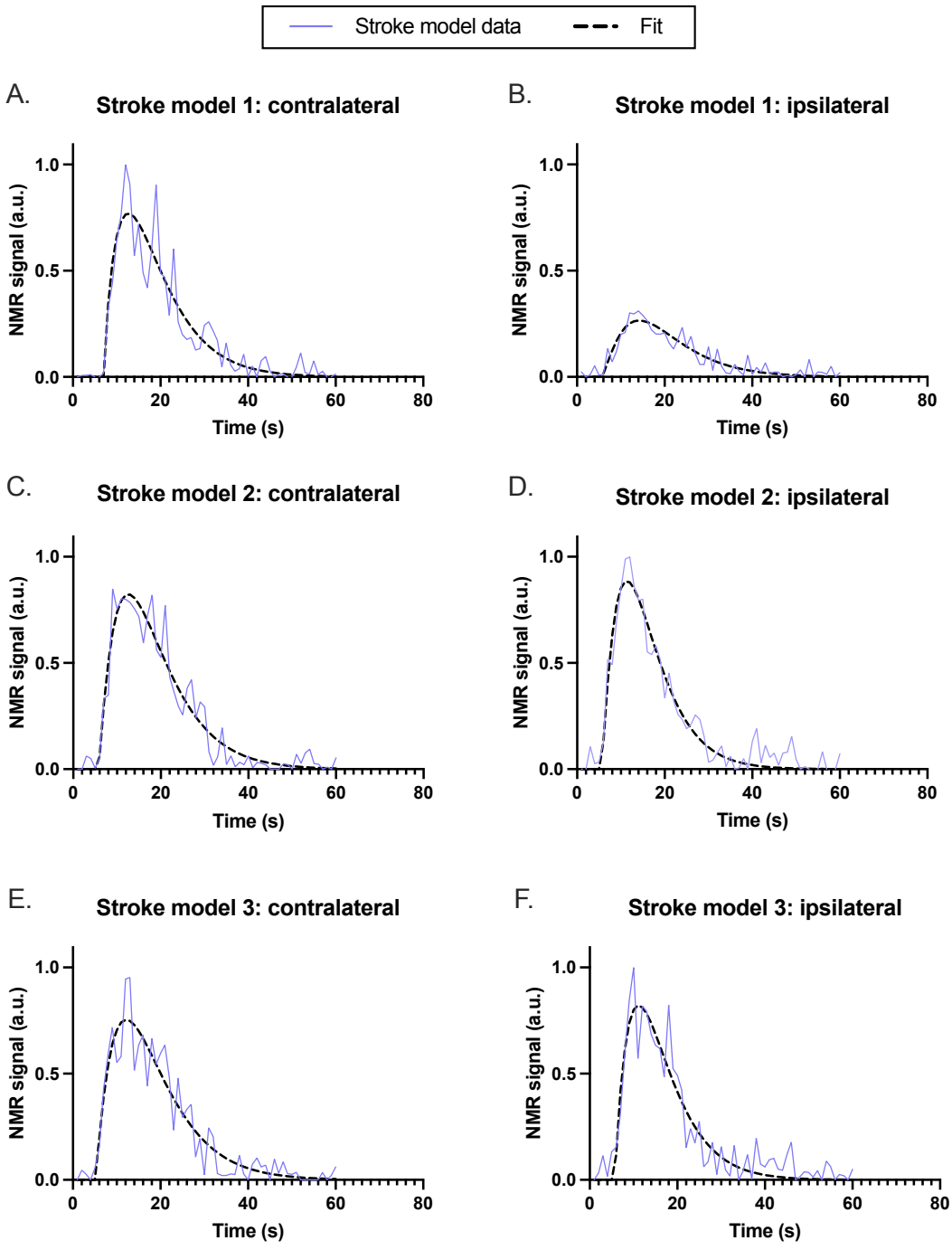

Figure 5.16: ^{15}N vascular traces: stroke models
^{15}N hyperpolarised data recorded from the stroke models. For each model, data from the two slices are fitted to the gamma-variate function.

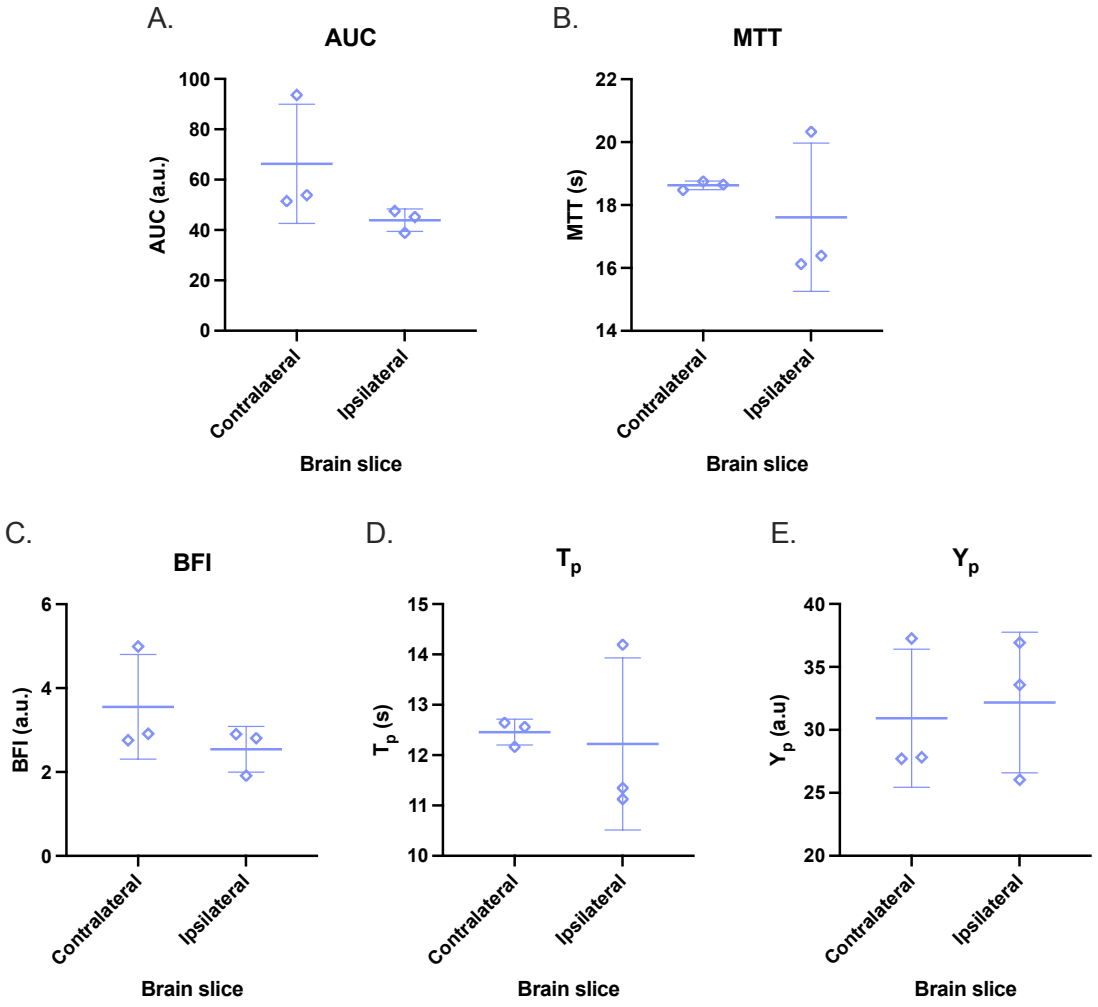

Figure 5.17: Vascular tracer parameters: stroke models
Dot plots summarising the extracted perfusion parameters from each hemisphere of the brain from the stroke models ($n = 3$) following administration of hyperpolarised $^{15}N_2$-urea. No significant differences between the extracted parameters were found.

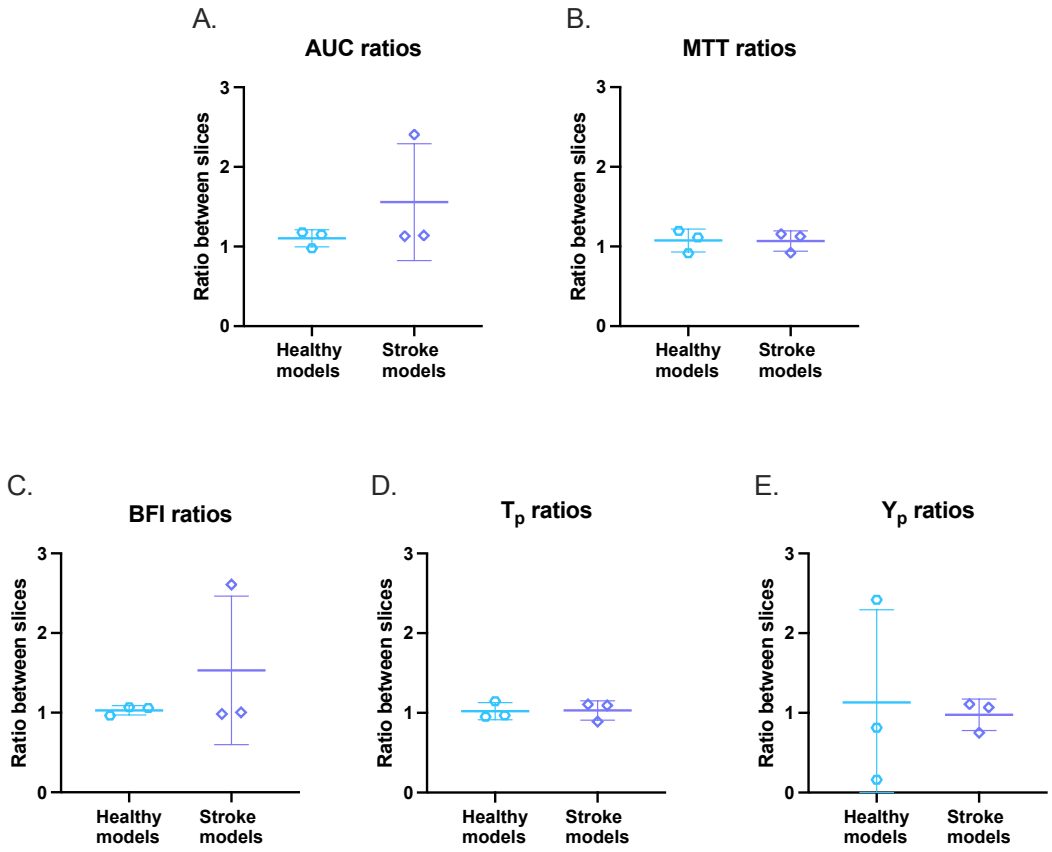

Figure 5.18: Ratios of the vascular tracer parameters
Dot plots summarising the ratio of the extracted perfusion parameters. Each dot represents the ratio of left and right hemispheres for the healthy model (circle) and stroke model (diamond) following administration of hyperpolarised $^{15}N_2$-urea. No significant differences were recorded between the healthy and stroke models.

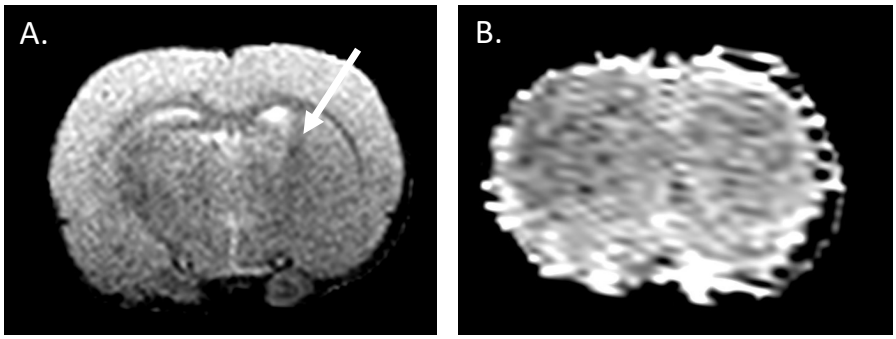

Figure 5.19: Examples of a ^{1}H image and perfusion parameter map
Examples of the proton-based images acquired from a stroke model. A) A T_2 weighted image where the stroke lesion is marked by a white arrow. B) A map of blood flow generated from the T_2 weighted images.

There was also a lack of significant findings following DSC imaging. Figure 5.20 summarises the perfusion parameters extracted from the ipsilateral hemisphere in the stroke model and the corresponding hemisphere in the healthy model. For example, the blood flow — increases in which are associated with elevated levels of perfusion — were recorded as $BF_{healthy} = 89.5 \pm 110.6\,ml/100g/min$ and $BF_{stroke} = 69.7 \pm 19.5\,ml/100g/min$ in the healthy and stroke models, respectively.

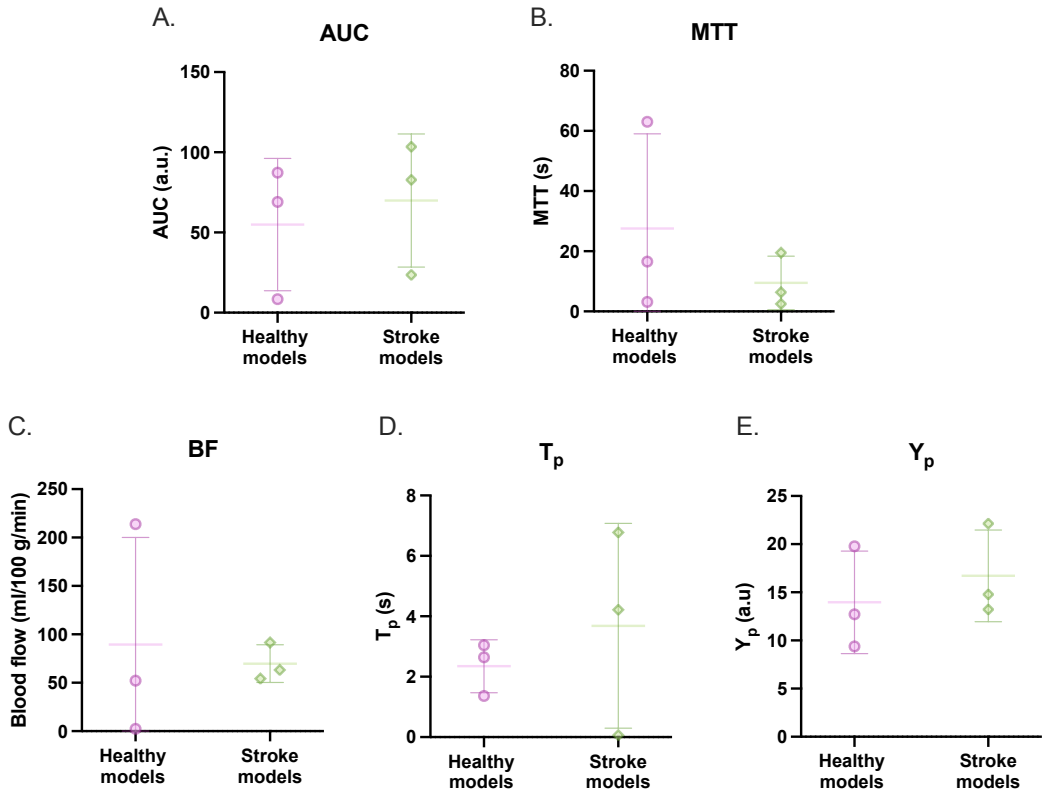

Figure 5.20: DSC: perfusion parameters
Dot plots summarising the perfusion parameters extracted from the DSC data. The parameters extracted from the ipsilateral hemisphere in the stroke model and the corresponding hemisphere in the healthy model are compared. No significant differences were recorded between the healthy and stroke models.

5.7.0.5 Discussion

This proof of concept study demonstrated the feasibility of detecting hyperpolarised $^{15}N_2$-urea signal *in vivo* with the optimised sample preparation. The assessment of perfusion with hyperpolarised $^{15}N_2$-urea was also shown to be possible, however, there was no detection of any differences between the healthy and stroke models. Whilst this could be due to the low levels of ^{15}N polarisation generated here, combined with the low sensitivity of the volume coil, there was also a lack of significant findings following DSC imaging. This may indicate unsuccessful generation of the stroke model which consequently led to the lack of and incorrect identification of stroke lesion(s) when selecting the position of the slice for the acquisition of the perfusion data for both techniques. Prior to the hyperpolarised scans, the behaviour of the two cohorts could have been examined. Behavioural differences between groups of healthy rats and those with endothelin-1 induced stroke have typically been tested using the sunflower seed task where rats are studied and timed whilst they open and consume the seeds[151].

5.8 Conclusion

This work demonstrated the feasibility of hyperpolarising $^{15}N_2$-urea and improving the achievable polarisation through direct deuteration. Trace amounts of gadolinium were also incorporated into the sample preparation which become diluted further still upon dissolution. A polarisation level of $3.19 \pm 1.14\,\%$ and a T_1 of $78.2 \pm 13.0\,\mathrm{s}$ were recorded from the optimal sample preparation which was observable *in vivo* in both a healthy and stroke model. Preliminary *in vivo* data suggests a ^{15}N hyperpolarised approach for the assessment of perfusion is possible, however, work is required to improve the sensitivity of the set up outlined here. The application of this technique could also be tested in extracranial tissue such as the kidneys.

Vino in bottiglia non soddisea la sete

Wine in the bottle doth not quench the thirst

— George Herbert

6 Discussion

Contents

6.1 Overview 215
6.2 Hyperpolarised ^{29}Si-silicon nanoparticles 216
6.3 Hyperpolarised ^{13}C-alanine 217
6.4 Hyperpolarised ^{15}N-urea 218

6.1 Overview

Significant advancements following the renaissance of DNP in the form of d-DNP have resulted in the establishment of a new branch of MRI. Termed "hyperpolarised MR", this imaging modality has shown to be a promising clinical tool for a myriad of pathologies. In particular, the rapid clinical translation of a ^{13}C-pyruvate HCA has given exciting preliminary evidence in support of the potential of hyperpolarised MR to aid diagnosis and inform treatment through monitoring changes in metabolism between healthy and diseased states. Yet, for widespread adoption into the clinic, the application of hyperpolarised MR needs to be expanded even further and hence the demand for a variety of X-nuclei HCAs to be added to the toolkit. Progress in the development and translation of other compounds as HCAs, however, has lagged behind that of ^{13}C-pyruvate for a multitude of reasons.

Ranging from hardware limitations to undesirable polarisation characteristics, this thesis aimed to address some of the main hurdles through the incorporation of various optimisation techniques.

6.2 Hyperpolarised ^{29}Si-silicon nanoparticles

In Chapter 3, a SiNP-based HCA was developed. Following optimisation that targeted steps across the whole d-DNP workflow, the main findings of this chapter can be summarised as:

- The first recordings of ^{29}Si hyperpolarised signal in Europe both in the solid and liquid state
- The combined effect of exogeneous radical structure and concentration on the hyperpolarisation of the SiNPs
- For 30 – 50 nm SiNPs, Nitroxide radicals, (specifically, 30 mM TEMPO) appeared to result in the greatest and most efficient polarisation transfer to the ^{29}Si nuclear spins
- The set up and optimisation of a d-DNP protocol for SiNPs that required three times less build-up time than that recommended for SiNP d-DNP samples and that led to the detection of a liquid state nuclear T_1 relaxation time of 32.5 minutes at room temperature[33]

In terms of future work, an avenue for reducing the polarisation build-up time further or improving the levels of polarisation achieved after five hours could be through the inclusion of microwave modulation which has previously been demonstrated for SiMPs[71].

The e-beam irradiation of SiNPs to generate endogenous radicals was also explored yet no beneficial effect was observed during d-DNP. This was thought to be due to recombination of defects at room temperature. Hence, future work could explore the e-beam irradiation of SiNP samples at cryogenic temperatures to preserve any resulting defects. Proposed methods for this are the adaptation of

the LinAc set up to incorporate a cold finger or through the utilisation of cryogenic TEM. The latter is hypothesised following reports of damage to crystalline silicon samples at beam energies of approximately 200 kV[68].

One caveat of hyperpolarised MR is the view that only "fast" biological processes can be monitored. The long nuclear T_1 relaxation time exhibited by SiNPs, such as that demonstrated within this Thesis, however, could potentially be leveraged to monitor much slower biological processes such as those related to gastrointestinal transport[29]. Alternatively, their structure and the flexible surface chemistry that they offer, opens the possibility of drug-loading for targeted delivery[152]. SiNPs could, therefore, be developed into hyperpolarised theragnostic agents to facilitate the monitoring of drug delivery and release. The release of medicines under certain pH conditions could minimise harm to healthy tissue, for example.

6.3 Hyperpolarised ^{13}C-alanine

Chapter 4 entailed the development of a ^{13}C-alanine HCA as an alternative probe to ^{13}C-pyruvate. ^{13}C-pyruvate is seen as the workhorse for d-DNP due to its approval for clinical use and the extensive metabolic studies conducted with it. Questions, however, have been raised with regards to its ability to accurately ascertain metrics of intracellular metabolism.

The main findings of this chapter included:

- The feasibility of endogenous radical generation within ^{13}C-alanine upon e-beam irradiation
- The tunability of radical concentration for d-DNP upon changes to the e-beam irradiation dose
- The first ever detection worldwide of ^{13}C hyperpolarised signal arising from polarisation transfer from e-beam irradiation induced radicals

- An extracted liquid state nuclear T_1 relaxation time of 67.3±10.9 s and polarisation level of 7.6±2.6 % following the application and optimisation of microwave modulation during d-DNP
- The *in vivo* detection of irradiated ^{13}C-alanine

The nonpersistent property of the irradiation induced radicals within alanine in the presence of moisture removed the need for the filtration step during dissolution and was hypothesised to lengthen the nuclear T_1 relaxation time in the liquid state. Future work could explore the extent of the prolongation through investigating different solvents for dissolution. The choice of D_2O made the effect of radical quenching upon dissolution inextricable from the use of a deuterated solvent which has also been shown to prolong T_1[153, 154].

The extension of nuclear T_1 relaxation times of ^{13}C agents beyond one minute also plays a part in the realisation of the concept of transportable HCAs. Hyperpolarised alanine samples that were manually removed from a polariser and stored for 16 hours at ∼4 K and a magnetic field strength of ∼1 T have previously been shown to retain some of their polarisation[155]. The ability to generate, store, and then transport HCAs would enable sites without a polariser to conduct hyperpolarised MR. Moreover, if this were conducted with irradiated ^{13}C-alanine samples, the irradiation in the high dose regime would, in addition to generating radicals for d-DNP, sterilise the substrate and thereby address a requirement for its clinical use. Ultimately, this work could lay the foundations for the e-beam irradiation of other amino acids or proteins to be used as HCAs to better investigate other metabolic pathways or perfusion properties.

6.4 Hyperpolarised ^{15}N-urea

Chapter 5 detailed the development of a ^{15}N labelled perfusion probe and the main findings can be summarised as follows:

- The design and build of a T&M circuit that enabled the direct monitoring of ^{15}N polarisation in the solid state

- The direct deuteration of ^{15}N-urea led to improvements in the polarisation characteristics
- The detection of ^{15}N polarisation *in vivo* as a hyperpolarised perfusion agent

Whilst the optimised ^{15}N-urea HCA was detectable *in vivo*, the low polarisation levels that were recorded and the instability of the combined surface coil and volume coil set up highlighted the need for the further development. The use of the volume coil as the receive coil during the proof of concept *in vivo* study likely played a factor in the lack of significant findings. Thus, the repair of the surface coil and the use of a more localised imaging sequence are suggested approaches for future work that could lead to greater sensitivity.

With the design and building of the ^{15}N T&M circuit, the optimisation of other ^{15}N-labelled compounds could be investigated for their suitability as a hyperpolarised perfusion agent. Among the other uses detailed in previous studies, the molecular imaging capabilities of ^{15}N-labelled compounds as pH sensors stand out[156]. Similar to the imaging of metabolism or perfusion, changes in pH levels can also be an indicator of illness or disease. Hence, the development of such X-nuclei HCAs underpins the notion of this thesis that the development of a wider range of probes has the potential to broaden the clinical application of hyperpolarised MR.

I guess my feet know where they want me to go
Walking on a country road

— James Taylor

7 Concluding Remarks

During the course of this research, the greatest hindrance to the progression of X-nuclei HCA development was identified as the stepwise approach required for their optimisation owing to the complexity of the physical processes underlying DNP. Whilst existing theories have shown to be robust to experimental testing, arguably the finer details of these processes remain to be entirely understood by the hyperpolarised MR research community. Indeed, a trial and error approach to experiments is often adopted which exacerbates the issue of stunted development and thereupon lies the need for streamlined and coordinated efforts[17].

Such efforts are already underway with the commencement of multicentre studies and focus is being diverted away from individual HCA substrates onto the d-DNP workflow as a whole[157]. In essence, developing HCAs for d-DNP and monitoring them using MRS/MRI is technically challenging and it is hoped the research summarised in this thesis will contribute, whether taken verbatim or repurposed in some way, to the expansion of hyperpolarised MR as a clinical technique.

References

[1] Jan H Ardenkjær-Larsen et al. "Increase in signal-to-noise ratio of > 10,000 times in liquid-state NMR". In: *Proceedings of the National Academy of Sciences* 100.18 (2003), pp. 10158–10163.

[2] VA Atsarkin. "Dynamic nuclear polarization: Yesterday, today, and tomorrow". In: *Journal of Physics: Conference Series*. Vol. 324. 1. IOP Publishing. 2011, p. 012003.

[3] J Wolber et al. "Generating highly polarized nuclear spins in solution using dynamic nuclear polarization". In: *Nuclear Instruments and Methods in Physics Research Section A: Accelerators, Spectrometers, Detectors and Associated Equipment* 526.1-2 (2004), pp. 173–181.

[4] Angus Z Lau, Jack J Miller, and Damian J Tyler. "Mapping of intracellular pH in the in vivo rodent heart using hyperpolarized [1-13C] pyruvate". In: *Magnetic Resonance in Medicine* 77.5 (2017), pp. 1810–1817.

[5] David O Guarin et al. "Development of dissolution dynamic nuclear polarization of [15N3] metronidazole: A clinically approved antibiotic". In: *Angewandte Chemie International Edition* 62.31 (2023), e202219181.

[6] Jessica Wahsner et al. "Chemistry of MRI contrast agents: current challenges and new frontiers". In: *Chemical reviews* 119.2 (2018), pp. 957–1057.

[7] Felix Bloch. "Nuclear induction". In: *Physical review* 70.7-8 (1946), p. 460.

[8] Stuart J Elliott et al. "Practical dissolution dynamic nuclear polarization". In: *Progress in Nuclear Magnetic Resonance Spectroscopy* 126 (2021), pp. 59–100.

[9] Mengxiao Liu and Christian Hilty. "Metabolic measurements of nonpermeating compounds in live cells using hyperpolarized NMR". In: *Analytical chemistry* 90.2 (2018), pp. 1217–1222.

[10] Hsueh-Ying Chen and Christian Hilty. "Implementation and characterization of flow injection in dissolution dynamic nuclear polarization NMR spectroscopy". In: *ChemPhysChem* 16.12 (2015), pp. 2646–2652.

[11] Albert W Overhauser. "Polarization of nuclei in metals". In: *Physical Review* 92.2 (1953), p. 411.

[12] W Th Wenckebach. "Dynamic nuclear polarization via the cross effect and thermal mixing: A. The role of triple spin flips". In: *Journal of Magnetic Resonance* 299 (2019), pp. 124–134.

[13] W Th Wenckebach. "Dynamic nuclear polarization via the cross effect and thermal mixing: B. Energy transport". In: *Journal of Magnetic Resonance* 299 (2019), pp. 151–167.

[14] A Comment et al. “Design and performance of a DNP prepolarizer coupled to a rodent MRI scanner”. In: *Concepts in Magnetic Resonance Part B: Magnetic Resonance Engineering: An Educational Journal* 31.4 (2007), pp. 255–269.

[15] W Th Wenckebach. “Dynamic nuclear polarization via thermal mixing: Beyond the high temperature approximation”. In: *Journal of Magnetic Resonance* 277 (2017), pp. 68–78.

[16] Jan Henrik Ardenkjaer-Larsen. “Hyperpolarization by dissolution dynamic nuclear polarization”. In: *Dynamic Hyperpolarized Nuclear Magnetic Resonance*. Springer, 2021, pp. 1–26.

[17] Chandrasekhar Ramanathan. “Dynamic nuclear polarization and spin diffusion in nonconducting solids”. In: *Applied Magnetic Resonance* 34.3-4 (2008), pp. 409–421.

[18] Alessandro Chessari et al. “Role of electron polarization in nuclear spin diffusion”. In: *Physical Review B* 107.22 (2023), p. 224429.

[19] IJ Lowe and S Gade. “Density-matrix derivation of the spin-diffusion equation”. In: *Physical Review* 156.3 (1967), p. 817.

[20] Alessandra Flori et al. “Dissolution dynamic nuclear polarization of non-self-glassing agents: spectroscopy and relaxation of hyperpolarized [1-13C] acetate”. In: *The Journal of Physical Chemistry A* 119.10 (2015), pp. 1885–1893.

[21] Erin B Adamson et al. “Magnetic resonance imaging with hyperpolarized agents: methods and applications”. In: *Physics in Medicine & Biology* 62.13 (2017), R81.

[22] Mohammed M Albannay et al. “Optimized microwave delivery in dDNP”. In: *Journal of Magnetic Resonance* 305 (2019), pp. 58–65.

[23] Simon Hu et al. “In vivo measurement of normal rat intracellular pyruvate and lactate levels after injection of hyperpolarized [1-13C] alanine”. In: *Magnetic resonance imaging* 29.8 (2011), pp. 1035–1040.

[24] O Burghaus et al. “A novel high-field/high-frequency EPR and ENDOR spectrometer operating at 3 mm wavelength”. In: *Measurement Science and Technology* 3.8 (1992), p. 765.

[25] Stefan Stoll and Arthur Schweiger. “EasySpin, a comprehensive software package for spectral simulation and analysis in EPR”. In: *Journal of magnetic resonance* 178.1 (2006), pp. 42–55.

[26] Stefan Stoll. “CW-EPR spectral simulations: Solid state”. In: *Methods in enzymology*. Vol. 563. Elsevier, 2015, pp. 121–142.

[27] AE Dementyev, DG Cory, and C Ramanathan. “Dynamic nuclear polarization in silicon microparticles”. In: *Physical review letters* 100.12 (2008), p. 127601.

[28] Nicholas Whiting et al. “Developing hyperpolarized silicon particles for in vivo MRI targeting of ovarian cancer”. In: *Journal of Medical Imaging* 3.3 (2016), p. 036001.

[29] Grzegorz Kwiatkowski et al. “Nanometer size silicon particles for hyperpolarized MRI”. In: *Scientific reports* 7.1 (2017), pp. 1–6.

[30] Myriam M Chaumeil, Chloé Najac, and Sabrina M Ronen. "Studies of metabolism using 13C MRS of hyperpolarized probes". In: *Methods in enzymology* 561 (2015), pp. 1–71.

[31] JW Aptekar et al. "Hyperpolarized Long-T1 Silicon Nanoparticles for Magnetic Resonance Imaging". In: *arXiv preprint arXiv:0902.0269* (2009).

[32] MC Cassidy et al. "In vivo magnetic resonance imaging of hyperpolarized silicon particles". In: *Nature nanotechnology* 8.5 (2013), pp. 363–368.

[33] Shivanand Pudakalakatti et al. "Hyperpolarized MRI with silicon micro and nanoparticles: Principles and applications". In: *Wiley Interdisciplinary Reviews: Nanomedicine and Nanobiotechnology* 13.6 (2021), e1722.

[34] Eugeny V Kryukov et al. "Determination of the temperature dependence of the dynamic nuclear polarisation enhancement of water protons at 3.4 Tesla". In: *Physical Chemistry Chemical Physics* 13.10 (2011), pp. 4372–4380.

[35] Sonia Colombo Serra, Alberto Rosso, and Fabio Tedoldi. "On the role of electron–nucleus contact and microwave saturation in thermal mixing DNP". In: *Physical Chemistry Chemical Physics* 15.21 (2013), pp. 8416–8428.

[36] Christian Griesinger et al. "Dynamic nuclear polarization at high magnetic fields in liquids." In: *Progress in nuclear magnetic resonance spectroscopy* 64 (2012), pp. 4–28.

[37] Kent R Thurber, Wai-Ming Yau, and Robert Tycko. "Low-temperature dynamic nuclear polarization at 9.4 T with a 30 mW microwave source". In: *Journal of Magnetic Resonance* 204.2 (2010), pp. 303–313.

[38] Quy Son Luu et al. "Applications and perspective of silicon particles in hyperpolarized 29Si magnetic resonance imaging". In: *Applied Spectroscopy Reviews* 55.6 (2020), pp. 476–490.

[39] Huan Chang and Shu-Qing Sun. "Silicon nanoparticles: Preparation, properties, and applications". In: *Chinese Physics B* 23.8 (2014), p. 088102.

[40] Luca Guerrini, Ramon A Alvarez-Puebla, and Nicolas Pazos-Perez. "Surface modifications of nanoparticles for stability in biological fluids". In: *Materials* 11.7 (2018), p. 1154.

[41] Hyeonglim Seo et al. "Hyperpolarized porous silicon nanoparticles: potential theragnostic material for 29Si magnetic resonance imaging". In: *ChemPhysChem* 19.17 (2018), pp. 2143–2147.

[42] Grzegorz Kwiatkowski et al. "Exploiting endogenous surface defects for dynamic nuclear polarization of silicon micro-and nanoparticles". In: *The Journal of Physical Chemistry C* 122.44 (2018), pp. 25668–25680.

[43] Alyxandra N Thiessen et al. "Silicon nanoparticles: Are they crystalline from the core to the surface?" In: *Chemistry of Materials* 31.3 (2019), pp. 678–688.

[44] Jacob W Aptekar et al. "Silicon nanoparticles as hyperpolarized magnetic resonance imaging agents". In: *ACS nano* 3.12 (2009), pp. 4003–4008.

[45] Tonya M Atkins et al. "Synthesis of long T 1 silicon nanoparticles for hyperpolarized 29Si magnetic resonance imaging". In: *ACS nano* 7.2 (2013), pp. 1609–1617.

[46] Debamalya Banerjee et al. “The interplay between the solid effect and the cross effect mechanisms in solid state 13C DNP at 95 GHz using trityl radicals”. In: *Journal of Magnetic Resonance* 230 (2013), pp. 212–219.

[47] Jingzhe Hu, Nicholas Whiting, and Pratip Bhattacharya. “Hyperpolarization of silicon nanoparticles with TEMPO radicals”. In: *The Journal of Physical Chemistry C* 122.19 (2018), pp. 10575–10581.

[48] Marta Mas-Torrent et al. “Attaching persistent organic free radicals to surfaces: how and why”. In: *Chemical Reviews* 112.4 (2012), pp. 2506–2527.

[49] Olivier Lafon et al. “Beyond the Silica Surface by Direct Silicon-29 Dynamic Nuclear Polarization”. In: *Angewandte Chemie International Edition* 36.50 (2011), pp. 8367–8370.

[50] Ümit Akbey et al. “Dynamic nuclear polarization of spherical nanoparticles”. In: *Physical Chemistry Chemical Physics* 15.47 (2013), pp. 20706–20716.

[51] Jan Henrik Ardenkjær-Larsen, S Macholl, and H Johannesson. “Dynamic nuclear polarization with trityls at 1.2 K”. In: *Applied Magnetic Resonance* 34.3-4 (2008), pp. 509–522.

[52] Enrico Ravera et al. “The effect of Gd on trityl-based dynamic nuclear polarisation in solids”. In: *Physical Chemistry Chemical Physics* 17.40 (2015), pp. 26969–26978.

[53] Jan Henrik Ardenkjaer-Larsen. “On the present and future of dissolution-DNP”. In: *Journal of Magnetic Resonance* 264 (2016), pp. 3–12.

[54] Fabian Jähnig et al. “Dissolution DNP using trityl radicals at 7 T field”. In: *Physical Chemistry Chemical Physics* 19.29 (2017), pp. 19196–19204.

[55] Goran Kovaevi and Branko Pivac. “Structure, defects, and strain in silicon-silicon oxide interfaces”. In: *Journal of Applied Physics* 115.4 (2014), p. 043531.

[56] Yoshio Nishi. “Study of silicon-silicon dioxide structure by electron spin resonance I”. In: *Japanese Journal of Applied Physics* 10.1 (1971), p. 52.

[57] Philip J Caplan et al. “Paramagnetic defects in silicon/silicon dioxide systems”. In: *Surface Science* 54.1 (1976), pp. 33–42.

[58] Li Wang. “DNP measurements of irradiated deuterated polyethylene”. In: *XVIth International Workshop in Polarized Sources, Targets, and Polarimetry (PSTP2015)*. 2015, p. 22.

[59] Scott L Carnahan et al. “High-field magic angle spinning dynamic nuclear polarization using radicals created by γ-irradiation”. In: *The Journal of Physical Chemistry Letters* 10.17 (2019), pp. 4770–4776.

[60] Andrea Capozzi et al. “Photoinduced nonpersistent radicals as polarizing agents for X-nuclei dissolution dynamic nuclear polarization”. In: *The Journal of Physical Chemistry C* 119.39 (2015), pp. 22632–22639.

[61] Andrea Capozzi et al. “Thermal annihilation of photo-induced radicals following dynamic nuclear polarization to produce transportable frozen hyperpolarized 13C-substrates”. In: *Nature communications* 8.1 (2017), p. 15757.

[62] Itai Katz and Aharon Blank. "Dynamic nuclear polarization in solid samples by electrical-discharge-induced radicals". In: *Journal of Magnetic Resonance* 261 (2015), pp. 95–100.

[63] RC Newman. "Defects in silicon". In: *Reports on Progress in Physics* 45.10 (1982), p. 1163.

[64] George D Watkins. "Intrinsic defects in silicon". In: *Materials science in semiconductor processing* 3.4 (2000), pp. 227–235.

[65] S Kaschieva et al. "Effect of MeV electron irradiation on Si-SiO2 structures". In: *Journal of Physics: Conference Series*. Vol. 514. 1. IOP Publishing. 2014, p. 012039.

[66] JW Corbett and GD Watkins. "Silicon divacancy and its direct production by electron irradiation". In: *Physical Review Letters* 7.8 (1961), p. 314.

[67] JW Corbett and GD Watkins. "Production of divacancies and vacancies by electron irradiation of silicon". In: *Physical Review* 138.2A (1965), A555.

[68] RF Egerton, P Li, and M Malac. "Radiation damage in the TEM and SEM". In: *Micron* 35.6 (2004), pp. 399–409.

[69] G Kissinger et al. "Investigation of the composition of the Si/SiO2 interface in oxide precipitates and oxide layers on silicon by STEM/EELS". In: *ECS Journal of Solid State Science and Technology* 6.7 (2017), N54.

[70] Yoshiyuki Ishimori et al. "Fast B1 mapping based on double-angle method with T1 correction using standard pulse sequence". In: *Journal of Medical Physics* 47.1 (2022), pp. 93–98.

[71] Daphna Shimon et al. "DNP-NMR of surface hydrogen on silicon microparticles". In: *Solid State Nuclear Magnetic Resonance* 101 (2019), pp. 68–75.

[72] Jae Mo Park et al. "In vivo assessment of intracellular redox state in rat liver using hyperpolarized [1-13C] Alanine". In: *Magnetic resonance in medicine* 77.5 (2017), pp. 1741–1748.

[73] Kayvan R Keshari and David M Wilson. "Chemistry and biochemistry of 13 C hyperpolarized magnetic resonance using dynamic nuclear polarization". In: *Chemical Society Reviews* 43.5 (2014), pp. 1627–1659.

[74] Maria da Graça Lütz et al. "Alanine prevents the in vitro inhibition of glycolysis caused by phenylalanine in brain cortex of rats". In: *Metabolic brain disease* 18 (2003), pp. 87–94.

[75] Philip Felig. "The glucose-alanine cycle". In: *Metabolism* 22.2 (1973), pp. 179–207.

[76] Walter Gordy, William B Ard, and Howard Shields. "Microwave spectroscopy of biological substances. I. Paramagnetic resonance in X-irradiated amino acids and proteins". In: *Proceedings of the National Academy of Sciences* 41.11 (1955), pp. 983–996.

[77] WW Bradshaw et al. "The use of alanine as a solid dosimeter". In: *Radiation research* 17.1 (1962), pp. 11–21.

[78] JW Nam. "Standardization of high doses in radiation processing." In: *IAEA bulletin* 30.4 (1988), pp. 41–43.

[79] Alexander Berne et al. “Monitoring electron energies during FLASH irradiations”. In: *Physics in Medicine & Biology* 66.4 (2021), p. 045015.

[80] DF Regulla and U Deffner. “Dosimetry by ESR spectroscopy of alanine”. In: *The International Journal of Applied Radiation and Isotopes* 33.11 (1982), pp. 1101–1114.

[81] Mohamed A Morsy. “Simple EPR/alanine dosimeter for medical application”. In: (2012).

[82] Olga F Sleptchonok, Vitaly Nagy, and Marc F Desrosiers. “Advancements in accuracy of the alanine dosimetry system. Part 1. The effects of environmental humidity”. In: *Radiation Physics and Chemistry* 57.2 (2000), pp. 115–133.

[83] Geoffrey P Jacobs. “Irradiation of pharmaceuticals: A literature review”. In: *Radiation Physics and Chemistry* 190 (2022), p. 109795.

[84] Eirik Malinen et al. “Alanine radicals, part 3: Properties of the components contributing to the EPR spectrum of X-irradiated alanine dosimeters”. In: *Radiation Research* 159.1 (2003), pp. 23–32.

[85] Einar Sagstuen et al. “Alanine radicals: Structure determination by EPR and ENDOR of single crystals X-irradiated at 295 K”. In: *The Journal of Physical Chemistry A* 101.50 (1997), pp. 9763–9772.

[86] Eirik O Jåstad et al. “In quest of the alanine r3 radical: Multivariate epr spectral analyses of x-irradiated alanine in the solid state”. In: *The Journal of Physical Chemistry A* 121.38 (2017), pp. 7139–7147.

[87] Mojgan Z Heydari et al. “Alanine radicals. 2. The composite polycrystalline alanine EPR spectrum studied by ENDOR, thermal annealing, and spectrum simulations”. In: *The Journal of Physical Chemistry A* 106.38 (2002), pp. 8971–8977.

[88] KJ Weeks and PG O’Shea. “Production of radioisotopes by direct electron activation”. In: *Medical Physics* 25.4 (1998), pp. 488–492.

[89] Alexandre I Ivannikov et al. “Formation of different types of paramagnetic centers in the alanine dosimeters exposed to alpha and gamma radiation-Study by EPR spectroscopy”. In: *Radiation Measurements* 140 (2021), p. 106467.

[90] James M Holton. “A beginner’s guide to radiation damage”. In: *Journal of synchrotron radiation* 16.2 (2009), pp. 133–142.

[91] Aurélien Bornet et al. “Microwave frequency modulation to enhance dissolution dynamic nuclear polarization”. In: *Chemical Physics Letters* 602 (2014), pp. 63–67.

[92] Yonatan Hovav et al. “Dynamic nuclear polarization using frequency modulation at 3.34 T”. In: *Journal of Magnetic Resonance* 238 (2014), pp. 94–105.

[93] Lloyd Lumata, Matthew E Merritt, and Zoltan Kovacs. “Influence of deuteration in the glassing matrix on 13 C dynamic nuclear polarization”. In: *Physical Chemistry Chemical Physics* 15.19 (2013), pp. 7032–7035.

[94] Peder Eric Zufall Larson and Jeremy W Gordon. “Hyperpolarized metabolic mriacquisition, reconstruction, and analysis methods”. In: *Metabolites* 11.6 (2021), p. 386.

[95] Lucian AB Purvis et al. "OXSA: an open-source magnetic resonance spectroscopy analysis toolbox in MATLAB". In: *PloS one* 12.9 (2017), e0185356.

[96] Kasper Hansen et al. "Hyperpolarized 13C MRI Reveals Large Changes in Pyruvate Metabolism During Digestion in Snakes". In: *Magnetic Resonance in Medicine* 88.2 (2022), pp. 890–900.

[97] Patricia V Turner et al. "Administration of substances to laboratory animals: equipment considerations, vehicle selection, and solute preparation". In: *Journal of the American Association for Laboratory Animal Science* 50.5 (2011), pp. 614–627.

[98] Sarah J Nelson et al. "Metabolic imaging of patients with prostate cancer using hyperpolarized [1-13C] pyruvate". In: *Science translational medicine* 5.198 (2013), 198ra108–198ra108.

[99] Surrin S Deen et al. "Hyperpolarized Carbon 13 MRI: Clinical Applications and Future Directions in Oncology". In: *Radiology: Imaging Cancer* 5.5 (2023), e230005.

[100] James T Grist et al. "Quantifying normal human brain metabolism using hyperpolarized [1–13C] pyruvate and magnetic resonance imaging". In: *Neuroimage* 189 (2019), pp. 171–179.

[101] Charles H Cunningham et al. "Hyperpolarized 13C metabolic MRI of the human heart: initial experience". In: *Circulation research* 119.11 (2016), pp. 1177–1182.

[102] Shuyu Tang et al. "Metabolic imaging with hyperpolarized 13C pyruvate magnetic resonance imaging in patients with renal tumorsinitial experience". In: *Cancer* 127.15 (2021), pp. 2693–2704.

[103] Daniel Xia et al. "Gadolinium released from MR contrast agents is deposited in brain tumors: in situ demonstration using scanning electron microscopy with energy dispersive X-ray spectroscopy". In: *Acta Radiologica* 51.10 (2010), pp. 1126–1136.

[104] Luis Hernandez-Garcia, Anish Lahiri, and Jonas Schollenberger. "Recent progress in ASL". In: *Neuroimage* 187 (2019), pp. 3–16.

[105] Jianxun Qu et al. "Recent progress in ASL outside the brain". In: *Chinese Journal of Academic Radiology* 4.4 (2021), pp. 220–228.

[106] Peter Marckmann et al. "Nephrogenic systemic fibrosis: suspected causative role of gadodiamide used for contrast-enhanced magnetic resonance imaging". In: *Journal of the American Society of Nephrology* 17.9 (2006), pp. 2359–2362.

[107] Tomonori Kanda et al. "High signal intensity in the dentate nucleus and globus pallidus on unenhanced T1-weighted MR images: relationship with increasing cumulative dose of a gadolinium-based contrast material". In: *Radiology* 270.3 (2014), pp. 834–841.

[108] Nozomu Murata et al. "Gadolinium tissue deposition in brain and bone". In: *Magnetic resonance imaging* 34.10 (2016), pp. 1359–1365.

[109] Michael F Tweedle, Paul Wedeking, and Krishan Kumar. "Biodistribution of radiolabeled, formulated gadopentetate, gadoteridol, gadoterate, and gadodiamide in mice and rats." In: *Investigative radiology* 30.6 (1995), pp. 372–380.

[110] Katerina Deike-Hofmann et al. “Glymphatic pathway of gadolinium-based contrast agents through the brain: overlooked and misinterpreted”. In: *Investigative radiology* 54.4 (2019), pp. 229–237.

[111] European Medicines Agency. *EMAs final opinion confirms restrictions on use of linear gadolinium agents in body scans*. 2017.

[112] Robert Brünjes and Thilo Hofmann. “Anthropogenic gadolinium in freshwater and drinking water systems”. In: *Water research* 182 (2020), p. 115966.

[113] Maximilian Fuetterer et al. “Hyperpolarized 13C urea myocardial first-pass perfusion imaging using velocity-selective excitation”. In: *Journal of Cardiovascular Magnetic Resonance* 19.1 (2017), pp. 1–12.

[114] Markus Durst et al. “α-trideuteromethyl [15N] glutamine: A long-lived hyperpolarized perfusion marker”. In: *Magnetic resonance in medicine* 76.6 (2016), pp. 1900–1904.

[115] Cornelius Von Morze et al. “Investigating tumor perfusion and metabolism using multiple hyperpolarized 13C compounds: HP001, pyruvate and urea”. In: *Magnetic resonance imaging* 30.3 (2012), pp. 305–311.

[116] Angus Z Lau et al. “Simultaneous assessment of cardiac metabolism and perfusion using copolarized [1-13C] pyruvate and 13C-urea”. In: *Magnetic resonance in medicine* 77.1 (2017), pp. 151–158.

[117] Mark D Lingwood et al. “Hyperpolarized water as an MR imaging contrast agent: feasibility of in vivo imaging in a rat model”. In: *Radiology* 265.2 (2012), pp. 418–425.

[118] Galen D Reed et al. “High Resolution ^{13}C MRI With Hyperpolarized Urea: In Vivo T_2 Mapping and ^{15}N Labeling Effects”. In: *IEEE transactions on medical imaging* 33.2 (2013), pp. 362–371.

[119] Jonas Milani et al. “Hyperpolarization of nitrogen-15 nuclei by cross polarization and dissolution dynamic nuclear polarization”. In: *Review of Scientific Instruments* 88.1 (2017).

[120] Hiroshi Nonaka et al. “A platform for designing hyperpolarized magnetic resonance chemical probes”. In: *Nature communications* 4.1 (2013), p. 2411.

[121] Felix Kreis et al. “Increasing the sensitivity of hyperpolarized [15N2] urea detection by serial transfer of polarization to spin-coupled protons”. In: *Magnetic Resonance in Medicine* 84.4 (2020), pp. 1844–1856.

[122] Joachim MO Vinther et al. “Design of a local quasi-distributed tuning and matching circuit for dissolution DNP cross polarization”. In: *Solid State Nuclear Magnetic Resonance* 102 (2019), pp. 12–20.

[123] Andrew Cho et al. “A non-synthetic approach to extending the lifetime of hyperpolarized molecules using D2O solvation”. In: *Journal of Magnetic Resonance* 295 (2018), pp. 57–62.

[124] Yury Kostyukevich et al. “Hydrogen/deuterium exchange in mass spectrometry”. In: *Mass Spectrometry Reviews* 37.6 (2018), pp. 811–853.

[125] John C Lindon, George E Tranter, and David Koppenaal. *Encyclopedia of spectroscopy and spectrometry*. Academic Press, 2016.

[126] Ayelet Gamliel et al. “Hyperpolarized [15N] nitrate as a potential long lived hyperpolarized contrast agent for MRI”. In: *Journal of Magnetic Resonance* 299 (2019), pp. 188–195.

[127] Riddhiman Sarkar et al. “Proton NMR of 15N-choline metabolites enhanced by dynamic nuclear polarization”. In: *Journal of the American Chemical Society* 131.44 (2009), pp. 16014–16015.

[128] Keiko Kumagai et al. “Synthesis and hyperpolarized 15N NMR studies of 15N-choline-d13”. In: *Tetrahedron* 69.19 (2013), pp. 3896–3900.

[129] R Scott Houliston et al. “pH and urea dependence of amide hydrogen-deuterium exchange rates in the β-trefoil protein hisactophilin”. In: *Biochemistry* 41.4 (2002), pp. 1182–1194.

[130] Lino R Becerra et al. “A spectrometer for dynamic nuclear polarization and electron paramagnetic resonance at high frequencies”. In: *Journal of Magnetic Resonance, Series A* 117.1 (1995), pp. 28–40.

[131] Aany Sofia Lilly Thankamony et al. “Dynamic nuclear polarization for sensitivity enhancement in modern solid-state NMR”. In: *Progress in Nuclear Magnetic Resonance Spectroscopy* 102 (2017), pp. 120–195.

[132] Joseph J Barchi Jr and Caitlin N Strain. “The effect of a methyl group on structure and function: Serine vs. threonine glycosylation and phosphorylation”. In: *Frontiers in Molecular Biosciences* 10 (2023), p. 1117850.

[133] Jan Henrik Ardenkjær-Larsen et al. “Cryogen-free dissolution dynamic nuclear polarization polarizer operating at 3.35 T, 6.70 T, and 10.1 T”. In: *Magnetic Resonance in Medicine* 81.3 (2019), pp. 2184–2194.

[134] Cristina Gabellieri et al. “Therapeutic target metabolism observed using hyperpolarized 15N choline”. In: *Journal of the American Chemical Society* 130.14 (2008), pp. 4598–4599.

[135] Ayelet Gamliel et al. “Signal enhancement of hyperpolarized 15N sites in solutionincrease in solid-state polarization at 3.35 T and prolongation of relaxation in deuterated water mixtures”. In: *NMR in Biomedicine* 35.11 (2022), e4787.

[136] Mariane Le Fur and Peter Caravan. “The biological fate of gadolinium-based MRI contrast agents: a call to action for bioinorganic chemists”. In: *Metallomics* 11.2 (2019), pp. 240–254.

[137] Arianna Ferrari et al. “Performance and reproducibility of 13C and 15N hyperpolarization using a cryogen-free DNP polarizer”. In: *Scientific Reports* 12.1 (2022), p. 11694.

[138] Talia Harris et al. “Long-lived 15N hyperpolarization and rapid relaxation as a potential basis for repeated first pass perfusion imaging–marked effects of deuteration and temperature”. In: *ChemPhysChem* 19.17 (2018), pp. 2148–2152.

[139] Enrico Chiavazza et al. “15N-permethylated amino acids as efficient probes for MRI-DNP applications”. In: *Contrast Media & Molecular Imaging* 8.5 (2013), pp. 417–421.

[140] Cristina Cudalbu et al. “Feasibility of in vivo 15 N MRS detection of hyperpolarized 15N labeled choline in rats”. In: *Physical Chemistry Chemical Physics* 12.22 (2010), pp. 5818–5823.

[141] Fernando Calamante et al. “Bolus delay and dispersion in perfusion MRI: implications for tissue predictor models in stroke”. In: *Magnetic Resonance in Medicine: An Official Journal of the International Society for Magnetic Resonance in Medicine* 55.5 (2006), pp. 1180–1185.

[142] Jina Lee et al. “Mr perfusion imaging for gliomas”. In: *Magnetic Resonance Imaging Clinics* 32.1 (2024), pp. 73–83.

[143] Giuseppe Muscogiuri et al. “Cardiac magnetic resonance tissue characterization in ischemic cardiomyopathy”. In: *Journal of Thoracic Imaging* 37.1 (2022), pp. 2–16.

[144] Rune B Nielsen et al. “Impaired perfusion and capillary dysfunction in prodromal Alzheimer’s disease”. In: *Alzheimer’s & Dementia: Diagnosis, Assessment & Disease Monitoring* 12.1 (2020), e12032.

[145] Anna Kufner et al. “Magnetic resonance imaging-based changes in vascular morphology and cerebral perfusion in subacute ischemic stroke”. In: *Journal of Cerebral Blood Flow & Metabolism* 41.10 (2021), pp. 2617–2627.

[146] Jeffrey R Petrella and James M Provenzale. “MR perfusion imaging of the brain: techniques and applications”. In: *American Journal of roentgenology* 175.1 (2000), pp. 207–219.

[147] Cornelius Von Morze et al. “Simultaneous multiagent hyperpolarized 13C perfusion imaging”. In: *Magnetic resonance in medicine* 72.6 (2014), pp. 1599–1609.

[148] Shawn B Frost et al. “An animal model of capsular infarct: endothelin-1 injections in the rat”. In: *Behavioural brain research* 169.2 (2006), pp. 206–211.

[149] Sandra Puentes et al. “Brain microvascular endothelial cell transplantation ameliorates ischemic white matter damage”. In: *Brain research* 1469 (2012), pp. 43–53.

[150] Juris Rumaks et al. “Search for stroke-protecting agents in endothelin-1-induced ischemic stroke model in rats”. In: *Medicina* 48.10 (2012), p. 77.

[151] Saeed Ansari et al. “Endothelin-1 induced middle cerebral artery occlusion model for ischemic stroke with laser Doppler flowmetry guidance in rat”. In: *JoVE (Journal of Visualized Experiments)* 72 (2013), e50014.

[152] Charu Bharti et al. “Mesoporous silica nanoparticles in target drug delivery system: A review”. In: *International journal of pharmaceutical investigation* 5.3 (2015), p. 124.

[153] Basile Vuichoud et al. “Hyperpolarization of deuterated metabolites via remote cross-polarization and dissolution dynamic nuclear polarization”. In: *The Journal of Physical Chemistry B* 118.5 (2014), pp. 1411–1415.

[154] Céline Taglang et al. “Late-stage deuteration of 13 C-enriched substrates for T 1 prolongation in hyperpolarized 13 C MRI”. In: *Chemical Communications* 54.41 (2018), pp. 5233–5236.

[155] Xiao Ji et al. “Transportable hyperpolarized metabolites”. In: *Nature communications* 8.1 (2017), p. 13975.

[156] Hyejin Park and Qiu Wang. “State-of-the-art accounts of hyperpolarized 15 N-labeled molecular imaging probes for magnetic resonance spectroscopy and imaging”. In: *Chemical Science* 13.25 (2022), pp. 7378–7391.

[157] Michael Vaeggemose, Rolf F. Schulte, and Christoffer Laustsen. “Comprehensive literature review of hyperpolarized Carbon-13 MRI: the road to clinical application”. In: *Metabolites* 11.4 (2021), p. 219.